

# COMPTES RENDUS DE L'ACADÉMIE DES SCIENCES

## *Géoscience* *Sciences de la Planète*



Volume 356, Special Issue S1, 2024

### **Special issue / Numéro spécial**

Magma degassing and its impact on the Earth's atmosphere: from magma oceans to lava lakes / *Impact atmosphérique du dégazage magmatique : des océans de magma aux lacs de lave*

### **Guest editors / Rédacteurs en chef invités**

Manuel Moreira, Bruno Scaillet, Clive Oppenheimer



ACADÉMIE  
DES SCIENCES  
INSTITUT DE FRANCE

Académie des sciences — Paris

ISSN: 1778-7025 (electronic)



# *Comptes Rendus*

---

## *Géoscience*

### **Objective of the journal**

*Comptes Rendus Géoscience* — *Sciences de la Planète* is an international peer-reviewed electronic journal, covering all areas of earth sciences and sustainable development.

It publishes original research articles, review articles, historical perspectives, pedagogical texts or conference proceedings, without length limit, in English or in French and in a format as flexible as necessary (figures, associated data, etc.).

*Comptes Rendus Géoscience* — *Sciences de la Planète* is published since 2020 with the centre Mersenne pour l'édition scientifique ouverte (Mersenne Center for open scientific publishing), according to a virtuous Diamond Open Access policy, free for authors (no author processing charges nor publishing fees) as well as for readers (immediate and permanent open access).

**Editorial director:** Étienne Ghys.

**Editors-in-chief:** Éric Calais, Michel Campillo, François Chabaux, Ghislain de Marsily.

**Associate editors:** Jean-Claude André, Pierre Auger, Mustapha Besbes, Sylvie Bourquin, Yves Bréchet, Marie-Lise Chanin, Philippe Davy, Henri Décamps, Sylvie Derenne, Michel Faure, François Forget, Claude Jaupart, Jean Jouzel, Eric Karsenti, Amaëlle Landais, Sandra Lavorel, Yvon Le Maho, Mickaele Le Ravalec, Hervé Le Treut, Benoit Noetinger, Carole Petit, Valérie Plagnes, Pierre Ribstein, Didier Roux, Bruno Scaillet, Marie-Hélène Tusseau-Vuillemin, Élisabeth Vergès.

**Editorial secretary:** Adenise Lopes.

### **About the journal**

*Comptes Rendus Géoscience* — *Sciences de la Planète* is published exclusively in electronic format. All information on the journal, as well as the full text of all articles, is available on its website at: <https://comptes-rendus.academie-sciences.fr/geoscience/>.

### **Author enquiries**

For any inquiries about submitting a manuscript, please refer to the journal's website: <https://comptes-rendus.academie-sciences.fr/geoscience/>.

### **Contact**

Académie des sciences

23 quai de Conti

75006 Paris (France)

[cr-geoscience@academie-sciences.fr](mailto:cr-geoscience@academie-sciences.fr)



The articles in this journal are published under the license  
Creative Commons Attribution 4.0 International (CC-BY 4.0)  
<https://creativecommons.org/licenses/by/4.0/deed.en>



---

## Contents / Sommaire

<b>Bruno Scaillet, Clive Oppenheimer, Manuel Moreira</b> Magma degassing and its impact on Earth's atmosphere: from magma oceans to lava lakes .....	1-3
<b>Stéphane Labrosse, Adrien Morison, Paul James Tackley</b> Solid-state mantle convection coupled with a crystallising basal magma ocean .....	5-21
<b>Chrystèle Sanloup, Clémence Leroy, Benjamin Cochain, Tobias Grützner, Qi Chen, Yoshio Kono, Guoyin Shen</b> Iodine speciation in basaltic melts at depth .....	23-33
<b>Francesco Vetere, Olivier Namur, Francois Holtz, Renat Almeev, Paola Donato, Francesco Frondini, Michele Cassetta, Alessandro Pisello, Diego Perugini</b> Influence of volatiles (H <sub>2</sub> O and CO <sub>2</sub> ) on shoshonite phase equilibria .....	35-52
<b>Camille Daffos, Caroline Martel, Laurent Arbaret, Rémi Champallier</b> Bubble connectivity in experimentally-sheared crystal-bearing silicic melts .....	53-70
<b>Yves Moussallam, Clive Oppenheimer, Bruno Scaillet</b> A novel approach to volcano surveillance using gas geochemistry .....	71-84
<b>Alessandro Aiuppa, Yves Moussallam</b> Hydrogen and hydrogen sulphide in volcanic gases: abundance, processes, and atmospheric fluxes .....	85-108
<b>Bruno Scaillet, Clive Oppenheimer, Raffaello Cioni, Stephane Scaillet, Yves Moussallam, Gaelle Prouteau, Joan Andujar</b> Constraining sulphur yields of trachytic and phonolitic volcanic eruptions: Tambora, Vesuvius, Laacher See and Campi Flegrei .....	109-126



## Foreword

Magma degassing and its impact on the Earth's atmosphere: from magma oceans to lava lakes

# Magma degassing and its impact on Earth's atmosphere: from magma oceans to lava lakes

Bruno Scaillet<sup>\*,a</sup>, Clive Oppenheimer<sup>b,c</sup> and Manuel Moreira<sup>a</sup>

<sup>a</sup> Institut des Sciences de la Terre d'Orléans, UMR 7327, CNRS–Université d'Orléans–BRGM – Université d'Orléans, Orléans, France

<sup>b</sup> Department of Geography, University of Cambridge, UK

<sup>c</sup> Istituto Nazionale di Geofisica e Vulcanologia, Osservatorio Etneo, Catania, Italy

*E-mails:* [bscaille@cnrs-orleans.fr](mailto:bscaille@cnrs-orleans.fr) (B. Scaillet), [co200@cam.ac.uk](mailto:co200@cam.ac.uk) (C. Oppenheimer), [manuel.moreira@cnrs-orleans.fr](mailto:manuel.moreira@cnrs-orleans.fr) (M. Moreira)

*Manuscript received 19 November 2024, accepted 12 December 2024.*



Photo: The persistent lava lake lying at the bottom of the crater of Ambrym volcano in Vanuatu, and the plume of gases and aerosol discharged by the convecting magma column sustaining the lava lake (credit: C. Oppenheimer).

\*Corresponding author

## Sommaire

1. Avant-propos
2. Labrosse *et al.*
3. Sanloup *et al.*
4. Vetere *et al.*
5. Daffos *et al.*
6. Moussallam *et al.*
7. Aiuppa *et Moussallam*
8. Scaillet *et al.*

Magmas contain significant quantities of volatile compounds, including water (H<sub>2</sub>O), carbon dioxide (CO<sub>2</sub>), sulphur, and halogen species, particularly at high pressures. Their separation through degassing is a critical process in planetary differentiation and plays a central role in shaping planetary atmospheres and climates. Key questions remain regarding the initial volatile inventory within planetary interiors and the mechanisms by which these volatiles are redistributed across the various layers of a planet.

In planets like the Earth, large-scale convection serves to erase pre-existing temperature or density gradients, often leading to partial melting of solid rocks, such as during adiabatic upwelling. These partial melts act as powerful sinks for most volatiles. As a result, magmas are among the primary conduits for volatile redistribution within planetary interiors. When magmas reach the surface, their degassing can impact atmospheric conditions over a range of temporal and spatial scales. This includes secular degassing, which has gradually contributed to the formation of present-day atmospheres, as well as the ephemeral effects of individual volcanic episodes, which can modify atmospheric chemistry and turbidity with resultant climatic change. Volcanic eruptions also have immediate local and regional impacts on surface environments and on society. As a result, scientists are continuously refining monitoring strategies to improve forecasting of the timing and progression of eruptions.

This special issue highlights several ongoing efforts to understand the behaviour of volatiles in magmatic systems. It opens with a contribution from Labrosse *et al.*, who explore the behaviour of a magma ocean at the base of the mantle. The authors develop a new set of equations to model the coupling between a crystallizing basal magma ocean and an overlying convecting mantle, as well as its interaction with the core. Although the role of volatiles is not

directly addressed in this study, it lays the groundwork for future investigations by considering the case of a magma ocean deficient in volatiles (e.g., water or CO<sub>2</sub>). Their results reveal large-scale geochemical heterogeneities that may help explain seismic observations of low-velocity zones at the core-mantle boundary.

In a separate study, Sanloup *et al.* investigate the behaviour of iodine in basaltic magmas under mantle pressures, particularly its speciation, using *in situ* X-ray measurements at high pressures and temperatures. Although iodine is a heavy halogen present in trace amounts in magmas (typically less than 1 ppm), it plays important roles in atmospheric chemistry, particularly in ozone depletion during explosive eruptions. The authors challenge previous assumptions by showing that, at high pressures, iodine binds to oxygen in the melt rather than to network-modifying cations (as is the case with chlorine). This finding suggests that oxidized iodine species may have been overlooked in past studies and could play a role in the degassing of water-poor magmas. This work highlights the need for further research into the speciation of iodine and other halogens in natural silicate melts.

Vetere *et al.* explore the effects of varying H<sub>2</sub>O and CO<sub>2</sub> contents on phase equilibria in a shoshonite basaltic magma sampled from Vulcano, an active volcano in the Aeolian Arc. Phase equilibria experiments are a powerful tool for constraining the effects of volatiles on magma behaviour and identify the storage conditions of magmas beneath active volcanoes. While H<sub>2</sub>O is well-known to depress the melting temperature of silicates, CO<sub>2</sub> was traditionally thought to have little such effect due to its lower solubility in silicate melts. However, Vetere *et al.* show that this is not the case for alkali-rich and water-poor melts, where high CO<sub>2</sub> concentrations decrease crystal fraction, potentially reflecting speciation effects linked to alkali elements. This finding underscores the need for further investigation into the effects of volatiles on such melts.

Daffos *et al.* examine how crystal content and strain influence the degassing behaviour of magmas during ascent in volcanic conduits. The loss or retention of volatiles during ascent dictates eruptive style at the surface. Magmas that retain most of their volatiles until approaching the surface tend to produce explosive eruptions, particularly in arc settings

where magmas are rich in water. Conversely, any factor that promotes volatile loss during ascent will act to reduce explosivity, often leading to lava or dome-forming eruptions. Daffos *et al.* demonstrate, through high-pressure experiments with bubble- and crystal-bearing magmas, that even moderate deformation at relatively low crystal fractions significantly enhances bubble connectivity, thereby facilitating gas loss during magma ascent. This has implications for understanding the dynamics of explosive eruptions, such as the infamous 1902 eruption of Montagne Pelée.

Moussallam *et al.* revisit geochemical gas data from several volcanic regions to identify signals of changes in deep magmatic processes, with a focus on temperature and oxygen fugacity ( $fO_2$ ). Gas monitoring is a key method for forecasting volcanic activity, as the composition and flux of gases escaping from magmatic reservoirs can indicate magma migration, recharge, hydrothermal interaction and pressurization. Using data from three well-monitored active volcanoes in Japan, the authors show that variations in temperature and  $fO_2$  can occur during the course of an eruption, with changes also observable through other petrological proxies. They propose that thermodynamic processing of routinely collected gas compositions could yield real-time insights into ongoing magmatic processes, thereby supporting hazard assessment.

In another study, Aiuppa and Moussallam examine global volcanic gas data to estimate fluxes of

hydrogen ( $H_2$ ) and hydrogen sulphide ( $H_2S$ ). These gases play a crucial role in the Earth's atmosphere, contributing to the balance of oxidized and reduced species, yet their global fluxes remain poorly constrained. The low concentrations of these gases and their rapid oxidation in the atmosphere make them difficult to measure accurately. The authors discuss the factors affecting  $H_2$  and  $H_2S$  concentrations in volcanic gases, such as cooling and rock interactions, and provide new insights into their global fluxes.

Finally, Scaillet *et al.* aim to quantify the sulphur yield from eruptions of alkali-rich and evolved magmas, such as phonolites and trachytes. These magmas have been associated with several major eruptions, including the 1815 eruption of Tambora, which had a significant impact on global climate and is associated with "the year without a summer" of 1816. While the atmospheric and climatic impact of the Tambora eruption has been widely studied, the potential climatic effects of other such events, like the 13 kyr calBP Laacher See eruption, remain uncertain. Scaillet *et al.* use thermodynamic calculations to show that the sulphur yield from alkali-rich magmas is not higher than that of their calc-alkaline counterparts, which dominate explosive eruptions. They suggest that the Laacher See eruption likely did not have a strong global climate impact, highlighting the importance of accurately assessing sulphur content under pre-eruptive conditions on a case-by-case basis.







Research article

## Magma degassing and its impact on the Earth's atmosphere: from magma oceans to lava lakes

# Solid-state mantle convection coupled with a crystallising basal magma ocean

Stéphane Labrosse<sup>✉,\*</sup>, Adrien Morison<sup>✉</sup>,<sup>a</sup> and Paul James Tackley<sup>✉</sup>,<sup>c</sup>

<sup>a</sup> LGLTPE, ENS de Lyon, Université de Lyon, 46 allée d'Italie, 69003 Lyon, France

<sup>b</sup> Univ Exeter, Phys & Astron, Exeter, Devon, England

<sup>c</sup> Department of Earth and Planetary Sciences, ETH Zürich, Sonneggstrasse 5, Zürich, 8092, Switzerland

*E-mails:* [stephane.labrosse@ens-lyon.fr](mailto:stephane.labrosse@ens-lyon.fr) (S. Labrosse), [A.Morison@exeter.ac.uk](mailto:A.Morison@exeter.ac.uk) (A. Morison), [paul.tackley@eaps.ethz.ch](mailto:paul.tackley@eaps.ethz.ch) (P. J. Tackley)

**Abstract.** Fractional crystallisation of a basal magma ocean (BMO) has been proposed to explain the formation of large scale compositional variations in the mantle and the persistence of partially molten patches in the lowermost mantle. We present a complete set of equations for the thermal and compositional evolution of the BMO and show that it can be implemented in a mantle convection code to solve the long term mantle evolution problem. The presence of the BMO modifies the dynamics of the mantle in several ways. The phase equilibrium at the bottom of the solid mantle implies a change of mechanical boundary condition, which helps solid state convection. The net freezing of the BMO implies a change of computational domain, which is treated by mapping the radial coordinate on a constant thickness domain. Fractional melting and freezing at the boundary makes the composition of the BMO and the solid mantle evolve, which is treated using Lagrangian tracers. A sample calculation shows that the persistence of the BMO and its long term evolution drastically changes the dynamics of the solid mantle by promoting downwelling currents and large scale flow. The gradual increase of the FeO content in the BMO and in the solid that crystallises from it leads to the stabilisation of large scale thermo-compositional piles at the bottom of the mantle, possibly explaining the observations from seismology.

**Keywords.** Thermal evolution, Mantle convection, Core cooling, Basal magma ocean.

*Manuscript received 21 May 2024, revised 3 October 2024, accepted 7 October 2024.*

## 1. Introduction

The long term evolution of the Earth is paced by convection in the solid mantle, which is much slower than the dynamics of the underlying liquid core. The present day structure of the mantle is rather well constrained, thanks to the tremendous progress of seismic tomography over the last few decades [e.g.

Fichtner et al., 2024], and is generally well understood in the context of mantle convection in a plate-tectonic regime [e.g. Coltice et al., 2019]. Paleogeographic reconstructions have been used to constrain models of mantle convection going back 1 Gyr [Flament et al., 2022] although, of course, the uncertainties regarding paleogeography increase drastically with ages larger than about 200 Myr, the age of the oldest oceanic plate. These studies generally consider the presence of chemically denser

\*Corresponding author

material in the form of thermochemical piles at the bottom of the mantle as a way to explain the seismically imaged large low shear velocity provinces (LLSVPs) [e.g. Hernlund and McNamara, 2015, for a review].

If we accept the chemical interpretation of LLSVPs, the question of their formation remains. Several scenarios have been proposed. The formation of the Earth could make the mantle initially chemically stratified in two layers and the slow erosion of the stratification by mantle convection could lead to the present state [e.g. Le Bars and Davaille, 2004]. Instead of gradually mixing an initial stratification, dense material produced by the extraction of the oceanic crust could accumulate at the bottom of the mantle after being subducted [Christensen and Hofmann, 1994, Nakagawa *et al.*, 2010, Li and McNamara, 2013]. A last scenario, which is the topic of the present paper, proposes that the fractional crystallisation of a basal magma ocean (BMO) can lead to the stabilisation of chemically different piles at the bottom of the mantle [Labrosse *et al.*, 2007].

In addition to LLSVPs, seismological studies of the deep mantle have uncovered regions of very reduced seismic velocity, on a much smaller scale than LLSVPs, termed ultra low velocity zones (ULVZs). These regions, that can be tens to hundreds of km wide, have seismic velocities about 30% (for S) and 10% (for P) smaller than the surrounding mantle, and a density a few percent larger [Rost *et al.*, 2005], while typical variations of the seismic velocities on the large scale are of the order of a few percent. These extreme velocity reductions, and the fact that the velocity of S waves is more reduced than that of P waves, has been used to imply the presence of partial melt [Williams and Garnero, 1996]. If indeed the mantle in contact with the core is currently partially molten, more melt should have been present in the past when the core was hotter. Indeed, we know that the Earth has been cooling down [Jaupart *et al.*, 2015] and the possibility of the core to be cooling faster than the mantle has been invoked [Driscoll and Bercovici, 2014, Labrosse, 2016, Patočka *et al.*, 2020] to solve the long standing thermal catastrophe problem for the thermal evolution of the Earth [Christensen, 1985]. The rapid core cooling is also a consequence of the necessity to maintain a convective dynamo with a large thermal conductivity of the core [Labrosse, 2015, Patočka *et al.*, 2020]. All these argu-

ments together led to the scenario of a basal magma ocean [Labrosse *et al.*, 2007].

The aim of this paper is to present a first step toward including a basal magma ocean in a fully dynamical model of mantle evolution. Starting with a mantle convection model, in this case StagYY [Tackley, 2008], a first ingredient to add is the possibility of a solid-melt phase change at the boundary with the underlying magma ocean. Compositional changes associated with the phase change are also required. Both aspects have already been reported and the implications of such a boundary have been explored [Labrosse *et al.*, 2018, Agrusta *et al.*, 2019, Bolrão *et al.*, 2021, Lebec *et al.*, 2023, 2024]. The possibility of melting and freezing at one of the horizontal boundaries helps convection in the solid. This effect is included by applying a phase change boundary condition [Alboussière *et al.*, 2010, Mizzon and Monnereau, 2013, Deguen *et al.*, 2013, Deguen, 2013, Labrosse *et al.*, 2018] controlled by a single dimensionless parameter, the phase change number  $\Phi$ . For small values of this parameter ( $\Phi \lesssim 10$ ), the phase change is fast and the critical Rayleigh number for the onset of convection is reduced compared to the situation without phase change or with a slow phase change ( $\Phi \gtrsim 10^3$ ). The heat and mass transfer is also enhanced by the phase change at the boundary.

These previous studies on the effect of a solid-liquid phase change at the boundary did not include the net evolution of the planet, with the possibility of volume change of the basal magma ocean. Including this effect requires several important modifications of the model, which are presented below. Firstly, a numerical treatment of the moving boundary at the bottom of the solid mantle is necessary and this is the topic of Section 2.1. This requires knowing the moving rate of the boundary, which can be determined from the energy balance of the BMO. The relevant theory is presented in Section 2.2. An example calculation is then presented in Section 3 before discussing the implications and limitations of the model in Section 4.

## 2. Physical and numerical model

### 2.1. Convection in the solid mantle

We start with a mantle convection numerical code, StagYY, which can solve the equations for mass,

composition, energy and momentum balances in an infinite-Prandtl-number fluid, like planetary mantles, in various geometries and with many complexities [Tackley, 2008]. This code is widely used in the geodynamics community and needs not be detailed here; only features directly relevant to the present study are presented. The code uses a finite volume approach for the mass, energy and momentum balances and a particle-in-a-cell (PIC) approach for composition [Tackley and King, 2003, Gerya and Yuen, 2003, Ismail-Zadeh and Tackley, 2012]. In the present study, we use the spherical annulus geometry [Hernlund and Tackley, 2008] since the sphericity is important for a proper surface to volume scaling in an evolving planet. In order to keep the study as simple as possible, we consider an incompressible mantle using the Boussinesq approximation, with all physical quantities uniform. With these assumptions, the solid part of the model is controlled by three dimensionless numbers, the Rayleigh number  $Ra$ , the internal heating rate  $H$  and the buoyancy number  $B$ , their usual definition being,

$$Ra = \frac{\alpha g \Delta T d^3}{\kappa \nu}, \quad H = \frac{\rho h d^2}{k \Delta T}, \quad B = \frac{\beta}{\alpha \Delta T}, \quad (1)$$

with  $\alpha$  and  $\beta$  the thermal and compositional (FeO) expansion coefficients, respectively,  $g$  the gravity,  $\kappa$  the thermal diffusivity,  $\nu$  the kinematic viscosity,  $\Delta T$  the temperature scale,  $d$  the thickness of the whole mantle (solid and BMO),  $\rho$  the density and  $h$  the time-evolving radioactive heating rate. Among the parameters entering the definition of the dimensionless numbers,  $\Delta T$  and  $d$  deserve a special discussion since the actual temperature drop across the solid mantle and its thickness, which are normally used as scales to define the dimensionless numbers, vary with the progressive crystallisation of the BMO. We use fixed values (see Appendix) and take into account the variations of the actual values as time-varying factors in the balance equations emerging from our way of dealing with the moving boundary, which is the main modification of the numerical model as presented in previous studies. The solid mantle shell is bounded by two spheres, the basal ocean-mantle boundary (BOMB) with dimensionless radius  $r_{\text{BOMB}}(t)$ , and the Earth surface with dimensionless radius  $R_E$ . We can map the time-varying

spherical shell to a constant one, between rescaled radii 1 and 2, by using as radial coordinate

$$z = 1 + \frac{r - r_{\text{BOMB}}}{R_E - r_{\text{BOMB}}}. \quad (2)$$

This change of radial coordinate implies a change of both radial and temporal derivatives, obtained using the chain rule. Considering a function  $f(r, t) = \tilde{f}(z, t)$ , we get

$$\frac{\partial f}{\partial r} = \frac{\partial z}{\partial r} \frac{\partial \tilde{f}}{\partial z} = \frac{1}{R_E - r_{\text{BOMB}}} \frac{\partial \tilde{f}}{\partial z}, \quad (3)$$

and so on for higher order derivatives. Consider now the time derivative,

$$\frac{\partial f}{\partial t} = \frac{\partial \tilde{f}}{\partial t} + \frac{\partial z}{\partial t} \frac{\partial \tilde{f}}{\partial z} = \frac{\partial \tilde{f}}{\partial t} - \dot{r}_{\text{BOMB}} \frac{R_E - r}{(R_E - r_{\text{BOMB}})^2} \frac{\partial \tilde{f}}{\partial z}, \quad (4)$$

the overdot standing for time derivative. Therefore, the change of BMO radius implies an additional advection term in the equation of energy balance when mapping the domain to a constant one. This additional advection is also applied to tracers. Introducing the time-dependent scaled solid mantle thickness,  $\Gamma = R_E - r_{\text{BOMB}}$ , the dimensionless balance equations for mass, momentum, energy, FeO mass fraction  $\xi$  and concentration  $c_{\text{HPE}}$  of heat producing elements (HPE) become

$$0 = \nabla \cdot \mathbf{u}, \quad (5)$$

$$0 = -\nabla p + \nabla^2 \mathbf{u} + Ra \Gamma^3 [(T - B\xi) - \langle T - B\xi \rangle] \mathbf{e}_z, \quad (6)$$

$$\Gamma^2 \frac{\partial T}{\partial t} = -\mathbf{u} \cdot \nabla T - \dot{\Gamma} \Gamma (2 - z) \frac{\partial T}{\partial z} + \nabla^2 T + H c_{\text{HPE}} \Gamma^2 \exp\left(-\frac{t \ln 2}{\tau_{\text{HPE}}}\right), \quad (7)$$

$$\Gamma^2 \frac{\partial \xi}{\partial t} = -\mathbf{u} \cdot \nabla \xi, \quad (8)$$

$$\Gamma^2 \frac{\partial c_{\text{HPE}}}{\partial t} = -\mathbf{u} \cdot \nabla c_{\text{HPE}}, \quad (9)$$

with  $\mathbf{u}$  the flow velocity,  $T$  the temperature,  $p$  the dynamical pressure. For simplicity, we consider only one heat producing element with a unique half life parameter  $\tau_{\text{HPE}}$  that represents a mean of the four main ones in the Earth,  $^{235}\text{U}$ ,  $^{238}\text{U}$ ,  $^{232}\text{Th}$  and  $^{40}\text{K}$ . The time derivative  $\dot{\Gamma}_{\text{BOMB}}$  is computed from the balance equations for the BMO, which are explained in the next section. This calculation requires knowing the fluxes of heat and FeO, which are directly computed

in StagYY from the temperature field and tracers, respectively. The change with time of bottom temperature,  $T_{\text{BOMB}}(t)$ , does not appear directly in the equations above but is applied as boundary condition at the bottom of the solid mantle. Therefore, the effective Rayleigh and buoyancy numbers at any given time are

$$Ra_{\text{eff}} = Ra\Gamma^3 T_{\text{BOMB}}, \quad B_{\text{eff}} = B \frac{(\langle \xi_{\text{bot}} \rangle - \langle \xi_{\text{top}} \rangle)}{T_{\text{BOMB}}}, \quad (10)$$

where the actual FeO mass fraction difference across the layer is introduced in the definition of the effective buoyancy number.

An important feature of the model, already included in StagYY for a few previous studies [Agrusta *et al.*, 2019, Bolrão *et al.*, 2021, Lebec *et al.*, 2023, 2024], is the solid–liquid phase change boundary condition at the bottom of the solid shell [e.g. Labrosse *et al.*, 2018],

$$2 \frac{\partial u_r}{\partial r} - p - \Phi u_r = 0, \quad (11)$$

$u_r$  being the radial velocity,  $p$  the dynamic pressure and  $\Phi$  the phase change number. This dimensionless parameter is the ratio of two timescales,  $\Phi = \tau_\phi / \tau_\eta$ , with  $\tau_\eta$  the timescale to create a topography from viscous stress in the mantle and  $\tau_\phi$  the timescale to erase it by convection in the liquid layer. The boundary condition, initially derived for the dynamics of the inner core [Deguen *et al.*, 2013], expresses the competition between the generation of a topography by viscous stress in the solid and its removal by melting and freezing. With this equation, the boundary condition can be the classical no-penetrative one for  $\Phi \rightarrow \infty$ , in which case the phase change is effectively prohibited ( $u_r = 0$ ), or of the flow-through type for small values of  $\Phi$ . This boundary condition strongly affects convection: for small values of  $\Phi$ , convection is easier to start [i.e. the critical Rayleigh number for the onset of convection is reduced, see Deguen, 2013, Labrosse *et al.*, 2018, Morison *et al.*, 2024], heat and mass transfer are increased and the wavelength of convection is increased compared to the situation usually considered in mantle convection [Agrusta *et al.*, 2019]. For a purely thermal problem [Deguen *et al.*, 2013], the phase change number can be expressed as

$$\Phi = \frac{\rho_s(\rho_l - \rho_s)Ld}{\rho_l^2 C_{\text{pl}}(m_{\text{ad}} - m_p)u_l\eta_s}, \quad (12)$$

with  $\rho_s$  and  $\rho_l$  the density of the solid and the liquid, respectively,  $L$  the latent heat of fusion,  $C_{\text{pl}}$  the heat capacity of the liquid,  $u_l$  the typical flow velocity in the magma ocean,  $\eta_s$  the viscosity of the solid and  $(m_{\text{ad}} - m_p)$  the difference between the adiabatic gradient in the liquid and the Clapeyron slope. Several parameters are rather uncertain but reasonable estimates give  $\Phi \sim 10^{-8}$  (see Appendix). With such a very small value, we are clearly in the flow-through regime. In that regime, down-welling currents reaching the boundary do not turn and, instead, melt to reach the BMO. For this to happen, the temperature has to reach the boundary temperature, which happens on a short length-scale. Resolving that thin boundary layer can be challenging at large Rayleigh number and we use here the technique introduced by Agrusta *et al.* [2019]: the fixed temperature boundary condition is replaced by a laterally varying Robin boundary condition representing the behaviour on the inner edge of the boundary layer:

$$\mathcal{H}_s(u_r + u_0)\theta + [1 - \mathcal{H}_s(u_r + u_0)]\frac{\partial \theta}{\partial r} = 0, \quad (13)$$

with  $\mathcal{H}_s$  a smooth approximation of the Heaviside function,  $\theta$  the temperature anomaly, and  $u_0$  the reference velocity at which the boundary condition switches behaviour. For  $u_r < -u_0$ , in downwelling regions, the outflow of solid material toward the BMO makes  $\mathcal{H}_s = 0$  and therefore leads to an imposed zero gradient. Conversely, where  $u_r > -u_0$ ,  $\mathcal{H}_s = 1$  and the value of the temperature is set to the freezing one. See Agrusta *et al.* [2019] for more details and benchmark comparisons.

The PIC method consists of using Lagrangian tracers in the domain to carry various quantities as they are transported by the flow, and averaging the relevant quantities on the finite volume grid to compute the flow solution. In the context of the present study, we use a unique compositional information, representing the FeO content of the mineral assemblage. A complexity added to this approach by the phase change boundary condition and already treated by Bolrão *et al.* [2021] comes from the fact that the flow crossing the phase change boundary implies exchange of FeO with the BMO. In practice, when solid material crosses the boundary by melting, the associated tracers are removed while new tracers are added to regions where crystallisation occurs. These new tracers are given the information associated with

their FeO content according to a simple phase diagram model (Equation (19)) [Bolrão *et al.*, 2021]. The net flux of FeO is computed by compiling the information carried by both removed and added tracers. The composition acts on the density through a linearised equation of state to give the last term on the right-hand-side of the momentum equation (6). The buoyancy number  $B$  measures the tendency of FeO entering from the BMO to stabilise against entrainment by thermal convection.

Note that this approach assumes a spherical boundary between the solid mantle and the BMO, i.e. a negligible topography of that boundary. The dynamic topography associated to convection in the solid mantle is in fact included in the theory that leads to the phase change boundary condition Equation (11) [see Labrosse *et al.*, 2018, for a full development], which assumes it to be small. This assumption is consistent with the fact that it is limited by convection in the liquid ocean that tends to erase it by mixing laterally solute and energy.

In addition to the phase change at the bottom boundary of the solid mantle, partial melting could in principle occur anywhere in the bulk, depending on the local temperature and the solidus of the local composition. This possibility is already implemented in StagYY [e.g. Nakagawa and Tackley, 2012], the melt being then extracted to the surface to form a crust, but has not been used in the present paper to focus on the phase change at the bottom boundary.

## 2.2. Evolution of the BMO

The flow of heat and FeO across the boundary between the solid mantle and the BMO makes the boundary move by melting or freezing according to the phase diagram and the conservation of heat and solute in the BMO. The phase diagram prescribes the temperature of the liquidus,  $T_L$ , and the solidus,  $T_S$ , as function of composition and pressure. At the boundary between the solid and the liquid, the temperature equals the solidus of the solid composition and the liquidus of the liquid composition. This dependence on composition makes this evolution depend also on the net flux of FeO between the solid and the liquid, which is due to the partitioning between the two phases upon crystallisation and melting. The heat flow out of the BMO controls the rate of cooling and crystallisation of the BMO to form the

solid mantle and the rate of cooling and crystallisation of core. The evolution of the BMO follows from the global energy balance in much the same way as the evolution of the core. The equations are therefore similar and we follow the theory presented by Labrosse [2015].

### 2.2.1. Evolving reference state

We consider the BMO to be composed of an entirely liquid magma, whose composition can evolve between two end-members, an MgO-rich one and an FeO-rich one. The composition is quantified by the mass fraction of FeO,  $\xi_1$ , the corresponding one in the solid mantle being  $\xi_s$ .

Fractional crystallisation at the top of the BMO releases FeO at the top, which drives compositional convection. Cooling from the top and heating by the underlying core also favor convection. Since both temperature and composition promote convection, we assume that the BMO stays well mixed at all times, such that  $\partial \xi_1 / \partial r = 0$ , and that it is also isentropic on average. Alternatively, the BMO could start stably stratified [Laneuville *et al.*, 2018] but we neglect this possibility in the present study.

We therefore consider a well-mixed isentropic magma ocean whose reference profile of density, temperature, chemical potential, mass fraction of FeO, etc., are linked by the phase equilibrium occurring at the top of the layer. The system is characterised by three state variables, the specific entropy  $s$ , the mass fraction of FeO in the magma  $\xi_1$  and pressure  $P$ . The reference state is well mixed,  $\partial \xi_1 / \partial r = 0$ , isentropic,  $\partial s / \partial r = 0$ , and hydrostatic,  $\partial P / \partial r = -\rho g$ . For the sake of simplicity, the density  $\rho$  is kept constant, and so is the gravitational acceleration  $g$ . In the reference state, the radial derivatives of the temperature  $T$  and chemical potential  $\mu$  come only from the pressure variation. The chemical potential can be obtained using thermodynamic identities by integration of [e.g. Braginsky and Roberts, 1995, Lister and Buffett, 1995, Labrosse, 2015]

$$\frac{\partial \mu}{\partial r} = \left( \frac{\partial \mu}{\partial P} \right)_{s, \xi} \frac{dP}{dr} = -\beta g, \quad (14)$$

$\beta$  being the coefficient of chemical contraction

$$\beta \equiv -\frac{1}{\rho} \left( \frac{\partial \rho}{\partial \xi_1} \right)_{P, s} = \rho \left( \frac{\partial \mu}{\partial P} \right)_{s, \xi}. \quad (15)$$

Note that for FeO in a magma,  $\beta$  here defined is negative. This is opposite to the case of light elements

in the core. Assuming, for simplicity,  $\beta$  and  $g$  to be constant, Equation (14) can readily be integrated to give

$$\mu = \mu^{\text{BOMB}} + \beta g(r_{\text{BOMB}} - r) \equiv \mu^{\text{BOMB}} + \mu' \quad (16)$$

with  $\mu^{\text{BOMB}}$  the chemical potential at the top of the BMO and  $\mu'$  the deviation from that value in the BMO.

Similarly, for the temperature we get the classical isentropic gradient:

$$\frac{\partial T}{\partial r} = \left( \frac{\partial T}{\partial P} \right)_{s,\xi} \frac{dP}{dr} = -\frac{\alpha g T}{C_p}, \quad (17)$$

with  $\alpha$  the thermal expansion coefficient and  $C_p$  the heat capacity at constant pressure. We know that  $\alpha$  generally decreases with pressure and therefore depth [Anderson *et al.*, 1992, Chopelas and Boehler, 1992, Duffy and Ahrens, 1993, Ricard, 2007, Ricard *et al.*, 2022] but since we consider here a magma ocean whose total thickness is a few 100 km only, we consider the assumption of a constant  $\alpha$  as sufficient. Therefore, Equation (17) can be integrated to give

$$T = T^{\text{BOMB}} \exp \left[ \frac{\alpha g (r_{\text{BOMB}} - r)}{C_p} \right], \quad (18)$$

with  $T^{\text{BOMB}}$  the temperature at the top of the BMO. This equation can be safely linearised if that simplifies the expressions.  $T^{\text{BOMB}}$  is equal to the liquidus corresponding to the composition of the magma ocean, which evolves with time. The liquidus also depends on pressure and, for simplicity, we assume a linear dependence of the liquidus on both pressure and mass fraction of FeO, yielding

$$T^{\text{BOMB}} = T_L(r_{\text{BOMB}}) = T_L(r_0) - \frac{\partial T_L}{\partial P} \rho g (r_{\text{BOMB}} - r_0) + \frac{\partial T_L}{\partial \xi} (\xi_1 - \xi_{l0}), \quad (19)$$

with  $r_0$  the initial position of the freezing front,  $\xi_{l0}$  the initial FeO mass fraction of the magma ocean and  $T_L(r_0)$  the corresponding liquidus value. This equation can be time differentiated to give

$$\frac{dT^{\text{BOMB}}}{dt} = -\frac{\partial T_L}{\partial P} \rho g \frac{dr_{\text{BOMB}}}{dt} + \frac{\partial T_L}{\partial \xi} \frac{d\xi_1}{dt}. \quad (20)$$

The two time derivatives on the right-hand-side can be related to each other using the equation for FeO conservation. This and other balance equations are derived in the next subsection.

The different profiles obtained above are only strictly valid in the well mixed isentropic bulk of the magma ocean and are complemented by boundary

layers on both top and bottom. However, as soon as the magma ocean is unstably stratified, which we assume here from the start, the Rayleigh number is enormous and convection is very efficient, which makes the super-isentropic temperature difference across the BMO very small [Labrosse *et al.*, 2007, Ulvrová *et al.*, 2012]. Therefore, we neglect the thickness of boundary layers and their associated temperature, composition and chemical potential jumps.

### 2.2.2. Balance equations

The mass fraction  $\xi_1$  of FeO in the BMO is assumed to be uniform, owing to the high efficiency of convective stirring in the liquid. However, it evolves with time due to interaction with the solid mantle due to fractional crystallisation at the boundary, and possibly exchange by diffusion through the core mantle boundary. The equations describing the evolution of  $\xi_1$  are derived for their introduction in StagYY. The integrated fluxes over the CMB and top surface of the BMO are denoted  $I^{\text{CMB}}$  and  $I^{\text{BOMB}}$ , respectively, and are counted positive upward. The global balance equation for the FeO content is

$$\frac{dM_{\text{BMO}} \xi_1}{dt} = I^{\text{CMB}} - I^{\text{BOMB}}, \quad (21)$$

$M_{\text{BMO}}$  being the mass of the BMO in the  $\xi_1 = 0$  limit. For the time being, we will neglect  $I^{\text{CMB}}$  since its treatment would require constraints on the partitioning between the liquid metal and the liquid silicate at the relevant pressure and temperature and a model for the vertical transfer of light elements at the top of the core. This could be a target for future developments.

With this assumption, Equation (21) can be developed to give

$$M_{\text{BMO}} \frac{d\xi_1}{dt} + 4\pi r_{\text{BOMB}}^2 \rho_0 \xi_1 \dot{r}_{\text{BOMB}} = -I^{\text{BOMB}}. \quad (22)$$

The flux to the solid mantle,  $I^{\text{BOMB}}$ , is due to the phase change happening at the boundary, with a crystallisation mass rate  $w$  associated with the solid radial velocity  $u_r$  at the boundary as computed in StagYY,  $u_r$ , by  $w = u_r - \dot{r}_{\text{BOMB}}$  since, in StagYY, the boundary is kept fixed by a continuous adjustment of the computation domain thickness (Section 2.1). We get

$$I^{\text{BOMB}} = \int_{\Omega_{\text{BOMB}}} \rho_0 \xi_s (u_r - \dot{r}_{\text{BOMB}}) d\Omega, \quad (23)$$

with  $\Omega_{\text{BOMB}}$  the surface of the boundary and  $\xi_s$  the mass fraction of FeO on the solid side of the boundary:

$$\xi_s = \begin{cases} D\xi_1, & u_r \geq 0 \\ \xi_s, & u_r < 0. \end{cases} \quad (24)$$

In regions of solid upwelling, fractional crystallisation occurs, producing a solid with a mass fraction  $\xi_s = D\xi_1$  with  $D < 1$  the partition coefficient of FeO between the solid and the liquid. Note that  $D$  depends on the composition and is related to the distribution coefficient  $K$  of the phase change, as detailed by Bolrão *et al.* [2021]. In regions of downwelling, the solid with a mass fraction  $\xi_s$  arrives in contact with the liquid and melts. Note that the composition of this solid may be different from that for equilibrium with the liquid at its liquidus temperature but melting can still proceed by pumping FeO from the liquid, which acts to reduce the mass fraction FeO in the liquid. This effect is balanced by the release of FeO in regions of crystallisation. The lateral transfer of FeO in the liquid occurs on a timescale,  $\tau_\phi$ , much shorter than the timescale for convection in the solid and the same timescale applies to the transfer of latent heat from regions of freezing to regions of melting. This is taken into account in the dimensionless number  $\Phi = \tau_\phi / \tau_\eta$  which parameterises the boundary condition applied for convection in the solid,  $\tau_\eta$  being the viscous timescale on which a topography is built as a result of viscous stress in the solid [Labrosse *et al.*, 2018].

Combining Equations (22) and (23) gives, after rearrangement:

$$\begin{aligned} & \left( 4\pi r_{\text{BOMB}}^2 \rho_0 \xi_1 - \int_{\Omega_{\text{BOMB}}} \rho_0 \xi_s d\Omega \right) \dot{r}_{\text{BOMB}} \\ & + \frac{4\pi}{3} \rho_0 (r_{\text{BOMB}}^3 - r_{\text{CMB}}^3) \dot{\xi}_1 \\ & = - \int_{\Omega_{\text{BOMB}}} \rho_0 \xi_s u_r d\Omega. \end{aligned} \quad (25)$$

The two integrals in Equation (25) are computed in StagYY at each time-step and that gives the relationship between  $\dot{r}_{\text{BOMB}}$  and  $\dot{\xi}_1$ . Equation (20) then allows us to express the rate of change of  $T^{\text{BOMB}}$  as a function of  $\dot{r}_{\text{BOMB}}$  only.

Note that in the case  $u_r = 0$ , which is obtained for  $\Phi = \infty$ ,  $\xi_s = D\xi_1$  is uniform and the mass flux of FeO to the solid mantle is  $I^{\text{BOMB}} = -4\pi r_{\text{BOMB}}^2 D\xi_1 \rho_0 \dot{r}_{\text{BOMB}}$ .

This flux is positive for  $\dot{r}_{\text{BOMB}} < 0$ , i.e. when crystallisation occurs. Equation (25) leads to

$$\dot{\xi}_1 = - \frac{3r_{\text{BOMB}}^2 \Delta\xi}{r_{\text{BOMB}}^3 - r_{\text{CMB}}^3} \dot{r}_{\text{BOMB}} \quad (26)$$

with  $\Delta\xi = \xi_1 - \xi_s$ . This equation was used in the original BMO paper [Labrosse *et al.*, 2007] but the general Equation (25) accounting for flow through the boundary is used in the present study.

The flux  $\mathbf{i}$  of FeO across both boundaries contributes to the total heat flux density  $\mathbf{q}$  as

$$\mathbf{q} = -k\nabla T + \mu\mathbf{i} \quad (27)$$

and we note the thermal part as

$$\mathbf{q}_T \equiv -k\nabla T. \quad (28)$$

Integrated over a surface  $\Omega$  (BOMB or CMB), we get

$$Q^\Omega = Q_T^\Omega + \mu^\Omega I^\Omega \quad (29)$$

with  $\mu^\Omega$  the average value of  $\mu$  over the surface  $\Omega$ .

The long term thermal evolution of the BMO is controlled by the integrated energy balance equation, which is written as [e.g. Braginsky and Roberts, 1995, Lister and Buffett, 1995]

$$\begin{aligned} & \int_{V_{\text{BMO}}} \rho \left( T \frac{\partial s_1}{\partial t} + \mu \frac{\partial \xi_1}{\partial t} \right) dV \\ & = \int_{\Omega_{\text{BOMB}}} \rho L (u_r - \dot{r}_{\text{BOMB}}) d\Omega \\ & + Q_R + Q^{\text{CMB}} - Q^{\text{BOMB}}, \end{aligned} \quad (30)$$

with  $Q_R$  the radiogenic heat production in the BMO and  $L$  the latent heat of melting, which contains two contributions:

$$L = T_L \Delta s + \mu \Delta \xi \quad (31)$$

$\Delta s = s_1 - s_s$  being the entropy of melting. The surface integral on the right-hand-side of Equation (30) is the total latent released or consumed by phase change at the boundary and is related to the crystallisation change rate  $u_r - \dot{r}_{\text{BOMB}}$ . The entropy contribution to the latent heat,  $T_L \Delta s$ , is uniform along the phase change boundary and, since  $\rho u_r$  averages to 0 at the interface, only the net crystallisation rate  $\dot{r}_{\text{BOMB}}$  contributes to that part. Combining Equation (30) with the global balance in FeO Equation (21)

and the expressions for the BOMB and CMB fluxes Equation (29) gives

$$\begin{aligned}
Q_T^{\text{BOMB}} = & - \int_{V_{\text{BMO}}} \rho T \frac{\partial s}{\partial t} dV \\
& - T_L(r_{\text{BOMB}}) \Delta s 4\pi r_{\text{BOMB}}^2 \dot{r}_{\text{BOMB}} + Q_R + Q_T^{\text{CMB}} \\
& + (\mu^{\text{CMB}} - \mu^{\text{BOMB}}) I^{\text{CMB}} - \frac{d\xi_1}{dt} \int_{V_{\text{BMO}}} \rho \mu' dV \\
& + \int_{\Omega_{\text{BOMB}}} \rho \mu^{\text{BOMB}} (\Delta \xi u_r + \xi_s \dot{r}_{\text{BOMB}}) d\Omega. \quad (32)
\end{aligned}$$

This equation has a simple interpretation: the heat flow out of the BMO has contributions from secular cooling, latent heat of freezing (positive for  $\dot{r}_{\text{BOMB}} < 0$ ), radiogenic heating, heat flow at the CMB, the flux of compositional energy due to the chemical flux at the CMB and the change of compositional energy content in the BMO. Note that the CMB flux term has a sign opposite to  $I^{\text{CMB}}$ , which is expected since mixing any dense component from the core would require energy.

This equation can be used to compute the thermal and compositional evolution of the BMO and the core for a given heat flow at the bottom of the solid mantle. Each term of the equation needs to be expressed as function of a minimum number of parameters, which is the next task here.

As stated above, we will neglect  $I^{\text{CMB}}$ , for now.  $Q_T^{\text{BOMB}}$  is provided at each time step by the convection model of the solid mantle, StagYY. Computing  $Q_R$  is straightforward for a given value of the partition coefficient of heat producing elements at the top of the BMO and their decay constants. The compositional energy term, the one involving  $\mu'$  in Equation (32), is easily related to rate of change of  $r_{\text{BOMB}}$  using Equations (16):

$$\begin{aligned}
E_{\chi 1} \equiv & - \frac{d\xi_1}{dt} \int_{V_{\text{BMO}}} \rho \mu' dV = -\rho_0 \beta g [r_{\text{BOMB}} V_{\text{BMO}} \\
& - \pi (r_{\text{BOMB}}^4 - r_{\text{CMB}}^4)] \frac{d\xi_1}{dt}. \quad (33)
\end{aligned}$$

Using Equation (25), this term can be related to  $\dot{r}_{\text{BOMB}}$ .

The second compositional term (last on the right-hand-side of Equation (32)) can be simplified assuming  $\mu^{\text{BOMB}}$ ,  $\rho$  and  $\xi_1$  to be constant and using the fact that  $u_r$  is 0 on average on the boundary. This gives

$$E_{\chi 2} = \rho_0 \mu^{\text{BOMB}} \int_{\Omega_{\text{BOMB}}} \xi_s (\dot{r}_{\text{BOMB}} - u_r) d\Omega. \quad (34)$$

The secular cooling term is expressed as

$$Q_C \equiv - \int_{V_{\text{BMO}}} \rho T \frac{\partial s}{\partial t} dV = - \int_{V_{\text{BMO}}} \rho C_p \frac{\partial T}{\partial t} dV, \quad (35)$$

which can be computed using the Equations (18) and (20):

$$\begin{aligned}
Q_C = & -4\pi \rho_0 C_p L_M^3 \left[ \frac{dT^{\text{BOMB}}}{dt} + \frac{\alpha g T^{\text{BOMB}}}{C_p} \dot{r}_{\text{BOMB}} \right] \\
& \times \int_{r_{\text{CMB}}/L_M}^{r_{\text{BOMB}}/L_M} x^2 \exp \left[ \frac{\alpha g L_M}{C_p} \left( \frac{r_{\text{BOMB}}}{L_M} - x \right) \right] dx. \quad (36)
\end{aligned}$$

Using Equation (20) and (26), this term can be expressed as an affine function of  $\dot{r}_{\text{BOMB}}$ .

The last term to deal with is the CMB heat flow. The thermal evolution of the core can be parameterised using the CMB temperature [Labrosse, 2015] and we therefore have all the equations needed to solve the coupled evolution of the solid mantle, the BMO and the core. For a liquid core (only situation implemented for the moment), the core cooling term is related to the rate of change of the CMB temperature by

$$Q_T^{\text{CMB}} = - \frac{4\pi}{3} \rho_N C_{pN} L_\rho^3 \frac{f_C \left( \frac{r_{\text{CMB}}}{L_\rho}, \gamma \right)}{\left( 1 - \frac{r_{\text{CMB}}^2}{L_\rho^2} - A_\rho \frac{r_{\text{CMB}}^4}{L_\rho^4} \right)^\gamma} \frac{dT^{\text{CMB}}}{dt}, \quad (37)$$

with  $\rho_N$  the density at the center of the core,  $C_{pN}$  the assumed constant heat capacity of the core,  $L_\rho$  and  $A_\rho$  the structure parameters describing the density variation with radius in the core,  $\gamma$  the Grüneisen parameter of the core and

$$\begin{aligned}
f_C(r, \gamma) = & 3 \int_0^r x^2 (1 - x^2 - A_\rho x^4)^{1+\gamma} dx \\
= & r^3 \left[ 1 - \frac{3}{5}(\gamma+1)r^2 \right. \\
& \left. - \frac{3}{14}(\gamma+1)(2A_\rho - \gamma)r^4 + O(r^6) \right]. \quad (38)
\end{aligned}$$

The boundary layers on both sides of the CMB are tiny, with temperature differences across them that are negligible compared to the temperature differences across the whole layers due to compressibility effects. Therefore, the cooling of the core must follow that of the BMO. More precisely, the CMB temperature is related to that at the top of the BMO using Equation (18):

$$T^{\text{CMB}} = T^{\text{BOMB}} \exp \left[ \frac{\alpha g}{C_p} (r_{\text{BOMB}} - r_{\text{CMB}}) \right]. \quad (39)$$



Therefore, the rate of change of  $T^{\text{CMB}}$  is

$$\frac{dT^{\text{CMB}}}{dt} = \left[ \frac{dT^{\text{BOMB}}}{dt} + \frac{\alpha g T^{\text{BOMB}}}{C_p} \dot{r}^{\text{BOMB}} \right] \times \exp \left[ \frac{\alpha g}{C_p} (r^{\text{BOMB}} - r^{\text{CMB}}) \right]. \quad (40)$$

The equations for the evolution of the BMO and the core presented in this section have been made dimensionless (see Appendix) and implemented in StagYY. In practice, at each time step, the temperature and composition fields in the solid mantle are used to compute the body force responsible for convection. The velocity and pressure fields resulting from the momentum balance are computed, which permits to compute the evolution of the temperature and composition fields, using tracers for the latter. The heat flow at the bottom of the solid mantle is also used to compute the evolution of the BMO and core.

### 3. Example of dynamical evolution

The model is controlled by many input parameters, the classical ones for mantle convection using StagYY [Tackley, 2008] and the additional ones for the BMO evolution, so that the parameter space is effectively enormous. Although we have run many cases, the goal of the present paper is not to provide a comprehensive study of this complex system but to show with one example a possible evolution of the Earth with a basal magma ocean. As will appear clearly, the model results are in some ways encouraging, in the sense that we obtain some of the expected features, in particular thermo-chemical structures that might explain some of the current seismological observations. On the other hand, some of the outcomes point toward strong limitations of this model, at least with the choice of parameters of this specific calculation. Future developments to solve these issues will then be discussed. Even though all the complexities of mantle convection that are included in the numerical code StagYY are also accessible with the BMO model, we restrict ourselves here to the simplest case, notably with a constant viscosity and compositional variations only due to the fractional crystallisation of the BMO.

The parameters specific to the basal magma ocean and its evolution are as follows: the initial thickness is taken to be 30% of the total mantle, the partition coefficients for FeO and the heat producing element

are  $K_{\text{FeO}} = 0.3$ ,  $K_{\text{HPE}} = 10^{-2}$ , respectively and the phase change parameter is  $\Phi = 3 \times 10^{-2}$ . The initial composition of the solid mantle and the BMO are uniform in both FeO and HPE and in equilibrium with each other according to these partition coefficients. The mean mass fraction of FeO is 0.1 while that for HPE makes the mean dimensionless internal heating rate equal to 5, which is somewhat smaller than the expected value for the bulk silicate Earth. The internal heating rate decays exponentially with a dimensionless half-life time of  $10^{-2}$ . The nominal Rayleigh and buoyancy numbers are  $Ra = 3 \times 10^7$ ,  $B = 5$ , respectively. These are defined using, as a temperature scale,  $\Delta T_m$ , an estimate for the melting temperature difference between the top and the bottom of the mantle, so that the dimensionless temperature across the solid  $\Delta T/\Delta T_M$  is of order one. The chosen value is  $\Delta T_M = 4000$  K. The compositional range implied by the definition of  $B$  is 1, which corresponds to the density difference between the MgO and FeO end-members. Since the range of temperature and composition actually encountered in the model are different from these defining values, a rescaling needs to be performed after the calculations, as discussed below. Other parameters are detailed in the Appendix.

Figure 1 shows the evolution of several key fields with time, the temperature (top row), mass fraction of FeO (middle row) and HPE (bottom row). The time of each snapshot is written at the top of each column. The BMO is depicted by a uniform pink layer to visualise its shrinking by crystallisation. The total duration of this calculation, which lasts until nearly full crystallisation of the BMO, is about  $t = 6.4 \times 10^{-3}$  (dimensionless), which is nearly half the dimensionless age of the Earth. This duration clearly depends on the value of several input parameters, and, in particular, is expected to decrease with an increase of the Rayleigh number, since this makes the heat flow increase, and decrease with the buoyancy number, since FeO buoyancy goes against thermal convection.

Convection first sets in at large scale (Figure 1), which is usual for convection with a phase change at the bottom boundary [Labrosse *et al.*, 2018, Morrison *et al.*, 2019, 2024]. Starting from a compositionally uniform mantle, variations of concentrations in FeO and HPEs soon develop from fractional crystallisation of the BMO. In the first three snapshots

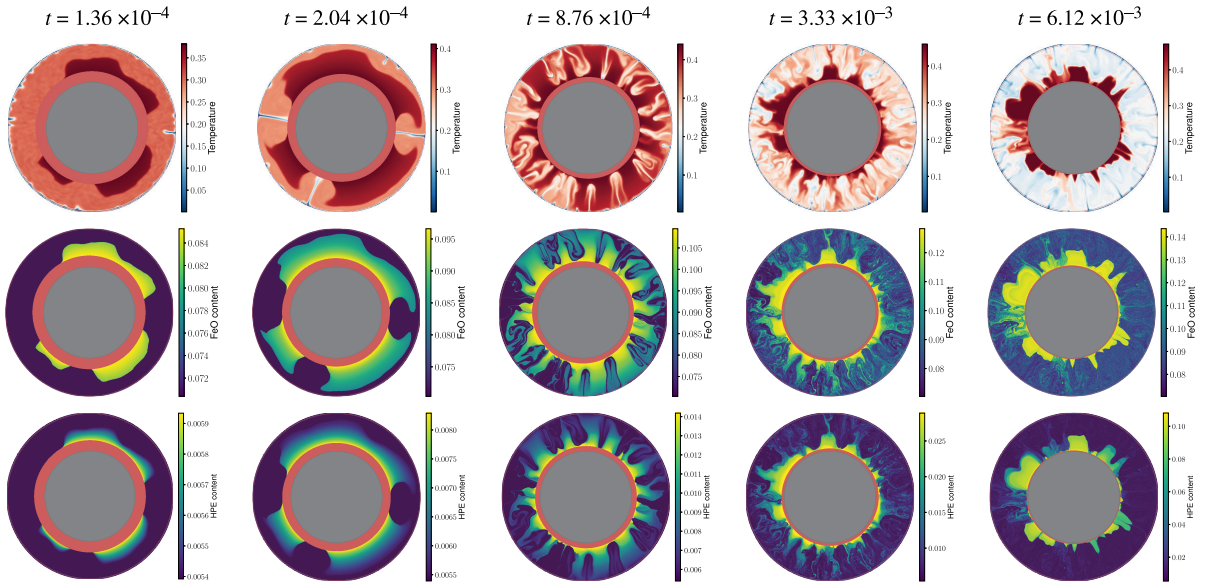


**Figure 1.** Evolution of the temperature (top row), FeO content (middle row) and concentration in heat producing elements (bottom row) as function of time, as indicated on the top. Note that the colorbar is adapted to each snapshot for maximum lisibility.

of Figure 1, variations in FeO content do not seem to affect the dynamics, which is controlled by cold plumes that reach the bottom boundary with the BMO and melt, as expected from previous studies of purely thermal convection with solid–liquid phase change [Agrusta *et al.*, 2019, Lebec *et al.*, 2023]. In the last two snapshots, FeO-enriched regions start forming dome-like structures from which hot plumes depart. This behaviour, that was predicted in the original BMO model [Labrosse *et al.*, 2007], happens when the FeO concentration contrasts become sufficient to compete with the thermal buoyancy.

To better understand the evolution, it is useful to study the mean temperature and composition profiles, as shown on Figure 2. The radius is scaled with the total thickness of the mantle (solid and magma ocean) so that the figure shows the crystallisation of the magma ocean with time.

The FeO mass fraction profiles show a gradual increase with time and, more importantly for the dynamics, an increase of radial contrast. As the BMO concentration in FeO becomes larger, the solids that form from it become enriched and therefore denser, which leads to the partial stratification observed on Figure 1. Figure 3 shows the evolution of the minimum FeO mass fraction at the upper

boundary,  $\min(\xi_{\text{FeO,top}})$ , and the maximum at the bottom boundary,  $\max(\xi_{\text{FeO,bot}})$ . The minimum value is stable, expressing the fact that no diffusion is allowed in this model, while the maximum value, after a rapid increase in the early evolution, increases with an almost constant time rate. The Buoyancy number in this calculation is set to a nominal value of  $B = 5$  but this corresponds to a change of composition between the MgO and FeO end-members and a dimensionless temperature change between 0 and 1. Since the model is evolving with time with fixed temperature and composition scales, the effective buoyancy number at each time is given by Equation (10). The value obtained is also shown on Figure 3. Comparison with the snapshots of Figure 1 suggests that a critical value of  $B_{\text{eff}} \sim 0.5$  makes the convective regime transition between the well mixed situation to the stratified one. Determining the dependence of that number on other parameters of the problem, in particular the Rayleigh number, falls beyond the scope of the present paper. It is however grossly consistent with the value of the buoyancy number needed to get partial entrainment or a doming regime in convection with a compositionally layered initial condition [Tackley, 1998, Davaille, 1999, Le Bars and Davaille, 2004].

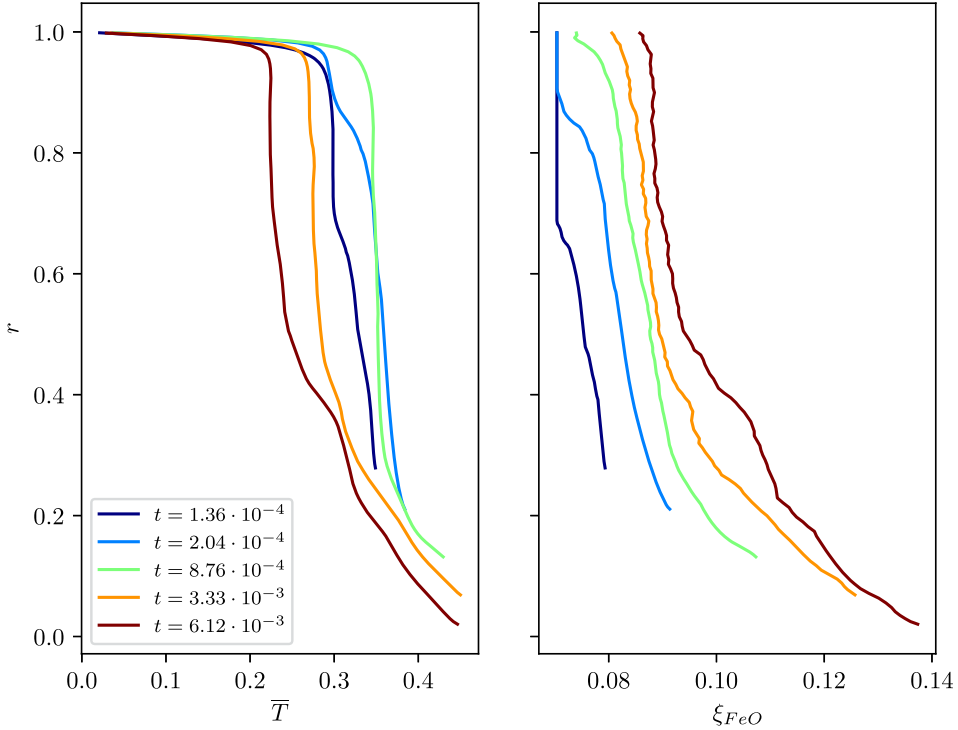


**Figure 2.** Temperature (left) and composition (right) mean profiles for the time steps corresponding to those of Figure 1. The radial position reflects the crystallisation of the BMO with time.

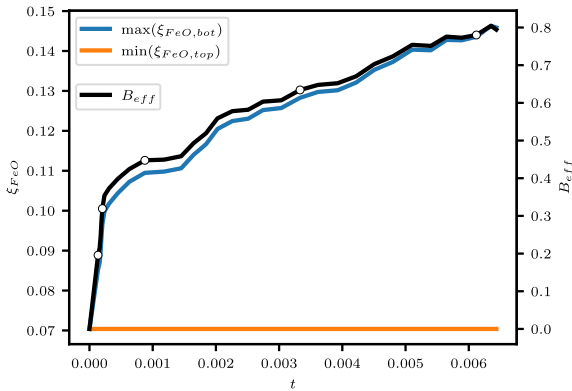


**Figure 3.** Time evolution of the minimum FeO mass fraction at the upper boundary,  $\min(\xi_{\text{FeO,top}})$ , the maximum at the bottom boundary,  $\max(\xi_{\text{FeO,bot}})$  (left axis) and the effective buoyancy number  $B_{\text{eff}}$ , right axis. Empty circles on the black line gives the position of the snapshots presented on Figure 1.

The bottom temperature, equal to the liquidus, also varies with time because of the combined effect

of the pressure (depth) and composition of the magma. With the choice of parameters made for this calculation, the pressure effect dominates over that of FeO mass fraction, which implies an increase of the liquidus with time. At the end of the calculation, the mass fraction of FeO increases faster than pressure at the BMO boundary (BOMB) which makes the liquidus decrease with time. Other choice of parameters would change this evolution and a more realistic phase diagram could be implemented in the future.

A striking feature of the temperature profiles shown on Figure 2 is that, for the long early period where the solid stays well mixed, the mean temperature is nearly independent of the radius and varies significantly only in the upper boundary. Therefore, no boundary layer exists at the bottom and, consequently, no focused hot plumes. This behaviour has already been observed from both linear and non-linear models [Labrosse *et al.*, 2018, Agrusta *et al.*, 2019] in cartesian geometry and results from the phase change boundary condition. In this scenario, hot plumes can only develop once the basal magma ocean gets crystallised enough to get  $\Phi \gtrsim 10^3$  or, as

in the present case, when a compositional stratification separates the phase change boundary from the bulk of the convecting mantle. It is worth recalling here that this model assumes an incompressible solid mantle within the Boussinesq approximation and the development with time of a significant temperature gradient at the bottom of the solid shell is due here solely to the stabilisation of dense thermochemical piles, not to any compressibility effect. To convert these temperature profiles to realistic ones for the Earth requires to add an isentropic temperature gradient.

The concentration in HPE, depicted on the bottom row of Figure 1, is somewhat similar to that of FeO since both come from fractional crystallisation of the BMO. However, because the partition coefficient is much smaller, the enrichment is slower and the mean concentration becomes significant only at the very end of the crystallisation process. Moreover, comparing the various FeO-enriched domes, we can see that their concentrations are not uniform: at the latest stages of their formation, small differences in crystallisation time result in large concentration variations, a phenomenon much less visible for the concentration in FeO which increases in a more gradual manner. Finally, the enrichment in HPEs of the domes makes them warm up and, in some calculations (not shown here), they become unstable at the end of the calculation.

#### 4. Discussion and the way ahead

The model presented in the previous section is the first application of the complete set of equations coupling the evolution of a basal magma ocean to convection in the solid mantle. As such, it provides some interesting results but has some limitations when application to Earth are considered.

First of all, this model is a proof of concept for the possibility of forming large scale compositional variations in the lower mantle from fractional crystallisation of the BMO, as can be seen on Figure 1. The fact that this situation arises at the end of this calculation is linked to the shrinking of the BMO, which is necessary to make its FeO mass fraction increase sufficiently for solids that crystallise from it to be dense enough. Our calculation stops when the BMO crystallises almost entirely. In the present model, the BMO is imposed to fully freeze when a

minimum thickness is reached, while it is assumed to be fully liquid before. In reality, we expect that, at some point, a transition should occur toward a two-phase layer, the present interpretation of ULVZs as partially molten being the last remnant pockets of it. The present model does not include the physics necessary to deal with this transition. This two-phase situation could last quite a long time, the last melt getting enriched in all the incompatible elements, in particular volatiles, which significantly depress the freezing point of the magma [Nomura *et al.*, 2014].

On the other hand, the thermal structure shown in Figures 1 and 2 may be difficult to reconcile with observations constraining the early Earth. Indeed, the absence of boundary layer at the bottom of the solid mantle implies that, except for thin downwelling plumes, the whole solid mantle in our model is at the same temperature as the bottom boundary. This situation, which results from the presence of phase change boundary condition at the bottom [Labrosse *et al.*, 2018, Agrusta *et al.*, 2019, Lebec *et al.*, 2023], is difficult to sustain when applied to the mantle of the Earth since it would lead to very high temperature below the lithosphere, possibly making most of the upper mantle liquid. We expect that such a state would lead to massive eruptions and the associated rapid cooling would not allow it to persist for the length of time implied here [Davies, 1990, Sleep, 2000]. One way to avoid that problem is to increase the value of the phase change parameter,  $\Phi$ . Indeed, for  $\Phi > 10^3$ , the dynamics is similar to that obtained for a non-penetrative boundary condition [Agrusta *et al.*, 2019] with a well-developed boundary layer on the solid side. However, the value of  $\Phi$  is expected to be on the low side, similar to the value used here, although it is difficult to estimate it precisely.

In the present model, the situation with a high upper mantle temperature persists as long as the solid stays well mixed but once a compositional stratification develops, the bulk of the mantle can cool down compared to its bottom boundary (Figure 2). The main problem therefore comes from the initial condition of the calculation. The one shown here starts from a compositionally uniform solid mantle and the variations of composition only arise from fractional crystallisation of the BMO, since testing the feasibility of this mechanism is one of the goals of this paper. The freezing of the surficial magma ocean is, however, likely to produce a compositional stratification of the

solid that could be included as initial condition of our calculations. For example, models of fractional crystallisation of the lunar or martian magma oceans [e.g. Hess and Parmentier, 1995, Elkins-Tanton *et al.*, 2003, Elkins-Tanton, 2012] suggest a gradual densification of the solid that make it prone to overturn and that should produce a solid mantle that is initially stably stratified. The degree of initial stratification can be rather extreme if the overturn happens after full crystallisation but several overturns are expected to occur during crystallisation [Ballmer *et al.*, 2017, Maurice *et al.*, 2017, Boukaré *et al.*, 2018, Morison *et al.*, 2019]. This initial stratification should therefore be considered as an input parameter whose effect should be quantified in future studies.

Alternatively, it could be desirable to run a model coupling the crystallisation of the surficial magma ocean to convection in the solid in order for the initial condition to result directly from this process. This means writing a set of equations similar to the one developed in Section 2.2 for the surficial magma ocean and including phase change boundary condition. Some progress has been done in that direction [Morison, 2019] but a systematic exploitation of this model is still needed and will be the topic of a future study.

## 5. Conclusions

This paper presents, for the first time, a complete set of equations for the evolution of a basal magma ocean coupled to a convecting mantle and a cooling core. This theory has been used to build a model, starting from the mantle convection code StagYY [Tackley, 2008], for the evolution of the whole Earth that tracks the fractional crystallisation of the BMO and the implied compositional evolution of the mantle. The BMO is treated as a well-mixed layer whose evolution is controlled by general energy and composition balance equations. The solid mantle is treated with a full convection model that includes the possibility of melting and freezing at its bottom boundary as a phase change boundary condition [Labrosse *et al.*, 2018].

The parameter space for this model is very large and, in this paper, we have only considered one typical case. It shows, for the first time in a self-consistent dynamical model, the feasibility of the scenario for the generation of large compositionally dense and

heterogenous anomalies proposed by Labrosse *et al.* [2007].

The phase change boundary condition at the bottom of the solid mantle has profound implications on its dynamics and thermal structure: as long as it is well mixed, its bulk temperature follows an isentropic upward extrapolation of the BMO liquidus. This would likely imply large amounts of melting in the upper mantle although, of course, a more thorough exploration of the parameter space is necessary to confirm that implication. In any case, that points toward the necessary discussion of the initial conditions, in particular concerning the compositional structure of the solid mantle, that results from the crystallisation of a surficial magma ocean. Models integrating that aspect in the evolution would help decipher this question.

Another interesting addition to this model would be to include a treatment of volatiles, and in particular water. Assuming water to be incompatible at high pressure, we can expect its concentration to increase in the basal magma ocean as it crystallises, which would help to maintain partial melt to the present day by decreasing the solidus [Nomura *et al.*, 2014]. The solid forming from it would gradually see its H content increase, with important implication on its viscosity and possibly on the melting and degassing of the mantle near the surface.

## Declaration of interests

The authors do not work for, advise, own shares in, or receive funds from any organization that could benefit from this article, and have declared no affiliations other than their research organizations.

## Acknowledgments

We gratefully acknowledge two very constructive reviews that pushed us to improve and clarify the presentation of our paper. The calculation was performed on the cluster of PSMN (Pôle Scientifique de Modélisation Numérique) of the ENS de Lyon.

## Appendix A. Dimensionless numbers and parameter values for the example calculation

We use dimensionless variables in the whole model, both for convection in the solid mantle and the

**Table 1.** Dimensionless parameters for the Basal Magma Ocean evolution

Symbol	Expression	Description	Run value
$\Gamma_0^-$	$\frac{R^- - R_c}{d}$	Initial BMO thickness	0.3
$T_{\text{BOMB},0}$	$\frac{T_{\text{BOMB}}(t=0)}{\Delta T}$	Initial BOMB temperature	0.37
$\xi_0$	$\xi(t=0)$	Initial FeO content	0.07
$c_{\text{HPE},0}$	$c_{\text{HPE}}(t=0)$	Initial HPE content	$5 \times 10^{-3}$
$B$	$-\frac{\beta}{\alpha \Delta T}$	Compositional buoyancy	5
$Di$	$\frac{\alpha g L_M}{C_p}$	BMO dissipation number	1.74
$T_{LP}$	$\frac{\rho g L_M}{\Delta T_M} \frac{\partial T_L}{\partial P}$	Pressure dependence of melting temperature	Depth-dependent from Fiquet <i>et al.</i> [2010]
$T_{L\xi}$	$\frac{1}{\Delta T_M} \frac{\partial T_L}{\partial \xi}$	Composition dependence of melting temperature	-0.125
$St$	$\frac{\Delta s}{C_p}$	Stefan number	0.3
$\tau_{\text{hpe}}$	$\frac{\tau_{\text{hpe},d} \mathcal{K}}{L_M^2}$	HPE half-life	0.02
$P_c$	$\frac{P_{c,d}}{\rho C_p L_M^3}$	Core cooling contribution	3.67

evolution of the BMO and core. The solid mantle part is explained in Section 2.1. The value expected for the phase change number  $\Phi$  can be estimated using its expression in Equation (12) using reasonable values for the various parameters:  $\rho_s \approx 5 \times 10^3 \text{ kg}\cdot\text{m}^{-3}$ ,  $\rho_l \approx 5.5 \times 10^3 \text{ kg}\cdot\text{m}^{-3}$ ,  $C_{pl} \approx 10^3 \text{ J}\cdot\text{K}^{-1}\cdot\text{kg}^{-1}$ ,  $\eta_s \approx 10^{22} \text{ Pa}\cdot\text{s}$ ,  $d \approx 3000 \text{ km}$ . For the latent heat, we use  $L = T\Delta S$ , with  $\Delta S = 652 \text{ J}\cdot\text{kg}^{-1}\cdot\text{K}^{-1}$  the entropy of melting [Stixrude *et al.*, 2009] and  $T \approx 4000 \text{ K}$  the melting temperature. The slopes of the isentropic profile and melting temperatures are estimated from Stixrude *et al.* [2009]:  $m_{\text{ad}} \approx 15 \text{ K}\cdot\text{GPa}^{-1}$ ,  $m_p \approx 4 \text{ K}\cdot\text{GPa}^{-1}$ . The least well constrained quantity is the flow velocity in the BMO and we tentatively set it to a value similar to that in the present-day core,  $u_1 \sim 10^{-4} \text{ m}\cdot\text{s}^{-1}$ . This gives  $\Phi \sim 4 \times 10^{-8}$ . For convection with a phase change boundary condition at one of the horizontal boundaries, the asymptotic limit of very small values of the phase change number is reached for  $\Phi \lesssim 10^{-1}$  [Labrosse *et al.*, 2018, Agrusta *et al.*, 2019, Morison *et al.*, 2024]. The value just estimated for the BOMB

puts it safely in that regime, irrespective of any possible overestimation of the flow velocity in the BMO. We therefore set this value to  $3 \times 10^{-2}$ , which is sufficiently low to get the proper behaviour.

The magma ocean evolution equations are made dimensionless with the following scales:

- $d$ , the total thickness of the mantle (solid and magma ocean), considered constant in this study for simplicity. For the Earth,  $d = 2900 \text{ km}$ .
- $\Delta T$ , an arbitrary reference temperature difference. In practice it is taken as an estimate for the melting temperature difference between the top and the bottom of the mantle, so that the dimensionless temperature across the solid is of order one. The chosen value is  $\Delta T = 4000 \text{ K}$ .
- $\rho$ , the reference density of the considered materials. For the Earth's mantle,  $\rho = 4000 \text{ kg}/\text{m}^3$ .

- $\kappa = k/(\rho C_p)$ , the diffusion coefficient  $\kappa = 10^{-6} \text{ m}^2/\text{s}$ , associated with the conductivity  $k = 4 \text{ W}/(\text{mK})$  and the heat capacity  $C_p = 10^3 \text{ J}\cdot\text{K}^{-1}\cdot\text{kg}^{-1}$ .

The dimensionless parameters arising from the non-dimensionalization are shown in Table 1. More detailed can be found in Morison [2019].

## References

- Agrusta, R., Morison, A., Labrosse, S., Deguen, R., Alboussière, T., Tackley, P. J., and Dubuffet, F. (2019). Mantle convection interacting with magma oceans. *Geophys. J. Int.*, 220, 1878–1892.
- Alboussière, T., Deguen, R., and Melzani, M. (2010). Melting-induced stratification above the Earth’s inner core due to convective translation. *Nature*, 466, 744–747.
- Anderson, O. L., Oda, H., and Isaak, D. (1992). A model for the computation of thermal expansivity at high compression and high temperatures: MgO as an example. *Geophys. Res. Lett.*, 19(19), 1987–1990.
- Ballmer, M. D., Lourenço, D. L., Hirose, K., Caracas, R., and Nomura, R. (2017). Reconciling magma-ocean crystallization models with the present-day structure of the Earth’s mantle. *Geochem. Geophys. Geosyst.*, 18(7), 2785–2806.
- Bolrão, D. P., Ballmer, M. D., Morison, A., Rozel, A. B., Sanan, P., Labrosse, S., and Tackley, P. J. (2021). Timescales of chemical equilibrium between the convecting solid mantle and over-/underlying magma oceans. *Solid Earth*, 12, 421–437.
- Boukaré, C.-E., Parmentier, E., and Parman, S. (2018). Timing of mantle overturn during magma ocean solidification. *Earth Planet. Sci. Lett.*, 491, 216–225.
- Braginsky, S. I. and Roberts, P. H. (1995). Equations governing convection in Earth’s core and the geodynamo. *Geophys. Astrophys. Fluid Dyn.*, 79, 1–97.
- Chopelas, A. and Boehler, R. (1992). Thermal expansivity in the lower mantle. *Geophys. Res. Lett.*, 19(19), 1983–1986.
- Christensen, U. R. (1985). Thermal evolution models for the Earth. *J. Geophys. Res.*, 90, 2995–3007.
- Christensen, U. R. and Hofmann, A. W. (1994). Segregation of subducted oceanic crust in the convecting mantle. *J. Geophys. Res.*, 99(B10), 19867–19884.
- Coltice, N., Husson, L., Faccenna, C., and Arnould, M. (2019). What drives tectonic plates? *Sci. Adv.*, 5(10), article no. eaax4295.
- Davaille, A. (1999). Simultaneous generation of hotspots and superswells by convection in a heterogeneous planetary mantle. *Nature*, 402, 756–760.
- Davies, G. F. (1990). Heat and mass transport in the early earth. In Newsome, H. E. and Jones, J. H., editors, *Origin of the Earth*, pages 175–194. Oxford University Press, New York.
- Deguen, R. (2013). Thermal convection in a spherical shell with melting/freezing at either or both of its boundaries. *J. Earth Sci.*, 24, 669–682.
- Deguen, R., Alboussière, T., and Cardin, P. (2013). Thermal convection in Earth’s inner core with phase change at its boundary. *Geophys. J. Int.*, 194, 1310–1334.
- Driscoll, P. and Bercovici, D. (2014). On the thermal and magnetic histories of Earth and Venus: Influences of melting, radioactivity, and conductivity. *Phys. Earth Planet. Inter.*, 236, 36–51.
- Duffy, T. S. and Ahrens, T. J. (1993). Thermal expansion of mantle and core materials at very high pressures. *Geophys. Res. Lett.*, 20(11), 1103–1106.
- Elkins-Tanton, L. T. (2012). Magma oceans in the inner solar system. *Ann. Rev. Earth Planet. Sci.*, 40, 113–139.
- Elkins-Tanton, L. T., Parmentier, E. M., and Hess, P. C. (2003). Magma ocean fractional crystallization and cumulate overturn in terrestrial planets: Implications for Mars. *Meteorit. Planet. Sci.*, 38(12), 1753–1771.
- Fichtner, A., Kennett, B. L. N., Tsai, V. C., et al. (2024). Seismic tomography 2024. *Bull. Seism. Soc. Am.*, 114, 1185–1213.
- Fiquet, G., Auzende, A. L., Siebert, J., Corgne, A., Bureau, H., Ozawa, H., and Garbarino, G. (2010). Melting of peridotite to 140 GigaPascals. *Science*, 329, 1516–1518.
- Flament, N., Bodur, Ö. F., Williams, S. E., and Merdith, A. S. (2022). Assembly of the basal mantle structure beneath Africa. *Nature*, 603(7903), 846–851.
- Gerya, T. V. and Yuen, D. A. (2003). Characteristics-based marker-in-cell method with conservative finite-differences schemes for modeling geological flows with strongly variable transport properties. *Phys. Earth Planet. Inter.*, 140, 293–318.
- Hernlund, J. and McNamara, A. (2015). 7.11 – the

- core–mantle boundary region. In Schubert, G., editor, *Treatise on Geophysics. Mantle Dynamics*, pages 461–519. Elsevier, Oxford, 2nd edition.
- Hernlund, J. W. and Tackley, P. J. (2008). Modeling mantle convection in the spherical annulus. *Phys. Earth Planet. Inter.*, 171(1–4), 48–54.
- Hess, P. C. and Parmentier, E. M. (1995). A model for the thermal and chemical evolution of the Moon's interior: implications for the onset of mare volcanism. *Earth Planet. Sci. Lett.*, 134, 501–514.
- Ismail-Zadeh, A. and Tackley, P. J. (2012). *Computational Methods for Geodynamics*. Cambridge University Press, Cambridge.
- Jaupart, C., Labrosse, S., Lucazeau, F., and Mareschal, J.-C. (2015). 7.06 – temperatures, heat, and energy in the mantle of the Earth. In Schubert, G. and Bercovici, D., editors, *Treatise on Geophysics. Mantle Dynamics*, pages 223–270. Elsevier, Oxford, 2nd edition.
- Labrosse, S. (2015). Thermal evolution of the core with a high thermal conductivity. *Phys. Earth Planet. Inter.*, 247, 36–55.
- Labrosse, S. (2016). Thermal state and evolution of the Earth core and deep mantle. In Terasaki, H. and Fischer, R., editors, *Deep Earth: Physics and Chemistry of the Lower Mantle and Core*, AGU Geophysical Monograph Series, pages 43–56. American Geophysical Union, Washington DC.
- Labrosse, S., Hernlund, J. W., and Coltice, N. (2007). A crystallizing dense magma ocean at the base of Earth's mantle. *Nature*, 450, 866–869.
- Labrosse, S., Morison, A., Deguen, R., and Alboussière, T. (2018). Rayleigh–Bénard convection in a creeping solid with a phase change at either or both horizontal boundaries. *J. Fluid Mech.*, 846, 5–36.
- Laneuville, M., Hernlund, J., Labrosse, S., and Guttenberg, N. (2018). Crystallization of a compositionally stratified basal magma ocean. *Phys. Earth Planet. Inter.*, 276, 86–92.
- Le Bars, M. and Davaille, A. (2004). Whole layer convection in a heterogeneous planetary mantle. *J. Geophys. Res.*, 109, article no. B03403.
- Lebec, L., Labrosse, S., Morison, A., and Tackley, P. J. (2023). Scaling of convection in high-pressure ice layers of large icy moons and implications for habitability. *Icarus*, 396, article no. 115494.
- Lebec, L., Labrosse, S., Morison, A., and Tackley, P. J. (2024). Effects of salts on the exchanges through high-pressure ice layers of large ocean worlds. *Icarus*, 412, article no. 115966.
- Li, M. and McNamara, A. K. (2013). The difficulty for subducted oceanic crust to accumulate at the Earth's core–mantle boundary. *J. Geophys. Res.*, 118(4), 1807–1816.
- Lister, J. R. and Buffett, B. A. (1995). The strength and efficiency of the thermal and compositional convection in the geodynamo. *Phys. Earth Planet. Inter.*, 91, 17–30.
- Maurice, M., Tosi, N., Samuel, H., Plesa, A.-C., Hüttig, C., and Breuer, D. (2017). Onset of solid-state mantle convection and mixing during magma ocean solidification. *J. Geophys. Res.: Planets*, 122(3), 577–598.
- Mizzon, H. and Monnereau, M. (2013). Implication of the lopsided growth for the viscosity of Earth's inner core. *Earth Planet. Sci. Lett.*, 361, 391–401.
- Morison, A. (2019). *Convection dans le manteau primitif en interaction avec des océans de magma globaux*. Phd thesis, Université de Lyon, ENS de Lyon.
- Morison, A., Labrosse, S., Deguen, R., and Alboussière, T. (2019). Timescale of overturn in a magma ocean cumulate. *Earth Planet. Sci. Lett.*, 516, 25–36.
- Morison, A., Labrosse, S., Deguen, R., and Alboussière, T. (2024). Onset of thermal convection in a solid spherical shell with melting at either or both boundaries. *Geophys. J. Int.*, 238, 1121–1136.
- Nakagawa, T. and Tackley, P. J. (2012). Influence of magmatism on mantle cooling, surface heat flow and urey ratio. *Earth Planet. Sci. Lett.*, 329–330, 1–10.
- Nakagawa, T., Tackley, P. J., Deschamps, F., and Connolly, J. A. D. (2010). The influence of MORB and harzburgite composition on thermo-chemical mantle convection in a 3-D spherical shell with self-consistently calculated mineral physics. *Earth Planet. Sci. Lett.*, 296(3–4), 403–412.
- Nomura, R., Hirose, K., Uesugi, K., Ohishi, Y., Tsuchiyama, A., Miyake, A., and Ueno, Y. (2014). Low core-mantle boundary temperature inferred from the solidus of pyrolite. *Science*, 343(6170), 522–525.
- Patočka, V., Šrámek, O., and Tosi, N. (2020). Minimum heat flow from the core and thermal evolution of the Earth. *Phys. Earth Planet. Inter.*, 305, article no. 106457.



- Ricard, Y. (2007). Physics of mantle convection. In Bercovici, D. and Schubert, G., editors, *Treatise of Geophysics. Mantle Dynamics*, volume 7, pages 253–303. Elsevier, Oxford.
- Ricard, Y., Alboussière, T., Labrosse, S., Curbelo, J., and Dubuffet, F. (2022). Fully compressible convection for planetary mantles. *Geophys. J. Int.*, 230(2), 932–956.
- Rost, S., Garnero, E. J., Williams, Q., and Manga, M. (2005). Seismological constraints on a possible plume root at the core-mantle boundary. *Nature*, 435, 666–669.
- Sleep, N. H. (2000). Evolution of the mode of convection within terrestrial planets. *J. Geophys. Res.*, 105, 17563–17578.
- Stixrude, L., de Koker, N., Sun, N., Mookherjee, M., and Karki, B. B. (2009). Thermodynamics of silicate liquids in the deep Earth. *Earth Planet. Sci. Lett.*, 278, 226–232.
- Tackley, P. J. (1998). Three-dimensional simulations of mantle convection with a thermochemical CMB boundary layer: D"? In Gurnis, M., Wyession, M. E., Knittle, E., and Buffett, B. A., editors, *The Core-Mantle Boundary Region*, pages 231–253. American Geophysical Union, Washington DC.
- Tackley, P. J. (2008). Modelling compressible mantle convection with large viscosity contrasts in a three-dimensional spherical shell using the yin-yang grid. *Phys. Earth Planet. Inter.*, 171(1–4), 7–18.
- Tackley, P. J. and King, S. D. (2003). Testing the tracer ratio method for modeling active compositional fields in mantle convection simulations. *Geochem. Geophys. Geosyst.*, 4(4), article no. 8302.
- Ulvrová, M., Labrosse, S., Coltice, N., Raback, P., and Tackley, P. J. (2012). Numerical modeling of convection interacting with a melting and solidification front: application to the thermal evolution of the basal magma ocean. *Phys. Earth Planet. Inter.*, 206–207, 51–66.
- Williams, Q. and Garnero, E. J. (1996). Seismic evidence for partial melt at the base of earth's mantle. *Science*, 273(5281), 1528–1530.





Research article

## Magma degassing and its impact on the Earth's atmosphere: from magma oceans to lava lakes

# Iodine speciation in basaltic melts at depth

Chrystèle Sanloup<sup>\*,a,b</sup>, Clémence Leroy<sup>a</sup>, Benjamin Cochain<sup>c</sup>, Tobias Grützner<sup>d</sup>, Qi Chen<sup>e</sup>, Yoshio Kono<sup>f</sup> and Guoyin Shen<sup>g</sup>

<sup>a</sup> Institut de minéralogie, physique des matériaux et cosmochimie, Sorbonne Université, CNRS, 4 Place Jussieu, France

<sup>b</sup> Institut Universitaire de France (IUF), Paris, France

<sup>c</sup> Institut de minéralogie, physique des matériaux et cosmochimie, Sorbonne Université, CNRS, 4 Place Jussieu, Paris, France

<sup>d</sup> Institut für Geowissenschaften, Goethe-Universität Frankfurt, Germany

<sup>e</sup> Department of Earth Science & Environmental Change, University of Illinois at Urbana Champaign, Urbana, IL, USA

<sup>f</sup> Department of Physics and Astronomy, Kwansei Gakuin University, Sanda, Japan

<sup>g</sup> HPCAT, X-ray Science Division, Argonne National Laboratory, Argonne, USA

*E-mails:* chrystele.sanloup@sorbonne-universite.fr (C. Sanloup), cl.clemenceleroy@gmail.com (C. Leroy), benjamin.cochain@gmail.com (B. Cochain), tobias.gruetzner@outlook.com (T. Grützner), qichen22@illinois.edu (Q. Chen), yoshiokono@kwansei.ac.jp (Y. Kono), gyshen@anl.gov (G. Shen)

**Abstract.** The speciation of iodine in basalts has been investigated by combining in situ X-ray diffraction at high pressures and temperatures up to 4.9 GPa and 1600 °C, and Raman spectroscopy on recovered high pressure glasses at ambient conditions. Both methods point to iodine being oxidized in basalts, whether molten or quenched as glasses. Observed interatomic distances and Raman vibrational modes are consistent with iodine being dissolved as complex iodate groups alike polyiodates or periodates, not as IO<sub>3</sub><sup>-</sup> groups. Iodine speciation in basalts therefore seems to reflect a trend amongst halogens, with lighter chlorine bonding to network modifying cations, and bromine changing affinity from network modifying cations to oxygen anions under pressure. In the absence of a fluid aqueous phase, iodine could thus reach the Earth's surface in basaltic magmas as an oxide, not as a reduced species.

**Keywords.** Iodine, Basalt, High pressure.

**Funding.** European Research council under the European Community's Seventh Framework Programme (FP7/20072013 Grant Agreement No. 259649), ANR Projet de Recherche Collaborative VOLC-HAL-CLIM (Volcanic Halogens: from Deep Earth to Atmospheric Impacts, ANR-18-CE01-0018), EU Marie Skłodowska-Curie Fellowship "ExCliso" (Project ID 101017762), CSC scholarship (#201806340094), DOE Office of Science by Argonne National Laboratory under Contract No. DE-AC0206CH11357.

*Manuscript received 25 July 2024, revised 23 October 2024, accepted 4 November 2024.*

\*Corresponding author

## 1. Introduction

Halogens can provide key insights into magmatic processes ranging from partial melting to volcanic eruptions [Webster *et al.*, 2018] if their behaviour is fully understood from fluorine to iodine. However, iodine is the least investigated halogen in magmatic and volcanic processes, in relation with its lowest abundance both in magmas [Kendrick *et al.*, 2012, 2014] and in volcanic plumes [Aiuppa *et al.*, 2005]. It is nonetheless an important element as it impacts atmospheric chemistry through ozone depletion [Solomon *et al.*, 1994], having the largest ozone-depleting efficiency [Cuevas *et al.*, 2022].

As for most elements, iodine speciation controls its solubility, transport, and eventual elemental and isotopic fractionation between coexisting phases. Progresses have been made towards the understanding of its transfer between reservoirs, especially between magmas and aqueous fluids to assess the extent of its degassing [Bureau *et al.*, 2000, Leroy *et al.*, 2019], but not on its speciation in natural magmas. There are besides no available *in situ* data on iodine speciation in silicate melts, *i.e.* under high temperature ( $T$ ) and high pressure ( $P$ ) conditions. Available data on iodine speciation in silicate glasses have been obtained using Raman, X-ray photoelectron and/or X-ray absorption spectroscopies on borosilicate melts quenched from high  $P$ - $T$  conditions [Ciccconi *et al.*, 2019, Morizet *et al.*, 2021], in order to understand and better predict iodine behaviour and eventual mobility in nuclear waste glasses. Consequently, there is a lack of data on iodine speciation in natural magmas in general, and in particular at the high  $P$ - $T$  conditions at which they form and ascend.

Here, we report *in situ* high  $P$ - $T$  synchrotron X-ray diffraction data (XRD) on basaltic magmas, and Raman spectroscopy data on recovered quenched glasses. High  $P$  are necessary to dissolve sufficient amount of iodine so that its effect on magmas properties can be measured, but more importantly because arc magmas that are produced at greater depths hence greater pressures than oceanic ridge basalts are the most relevant to investigate iodine speciation, due to recycling of marine sedimentary components that bring iodine to the arc magma source [Muramatsu and Wedepohl, 1998].

The choice of Saint Vincent island (Lesser Antilles arc) basalt [Pichavant *et al.*, 2002] and of Mount Etna

basalt (from 2002/2003 South scoria [Gennaro *et al.*, 2019]) was guided by the need to reflect a range of volatile-rich basalts, with high MgO Saint Vincent basalt being representative of one type of primary magma in subduction zones, and Mount Etna alkali basalt representative of later stage basalt differentiated through fractional crystallization and degassing.

## 2. Materials and methods

### 2.1. Glass synthesis

Starting natural basalt samples were ground, doped with NaI as iodine source, and with deionised milli-Q water added in the case of Saint Vincent basalt. When investigating the local environment of a trace element in a magma, one must reach a compromise between lowest amount possible and detection above noise level to avoid interaction between iodine ions that would occur for elevated concentrations. Two iodine levels were targeted, circa 3 wt% for the Saint Vincent basalt, and circa 1 wt% for the Etna basalt. Since iodine solubility increases with  $P$ , I-doping was done at 3.5 GPa and 1600 °C for the Saint Vincent basalt using platinum capsules welded at both ends, and at 1 GPa and 1350 °C for the Etna composition using gold-palladium capsules which have a lower  $T$ -stability but prevent Fe loss to the capsule unlike for Saint Vincent basalt that became almost FeO-free. Having two different FeO content turned out to be essential in assessing iodine local environment in the melt (*cf.* Section 3.2). For both compositions, I-free glasses were synthesized under the same conditions. High  $P$ - $T$  conditions were generated by a Depth of the Earth piston cylinder press using a half inch talc-pyrex cell assembly with a graphite heater;  $T$  was monitored using a W/Re thermocouple, run duration at high  $T$  was one hour.

### 2.2. High $P$ - $T$ X-ray diffraction experiments

The recovered glass from piston cylinder press experiments was extracted from the platinum or gold-palladium capsule, crushed, and loaded in either graphite capsule (Saint Vincent basalt) or in single crystal diamond capsules with inner graphite caps and sealed under  $P$  by Pt-5%Rh caps (Etna basalt). High  $P$ - $T$  conditions (Table 1) were achieved using a Paris-Edinburgh press with cell-assembly (Figure 1) as described in Yamada *et al.* [2011]. This

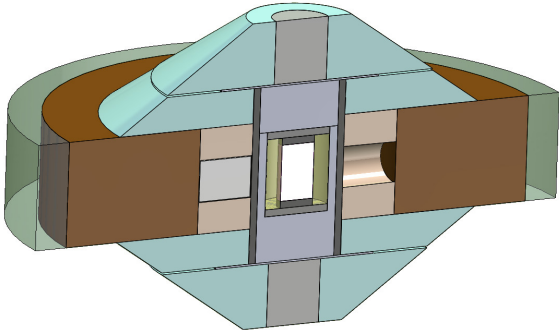


**Figure 1.** Sketch of the cell-assembly used for in situ high  $P$ - $T$  X-ray diffraction experiments [Yamada *et al.*, 2011]. Sample (inner white rectangle) is packed either in a graphite capsule or in a single crystal diamond cylinder (as drawn here, inner diameter: 1.0 mm), covered by inner graphite caps and sealed by Pt-Rh caps.

cell-assembly is designed to optimize the sample signal by using low absorbing materials along the X-ray path (boron epoxy and hBN windows inside the MgO ring outside the graphite heater), while ZrO<sub>2</sub> parts away from the X-ray path insure cell-assembly stability at high  $P$ - $T$  conditions. Talc powder was added on top and bottom of graphite capsules, to act as  $fO_2$  buffer. Temperature was calculated from power- $T$  curve calibrated against melting temperatures of salts [Kono *et al.*, 2014], and  $P$  was calculated from the cell volume of MgO cylinder surrounding sample capsule [Kono *et al.*, 2010]. Uncertainties on  $P$  and  $T$  are respectively 0.3 GPa and 80 °C. While most runs were carried at  $T$  above the liquidus, two experiments were run between solidus and liquidus  $T$  (TGH25 and TGH26).

In situ high  $P$ - $T$  experiments were conducted using energy-dispersive XRD on beamline 16-BM-B at the Advanced Photon Source (Argonne, USA). The incident beam was collimated by tungsten slits (0.3 mm vertical  $\times$  0.1 mm horizontal) and the diffracted signal was collected by an energy-dispersive germanium solid-state detector. In the molten state, X-ray diffraction data were collected at different  $2\theta$  angles (2°, 2.7°, 3.5°, 5°, 7°, 10°, 15°, 20°, and 27°) thus covering up to 15 Å<sup>-1</sup> in  $q$ -space ( $q = 4\pi E \sin\theta / 12.398$ , where  $E$  is the energy of the X-rays in keV ranging up to 125 keV).

The multi-angle energy dispersive X-ray diffraction spectra were converted into the structure factor  $S(q)$  using analysis software package (aEDXD) program developed by Changyong Park [Kono *et al.*, 2014]. The real-space radial distribution function,  $g(r)$ , that described the short-order range structure (i.e. interatomic relations within 5–6 Å) was obtained by Fourier Transform of the spline smoothed  $S(q)$ :

$$g(r) = 1 + \frac{1}{4\pi r n} \int_0^{q_{\max}} q(S(q) - S_{\infty}) \sin(qr) dq \quad (1)$$

where  $n$  is the atomic density in atoms per Å<sup>3</sup> ( $n = N_A M / \rho$ , with  $N_A$  the Avogadro's constant,  $M$  the mean atomic molar mass of samples, and  $\rho$  their mass density).

### 2.3. Starting and recovered samples analyses

Samples were polished for textural analyses using a Zeiss Ultra 55 field emission scanning electron microscope (SEM) at OSU Ecce Terra, Sorbonne Université, followed by chemical analyses (Table 1) carried at the Camparis center, Sorbonne Université, using a Cameca SX-FIVE electron probe microanalyser (EPMA) with accelerating voltage set at 15 keV, beam current at 4 nA, and a defocussed beam (7 μm radius).

Raman spectra were recorded on a Jobin Yvon Horiba HR460 spectrometer using a single-grating monochromator with 1500 gratings/mm and an argon laser (514.5 nm wavelength).

## 3. Results

### 3.1. Quenched texture and composition of starting and recovered glasses

Nanosize iodine droplets are observed on Saint Vincent basalt starting glasses (PC82 and PC83, Figure 2a), and could either be quench products or due to iodine oversaturation as those samples have the highest iodine content (Table 1). Such nanodroplets are not observed in other samples, including Saint Vincent glass recovered from XRD experiment which moreover was conducted at higher  $P$  (APS run 13) than during piston-cylinder press synthesis, i.e. at conditions of higher iodine solubility. Iodine was thus fully dissolved in molten basalts probed by XRD.

Recovered Etna basalt samples from XRD experiments, either I-doped or not, contain droplets of

**Table 1.** Chemical analyses (wt%). Starting and recovered samples

Sample <i>P-T</i> conditions	SiO <sub>2</sub>	TiO <sub>2</sub>	Al <sub>2</sub> O <sub>3</sub>	FeO	MgO	CaO	Na <sub>2</sub> O	K <sub>2</sub> O	I	Total*
	(Standard deviations)									
Saint Vincent basalt (glass), starting and recovered samples from XRD experiments										
PC82**	46.91	1.37	15.16	0.95	11.58	10.58	2.98	0.50	2.97	96.59
3.5 GPa-1600 °C	(0.51)	(0.27)	(0.09)	(0.15)	(0.18)	(0.08)	(0.58)	(0.04)	(0.22)	
PC83	47.95	1.36	15.57	1.24	12.33	10.94	2.84	0.46	2.90	95.59
3.5 GPa-1600 °C	(0.92)	(0.10)	(0.47)	(0.13)	(0.19)	(0.34)	(0.18)	(0.07)	(0.14)	(1.28)
APS run 13	47.16	1.30	15.42	0.70	12.42	10.78	2.55	0.38	2.26	93.2
4.7 GPa-1600 °C	(0.86)	(0.07)	(0.40)	(0.10)	(0.23)	(0.18)	(0.11)	(0.09)	(0.19)	(1.13)
APS run 26	51.14	1.14	16.52	0.58	12.97	11.57	2.41	0.48	–	97.06
4.9 GPa-1600 °C	(0.93)	(0.11)	(0.32)	(0.15)	(0.16)	(0.27)	(0.11)	(0.05)	–	(0.72)
Etna basalt (glass), recovered samples from XRD experiments										
APS Etna2002	49.38	1.92	18.35	3.86	5.91	11.38	3.63	2.24	–	96.91
1.0 GPa-1250 °C	(0.46)	(0.15)	(0.40)	(0.37)	(0.14)	(0.25)	(0.16)	(0.24)	–	(0.79)
APS 20BaM19	46.79	1.94	17.31	3.88	6.88	11.49	3.82	2.06	0.80	95.20
1.3 GPa-1120 °C	(0.66)	(0.10)	(0.29)	(0.04)	(0.10)	(0.31)	(0.13)	(0.13)	(0.09)	(0.81)
Etna basalt (glass+clinopyroxenes), recovered samples from X-ray diffraction (XRD) experiments										
APS TGH25 glass	49.73	2.00	19.20	7.04	3.55	8.40	4.73	2.91	–	97.85
3.7 GPa-1450 °C	(0.97)	(0.05)	(0.28)	(0.34)	(0.09)	(0.32)	(0.17)	(0.21)		(1.19)
APS TGH27 glass	50.30	1.85	19.31	3.52	4.35	7.55	4.76	3.09	1.15	96.23
3 GPa-1550 °C	(0.58)	(0.11)	(0.54)	(0.23)	(0.16)	(0.17)	(0.21)	(0.19)	(0.10)	(0.17)

\* Note that ‘Total’ does not include water content, that varies from 1.6(0.3) to 3.8(0.5) wt% as measured only for PC83 and PC82 respectively Leroy *et al.* [2019].

\*\* Data from Leroy *et al.* [2019]. Note that Etna basalt samples were recovered from XRD experiments still embedded in their diamond capsule, hence high quality polishing could not be achieved.

metallic iron (Figure 2c), indicating reduction from FeO. This is not observed in recovered Saint Vincent glasses, as those contained very little FeO in the starting glass (less than 1 wt%, Table 1), and remained homogeneous (Figure 2b).

### 3.2. Melt structure: X-ray diffraction

To investigate the effect of iodine on melt structure, both I-doped and I-free basaltic melts were probed. In case of co-existence of melt and crystals, the press was moved relative to X-ray beam position until area free of crystals could be probed. Amongst the three pairs of I-doped/I-free runs (Table 1), two provided sufficiently high quality data to extract radial

distribution functions (APS runs 13/26 and APS TGH25/27, Figure 3). The structure factor,  $S(q)$ , of the I-doped melts have a weaker first-sharp diffraction peak (highest intensity near  $2 \text{ \AA}^{-1}$  on Figure 3 left panel) compared to the I-free melts, indicative of a lesser degree of medium-range order [Salmon, 1994], in other words, a lesser degree of polymerisation. APS runs 13 and 26 have different hydration levels in the starting samples (1.6 vs 3.8 wt% H<sub>2</sub>O), which also contributes to a lesser degree of depolymerisation in I-doped APS run 13. However Etna basalts were not hydrated prior to XRD experiments, but are similarly impacted by the presence of iodine.

The effect of iodine on the radial distribution function  $g(r)$  (Figure 3 right panel) is less

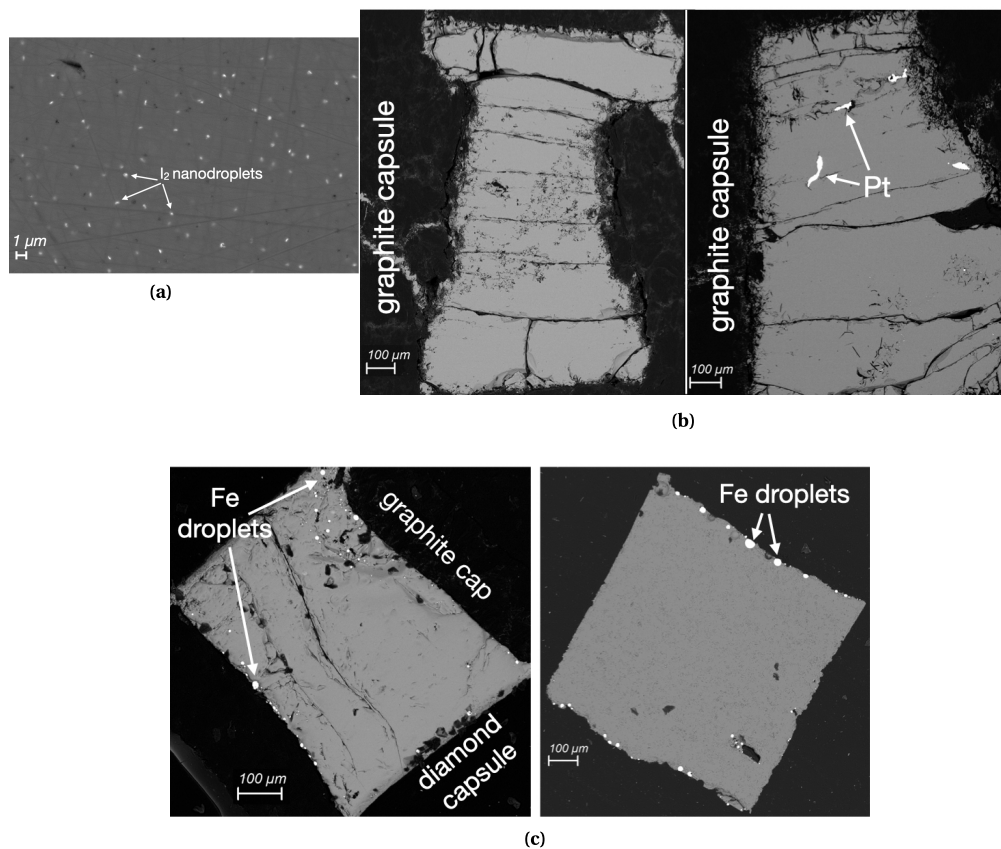


**Figure 2.** SEM images of quenched glasses recovered from piston-cylinder runs and in situ high  $P$ - $T$  X-ray diffraction (XRD) experiments. (a) Starting sample PC82 (Saint Vincent basalt, I-doped). (b) Saint Vincent basalt in graphite capsule recovered from XRD experiments (left: run 13, I-doped, right: run 26, I-free). (c) Etna basalt recovered from XRD experiments (left: 20BaM19, I-doped, in diamond capsule, right: Etna2002, I-free, extracted from diamond capsule). Bright zones are either I<sub>2</sub> droplets (a), Pt bits inherited from the previous piston-cylinder run using Pt capsules (b right), or metallic Fe droplets (c).

pronounced. The small contribution near  $3 \text{ \AA}^{-1}$  on  $S(q)$  for run APS TGH27 stems from dispersed Fe droplets in the magma, and translates into a contribution peaking at  $2.5 \text{ \AA}^{-1}$  on  $g(r)$ , consistently with reported XRD data on molten Fe [Sanloup *et al.*, 2000] and with the observation of Fe droplets on recovered samples (Figure 2c). Interestingly, we do not observe this contribution of molten Fe for the I-free run APS TGH25, attesting that reduction of Fe was less extensive in the I-free basalt (Table 1). Diffusion of hydrogen through the Pt-Rd caps, and/or diffusion of C from the inner graphite caps, can not be excluded as other causes of Fe reduction, but the difference between I-free and I-doped samples is significant.

To better evidence the contribution of iodine atoms to the radial distribution function, we used the APS run13/26 datasets, that are not impacted by the contribution of molten Fe to the XRD signal. The difference between reduced radial distribution functions,  $G(r) = 4\pi r \rho(g(r) - 1)$ , for I-doped and I-free basalts was calculated after normalisation of  $g(r)$  to the Si-O contribution (Figure 4). Note that while this procedure enables to evidence interatomic distances, it is not sufficient to calculate accurate coordination numbers. To do so, the full  $g(r)$  should be simulated against the sum of all partial pair distribution functions, but this is challenging for such small differences. Two interatomic distances

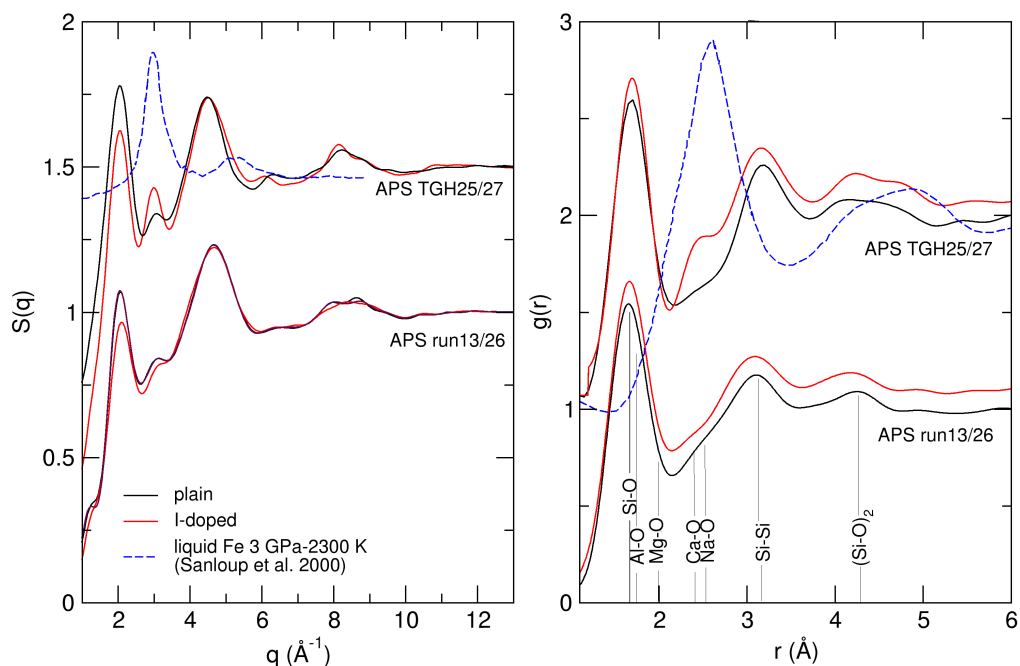


**Figure 3.** Right panel: structure factors,  $S(q)$ ; left panel: radial distribution functions,  $g(r)$ .

are visible at 2.2  $\text{\AA}$  and at 3.5  $\text{\AA}$  (Figure 4), and due to the normalisation procedure to the Si-O contribution, we cannot exclude that distances shorter than 2  $\text{\AA}$  also exist. These contributions are either I-related or enhanced contributions due to the presence of iodine. XRD is sensitive to the electrons, the intensity of the signal evolves with  $Z^2$  ( $Z$ , atomic number). Iodine being a very heavy element, its scattering is 4 times stronger than that of Fe, and 14 times stronger than that of Si. Hence the likeliest possibility is that differences on radial distribution function between I-doped and I-free basalts are due to iodine, and not to other elements even if their abundances may vary slightly. The potential contribution of Fe-O nevertheless needs to be discussed, as its contribution to  $g(r)$  in a basalt is at 2.07  $\text{\AA}$  and 3.4  $\text{\AA}$  (Fe-O and Fe-Fe interatomic distances respectively [Guillot and Sator, 2007]), all other main interatomic distances being different (see position of main cation-oxygen interatomic distances on Figure 3). However, it cannot be the case since FeO content is similar between I-free and I-doped Saint Vincent basalt, and this content is lower than 1 wt% hence the expected contribution is very low. These

additional contributions in I-doped  $G(r)$  can neither be attributed to an eventual  $P$  difference between I-doped and I-free basalts. The maximum  $P$  (4.9 GPa) reached in these experiments can induce changes of coordination number for some cation-oxygen bonds, but it is way too modest to induce a contraction of interatomic distances. Na-O for instance contracts by 0.02% between 0 GPa and 5 GPa [Karki et al., 2018], all other main cation-oxygen distances change even less.

Amongst reported I-X bonds for iodine compounds, the 2.2  $\text{\AA}$  distance is shorter than iodine-iodine (2.7  $\text{\AA}$ ) or iodine-metal bonds (3.2  $\text{\AA}$ -4.0  $\text{\AA}$ ), and closer to iodine-oxygen bonds reported for crystalline iodates (1.8-2.2  $\text{\AA}$  range), the longest I-O bonds corresponding to medium intramolecular bonds with a single covalent bond character [Gautier-Luneau et al., 2010, Abudouwufu et al., 2020], indicative that we are not looking at  $\text{IO}_3^-$  units here (I-O bond length nearer 1.8  $\text{\AA}$ ), but at more complex iodates. The longer 3.5  $\text{\AA}$  distance is too long for Na-I or Ca-I, but matches well with the I-I interatomic distance in polyiodates such as  $\text{K}_2\text{Na}(\text{IO}_3)_2(\text{I}_3\text{O}_8)$  [Abudouwufu et al., 2020].



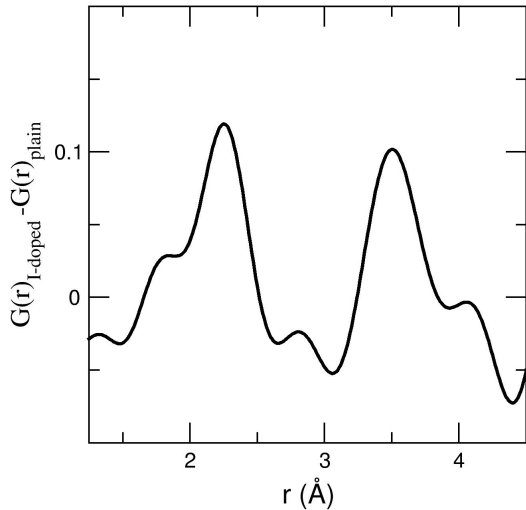


**Figure 4.** The iodine contribution to the reduced  $G(r)$  radial distribution function, as obtained from the difference between APS run 13 and APS run 26 XRD datasets.

### 3.3. Melt structure: Raman spectroscopy

Some starting and recovered samples were analysed by Raman spectroscopy (Figure 5). We note that it is difficult to obtain Raman spectra on these natural compositions due to an inherent high level of fluorescence, and in particular in the intramolecular water range (e.g. [2800–3600]  $\text{cm}^{-1}$ ). Iodine–iodine signature is visible on starting sample PC82, with bands at 114  $\text{cm}^{-1}$  and 154  $\text{cm}^{-1}$ , consistently with the observation of nano-size iodine ( $\text{I}_2$ ) bubbles by SEM (Figure 2a), bands that are also observed in the I-richest borosilicate glass in Cicconi *et al.* [2019] and were attributed to NaI bonds but seem more consistent with  $\text{I}_2$  signal. There is no visible iodine–iodine nor metal–iodine contribution on any spectra measured on samples recovered from XRD experiments. Instead there is the systematic presence of four small but clear vibrational bands in I-doped samples at 615  $\text{cm}^{-1}$ , 647  $\text{cm}^{-1}$  (this one on top of a broader band by comparison with I-free samples), 1098  $\text{cm}^{-1}$ , and 1177  $\text{cm}^{-1}$ . Interestingly, there is also a broad band circa 640–660  $\text{cm}^{-1}$  in I-doped borosilicate glasses (Figure 5), albeit not discussed by the authors. While we are most likely observing oxidized iodine in these glasses, it is not in the form of  $\text{IO}_3^-$  units that give rise to bands in the [700–800]  $\text{cm}^{-1}$

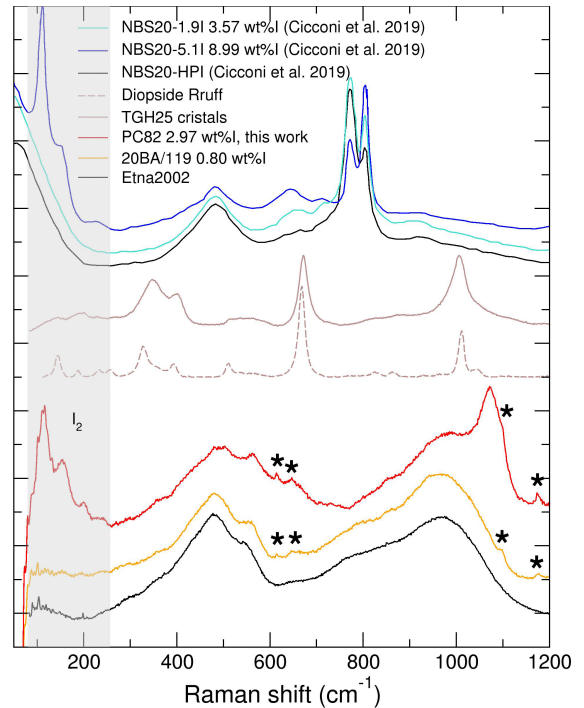


**Figure 5.** Raman spectra collected on an iodine over-saturated sample (PC82), and on two recovered samples from in situ X-ray diffraction experiments (I-doped 20BA/M19 and I-free Etna2002), Raman spectra collected on I-doped and plain borosilicate glasses (NBS20) [Cicconi *et al.*, 2019] are shown for comparison. For I-doped basaltic glasses,  $\text{I}_2$  related modes are observed below 200  $\text{cm}^{-1}$  for PC82 (grey shaded area), and iodate-related modes are marked by asterisks. Note that PC82-Saint Vincent basaltic composition (3.8 wt%  $\text{H}_2\text{O}$ ) is less polymerised, as seen by the increased band near 1070  $\text{cm}^{-1}$ . For borosilicate glasses, the strong bands in the [740–840]  $\text{cm}^{-1}$  are related to borate rings and boroxol.

range [Cicconi *et al.*, 2019], but of more complex iodate forms alike hydrated periodate groups. For instance, mixed salt  $\text{Cs}_2[\text{I}(\text{OH})_3\text{O}_3]\cdot\text{CsSO}_4(\text{H})\text{H}_5\text{IO}_6$  has its strongest band at 651  $\text{cm}^{-1}$ , attributed to I–O  $\text{IO}_6^{5-}$  symmetric stretching vibration [Romanchenko *et al.*, 2004]. The two highest Raman shift modes fall within the range reported for  $\delta$  I–O–H modes in octahedral periodates, i.e. [1050–1190]  $\text{cm}^{-1}$  [Dengel *et al.*, 1993].

#### 4. Discussion

Iodine induces changes in the silicate melt network structure, observed here by a lesser degree of polymerisation as probed by X-ray diffraction, and reported on the basis of Raman spectroscopy on Fe-free alkali-rich felsic magmas [Faranda, 2023], and Fe-free borosilicate glasses [Cicconi et al., 2019, Morizet et al., 2021]. While this behaviour is noticeable for experimental levels of I-doping in the order of 1 or more wt%, and is a relevant property in the context of nuclear waste glasses, it is not expected for natural levels of I content in magmas. The network modifying role of I however does indicate that I is not retained passively in the voids or in the ring structure of magmas, nor that it removes Na or K ions from the melt oxides otherwise the opposite effect would be observed, i.e. enhanced polymerisation.

The coexistence of reduced iodide ( $I^-$ ) and oxidized iodate ( $IO_3^-$ ) species in  $SiO_2$  poor (14–33 wt%  $SiO_2$ ) borosilicate glasses [Cicconi et al., 2019] synthesized at 1.5 kbar in the  $B_2O_3$ – $SiO_2$ – $Na_2O$  system, was reported based on combined Raman and X-ray Absorption Near Edge Structure (XANES) spectroscopies. However, as mentioned above, the Raman data also showed vibrational modes corresponding to  $IO_6^{5-}$  groups. More complex high  $P$  aluminoborosilicate glasses in the system  $SiO_2$ – $Al_2O_3$ – $B_2O_3$ – $CaO$ – $Na_2O$  investigated by X-ray photoelectron and extended X-ray absorption spectroscopies have a large predominance of iodide species [Morizet et al., 2021], in addition to iodates for their most  $SiO_2$  poor composition (NH glass, 43 wt%  $SiO_2$ ), although reconciling information from both types of spectroscopies proved difficult. It is important to note that borosilicate glasses are not ideal analogues for basaltic melts, but they share the same characteristic to have a low degree of polymerisation and high I solubility. Last but not least, Leroy et al. [2019] observed only  $I_2$  signals on in situ Raman spectra of I-doped haplogranite melt coexisting with hydrous fluid. This points out that I speciation depends on magma polymerisation, e.g. on the  $SiO_2+Al_2O_3$  content, and also on its FeO content. This, in turn, could underpin the lower solubility of I in  $SiO_2$ -rich well polymerised magmas [Cicconi et al., 2019, Leroy et al., 2019].

The potential role of FeO is highlighted here by the amount of reduced iron that is higher for I-doped

samples than I-free samples run for similar duration at high  $T$  (TGH25 and TGH26, Table 1), indicating that FeO was the likely source of oxygen to form periodates, leading to the formation of metallic Fe. This effect is unfortunately not clear for I-free Etna2002 compared to I-doped 20BA/M19, with similar FeO content in the quenched glass which could result from Etna2002 shorter run duration. In the case of Saint Vincent basalt experiments, the starting glass was already almost FeO free (Table 1) after piston-cylinder press iodine and water doping using platinum capsules. Hence the most obvious source of oxygen was water for this composition.

Iodine speciation in basalts as an oxide is quite unique amongst halogens elements. X-ray absorption spectroscopy measurements on glasses recovered from high  $P$ – $T$  conditions have mostly targeted chlorine and bromine speciation so far. Chlorine bonds to network modifying cations [Evans et al., 2008, Thomas et al., 2023], in particular to Ca, Fe and Mg, to a lesser extent to Na, and in the case of the most  $SiO_2$  rich melts also to Si [Thomas et al., 2023]. The higher affinity of chlorine for alkaline-earth cations than for alkaline cations was confirmed for borosilicate glasses [Jolivet et al., 2023]. Bromine speciation in silica-rich magmas changes between low  $P$ , with Br–Na bonds and a hydration shell, to a closer oxygen environment above 2 GPa [Cochain et al., 2015, Louvel et al., 2020] although whether oxygen belongs to water molecules or to the silicate network could not be deciphered. Bromine speciation besides remains to be investigated in basaltic compositions. The bulk silicate Earth (BSE) contains approximately ten times more Br than I [Kendrick et al., 2017, Guo and Korenaga, 2021], the Br/I ratio raises in MORB and arc basalts (circa 50, [Kendrick et al., 2014]), and even slightly more in atmospheric volcanic plumes (58–87, [Aiuppa et al., 2005]). Differences in Br and I speciation in magmas could, at least partially, underpin this behaviour.

#### 5. Conclusion

While iodine is generally thought as present in nature either as iodide ( $I^-$ ), iodate ( $IO_3^-$ ), or elemental iodine ( $I_2$ ), we show here that it is stable in basaltic melts and glasses as a more complex iodate such as polyiodates or orthoperiodates. It is thus possible that this peculiar speciation of iodine might have been

missed in past investigations, in particular when using spectroscopic methods that require the collection of data on reference materials and for which only  $I^-$ ,  $I_2$  and  $IO_3^-$  were looked for. An alternative to reference materials is to use an input model, but this is very difficult to have for non-crystalline materials. In this respect, the X-ray diffraction method used here is not standard- nor model-dependent. But it can only be applied to the study of the heaviest—hence most scattering—I element. Indeed, with solubilities reaching only a few wt% in compressed basalts, its detection is clear but remains small, demonstrating that any lighter halogen element will not be detectable by this method. Iodine as orthoperiodate is observed in basaltic melts generated between 1.5 GPa and 4.9 GPa in the present study, but similarity in Raman spectroscopy data shows that this oxidized state extends to  $SiO_2$ -poor borosilicate melts at 1.5 kbar [Cicconi *et al.*, 2019]. It does not however extend to  $SiO_2$ -rich compositions, as only  $I_2$  signal was observed on Raman spectra measured on compressed I-doped haplogranite melt [Leroy *et al.*, 2019], and mostly as iodide in  $SiO_2$ -rich high  $P$  aluminoborosilicate glasses [Morizet *et al.*, 2021].

Interestingly, formation of iodates has also been observed during circulation of water-iodide solutions through volcanic rock cores at ambient conditions [Neil *et al.*, 2020], on the basis of UV spectroscopy measurements. This was interpreted as resulting from the retention of oxidized I by minerals in volcanic rocks, concomitantly with reduction of ferric ions. In conjunction with the present results, this points out that future studies should be dedicated to elucidating simultaneously the speciation of I and Fe in magmas to fully understand I behaviour in petrologic and volcanic processes.

### Declaration of interests

The authors do not work for, advise, own shares in, or receive funds from any organization that could benefit from this article, and have declared no affiliations other than their research organizations.

### Acknowledgments

Natural basaltic samples from Saint Vincent and Mount Etna were provided by G. Prouteau from Institut des Sciences de la Terre d'Orléans. We acknowledge K. Curtis-Benson for providing parts for

cell assemblies and arranging shipments before and after experiments at the Advanced Photon Source, K. Béneut for use of the Raman spectroscopy platform at IMPMC, O. Boudouma for SEM measurement and N. Rivodini for EPMA analyses at OSU Ecce Terra, Sorbonne Université. This work was supported by the European Research Council under the European Community's Seventh Framework Programme (FP7/20072013 Grant Agreement No. 259649 to CS), TG was supported by the ANR Projet de Recherche Collaborative VOLC-HAL-CLIM (Volcanic Halogens: from Deep Earth to Atmospheric Impacts, ANR-18-CE01-0018) and is grateful for an EU Marie Skłodowska-Curie Fellowship "ExCliso" (Project ID 101017762), QC was supported by CSC scholarship (#201806340094). HPCAT operations are supported by DOE NNSA's Office of Experimental Sciences. The Advanced Photon Source is a U.S. Department of Energy (DOE) Office of Science User Facility operated for the DOE Office of Science by Argonne National Laboratory under Contract No. DE-AC02-06CH11357.

### References

- Abudouwufu, T., Zhang, M., Cheng, S., Zeng, H., Yang, Z., and Pan, S. (2020).  $K_2 Na(IO_3)_2 (I_3O_8)$  with strong second harmonic generation response activated by two types of isolated iodate anions. *Chem. Mater.*, 32(8), 3608–3614.
- Aiuppa, A., Federico, C., Franco, A., *et al.* (2005). Emission of bromine and iodine from Mount Etna volcano. *Geochem. Geophys. Geosystems*, 6, article no. Q08008.
- Bureau, H., Keppler, H., and Métrich, N. (2000). Volcanic degassing of bromine and iodine: experimental fluid/melt partitioning data and applications to stratospheric chemistry. *Earth Plan. Sci. Lett.*, 183(1–2), 51–60.
- Cicconi, M. R., Pili, E., Grousset, L., Florian, P., Bouillard, J. C., Vantelon, D., and Neuville, D. R. (2019). Iodine solubility and speciation in glasses. *Sci. Rep.*, 9, article no. 7758.
- Cochain, B., Sanloup, C., de Grouchy, C., Crépinson, C., Bureaud, H., Leroy, C., Kantor, I., and Irifune, T. (2015). Bromine speciation in hydrous silicate melts at high pressure. *Chem. Geol.*, 404, 18–26.
- Cuevas, C. A., Fernandez, R. P., Kinnison, D. E., *et al.* (2022). The influence of iodine on the Antarctic

- stratospheric ozone hole. *Proc. Natl. Acad. Sci. USA*, 119(7), article no. e2110864119.
- Dengel, A., Griffith, W., Mostafa, S., and White, A. (1993). Raman and infrared study of some metal periodato complexes. *Spectrochim. Acta A*, 49(11), 1583–1589.
- Evans, K. A., Mavrogenes, J. A., O'Neill, H. S., Keller, N. S., and Jang, L. Y. (2008). A preliminary investigation of chlorine XANES in silicate glasses. *Geochem. Geophys. Geosystems*, 9, article no. Q10003.
- Faranda, F. (2023). *Behavior of halogens (Cl, Br, I) in alkali-rich felsic magmas at crustal depth : an experimental approach*. Phd thesis, Université d'Orléans, France.
- Gautier-Luneau, I., Suffren, Y., Jamet, H., and Pilme, J. (2010). Reinterpretation of three crystal structures of alkali oxiodate(v) - description of the  $[I_3O_8]^-$  anion and the infinite 2D  $[I_3O_8]_{\infty}^-$  anion. *Z. Anorg. Allg. Chem.*, 636(7), 1368–1379.
- Gennaro, E., Iacono-Marziano, G., Paonita, A., Rottolo, S. G., Martel, C., Rizzo, A. L., Pichavant, M., and Liotta, M. (2019). Melt inclusions track melt evolution and degassing of Etnean magmas in the last 15 ka. *Lithos*, 324, 716–732.
- Guillot, B. and Sator, N. (2007). A computer simulation study of natural silicate melts. Part I: low pressure properties. *Geochim. Cosmochim. Acta*, 71, 1249–1265.
- Guo, M. and Korenaga, J. (2021). A halogen budget of the bulk silicate Earth points to a history of early halogen degassing followed by net re-gassing. *Proc. Natl. Acad. Sci. USA*, 118(51), article no. e2116083118.
- Jolivet, V., Morizet, Y., Trcera, N., Fernandez, V., and Suzuki-Muresan, T. (2023). Incorporation of chlorine in nuclear waste glasses using high-pressure vitrification: Solubility, speciation, and local environment of chlorine. *Am. Mineral.*, 108(6), 1032–1042.
- Karki, B. B., Ghosh, D. B., and Bajgain, S. K. (2018). *Simulation of Silicate Melts Under Pressure*. Elsevier, Amsterdam. chapter 16.
- Kendrick, M. A., Arculus, R. J., Danyushevsky, L. V., Kamenetsky, V. S., Woodhead, J. D., and Honda, M. (2014). Subduction-related halogens (Cl, Br and I) and H<sub>2</sub>O in magmatic glasses from Southwest Pacific Backarc basins. *Earth Plan. Sci. Lett.*, 400, 165–176.
- Kendrick, M. A., Hemond, C., Kamenetsky, V. S., Danyushevsky, L., Devey, C. W., Rodemann, T., Jackson, M. G., and Perfit, M. R. (2017). Seawater cycled throughout Earth's mantle in partially serpentinized lithosphere. *Nat. Geosci.*, 10(3), 222–228.
- Kendrick, M. A., Woodhead, J. D., and Kamenetsky, V. S. (2012). Tracking halogens through the subduction cycle. *Geology*, 40(12), 1075–1078.
- Kono, Y., Irifune, T., Higo, Y., Inoue, T., and Barnhoorn, A. (2010). P–V–T relation of MgO derived by simultaneous elastic wave velocity and in situ x-ray measurements: A new pressure scale for the mantle transition region. *Phys. Earth Planet. Int.*, 183, 196–211.
- Kono, Y., Park, C., Kenney-Benson, C., Shen, G., and Wang, Y. (2014). Toward comprehensive studies of liquids at high pressures and high temperatures: Combined structure, elastic wave velocity, and viscosity measurements in the Paris-Edinburgh cell. *Phys. Earth Planet. Int.*, 228, 269–280.
- Leroy, C., Bureau, H., Sanloup, C., et al. (2019). Xenon and iodine behaviour in magmas. *Earth Planet. Sci. Lett.*, 522, 144–154.
- Louvel, M., Sanchez-Valle, C., Malfait, W. J., Pokrovski, G. S., Borca, C. N., and Grolimund, D. (2020). Bromine speciation and partitioning in slab-derived aqueous fluids and silicate melts and implications for halogen transfer in subduction zones. *Solid Earth*, 11(4), 1145–1161.
- Morizet, Y., Jolivet, V., Trcera, N., Suzuki-Muresan, T., and Hamon, J. (2021). Iodine local environment in high pressure borosilicate glasses: An x-ray photoelectron spectroscopy and x-ray absorption spectroscopy investigation. *J. Nucl. Mater.*, 553, article no. 153050.
- Muramatsu, Y. and Wedepohl, K. (1998). The distribution of iodine in the Earth's crust. *Chem. Geol.*, 147(3–4), 201–216.
- Neil, C. W., Telfeyan, K., Sauer, K. B., Ware, S. D., Reimus, P., Boukhalfa, H., Roback, R., and Brug, W. P. (2020). Iodine effective diffusion coefficients through volcanic rock: Influence of iodine speciation and rock geochemistry. *J. Contam. Hydrol.*, 235, article no. 103714.
- Pichavant, M., Mysen, B. O., and Macdonald, R. (2002). Source and H<sub>2</sub>O content of high-MgO magmas in island arc settings: an experimental study of a primitive calc-alkaline basalt from St. Vincent,

- Lesser Antilles arc. *Geochim. Cosmochim. Acta*, 66, 2193–2209.
- Romanchenko, E., Shilov, G., Dobrovolskii, Y., Chernyak, A., Karelin, A., and Atovmyan, L. (2004). Mixed salt  $\text{Cs}_2[\text{I}(\text{OH})_3\text{O}_3] \cdot \text{CsSO}_4(\text{H})\text{H}_5\text{IO}_6$ : Synthesis, crystal structure, and properties. *Russ. J. Coord. Chem.*, 30(7), 453–458.
- Salmon, P. S. (1994). Real space manifestation of the first sharp diffraction peak in the structure factor of liquid and glassy materials. *Proc. Math. Phys. Sci.*, 445, 351–365.
- Sanloup, C., Guyot, F., Gillet, P., Fiquet, G., Hemley, R., Mezouar, M., and Martinez, I. (2000). Structural changes in liquid Fe at high pressures and high temperatures from synchrotron x-ray diffraction. *Europhys. Lett.*, 52, 151–157.
- Solomon, S., Garcia, R., and Ravishankara, A. (1994). On the role of iodine in ozone depletion. *J. Geophys. Res. Atmos.*, 99(D10), 20491–20499.
- Thomas, R. W., Wade, J., and Wood, B. J. (2023). The bonding environment of chlorine in silicate melts. *Chem. Geol.*, 617, article no. 121269.
- Webster, J. D., Baker, D. R., and Aiuppa, A. (2018). Halogens in mafic and intermediate-silica content magmas. In Harlov, D. and Aranovich, L., editors, *Role of Halogens in Terrestrial and Extraterrestrial Geochemical Processes: Surface, Crust, and Mantle*, pages 307–430. Springer Geochemistry, Cham.
- Yamada, A., Wang, Y., Inoue, T., Yang, W., Park, C., Yu, T., and Shen, G. (2011). High-pressure x-ray diffraction studies on the structure of liquid silicate using a Paris-Edinburgh type large volume press. *Rev. Sci. Instrum.*, 82, article no. 015103.





Research article

Magma degassing and its impact on the Earth's atmosphere: from magma oceans to lava lakes

# Influence of volatiles (H<sub>2</sub>O and CO<sub>2</sub>) on shoshonite phase equilibria

Francesco Vetere<sup>\*,a,b</sup>, Olivier Namur<sup>\*,b,c</sup>, Francois Holtz<sup>\*,b</sup>, Renat Almeev<sup>\*,b</sup>, Paola Donato<sup>\*,d</sup>, Francesco Frondini<sup>\*,e</sup>, Michele Cassetta<sup>\*,f,g</sup>, Alessandro Pisello<sup>\*,e</sup> and Diego Perugini<sup>\*,e</sup>

<sup>a</sup> Department of Physical Sciences, Earth and Environment, University of Siena, 53100, Italy

<sup>b</sup> Leibniz University of Hannover, Institute for Mineralogy, Callinstrasse 3, Hannover, D-30167, Germany

<sup>c</sup> Department of Earth and Environmental Sciences, KU Leuven, 3001 Leuven, Belgium

<sup>d</sup> Department of Biology, Ecology and Earth Sciences, University of Calabria, 87036 Arcavacata di Rende CS, Italy

<sup>e</sup> Department of Physics and Geology University of Perugia, piazza Università, 06100 Perugia, Italy

<sup>f</sup> Department of Computer Sciences, University of Verona, I-37134 Verona, Italy

<sup>g</sup> Department of Industrial Engineering, University of Trento, I-38122 Trento, Italy

*E-mails:* francesco.vetere@unisi.it (F. Vetere), olivier.namur@kuleuven.be (O. Namur), f.holtz@mineralogie.uni-hannover.de (F. Holtz), r.almeev@mineralogie.uni-hannover.de (R. Almeev), paola.donato@unical.it (P. Donato), francesco.frondini@unipg.it (F. Frondini), michele.cassetta@univr.it (M. Cassetta), alessandropisello@gmail.com (A. Pisello), diego.perugini@unipg.it (D. Perugini)

**Abstract.** Experiments were performed at 500 MPa, 1080 °C and water activities ( $a_{\text{H}_2\text{O}}$ ) from 0.0 to 1.0, in fluid-present and fluid-absent conditions, with the aim of constraining the effect of volatiles on phase equilibrium assemblages of a shoshonite from Vulcanello (Aeolian Islands, Italy). Experiments were run both under reducing and oxidizing conditions and results show that proportions, shapes and size of crystals vary as a function of the volatile composition ( $X_{\text{H}_2\text{O}}$  and  $X_{\text{CO}_2}$ ) and volatile content. Clinopyroxene (Cpx) is the main crystallising phase and is compositionally analogous to Cpx crystals found in the natural rock. Plagioclase (Pl) is stable only for water activity lower than 0.1, whereas Fe-Ti oxides are present in all experimental runs, except for those where  $\log f_{\text{O}_2}$  was lower than -9, ( $\Delta\text{NNO} -0.11$ ) irrespective of the presence of CO<sub>2</sub>. The addition of CO<sub>2</sub> (2.8 wt%) in nominally dry experimental charges substantially reduces the crystallinity by ca. 1/3 compared to volatile free experiments. This result has important consequences upon the physical properties of the magma because it influences its viscosity and, as a consequence, velocity during its travel to the Earth surface.

\*Corresponding author

Assuming that the widths of Vulcanello conduits vary from 0.5 to 1.5 m, estimates of the ascent velocity vary in the range  $1.5 \times 10^{-4}$ – $3.5 \times 10^{-2}$  m·s<sup>-1</sup> for CO<sub>2</sub> free systems and from  $5.7 \times 10^{-4}$ – $1.3 \times 10^{-1}$  m·s<sup>-1</sup> for CO<sub>2</sub> bearing systems.

Since shoshonitic magmas are common not only in the Italian volcanic provinces (Aeolian Arc, Campi Flegrei, Ischia Island, Pontine Islands, Monti Cimini, Monte Amiata, Capraia Island, Radicofani, Roccamonfina) but also in different volcanoes worldwide (Yellowstone, Mariana Arc, Kurile Arc, Tonga Arc, Andean Arc, Kamchatka Arc), we suggest that the new data will be useful to better understand shoshonitic magma behaviour under relevant geological scenarios. As such, we also suggest that hazard evaluation should incorporate the probability of very rapid ascent of poorly-evolved melts from depth.

**Keywords.** Vulcanello, Shoshonite, Phase equilibria, Mineral assemblage, H<sub>2</sub>O–CO<sub>2</sub>.

*Manuscript received 24 February 2023, revised and accepted 22 June 2023.*

## 1. Introduction

Volatiles dissolved in magmas are key parameters to understand geophysical and geochemical signals at depth, as their exsolution provides the needed driving force for magma rise and, possibly, trigger explosive eruptions. Being a multiphase system, most magmas are composed of phenocrysts coexisting with a volatile bearing silicate melt (e.g. H<sub>2</sub>O, CO<sub>2</sub>, S species, F, Cl, etc...). Phase equilibrium studies are of paramount importance to better decipher magma storage conditions and physical properties during ascent to the surface. Thus, the role of parameters governing equilibrium between melt and phenocrysts such as pressure, temperature, redox state, volatile content, must be known. The best way to constrain magma storage conditions of volcanic rocks and changes occurring during ascent is to compare the natural solid assemblages with the phase assemblage and compositions obtained through phase-equilibrium experiments in which all these parameters are controlled [e.g., Martel *et al.*, 2019]. Dissolved volatiles are known to affect the rheological properties of magmas during ascent to the Earth's surface and H<sub>2</sub>O is the most important volatile in igneous systems since it affects density, viscosity, as well as phase equilibria, including crystallinity and liquidus temperature [e.g., Burnham, 1981, Schulze *et al.*, 1997]. It is well known that the amount of dissolved water in melts, as well as the mode of degassing in magma conduits, both affect eruptive styles [e.g., effusive vs. explosive, Sisson and Layne, 1992; plinian vs. pelean, Martel *et al.*, 1998].

However, water is not the only volatile component in magmas. Over the last decades researchers have focused their efforts on trying to understand how different volatile ratios, such as H<sub>2</sub>O/CO<sub>2</sub>, can influence the magma properties in terms of phase equilibria,

mobility of chemical elements, and the amount, shape and size of crystals [e.g. Kent, 2008, Martel *et al.*, 2019, and references therein]. The presence of CO<sub>2</sub> reduces water activity and it is commonly assumed that the decreasing H<sub>2</sub>O/CO<sub>2</sub> ratio in the melt results in an increase of the liquidus temperature and crystal/melt ratio in most silicate systems [e.g., Clemens and Wall, 1981, Scaillet and Evans, 1999]. However, the results of some experimental studies seem to indicate that the opposite may occur in basaltic or depolymerized systems at very high CO<sub>2</sub> concentrations (low water activities) [Giuffrida *et al.*, 2017]. These results are unexpected and contrast with our common assumption of the role of CO<sub>2</sub>–H<sub>2</sub>O-bearing fluids on phase relationships.

In order to expand the experimental dataset on the effect of CO<sub>2</sub> on phase equilibria, we present new H<sub>2</sub>O- and CO<sub>2</sub>-bearing high temperature and high pressure crystallization experiments performed on a shoshonitic composition from the Vulcanello peninsula (Island of Vulcano, Aeolian Island, Italy). Experiments were targeted to investigate the phase stabilities at pressure and temperature conditions relevant for/to some of the southern Italy volcanoes such as Vulcanello and, possibly, to other chemically similar volcanic systems. We discuss experimental results in terms of phase equilibria but we also address how both H<sub>2</sub>O and CO<sub>2</sub> volatiles affect rheological properties of the magma depending on their content.

### 1.1. *Vulcanello magmatic source and products*

Based on the analysis of fluid inclusions in quartz xenoliths, Zanon *et al.* [2003] provided evidence that the deepest level of magma storage at Vulcanello is located between 17 and 21 km, close to the Moho [21–25 km; Falsaperla *et al.*, 1985] and excluded significant magma ponding at mid-crustal levels. This is



in accordance with the aeromagnetic data at Vulcano pointing to a magma reservoir between 18 and 21 km depth [De Ritis *et al.*, 2013]. Moreover, Zanon *et al.* [2003] provided and estimate for Vulcanello magmas temperature of  $1083 \pm 40$  °C.

The formation of Vulcanello occurred during the last Eruptive Epoch of the island of Vulcano [Eruptive Epoch 8, De Astis *et al.*, 2013], between AD 1100 to 1250 [Arrighi *et al.*, 2006], simultaneously to effusive and explosive activity in the La Fossa crater [Fusillo *et al.*, 2015].

The lava platform comprises several superimposed shoshonitic lava flows, which, together with the products of explosive activity that form a scoria cone, were the first subaerial products of the peninsula (Vulcanello 1). The rocks composing the lava platform are mainly shoshonitic and contain large (up to 1.5 cm) xenocrysts of plagioclase [Davì *et al.*, 2009, De Astis *et al.*, 2013, Fusillo *et al.*, 2015]. After a short time break, the activity resumed with explosive eruptions (Vulcanello 2) which led to the formation of a second cone during a single eruptive unit, showing 3-m-thick fallout deposit having shoshonitic composition [Fusillo *et al.*, 2015]. Following Vulcanello 2, no activity took place during ~500 years. Subsequently, lava emission resulted in the emplacement of the latitic Roveto lava flow, that was followed by three explosive phases leading to the edification of Vulcanello 3 cone. These rocks are latitic in composition with the presence of clinopyroxenes megacrysts [ca. 1.5 cm; Fusillo *et al.*, 2015]. The activity of Vulcanello 3 ended with the emplacement of a final lava flow (Valle dei Mostri latitic lava flow), which flowed in the same direction than the Roveto latitic lava flow [Fusillo *et al.*, 2015, Nicotra *et al.*, 2018, Davì *et al.*, 2009].

## 2. Experimental and analytical methods

### 2.1. Starting material and experiments

The starting material of our experiments is a natural scoria lava from Vulcanello 1. The bulk rock composition (Table 1) is characterized by  $\text{SiO}_2 = 53.40$  wt% and  $\text{Na}_2\text{O} + \text{K}_2\text{O} = 8.76$  wt%. In the total Alkali-Silica (TAS) diagram this composition plots in the field of shoshonite (Table 1). The modal abundance of phenocrysts, mainly composed

**Table 1.** Compositions of starting glass

	VL0 (wt%)	std	Vetere <i>et al.</i> [2007] (wt%)
<i>n</i>	100		100
$\text{SiO}_2$	53.40	0.41	53.47
$\text{TiO}_2$	0.70	0.04	0.71
$\text{Al}_2\text{O}_3$	15.78	0.24	15.48
FeO	8.04	0.36	8.39
MnO	0.10	0.12	0.10
MgO	4.88	0.15	4.88
CaO	8.81	0.22	8.51
$\text{Na}_2\text{O}$	3.66	0.23	3.66
$\text{K}_2\text{O}$	3.71	0.13	4.72
$\text{P}_2\text{O}_5$	0.62	0.21	
LOI			
Total	99.76		99.92

Notes: Oxide components are given in wt%. Errors represent one standard deviation (std). Shoshonite studied by Vetere *et al.* [2007] is also reported for comparison.

of clinopyroxene (Cpx) and plagioclase (Pl), is 8–11 vol%. The phenocrysts often contain inclusions of Fe–Ti oxides. As reported in Davì *et al.* [2009] the composition of clinopyroxene and feldspar phenocrysts ranges between  $\text{Wo}_{49-44}\text{En}_{36-42-36}\text{Fs}_{9-20}$  and  $\text{An}_{5-46}\text{Ab}_{51-52}\text{Or}_{3-43}$ , respectively. Feldspar microphenocrysts show a similar composition to that of phenocrysts ( $\text{An}_{3-35}\text{Ab}_{51-61}\text{Or}_{4-46}$ ). Olivine has a compositional range  $\text{Fo}_{42-62}$  and the Fe–Ti oxides have Usp content close to 14 mol%. The groundmass consists of glass, leucite (Lc), Fe–Ti oxides, Cpx, Pl and small amount of olivine (Ol).

Sample preparation prior to high-pressure experiments was performed at the Petro-Volcanology Research Group laboratories of the University of Perugia (PVRG; <http://pvrg.unipg.it>). About 100 g of crushed bulk rock was melted in a Pt crucible in air at 1600 °C for 4 h in a  $\text{Pt}_{80}\text{Rh}_{20}$  crucible. Melting was performed in a Nabertherm HT 04/17  $\text{MoSi}_2$ -heated box furnace. The melt was quenched to a glass by pouring it on a brass plate. The glass was crushed, re-melted and quenched again using the same procedure. This technique ensured compositional homogeneity of the glass and avoided crystal-

lization [Vetere *et al.*, 2015a]. The composition of the glass and the absence of crystals were controlled by electron microprobe imaging and measurements with a CAMECA SX 100 at the Institute of Mineralogy University of Hannover (see details below; Table 1).

The  $NBO/T$  parameter corresponds to the number of non-bridging oxygens (NBO) per tetrahedrally coordinated cation ( $T$ ) and is a good proxy to depict the structure of silicate melts in terms of polymerization [Mysen and Richet, 2005]. This ratio can be calculated as follows:

$$\frac{NBO}{T} = \frac{1}{T} \times \sum_{i=1}^i n \times M_i^{n+} \quad (1)$$

where  $T$  is the total atomic abundance of tetrahedrally coordinated cations,  $M$  is the proportion of network modifying cations  $i$ , with electrical charge  $n+$  after subtraction of the portion required for charge-balancing trivalent cations on tetravalent sites [Mysen and Richet, 2005]. Our starting composition has a  $NBO/T$  of 0.39. The fragility,  $F$ , of our starting composition, was also calculated and has a value of 0.60. This parameter is useful to estimate the deviation from Arrhenian behaviour upon cooling in a plot relating viscosity and the scaled temperature ( $T_g/T$ ) while approaching the glass transition temperature  $T_g$  [Angell, 1995, Giordano and Dingwell, 2003]. Both the  $NBO/T$  and  $F$  point to a high degree of depolymerisation of our starting material.

In order to prepare volatile-bearing charges, we used the following procedure:

The capsules ( $Au_{80}Pd_{20}$ ; 5 mm diameter, 3 cm in length, previously annealed at 1100 °C for 10 min and then welded on one end) were filled with the following procedure: (a) the capsule was charged with the desired amounts of  $\pm H_2O \pm Ag_2C_2O_4$  + glass powder ( $Ag_2C_2O_4$  is the source for  $CO_2$  as the silver oxalate decomposes during heating and generates the carbon dioxide); (b) a steel piston was used to gently compact the charge; (c) to avoid any volatiles release, the capsule was tightly squeezed on top, rolled up in a wet tissue, and frozen by placing it into a bath of liquid nitrogen; (d) the upper end of the capsule was welded shut with a conventional graphite-arc welder. In agreement with literature data on the Vulcanello magmatic source (21–17 km depth and  $1083 \pm 40$  °C, see above) we performed experiments at 500 MPa

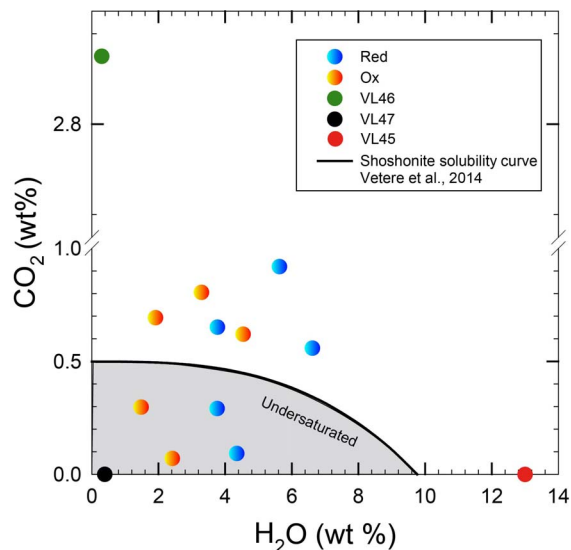


**Figure 1.**  $H_2O$  and  $CO_2$  concentrations added to the capsules before experiment (at 500 MPa and 1080 °C). The shaded area represent the undersaturated conditions in accord with the modeled  $H_2O$  and  $CO_2$  concentrations at fluid saturation obtained by Vetere *et al.* [2014, 2011] for the same composition is also shown (solid black curve). Orange and blue symbols indicate experiments performed at reduced and oxidized conditions, respectively, (see Table 3). Green and black circles are nominally anhydrous VL46 and 47 experiments, respectively (Table 3). Red dot refers to the sample with the highest water content.

and 1080 °C for 70 h, in order to shed light on processes relevant to the magmatic source of Vulcanello magma.

A total of 13 experiments with variable volatile contents (see Figure 1) were performed at 500 MPa and 1080 °C (Tables 2 and 3). Experiments were done in an internally heated pressure vessel (IHPV) equipped with a rapid-quench sample holder at the Institute für Mineralogy, Leibniz University of Hannover (Germany). Details for the IHPV are provided in Berndt *et al.* [2002]. Temperature was measured using four unsheathed S-type thermocouples (precision of temperature was  $\pm 5$  °C). The IHPV was pressurized with argon. Pressure was monitored

**Table 2.** Results of microprobe analyses of residual glasses

	VL32	std	VL33	std	VL34	std	VL36	std
SiO <sub>2</sub>	54.86	0.39	55.53	0.47	54.28	0.60	52.17	0.55
TiO <sub>2</sub>	0.71	0.05	0.73	0.04	0.73	0.06	0.71	0.04
Al <sub>2</sub> O <sub>3</sub>	20.61	0.26	20.71	0.34	19.87	0.22	17.99	0.23
FeOT	1.81	0.57	1.21	0.27	1.99	0.31	2.95	0.18
MnO	0.10	0.06	0.09	0.04	0.15	0.09	0.13	0.11
MgO	1.72	0.15	1.51	0.57	2.13	0.37	3.07	0.46
CaO	4.70	0.31	4.13	0.27	5.16	0.27	6.23	0.10
Na <sub>2</sub> O	6.32	0.26	6.66	0.16	6.08	0.21	5.42	0.17
K <sub>2</sub> O	4.91	0.39	5.11	0.21	4.82	0.28	4.25	0.32
P <sub>2</sub> O <sub>5</sub>	0.49	0.14	0.56	0.21	0.45	0.10	0.46	0.16
Total	96.23		96.24		95.66		93.38	
H <sub>2</sub> O	3.77		3.76		4.34		6.62	
	VL37	std	VL38	std	VL39	std	VL41	std
SiO <sub>2</sub>	55.50	0.68	56.03	0.47	55.72	0.91	53.90	0.21
TiO <sub>2</sub>	0.45	0.13	0.49	0.10	0.49	0.09	0.62	0.05
Al <sub>2</sub> O <sub>3</sub>	20.35	1.03	20.67	0.62	20.18	0.72	18.57	0.27
FeOT	4.32	1.07	4.12	0.70	3.96	0.58	4.64	0.23
MnO	0.12	0.05	0.09	0.10	0.09	0.10	0.10	0.11
MgO	1.29	0.38	1.14	0.23	1.10	0.32	2.00	0.37
CaO	3.99	0.40	3.69	0.42	3.60	0.32	4.66	0.17
Na <sub>2</sub> O	6.65	0.35	6.74	0.38	6.95	0.17	5.87	0.10
K <sub>2</sub> O	4.86	0.27	5.04	0.24	5.07	0.26	4.65	0.18
P <sub>2</sub> O <sub>5</sub>	0.57	0.23	0.51	0.16	0.50	0.17	0.46	0.12
Total	98.10		98.52		97.66		95.47	
H <sub>2</sub> O	1.90		1.48		2.34		4.53	
	VL45	std	VL46	std	VL47	std		
SiO <sub>2</sub>	51.36	0.99	56.02	0.83	55.69	0.44		
TiO <sub>2</sub>	0.63	0.02	0.76	0.02	0.75	0.04		
Al <sub>2</sub> O <sub>3</sub>	15.01	0.24	18.10	0.34	18.55	0.64		
FeOT	7.29	0.41	7.15	0.46	6.75	0.41		
MnO	0.10	0.10	0.13	0.08	0.18	0.09		
MgO	4.19	0.29	2.40	0.10	2.23	0.39		
CaO	7.34	0.44	4.33	0.12	4.48	0.66		
Na <sub>2</sub> O	2.81	0.39	6.07	0.26	6.21	0.20		
K <sub>2</sub> O	3.61	0.13	4.01	0.08	4.01	0.27		
P <sub>2</sub> O <sub>5</sub>	0.51	0.04	0.74	0.03	0.75	0.07		
Total	91.85		99.70		99.61			
H <sub>2</sub> O	8.15		0.30		0.39			

Notes: H<sub>2</sub>O represent the water content estimated by difference methods. Microprobe data are reported for all the residual glasses investigated in wt% together with errors represented by one standard deviation (std).

**Table 3.** Phase assemblage results derived from image analyses methods

	H <sub>2</sub> O <sub>in</sub> (wt%)	CO <sub>2</sub> (wt%)	$a_{\text{H}_2\text{O}^{\text{f}}}$	$\log f_{\text{O}_2}$	$\Delta\text{QFM}$	CPx			Plg			Ox	$\Phi_{\text{tot}}$ (area%)	
						Fs	Wo	En	An	Or	Ab			$\Phi_{\text{Plg}}$ (area%)
VL32 <sup>#</sup>	3.5	0.651	0.36	-10.80	-1.37	17.31	46.40	36.28	16.1					16
VL33 <sup>#</sup>	3.5	0.291	0.35	-10.82	-1.39	13.25	47.03	39.71	16.3					16
VL34 <sup>#</sup>	4.2	0.092	0.44	-10.64	-1.21	16.11	45.87	38.00	14.3					14
VL35 <sup>#</sup>	5.5	0.919	0.61	-10.35	-0.92				10.7					11
VL36 <sup>#</sup>	6.5	0.558	0.74	-10.18	-0.75				10.2					10
VL37	2.0	0.693	0.14	-7.64	1.79				15.8				1.7	17
VL38	1.5	0.297	0.09	-8.01	1.42				18.1				1.7	22
VL39	2.5	0.070	0.19	-7.38	2.05				18.7				1.9	21
VL40	3.0	0.805	0.31	-6.94	2.49	15.67	41.34	42.96	17.0				1.5	18
VL41	4.5	0.620	0.48	-6.57	2.86	16.45	47.85	35.68	14.0				1.4	15
VL45 <sup>\$</sup>	13.0	0.000	1.00	-4.94	4.49									3
VL46*	0.0	2.830	0.01	-10.26	-0.83	17.33	42.91	39.75	15.3	33.58	9.60	56.82	5.9	21
VL47*	0.0	0	0.02	-8.92	0.51	17.90	42.42	39.68	21.6	32.91	9.40	57.69	8.8	30

Crystals composition are also reported.

Note: Crystallinity ( $\Phi$ ) is reported in vol% and derived from 500 MPa and temperature of 1080 °C experiments. H<sub>2</sub>O and CO<sub>2</sub> are reported in wt%. Water activity is also reported for all run while phase compositions are reported for most of the experimental runs except for those were crystal size was too small in order to be analyses. <sup>#</sup>Denote experiments performed at controlled  $f_{\text{O}_2}$ . \*Denote experiments were no water was added to the charges. <sup>\$</sup>Denote experiments with quench crystals. <sup>f</sup>Water activity is calculated from the amount of water estimated by the difference method (see Table 2).

using digital pressure transducers having an uncertainty of about 1 MPa. The variation of pressure during the experiments was  $\leq 5$  MPa. Some experiments were performed at the intrinsic oxygen fugacity ( $fO_2$ ) conditions of the pressure vessel which was found to be close to QFM+4 (the intrinsic  $fO_2$  corresponding to  $H_2O$ -saturated conditions), with QFM being the quartz–fayalite–magnetite equilibrium [Berndt *et al.*, 2002]. At  $H_2O$ -undersaturated conditions,  $fO_2$  is lower, depending on the prevailing water activity [QFM–0.8 to QFM+3; Botcharnikov *et al.*, 2005]. In our experiments  $fO_2$  was calculated using the following relation:

$$\log fO_2 = \log fO_2(\text{at } XH_2O_{\text{in}} = 1) - 2 \log XH_2O_{\text{in}}. \quad (2)$$

[Scaillet and Evans, 1999]. We estimate that the maximum error on the calculated  $fO_2$  is about 0.2–0.3 log units according to Botcharnikov *et al.* [2005]. Other experiments were performed under controlled  $fO_2$  conditions (QFM–0.7 to QFM–1.4) by adding  $H_2$  to the Ar pressure medium. The hydrogen fugacity ( $fH_2$ ) in these experiments was monitored using a Shaw membrane as described in Berndt *et al.* [2002]. The  $fH_2$  was adjusted to be  $fH_2 = 20$  bar at experimental P–T conditions. Experiments were drop quenched with a cooling rate of approximately 150–200 °C/s [Berndt *et al.*, 2002]. For one experiment (Table 3), it was not possible to avoid the formation of quench crystals due to the relatively high amount of added water (see results for details).

## 2.2. Electron microprobe and image analyses

All run-products were mounted in epoxy, ground flat and polished for textural and chemical analyses. Glasses and minerals produced during the experiments were analysed using a Cameca SX100 microprobe at the Institute of Mineralogy. An accelerating voltage of 15 kV was used with a beam current of 15 nA for silicate minerals and oxides and 6 nA for glasses. The beam was defocused to at least 15  $\mu\text{m}$  for glass analyses and focused to  $< 2$   $\mu\text{m}$  for the analysis of crystal phases. All elements were analysed with a counting time of 10 s on peak. Standards used for calibration were  $Fe_2O_3$ , MgO,  $MnTiO_3$  (Mn and Ti), albite (Na), wollastonite (Si for mineral and glass and Ca for glass), apatite (P and F for glass and F, Ca and P for apatite), orthoclase (K), anhydrite (Ca and S). Standard deviations reported in Table 2 were

calculated based on 10 to 20 analysed spots on the same sample. Raw data were corrected with the software “Peak Sight” and “PAP” matrix [Pouchou and Pichoir, 1991]. Precision and accuracy were determined by measuring reference glasses VG-568 (rhyolite) and VG-2 (basalt) from Smithsonian standards collection [Jarosewich, 2002].

Due to the presence of crystals in experimental charges, the water content of the glasses was estimated following the “by-difference” method described in Devine *et al.* [1995]. Following Parat *et al.* [2008], we estimate that the error on determination of  $H_2O$  content is  $\sim 0.5$  wt%.  $CO_2$  in glasses were not determined but estimated from the solubility curve in Figure 1.

Back-scattered electron (BSE) images were collected with a Philips FEG (Field Emission Gun) Quanta 200F equipped with a Si/Li-SUTW detector (EDAX, Philips Electronics) installed at the University of Calabria (Italy). Representative BSE images were collected at different magnifications (400 $\times$  up to 1600 $\times$ ) depending on the crystal size. Surface percentage of the different phases was determined for all images using grey levels with Image-ProPlus 6.0 [see details in Vetere *et al.*, 2015a]. Seven to ten BSE images obtained in different parts of the same section were evaluated for homogeneity. We quantified surface fractions of glass, clinopyroxene, spinel, plagioclase and gas bubbles. In total, 110 BSE images were analysed.

## 3. Results

The crystalline phases observed in our experiments are clinopyroxene (Cpx), plagioclase (Pl), and Fe–Ti oxides (Ox) in various proportions, depending on the fraction of volatiles dissolved in the melt. The results show that Cpx is the main phase with abundance increasing from 10.2% to 21.6% as  $aH_2O$  decreases from 0.74 to nearly zero (Table 3). Water activity also plays a major role on the stability of Pl that is only present in experiments with a melt  $H_2O$  content  $\leq 1$  wt% (Table 3). Plagioclase has a maximum abundance of 8.8% in the volatile-free sample (VL 47\* in Table 3). Minor Fe–Ti oxides ( $\leq 2\%$ ) are present in samples equilibrated under relatively high oxygen fugacity conditions.

Based on the amounts of added volatiles and in agreement with solubility model and data

[e.g. Vetere *et al.*, 2014] one can distinguish between fluid-saturated (fluid present) and fluid-undersaturated (fluid absent) runs with respect to  $\text{H}_2\text{O} + \text{CO}_2$  (Figure 1).

Quenched melt (residual glass) is present in all run products with a mode ranging from 70% in VL47\* to 97% in VL45<sup>s</sup> (Table 3). This wide range of melt fraction at constant pressure and temperature shows the importance of water activity ( $a\text{H}_2\text{O}$ ) on the liquidus temperature and crystallinity. All glass compositions, including the starting composition, are listed in Tables 1 and 2 and are illustrated in Figure 2. The compositions of residual glasses range from 51 to 56 wt%  $\text{SiO}_2$  (Table 2 and Figure 2). Glass compositions evolve as a function of the degree of crystallinity. We however note that a larger crystallinity does not always correspond to an enrichment of  $\text{SiO}_2$  in the residual glass (compare Table 2 and 3). We also note that in the experiment performed under oxidizing and water-saturated (no  $\text{CO}_2$ ) conditions, the conditions are close to the liquidus and the melt has a composition very similar to that of the starting glass (although comparing alkali content in the VL45 and starting material we do note a difference of ca. 0.5 wt% of  $\text{Na}_2\text{O}$  possibly due to the EPMA measurements conditions; red point in Figures 1 and 2). Experiments performed at reducing conditions and containing both water and  $\text{CO}_2$  show a  $\text{SiO}_2$  trend that increases nearly linearly as the  $\text{MgO}$  content decreases. The same observation can be done for,  $\text{Na}_2\text{O}$  and  $\text{K}_2\text{O}$ . The total  $\text{FeO}$  decreases with decreasing  $\text{MgO}$  but  $\text{FeO}$  concentrations are always higher in oxidized experiments than in reduced experiments at a given  $\text{MgO}$  content, suggesting a possible  $\text{Fe}$ -loss to the capsule wall at reducing conditions, as discussed below.  $\text{TiO}_2$  is relatively constant in reduced experiments but decreases with decreasing  $\text{MgO}$  in oxidized runs. Due to the crystallization of the main phase Cpx,  $\text{CaO}$  continuously decreases with  $\text{MgO}$  (with increasing crystallinity).

Eight experiments were performed at volatile saturated conditions and six at volatile undersaturated conditions (Figure 1). Figure 3 shows the variation of crystal content as a function of water content. The general trend indicates that the higher the amount of water in the melt, the lower the amount of crystals, as expected from the numerous previous phase relationships conducted so far. No significant difference between fluid-absent and fluid-

present runs is detected in terms of crystal content in samples with an amount of water added to the system that is larger than 1.0 wt%. Thus, we did not detect a substantial difference in crystal content between experiments performed at fluid-saturated and fluid-undersaturated conditions if the  $a\text{H}_2\text{O}$  is similar. For example, we investigated the effect of increased  $\text{CO}_2$  concentration in water-rich samples (i.e. up to 3.7 wt%  $\text{H}_2\text{O}$ ; sample VL32 and VL33, see Table 3) by performing two experiments with a total amount of  $\text{CO}_2$  from 6500 ppm (fluid-saturated) and 2900 ppm (fluid-undersaturated). No difference between  $\text{CO}_2$ -rich and  $\text{CO}_2$ -poor samples was observed in terms of crystallinity. In particular, both melts showed Cpx contents of ~16% (Table 3). In contrast, our experiments show that, at very low  $\text{H}_2\text{O}$  content, the presence of  $\text{CO}_2$  causes a substantial decrease of crystal content. A difference up to 10 area% in crystal content is observed between samples VL46 and VL47 (see Table 3), where the first charge contains a large amount of  $\text{CO}_2$  (2.8 wt%, nominally dry, no water added) while VL47 is nearly volatile free. It is emphasized that this difference of 10 area% in crystallinity determined by image analysis is also consistent with mass balance calculations. Using the GeoBalance program [Excel VBA program for mass balance calculation; Li *et al.*, 2020] the residual melts in VL47 can be best reproduced if 6 wt% Pl and 30 wt% Cpx crystallize from the starting material (the mineral compositions from experimental products were considered for the calculation, see Table 3). For VL46, mass balance calculation indicates the crystallization of 3 wt% Pl and 25 wt% Cpx, pointing to the possible role of  $\text{CO}_2$  on phase proportions as discussed below.

The alphaMELTS code was used to further elucidate the phase evolution observed in this study. The alphaMELTS (V. 1.9) software provides a simple text-based interface to subroutine versions of the algorithms MELTS [Asimow and Ghiorso, 1998, Smith and Asimow, 2005, Ghiorso *et al.*, 2002, Ghiorso and Sack, 1995]. It allows to calculate equilibrium assemblages along a thermodynamic path set by the user (details are provided by: <http://melts.ofm-research.org/> and <https://magmasource.caltech.edu/forum/>). Results of the simulations are shown in Figure 4 comparing the crystals content measured via Image Analyses and calculated by using alphaMELTS. There is a good correlation between calculated and measured

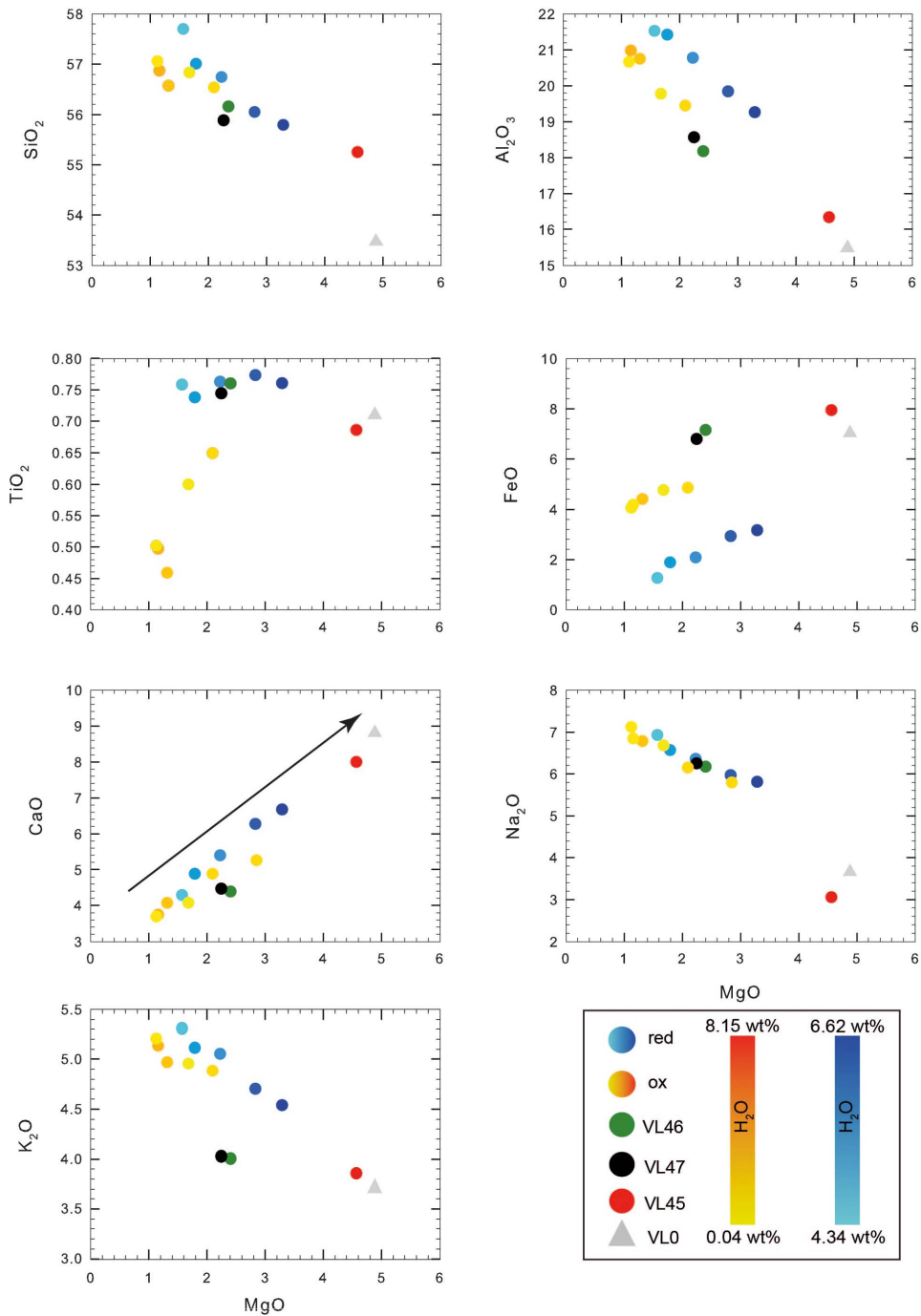


**Figure 2.** Change of the residual glass composition (in wt% of element concentrations) in the silicate melts. The analyses are recalculated to a total of 100%. The arrow on the CaO vs. MgO plot indicates the vector pointing to the Cpx composition. The grey triangle refers to the starting material composition while reddish and bluish circles indicate experiments performed at oxidized and reduced conditions, respectively, as reported in Tables 2 and 3. Red dot as in Figure 1.

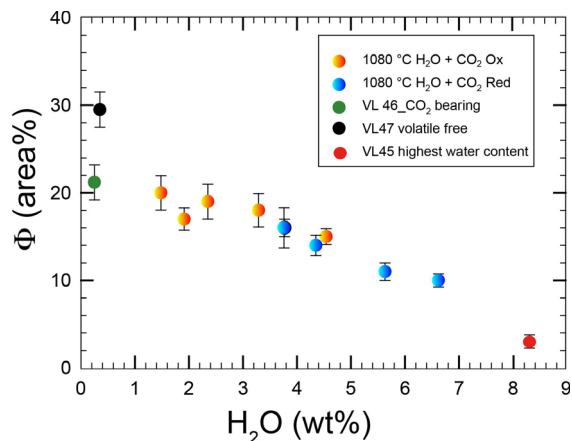


**Figure 3.** Evolution of crystallinity vs. water content of experiments presented in Table 3. Note the variation on crystallinity between CO<sub>2</sub> bearing and CO<sub>2</sub> free sample in nominally dry experimental charges. Symbols as in Figure 1.

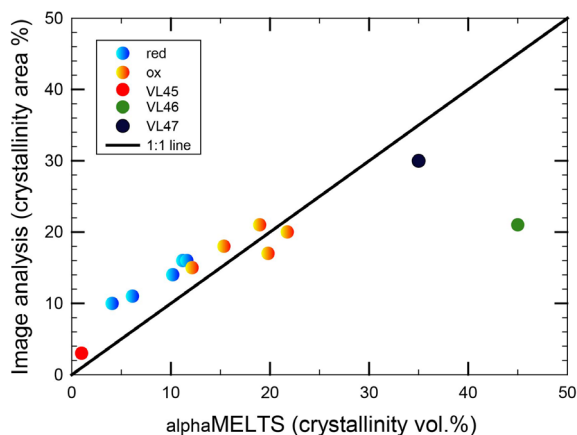


**Figure 4.** Comparison between Image Analyses measurements and calculated amount of crystals by alphaMELTS approach. Note the good correlation for most of the sample. VL46 sample, instead shows a large departure relatively to the 1:1 line (green circle).

data, although VL46 sample shows a calculated crystallinity higher than 40 vol% (expected from equilibrium thermodynamic calculation) whereas the experimentally observed crystallinity is much lower (Figure 4 and Table 3).

## 4. Discussion

### 4.1. Effect of volatiles on phase equilibria

In order to test for equilibrium condition in our experiments we can refer to models proposed by Putirka [2008]. Tests for equilibrium between Cpx and a coexisting liquid can be made by comparing observed and predicted values for Fe–Mg exchange, or  $K_D(\text{Fe–Mg})^{\text{cpx-liq}}$ , which should be  $0.28 \pm 0.08$  for Cpx (Putirka,2008; considering  $\text{FeO}=\text{FeO}_{\text{tot}}$ ). Our results show values ranging from 0.236 and 0.248 when using compositions in Table 2, indicating compositions close to equilibrium.

The glasses of our isothermal experiments show geochemical trends that are entirely controlled by the degree of crystallinity that itself depends on the composition and amount of volatiles in the system. The evolution trends for most of the elements (Ca, Mg, Si, Al) are consistent with the crystallization of Cpx (Figure 2), which predominates the solid phase. Ti is almost constant in experiments performed at reduced conditions whereas its abundance is lower in the experiments performed under oxidized conditions, due to the crystallization of Fe–Ti oxides in the latter. The composition of melts from two experiments (VL46 and VL47 at very low H<sub>2</sub>O content; Tables 2 and 3) deviates slightly from the general trend for some elements and can be explained by the presence of Pl in the run products (Figure 5).

The amount of CO<sub>2</sub> that can be dissolved in melts is lower than that of H<sub>2</sub>O and the solubility of both volatiles has been investigated as a function of pressure in a variety of melt compositions [e.g., Brooker *et al.*, 2001, King and Holloway, 2002, Holloway and Blank, 1994, Dixon and Stolper, 1995, Dixon *et al.*, 1995, Jakobsson, 1997, Morizet *et al.*, 2010, Baker and Alletti, 2012, Schanofski *et al.*, 2019]. Carbon species (CO<sub>2</sub>, CH<sub>4</sub>, and CO) have low solubility in basalt and shoshonite melts [at 500 MPa < 4500 ppm CO<sub>2</sub>, Shishkina *et al.*, 2014, Vetere *et al.*, 2014, Behrens *et al.*, 2009, Botcharnikov *et al.*, 2006] and carbonate minerals are not stable in mafic melts. It could therefore be anticipated that (for low CO<sub>2</sub> melt concentrations) CO<sub>2</sub> has no effect on phase compositions and proportions when compared to CO<sub>2</sub>-free dry systems. Indeed, samples with high water contents do not show any important differences in terms of crystallinity between CO<sub>2</sub>-bearing and CO<sub>2</sub>-free samples (Figure 3). This indicates that water plays the most



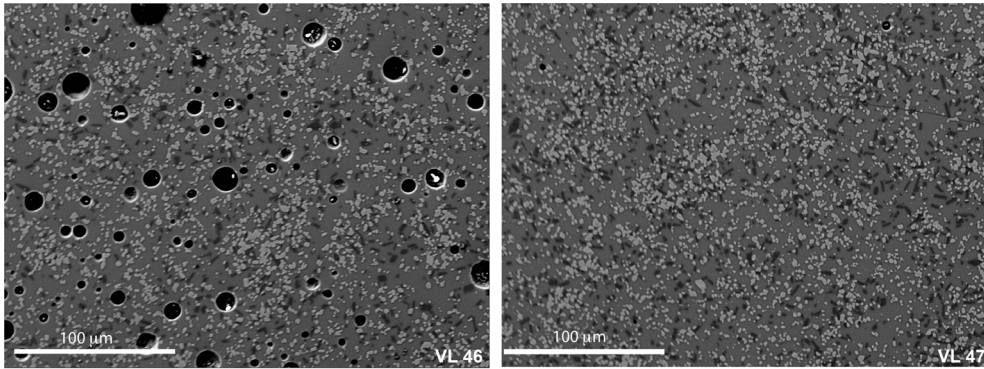
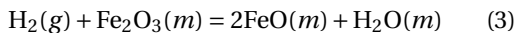


**Figure 5.** BSE images of sample VL46 and VL47 (see Table 3) after annealing at 1080 °C and pressure of 500 MPa. In particular, as 2.8 wt% CO<sub>2</sub> is added to the system, the crystal content decreases by about 10 area%, and also the relative amount of single crystal phases (Cpx and Pl) decreases (VL46\*, Table 3). Clinopyroxene amount varies from 21.6 to 15.1 area% while plagioclase slightly decreases from 8.8 to 5.9 area% (VL46\* and VL47\*, Table 3).

important role on controlling the crystallization temperatures and that the role of minor to moderate CO<sub>2</sub> concentrations is subordinate. However, for systems with low water and relatively high CO<sub>2</sub> levels, this observation seems not to be valid. The difference of 10% in crystallinity found between nominally dry samples (fluid absent and pure CO<sub>2</sub> fluid) implies that CO<sub>2</sub> does not behave as a fully inert component, only reducing water activity. Following the determinations of Husen *et al.* [2016], it is emphasized that the melts synthesized at nominally dry fluid-absent conditions in the internally-heated pressure vessel used at Hannover probably contain at least 0.5 wt% H<sub>2</sub>O. Absolutely dry conditions can never be realized because entrapment of adsorbed water during capsule preparation cannot be avoided and because hydrogen can diffuse through the capsule material at high temperature. This process is partially related to reduction of ferric iron to ferrous iron in the melt during the high *T*-*P* experiments following the reaction



where *m* refers to the melt phase and *g* the gas phase. Thus, the difference between fluid-absent and fluid-present experiments can be considered as a minimum value and may be even larger than determined in this study, if absolutely H<sub>2</sub>O-free systems are considered.

Although experimental conditions are very different, our observations are in agreement with

observations of Fiege *et al.* [2015] showing that the addition of ~2000 ppm of CO<sub>2</sub> to a hydrous basaltic melt (5 wt% H<sub>2</sub>O) has a small effect on crystal content (Cpx, Spl) and glass fractions (during decompression). Nevertheless, when evaluating in detail those data, we can see that samples containing only H<sub>2</sub>O show relatively higher abundance of Cpx compared to those containing both H<sub>2</sub>O and CO<sub>2</sub>. Experiments simulating the effects of CO<sub>2</sub> fluxing conducted by Giuffrida *et al.* [2017] also indicate that the addition of CO<sub>2</sub> to a partially crystallized basalt can influence the phase proportion and result in a partial dissolution of Cpx, in contrast to the common assumption. Vetere *et al.* [2015b] noted that the crystallinity of Etna basalt decreases as CO<sub>2</sub> is added to the system, which is in agreement with the data from this study on a shoshonitic system. In particular, in those experiments, Pl was the most abundant mineral phase, but Pl was absent when only CO<sub>2</sub> was added to the experimental charge. In addition, CO<sub>2</sub> appeared to lower Cpx abundance [Vetere *et al.*, 2015b]. Thus, CO<sub>2</sub> may not act as a complete inert phase in mafic systems in which it is mainly incorporated as carbonate species.

A closer look on data presented in Figure 3 allows us to further discuss the effect of the CO<sub>2</sub> in magmatic systems. In fact, Figure 3 shows, at least for added water content higher than 2 wt%, a nearly linear correlation between crystallinity and added wa-

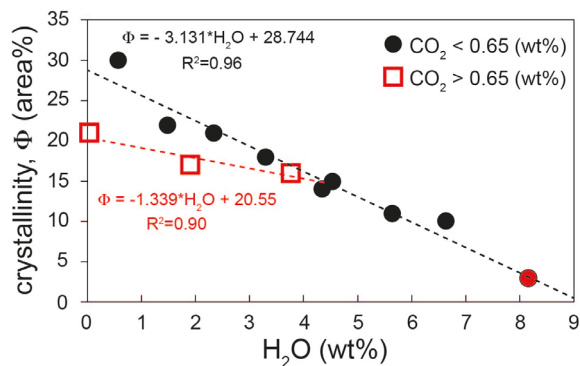


**Figure 6.** Insight on the evolution of crystallinity vs. water content of experiments presented in Table 3. Note the variation on crystallinity (red and black dashed curves) between samples having water content lower than 3.5 wt% with  $\text{CO}_2 > 0.65$  wt% and  $\text{CO}_2 < 0.65$  wt%. Equations curves are also reported.

ter content, independently on  $f\text{O}_2$ . In Figure 6 we show that, if the amount of added  $\text{CO}_2$  is larger than 0.65 wt% and added water content is close or lower than 2 wt%, the crystallinity of the run products becomes lower than what would be predicted from the nearly linear trend between crystallinity and added water, as highlighted by the dashed black and red lines (Figure 6).

More in details, the flushing experiment performed by Giuffrida *et al.* [2017], showed that a  $\text{CO}_2$ -rich fluid phase leads to an increase of the amount of Cpx and a decrease of the abundance of Pl at 300 MPa. This decrease of Pl proportion is associated with a change in An content. Although the conditions are very different, as described above, this proves an effect of  $\text{CO}_2$  on phase stability. Even if small, we also observed a change in An content from  $\text{CO}_2$  free to  $\text{CO}_2$  bearing (VL46 to VL47) as observed in Giuffrida *et al.* [2017] from high to low pressure experiments on Etna basalt. The glass compositions presented in Table 2 also highlight some differences between VL46 and VL47 samples. The  $\text{SiO}_2$  and  $\text{Al}_2\text{O}_3$  concentrations are lower in VL46 whereas FeO and CaO concentrations are higher in VL46. This leads to a small variation of  $\text{NBO}/T$  (0.33 to 0.28) but could mirror the small mineral chemistry variations that we observed. Finally, a liquidus temperature depression, caused by dissolved  $\text{CO}_2$  in melt, is expected and this depres-

sion may range from negligible to several hundred degrees depending on silicate melts composition and pressure [Eggler, 1975, 1976, Mysen and Boettcher, 1975, Eggler and Kadik, 1979, Eggler and Rosenhauer, 1978, Boettcher *et al.*, 1987, Boettcher, 1984]. The extent of this depression is linked to the solubility and solubility mechanism(s) of  $\text{CO}_2$  in the melt. For instance, the liquidus temperature depression of the  $\text{CaMgSi}_2\text{O}_6$ - $\text{CO}_2$  system compared to the volatile free system illustrates this mechanism [Eggler and Rosenhauer, 1978, Mysen and Richet, 2005].

Finally, it is emphasized that the difference in liquidus temperature for the  $\text{CO}_2$  bearing and  $\text{CO}_2$  free compositions (samples VL46 and VL47) observed experimentally at 500 MPa could not be reproduced with alphaMELTS, with  $T_L$  of 1223 °C and 1231 °C, respectively. Thus, the application of thermodynamic models to predict the role of high  $\text{CO}_2$  concentrations on phase stability in water-poor systems needs to be reconsidered. This appears to be particularly relevant in Italian volcanic systems, which are often reacting with carbonates.

#### 4.2. Implications for magma dynamics

The data presented above (literature data and our new experimental results) can have profound implications upon the rheological behavior of magmas. In particular, viscosity is highly influenced by the amount of solid phases. This, in turn, might influence the way magma ascends towards the Earth surface and eventually erupts.

The Vulcanello peninsula formed by effusions from a 600 m long, 0.5 to 1.5 m wide eruptive fissure (dike) [Vetere *et al.*, 2007, and reference therein]. Based on the analysis of fluid inclusions in quartz xenoliths we assume for the storage of the shoshonitic magma a trapping depth between 21.5 and 17 km (corresponding to the Moho depth) [Zanon *et al.*, 2003, Peccerillo *et al.*, 2006]. As such, a possible deep storage reservoir could be hypothesised from which, during the eruptive phase of Vulcanello 1, the magma moved directly to the surface, without intermediate storage into the crust [Davì *et al.*, 2009, Nicotra *et al.*, 2018]. Taking into account the water free samples VL46 and VL47 (Figure 5), having a crystal content of about 20 and 30 area%, respectively, we can calculate the effective viscosity of the crystal bearing system using the models

proposed by Sato [2005] and Vona *et al.* [2011] [ $\eta_r = \eta_{\text{eff}}/\eta_m$  where  $\eta_r$  is the relative viscosity,  $\eta_{\text{eff}}$  is the effective viscosity of the liquid containing a fraction of crystals, and  $\eta_m$  is the viscosity of the melt using the model of Vetere *et al.*, 2007]. Moreover, as required by the Vona *et al.* [2011] model, using image analysis technique on BSE images collected after experiments, one can extract and characterize the crystal shapes from the input grey-scale slides, without considering the possible presence of nanometric crystals [Cassetta *et al.*, 2023]. Procedures are described in Dellino and La Volpe [1996] and Loncaric [1998]. The aspect ratio (AS = major axis/minor axis) parameter providing information on the particles elongation was determined following [Cox and Budhu, 2008]. Results indicate that for our experiments the average AS for Pl is 2.5 and for Cpx is 1.7 while Fe–Ti oxides (when present) have AS close to 1. By taking into account these results, viscosity values of  $10^{4.0}$ – $10^{4.4}$  Pa·s are obtained for system containing 20 and 30 area% of crystals, respectively by using the Vona *et al.* [2011] model. These values are comparable to those obtained using the model proposed by Sato [2005, *i.e.*  $10^{3.9}$  and  $10^{4.2}$  Pa·s].

Figure 7 shows the variation of viscosity of the shoshonitic magma as a function of the crystal and volatile contents. The increase in viscosity is clearly related to the decrease of the volatile content and the relative increase of solid phases.

Considering that magma ascent in dykes is strongly conditioned by dyke width, magma ascent in narrow dykes could be obstructed by magma crystallization. Critical dyke widths were calculated by Petford *et al.* [1994] for magma with felsic composition showing similar viscosities as those investigated here [see also Scaillet *et al.*, 1996]. Results show that dykes thinner than 1 m can hardly propagate from very large depths. We are aware that narrow dykes (<1 m) cannot be approximated to a smooth tabular shape with a constant dyke width, due to the natural roughness of rock fracture planes. However, by doing the identical exercise as in Petford *et al.* [1994], and taking into account (a) basaltic magma temperature, (b) freezing point, (c) rock country temperature (1200 °C, 700 °C and 300 °C respectively), (d) the latent heat for basalt (400 J/g) and (e) the specific heat of basaltic magma ( $1.0 \text{ J}\cdot\text{g}^{-1}\cdot\text{°C}^{-1}$ ), the critical size for dikes reduces to 0.3 m. Thus, we have some constrains for the following discussion.

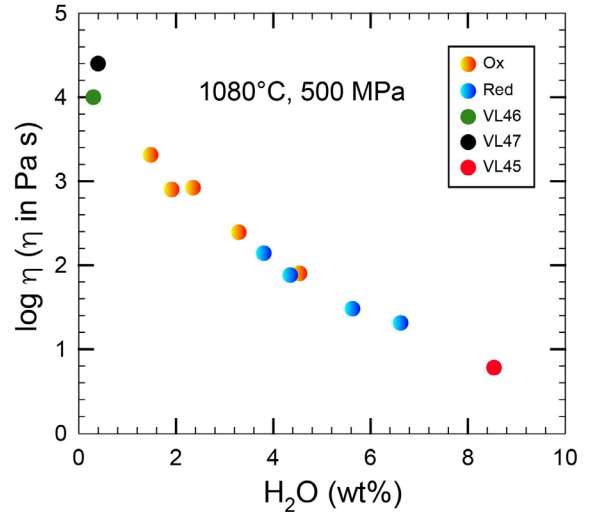


**Figure 7.** Variation of viscosity vs. water content for samples reported in Table 3. Symbols are identical to those reported in Figures 2 and 3 (see text for details).

In order to calculate a possible ascent velocity ( $u$ ;  $\text{m}\cdot\text{s}^{-1}$ ) of these magmas we can use the relation of Lister and Kerr [1991] for laminar flow:

$$u = (w^2/3\eta)\Delta\rho g. \quad (4)$$

As stated above, the eruptive fissure at Vulcanello has width  $\leq 1.5$  m. If now we consider a density contrast between magma and country rock of  $\Delta\rho = 275 \text{ kg}/\text{m}^3$  as reported in Vetere *et al.* [2007], and  $\eta = 10^{3.5}$  Pa·s for a system containing melt with 0.3 wt% H<sub>2</sub>O (see also Table 3 samples VL46, VL47), we can estimate a possible rise velocity of such magmas, assuming that the width of the conduits varies from 0.1 to 1.5 m. Results are presented in Figure 8a where the ascent velocity is found to vary in the range  $u(\text{CO}_2 \text{ free}) = 1.5 \times 10^{-4}$ – $3.5 \times 10^{-2}$  m/s, and  $u(\text{CO}_2 \text{ bearing}) = 5.7 \times 10^{-4}$ – $1.3 \times 10^{-1}$  m/s. The estimated velocity is subject to an abrupt increase if we consider H<sub>2</sub>O–CO<sub>2</sub> bearing systems. Considering that at Vulcanello the water content is estimated between 0.3 and 1.9 wt% [analysis of melt inclusions from shoshonitic samples of Vulcanello in Gioncada *et al.*, 1998 and Clocchiatti *et al.*, 1994a,b] and considering a temperature of 1080 °C [the estimated temperature for Vulcanello magmas is  $1083 \pm 40$  °C, Zanon *et al.*, 2003], a crystallinity of 17 area% can be expected for H<sub>2</sub>O- and CO<sub>2</sub>-bearing samples (e.g. VL37; Table 3). At these

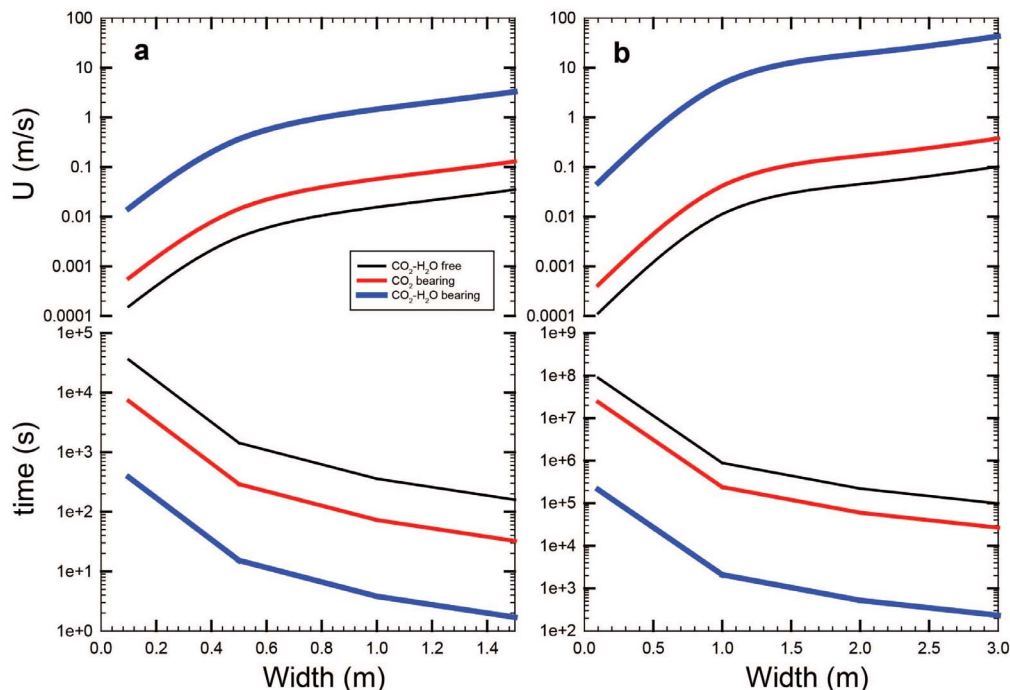


**Figure 8.** (a,b) Velocities and ascent times evolution vs. conduits size for Vulcanello (a) and hypothetical volcanic systems with dike widths  $\leq 3$  m and a density contrast between magma and country rock  $\Delta\rho = 200 \text{ kg/m}^3$  (b). Please refer to text for details.

conditions the magma viscosity is about  $10^{2.8}$  Pa-s and its ascent velocity ( $1.5 \times 10^{-2}$ – $3.3$  m/s as  $w$  varies from 0.1 to 1.5 m, respectively, Figure 7) would be faster than in a volatile-free magma (see  $u(\text{CO}_2 \text{ free})$  given above). Thus, in case of a nominally dry magmatic system rising in conduits having width 1.5 m, the time to reach the surface starting from a depth of 20 km is slightly lower than 4 years. However, if  $\text{CO}_2$  is present, this duration decreases to  $\sim 300$  days, and  $< 2$  h are estimated assuming that 2.0 wt%  $\text{H}_2\text{O}$  + 0.6 wt%  $\text{CO}_2$  are dissolved in the melt. Although these short timescales cannot be applied to the Vulcanello magma, which has lower volatile [Clocchiatti *et al.*, 1994a,b], they could be relevant to other shoshonitic volcanic systems.

As a further example, by making identical considerations as above, we can consider a hypothetical scenario with a viscosity  $\eta = 10^{3.5}$  Pa-s (for a system containing melt + 0.3 wt%  $\text{H}_2\text{O}$  see Table 3, samples VL46, VL47). Thus, if dyke widths are  $\leq 3$  m and the density contrast between magma and country rock is  $\Delta\rho = 200 \text{ kg/m}^3$  and adopting Equation (4), we can have an estimate of the possible rise velocity as pre-

sented in Figure 8b. In this case, results are:  $u(\text{CO}_2 \text{ free}) = 1.1 \times 10^{-4}$ – $1.0 \times 10^{-1}$  m/s, and  $u(\text{CO}_2 \text{ bearing}) = 4.2 \times 10^{-4}$ – $3.7 \times 10^{-1}$  m/s. Finally, if we consider  $\text{H}_2\text{O}$ – $\text{CO}_2$  bearing systems with concentrations similar to the experiments VL32 or VL33 (Table 3) and a temperature of 1080 °C, the lower crystallinity allows magma to have viscosity in the order of  $10^2$  Pa-s and, as consequence, to rise much faster in the range  $4.7 \times 10^{-2}$ – $42.9$  m/s as  $w$  varies from 0.1 to 3 m, respectively (Figure 8). It is important to keep in mind that in dynamic magmatic systems (during ascent) the  $\text{CO}_2$  release is relatively rapid and possibly can locally accelerate magma ascent.

## 5. Conclusions

Crystallization experiments of a natural shoshonite were performed at 500 MPa, and 1080 °C and water activities  $a_{\text{H}_2\text{O}}$  from 0.01 to 1.00. Results show that clinopyroxene is the main crystallizing phase and plagioclase is found to be a stable phase only for water activity lower than 0.1, while spinel is present

in all the runs except in those where  $\log f_{\text{O}_2}$  was lower than  $-9$  ( $\Delta\text{NNO} = -0.11$ ).

Interestingly, at low water activity (below 0.1) the addition of  $\text{CO}_2$  at constant water content reduces the crystallinity of shoshonitic systems. This behaviour is not predicted by classical thermodynamic models. Thus, in the case of  $\text{CO}_2$ -rich and  $\text{H}_2\text{O}$ -poor systems, magmas become less viscous due to the relative decrease in crystallinity. The application of viscosity models to our experimental dataset allows us to infer the possible ascent velocity and ascent time of this type of shoshonitic  $\text{H}_2\text{O}$ -poor magmas from Vulcanello.

Since the magmatic composition used for our study is chemically similar to many Italian volcanic systems (Aeolian Arc, Campi Flegrei, Ischia Island, Pontine Islands, Monti Cimini, Monte Amiata, Capraia Island, Radicofani, Roccamonfina) and also to other systems worldwide (Yellowstone, Mariana Arc, Kurile Arc, Tonga Arc, Andean Arc, Kamchatka Arc), we suggest that our observations will be useful to better understand shoshonitic magma behaviour under relevant geological scenarios. The probability of very rapid ascent of less-evolved melts from depth has to be taken into account for future volcanic crisis and hazard evaluation.

## Conflicts of interest

Authors have no conflict of interest to declare.

## Acknowledgements

This study was funded by the “Piano di Sostegno alla Ricerca 2022 per finanziamenti a progetti di ricerca Curiosity-driven (F-CUR\_CREAMI)” to FV.

## References

- Angell, C. A. (1995). Formation of glasses from liquids and biopolymers. *Science*, 267, 1924–1935.
- Arrighi, S., Tanguy, J. C., and Rosi, M. (2006). Eruptions of the last 2200 years at Vulcano and Vulcanello (Aeolian Islands, Italy) dated by high-accuracy archeomagnetism. *Phys. Earth Planet. Inter.*, 159, 225–233.
- Asimow, P. D. and Ghiorso, M. S. (1998). Algorithmic modifications extending MELTS to calculate sub-solidus phase relations. *Am. Mineral.*, 83, 1127–1132.
- Baker, D. R. and Alletti, M. (2012). Fluid saturation and volatile partitioning between melts and hydrous fluids in crustal magmatic systems: The contribution of experimental measurements and solubility models. *Earth Sci. Rev.*, 114, 298–324.
- Behrens, H., Misiti, V., Freda, C., Vetere, F., Botcharnikov, R. E., and Scarlato, P. (2009). Solubility of  $\text{H}_2\text{O}$  and  $\text{CO}_2$  in ultrapotassic melts at 1200 and 1250 °C and pressure from 50 to 500 MPa. *Am. Mineral.*, 94, 105–120.
- Berndt, J., Liebske, C., Holtz, F., Freise, M., Nowak, M., Ziegenbein, D., Hurkuck, W., and Koepke, J. (2002). A combined rapid-quench and  $\text{H}_2$ -membrane setup for internally heated pressure vessels: Description and application for water solubility in basaltic melts. *Am. Mineral.*, 87, 1717–1726.
- Boettcher, A. L. (1984). The system  $\text{SiO}_2\text{--H}_2\text{O--CO}_2$ : melting solubility mechanisms of carbon and liquid structure to high pressures. *Am. Mineral.*, 69, 823–834.
- Boettcher, A. L., Luth, R. W., and White, B. S. (1987). Carbon in silicate liquids: the systems  $\text{NaAlSi}_3\text{O}_8\text{--CO}_2$ ,  $\text{CaAl}_2\text{Si}_2\text{O}_8\text{--CO}_2$ , and  $\text{KAlSi}_3\text{O}_8\text{--CO}_2$ . *Contrib. Mineral. Petrol.*, 97, 297–304.
- Botcharnikov, R. E., Behrens, H., and Holtz, F. (2006). Solubility and speciation of C–O–H fluids in andesitic melt at  $T = 1100\text{--}1300$  °C and  $P = 200$  and 500 MPa. *Chem. Geol.*, 229, 125–143.
- Botcharnikov, R. E., Freise, M., Holtz, F., and Behrens, H. (2005). Solubility of C–O–H mixtures in natural melts: New experimental data and application range of recent models. *Ann. Geophys.*, 48, 633–646.
- Brooker, R. A., Kohn, S. C., Holloway, J. R., and McMillan, P. F. (2001). Structural controls on the solubility of  $\text{CO}_2$  in silicate melts Part I: bulk solubility data. *Chem. Geol.*, 174, 225–239.
- Burnham, C. W. (1981). The nature of multicomponent aluminosilicate melts. In Rickard, D. T. and Wickman, F. E., editors, *Chemistry and Geochemistry of Solutions at High Temperatures and Pressures*, pages 197–229. Pergamon Press, New York.
- Cassetta, M., Vetere, F., Zanatta, M., Perugini, D., Alvaro, M., Giannetta, B., Zacccone, C., and Daldosso, N. (2023). Micro-Raman spectroscopy for a comprehensive understanding of the structural evolution of Basaltic-Andesite and Trachybasalt multiphase systems. *Chem. Geol.*, 616, article no. 121241.

- Clemens, J. D. and Wall, V. J. (1981). Origin and crystallization of some peraluminous (S-type) granitic magmas. *Can. Mineral.*, 19, 111–131.
- Clocchiatti, R., Del Moro, A., Gioncada, A., Joron, J. L., Mosbah, M., Pinarelli, L., and Sbrana, A. (1994a). Assessment of a shallow magmatic system: the 1888–1890 eruption, Vulcano Island, Italy. *Bull. Volcanol.*, 56, 466–486.
- Clocchiatti, R., Gioncada, A., Mosbah, M., and Sbrana, A. (1994b). Possible deep origin of sulfur output at Vulcano (southern Italy) in the light of melt inclusions studies. *Acta Vulcanol.*, 5, 49–54.
- Cox, M. R. and Budhu, B. (2008). A practical approach to grain shape quantification. *Eng. Geol.*, 96, 1–16.
- Davì, M., De Rosa, R., Donato, P., Vetere, F., Barca, D., and Cavallo, A. (2009). Magmatic evolution and plumbing system of ring-fault volcanism: the Vulcanello Peninsula (Aeolian Islands, Italy). *Eur. J. Mineral.*, 21, 1009–1028.
- De Astis, G., Lucchi, F., Dellino, P., La Volpe, L., Tranne, C. A., Frezzotti, M. L., and Peccerillo, A. (2013). Geology, volcanic history and petrology of Vulcano (central Aeolian archipelago). *Geol. Soc. Lond. Mem.*, 37(1), 281–349.
- De Ritis, R., Ravat, D., Ventura, G., and Chiappini, M. (2013). Curie isotherm depth from aero-magnetic data constraining shallow heat source depths in the central Aeolian Ridge (Southern Tyrrhenian Sea, Italy). *Bull. Volcanol.*, 75, article no. 710.
- Dellino, P. and La Volpe, L. (1996). Image processing analysis in reconstructing fragmentation and transportation mechanisms of pyroclastic deposits. The case of Monte Pilato-Rocche Rosse eruptions, Lipari (Aeolian islands, Italy). *J. Volcanol. Geotherm. Res.*, 71, 13–29.
- Devine, J. D., Gardner, J. E., Brack, H. P., Layne, G. D., and Rutherford, M. J. (1995). Comparison of microanalytical methods for estimating H<sub>2</sub>O contents of silicic volcanic glasses. *Am. Mineral.*, 80, 319–328.
- Dixon, J. E. and Stolper, E. M. (1995). An experimental study of water and carbon dioxide solubilities in Mid-Ocean Ridge Basaltic liquids. Part II: applications to degassing. *J. Petrol.*, 36, 1633–1646.
- Dixon, J. E., Stolper, E. M., and Holloway, J. R. (1995). An experimental study of water and carbon dioxide solubilities in mid-ocean ridge basaltic liquids. Part I: Calibration and solubility models. *J. Petrol.*, 36, 1607–1631.
- Eggler, D. H. (1975). CO<sub>2</sub> as a volatile component in the mantle: the system Mg<sub>2</sub>SiO<sub>4</sub>–SiO<sub>2</sub>–H<sub>2</sub>O–CO<sub>2</sub>. *Phys. Chem. Earth*, 9, 869–881.
- Eggler, D. H. (1976). Does CO<sub>2</sub> cause partial melting in the low-velocity layer of the mantle? *Geology*, 4(2), 69–72.
- Eggler, D. H. and Kadik, A. A. (1979). The system NaAlSi<sub>3</sub>O<sub>8</sub>–H<sub>2</sub>O–CO<sub>2</sub>: I. Compositional and thermodynamic relations of liquids and vapors coexisting with albite. *Am. Mineral.*, 64, 1036–1049.
- Eggler, D. H. and Rosenhauer, M. (1978). Carbon dioxide in silicate melts. II. Solubilities of CO<sub>2</sub> and H<sub>2</sub>O in CaMgSi<sub>2</sub>O<sub>6</sub> (diopside) liquids and vapors at pressures to 40 kb. *Am. J. Sci.*, 278, 64–94.
- Falsaperla, S., Neri, G., and Velardita, S. (1985). Struttura della crosta superiore dell'area delle isole Eolie. *Rend. Osserv. Geofis. Reggino*, XXIX, 103–111.
- Fiege, A., Vetere, F., Holtz, F., Simon, A., and Iezzi, G. (2015). Crystallization induced by decompression in basaltic system: implication for magma ascent and degassing. *Chem. Geol.*, 411, 310–322.
- Fusillo, R., Di Traglia, F., Gioncada, A., Pistolesi, M., Wallace, P. J., and Rosi, M. (2015). Deciphering post-caldera volcanism: insight into the Vulcanello (Island of Vulcano, Southern Italy) eruptive activity based on geological and petrological constraints. *Bull. Volcanol.*, 77, article no. 76.
- Ghiorso, M. S., Hirschmann, M. M., Reiners, P. W., and Kress III, V. C. (2002). The pMELTS: A revision of MELTS for improved calculation of phase relations and major element partitioning related to partial melting of the mantle to 3 GPa. *Geochem. Geophys. Geosyst.*, 3(5), 1–36.
- Ghiorso, M. S. and Sack, R. O. (1995). Chemical mass transfer in magmatic processes: IV. A revised and internally consistent thermodynamic model for the interpretation and extrapolation of liquid–solid equilibria in magmatic systems at elevated temperatures and pressures. *Contrib. Mineral. Petrol.*, 119, 197–212.
- Gioncada, A., Clocchiatti, R., Sbrana, A., Bottazzi, P., Massare, D., and Ottolini, L. (1998). A study of melt inclusions at Vulcano (Aeolian Islands, Italy): insights on the primitive magmas and on the volcanic feeding system. *Bull. Volcanol.*, 60, 286–306.
- Giordano, D. and Dingwell, D. B. (2003). The kinetic fragility of natural silicate melts. *J. Phys. Condens. Matter*, 15, 945–954.

- Giuffrida, M., Vetere, F., Viccaro, M., and Holtz, F. (2017). The effect of CO<sub>2</sub> flushing on Etnean magmas: an experimental approach. *Contrib. Mineral. Petrol.*, 172, article no. 90.
- Holloway, J. R. and Blank, J. G. (1994). Application of experimental results to C–O–H species in natural melts. In Carroll, M. R. and Holloway, J. R., editors, *Volatiles in Magmas*, volume 30 of *Reviews in Mineralogy*, pages 187–230. Mineralogical Society of America, Chantilly, VA.
- Husen, A., Almeev, R. R., and Holtz, F. (2016). The effect of H<sub>2</sub>O and pressure on multiple saturation and liquid lines of descent in basalts from the Shatsky Rise. *J. Petrol.*, 57(2), 309–344.
- Jakobsson, S. (1997). Solubility of water and carbon dioxide in an icelandite at 1400 °C and 10 kilobars. *Contrib. Mineral. Petrol.*, 127, 129–135.
- Jarosewich, E. J. (2002). Smithsonian microbeam standards. *J. Res. Natl. Inst. Stand. Technol.*, 107(6), 681–685.
- Kent, A. J. R. (2008). Melt inclusions in basaltic and related volcanic rocks. In Putirka, K. D. and Tepley III, F. J., editors, *Minerals, Inclusions and Volcanic Processes*, volume 69 of *Reviews in Mineralogy and Geochemistry*, pages 273–331. Mineralogical Society of America and Geochemical Society.
- King, P. L. and Holloway, J. R. (2002). CO<sub>2</sub> solubility and speciation in intermediate (andesitic) melts: The role of H<sub>2</sub>O and composition. *Geochim. Cosmochim. Acta*, 66, 1627–1640.
- Li, X., Zhang, C., Almeev, R. R., and Holtz, F. (2020). GeoBalance: An Excel VBA program for mass balance calculation in T geosciences. *Geochemistry*, 80, article no. 125629.
- Lister, J. R. and Kerr, R. C. (1991). Fluid-mechanical models of crack propagation and their application to magma transport in a dyke. *J. Geophys. Res.*, 96, 10049–10077.
- Loncaric, S. (1998). A survey of shape analysis techniques. *Pattern Recognit.*, 31, 983–1001.
- Martel, C., Brooker, R. A., Andújar, J., Pichavant, M., Scaillet, B., and Blundy, J. D. (2019). Experimental simulations of magma storage and ascent. In *Advances in Volcanology*, pages 101–110. Springer, Cham.
- Martel, C., Pichavant, M., Bourdier, J.-L., Holtz, F., and Scaillet, B. (1998). Magma storage conditions and control of eruption regime in silicic volcanoes: experimental evidence from Mt. Pele. *Earth Planet. Sci. Lett.*, 156(1–2), 89–99.
- Morizet, Y., Paris, M., Gaillard, F., and Scaillet, B. (2010). C–O–H fluid solubility in haplobasalt under reducing conditions: an experimental study. *Chem. Geol.*, 279, 1–16.
- Mysen, B. O. and Boettcher, A. L. (1975). Melting of a hydrous mantle. I. Phase relations of natural peridotite at high pressures and temperatures with controlled activities of water, carbon dioxide and hydrogen. *J. Petrol.*, 16, 520–548.
- Mysen, B. O. and Richet, P. (2005). *Silicate Glasses and Melts, Properties and Structure*. Elsevier, Amsterdam.
- Nicotra, E., Giuffrida, M., Viccaro, M., Donato, P., D’Orlando, C., Paonita, A., and De Rosa, R. (2018). Timescales of pre-eruptive magmatic processes at Vulcano (Aeolian Islands, Italy) during the last 1000 years. *Lithos*, 316–317, 347–365.
- Parat, F., Holtz, F., and Feig, S. (2008). Pre-eruptive Conditions of the Huerto Andesite (Fish Canyon System, San Juan Volcanic Field, Colorado): Influence of volatiles (C–O–H–S) on phase equilibria and mineral composition. *J. Petrol.*, 49, 911–935.
- Peccherillo, A., Frezzotti, M. L., De Astis, G., and Ventura, G. (2006). Modeling the magma plumbing system of Vulcano (Aeolian Island, Italy) by integrative fluid-inclusion geobarometry, petrology and geophysics. *Geology*, 34, 17–20.
- Petford, N., Lister, R. J., and Kerr, R. C. (1994). The ascent of felsic magma in dykes. *Lithos*, 32, 161–168.
- Pouchou, J. L. and Pichoir, F. (1991). Quantitative analysis of homogeneous or stratified microvolumes applying the model “PAP”. In *Electron Probe Quantification*, pages 31–75. Springer, Boston, MA.
- Putirka, K. (2008). Thermometers and barometers for volcanic systems. In Putirka, K. and Tepley, F., editors, *Minerals, Inclusions and Volcanic Processes*, volume 69 of *Reviews in Mineralogy and Geochemistry*, pages 61–120. Mineralogical Society of America, Chantilly, VA.
- Sato, H. (2005). Viscosity measurements of subliquidus magmas: 1707 basalt of Fuji volcano. *J. Mineral. Petrol. Sci.*, 100, 133–142.
- Scaillet, B. and Evans, B. W. (1999). The June 15, 1991 eruption of Mount Pinatubo. I. Phase equilibria and pre-eruption P–T–fO<sub>2</sub>–fH<sub>2</sub>O conditions of the dacite magma. *J. Petrol.*, 40, 381–411.

- Scaillet, B., Holtz, F., Pichavant, M., and Schmidt, M. (1996). Viscosity of Himalayan leucogranites: Implications for mechanisms of granitic magma ascent. *J. Geophys. Res.*, 101, 27691–27699.
- Schanofski, M., Fanara, S., and Schmidt, B. C. (2019). CO<sub>2</sub>–H<sub>2</sub>O solubility in K-rich phonolitic and leucitic melts. *Contrib. Mineral. Petrol.*, 174, article no. 52.
- Schulze, F., Behrens, H., Holz, F., Ruox, J., and Johannes, W. (1997). The influence of H<sub>2</sub>O on the viscosity of a haplogranitic melt. *Am. Mineral.*, 81, 1155–1165.
- Shishkina, T., Botcharnikov, R. E., Holtz, F., Almeev, R. R., Jazwa, A. M., and Jakubiak, A. A. (2014). Compositional and pressure effects on the solubility of H<sub>2</sub>O and CO<sub>2</sub> in mafic melts. *Chem. Geol.*, 277, 115–125.
- Sisson, T. W. and Layne, G. D. (1992). H<sub>2</sub>O in basalt and basaltic andesite glass inclusions from four subduction-related volcanoes. *Earth Planet. Sci. Lett.*, 117, 619–635.
- Smith, P. M. and Asimow, P. D. (2005). Adibat\_1ph: A new public front-end to the MELTS, pMELTS, and pHMELTS models. *Geochem. Geophys. Geosyst.*, 6, article no. Q02004.
- Vetere, F., Behrens, H., Botcharnikov, R., Holtz, F., and Fanara, S. (2014). The role of alkalis in the solubility of H<sub>2</sub>O and CO<sub>2</sub> in silicate melts. Implication for phonotephritic magmas. *Contrib. Mineral. Petrol.*, 167, 1–17.
- Vetere, F., Behrens, H., Misiti, V., Ventura, G., De Rosa, R., Holtz, F., and Deubener, J. (2007). Viscosity of shoshonitic melt (Vulcanello Aeolian Islands, Italy) and inference on the dynamics of magma ascent. *Chem. Geol.*, 245, 89–102.
- Vetere, F., Botcharnikov, R. R., Behrens, H., Holtz, F., and De Rosa, R. (2011). Solubility of H<sub>2</sub>O and CO<sub>2</sub> in shoshonitic melts at 1250 °C and pressure from 50 to 400 MPa. *J. Volcanol. Geotherm. Res.*, 202, 251–261.
- Vetere, F., Iezzi, G., Behrens, H., Holtz, F., Ventura, G., Misiti, V., Cavallo, A., Mollo, S., and Dietrich, M. (2015a). Glass forming ability and crystallization behaviour of sub-alkaline silicate melts. *Earth Sci. Rev.*, 150, 25–44.
- Vetere, F., Mollo, S., Giacomoni, P. P., Iezzi, G., Coltorti, M., Ferlito, C., Holtz, F., Perugini, D., and Scarlato, P. (2015b). Experimental constraints on the origin of pahoehoe “cicirara” lavas at Mt. Etna volcano (Sicily, Italy). *Bull. Volcanol.*, 77, article no. 44.
- Vona, A., Romano, C., Dingwell, D. B., and Giordano, D. (2011). The rheology of crystal-bearing basaltic magmas from Stromboli and Etna. *Geochim. Cosmochim. Acta*, 75, 3214–3236.
- Zanon, V., Frezzotti, M. L., and Peccerillo, A. (2003). Magmatic feeding system and crustal magma accumulation beneath Vulcano Island (Italy): evidence from fluid inclusions in quartz xenoliths. *J. Geophys. Res.*, 108, 1–13.





Research article

## Magma degassing and its impact on the Earth's atmosphere: from magma oceans to lava lakes

# Bubble connectivity in experimentally-sheared crystal-bearing silicic melts

Camille Daffos<sup>a</sup>, Caroline Martel<sup>\*,\*,b</sup>, Laurent Arbaret<sup>\*,b</sup> and Rémi Champallier<sup>\*,b</sup>

<sup>a</sup> Institut des Sciences de la Terre d'Orléans (ISTO), Univ. Orléans, CNRS, BRGM, UMR 7327, Orléans, France

E-mails: [camille.daffos@univ-orleans.fr](mailto:camille.daffos@univ-orleans.fr) (C. Daffos), [caroline.martel@cnrs-orleans.fr](mailto:caroline.martel@cnrs-orleans.fr) (C. Martel), [laurent.arbaret@univ-orleans.fr](mailto:laurent.arbaret@univ-orleans.fr) (L. Arbaret), [remi.champallier@cnrs-orleans.fr](mailto:remi.champallier@cnrs-orleans.fr) (R. Champallier)

**Abstract.** The explosivity of an eruption is mainly controlled by the ability of gases to escape the magma column. Indeed, magmas able to evacuate gases mostly erupt effusively whereas magmas that retain pressurised gases are likely to trigger explosive events. In order to evaluate the explosive potential of magmas residing at shallow level, we investigated the influence of crystal content and shear on the development of bubble connectivity in bubble- and crystal-bearing silicic melts. The pre-deformed samples contain 0 to 50 vol% of plagioclase crystals (40–90  $\mu\text{m}$  size) in a hydrated haplogranitic melt with 20–30 vol% vesicularity mainly consisting of decompression-induced  $\text{H}_2\text{O}$  bubbles (~20–250  $\mu\text{m}$  in diameter). The samples were deformed in torsion at a temperature of 650 °C (crystal-free) or 750 °C (crystal-bearing), confining pressure of 50 MPa, constant moderate shear rate of  $2 \times 10^{-4} \text{ s}^{-1}$ , and low strains ( $\gamma < 2$ ). The sample microtextures and three-dimensional pore network show that bubbles are mostly isolated in crystal-poor (0–10 vol%) samples, whereas bubble connection reaches more than 70% in crystal-rich (30–50 vol%) samples, whether deformed or not. With increasing strain from  $\gamma = 0$  to 2, bubbles re-organise in shear zones by forming channels. Therefore, moderately-porous (20–30 bulk vol%) crystal-rich magmas emplacing at shallow depths, such as in upper conduits or lava domes, may be highly permeable via a process of gas channelling effective at very low strains ( $\gamma < 2$ ). This implies that violent explosions of lava domes producing devastating surges require additional mechanisms of gas pressurisation in moderately-porous crystal-rich magmas.

**Keywords.** Degassing, Mush, Rhyolite, Shear, Experiments.

Manuscript received 19 August 2022, revised 4 December 2022, accepted 27 April 2023.

## 1. Introduction

The explosivity of an eruption is mainly controlled by the ability of gases to escape the magma column, with overpressured gases trapped in melt likely to lead to an explosive eruption, whereas efficient outgassing may lead to effusive activity [Eichelberger

et al., 1986, Woods and Koyaguchi, 1994]. The conditions under which gas escapes the magma is thus a prerequisite to predict the eruptive dynamics, and depend on an interplay of many parameters involving magma characteristics [e.g., composition, temperature, volatile and crystal contents; Takeuchi et al., 2021, Popa et al., 2021] and emplacement conditions [e.g. flow and conduit properties, rates of decompression and shear; Cassidy et al., 2018].

An ascending volatile-saturated magma exsolves

\*Corresponding author

gases that are accommodated through bubble nucleation or growth of pre-existing bubbles in case of an initial volatile phase in excess. In highly viscous magmas (viscosity  $>10^6$  Pa·s), bubbles are usually trapped in the melt and cannot easily migrate independently of the liquid to outgas via separated flow. If physical and time conditions permit, bubbles connect by coalescing and can develop gas channels that ultimately make the magma permeable to gases, thus allowing outgassing through fractured dome rocks or conduit walls. Rates of gas escape in silica-rich melts are difficult to assess because they depend on intrinsic parameters, such as the bubble characteristics [e.g., vesicularity, Klug and Cashman, 1996; pore aperture size, Wright *et al.*, 2009, Degruyter *et al.*, 2010; bubble number density; Bain *et al.*, 2019; bubble network, Burgisser *et al.*, 2017], and external parameters related to magma emplacement kinetics. Among these external parameters, decompression rate has been demonstrated to affect bubble connectivity and permeability. The studies dealing with decompression-induced bubbles developing isotropically highlighted permeability increase at vesicularities mostly  $>50$  vol% [Burgisser and Gardner, 2005, Takeuchi *et al.*, 2005, Okumura *et al.*, 2012, Martel and Iacono-Marziano, 2015]. Thereafter, shear has been demonstrated to drastically affect bubble connectivity and permeability, by promoting bubble coalescence [Okumura *et al.*, 2008] and outgassing [Okumura *et al.*, 2009, Shields *et al.*, 2016], but also by alternately favouring and preventing connectivity where deformation resulted in magma compaction [Gonnermann *et al.*, 2017]. If magma viscosity and/or shear rate are high enough, permeability development may proceed through magma fracturing [Stasiuk *et al.*, 1996, Tuffen *et al.*, 2003, Castro *et al.*, 2012, Gaunt *et al.*, 2014, Kushnir *et al.*, 2017].

Many studies have been dedicated to crystal-free or -poor melts, but magmas can be highly crystallized, which affects the development of bubble connectivity. Estimates of the percolation threshold commonly range from 30 vol% [Saar and Manga, 1999, Blower, 2001] to 80 vol% vesicularity [Westrich and Eichelberger, 1994, Takeuchi *et al.*, 2008, Wright *et al.*, 2009], with the highest values characterizing rapidly-decompressed crystal-free magmas. Okumura *et al.* [2012] experimentally decompressed rhyolitic melts containing 30 and 50 vol% corundum crystals, and concluded that gas permeability re-

mained low until vesicularity reached  $>68$  vol%. Lindoo *et al.* [2017] and deGraffenried *et al.* [2019] decompressed mafic and rhyolitic magmas, respectively, and reported a decrease of the percolation threshold from  $>60$  to  $<50$  vol% in the presence of more than about 20 vol% crystals. Parmigiani *et al.* [2017] numerically modelled the outgassing efficiency of a magmatic volatile phase in crystal-rich (mush-like) magmas, highlighting gas permeability from very low porosities ( $\sim 10$  vol%) via a mechanism of channelling by which crystals build sustainable channels for gas percolation. Such a permeability development and outgassing at low vesicularity and high crystal content could explain the low porosity values inferred to occur in the volcanic conduit prior to Vulcanian eruptions [Collombet *et al.*, 2021].

In crystal-bearing silicic magmas, the bubble network mostly rearranges under decompression in the central part of the volcanic conduit and simple-shear deformation at conduit edges or in lava domes where the rearrangement of the stressed crystal framework is facilitated by strain localization. To understand the processes governing the development of degassing pathways in crystal-rich silicic magmas, few studies have been dedicated to deform three-phase (melt, bubbles, crystals) magmas in simple shear using high-temperature and high-pressure deformation rigs of Paterson type. Laumonier *et al.* [2011] deformed a haplotonalitic melt containing 50 vol% plagioclase crystals and 11 vol% porosity, at temperature ( $T$ ) of 600 °C, confining pressure ( $P$ ) of 200 MPa, bulk finite shear strains ( $\gamma$ ) of 1.3 and shear rates ( $\dot{\gamma}_r$ ) from  $3 \times 10^{-5}$  to  $1 \times 10^{-3} \text{ s}^{-1}$ . They highlighted gas accumulation in local microstructures caused by shear-induced crystal fabric (local  $\gamma$  up to  $\sim 9$ ). Shields *et al.* [2014] sheared haplogranitic melts spanning crystal contents from 0 to 42 vol% and CO<sub>2</sub>-bubble contents from 12 to 36 vol%, at  $T < 600$  °C,  $P$  of 150–200 MPa,  $\gamma$  up to 10, and  $\dot{\gamma}_r$  from  $1 \times 10^{-4}$  to  $5 \times 10^{-4} \text{ s}^{-1}$ . They did not observe bubble coalescence and outgassing took place via sample-wide fracturing. These results of sample permeability reached by fracturing agreed with those obtained by Kushnir *et al.* [2017] using crystal-free haplogranitic melts with  $\sim 15$  vol% argon bubbles deformed at magmatic  $T$  of 880 °C,  $P$  of 60 MPa,  $\gamma$  up to 7, and  $\dot{\gamma}_r$  of  $1 \times 10^{-4}$  to  $8 \times 10^{-4} \text{ s}^{-1}$ . Pistone *et al.* [2012] sheared haplogranitic melts with 24 to 65 vol% quartz crystals and 9–12 vol% CO<sub>2</sub> bubbles, at  $T$  of 450–750 °C,

$P$  of 200 MPa,  $\gamma$  up to 8, and  $\gamma_r$  from  $5 \times 10^{-6}$  to  $4 \times 10^{-3} \text{ s}^{-1}$ . In the crystal-poor (24–44 vol%) samples, the authors reported bubble stretching with increasing strain, facilitating coalescence (for  $\gamma > 2$  and for increasing  $\gamma_r$ ) and gas channel formation, eventually leading to outgassing along the walls of the sample container. In the crystal-rich (55–65 vol%) samples, however, bubble stretching was localized in shear bands where the crystal framework (including crystal breakage) prevented gas loss.

These experimental studies provided information on the deformation of three-phase magmas at  $P$  of  $\sim 200$  MPa,  $T$  mostly close to the glass transition, for bubble contents mostly  $< 15$  vol%, and for  $\gamma$  up to  $\sim 10$ . We aim at extending these studies to the investigation of the effect of a crystal network on bubble connectivity and gas percolation in bubbly crystal-bearing magmas emplacing at shallow depth, such as in upper volcanic conduits or lava domes, from which explosive eruptions may be triggered. We performed simple shear experiments in a Paterson rig, using three-phase magmas consisting of 0 to 50 bulk vol% plagioclase crystals and 15–30 bulk vol%  $\text{H}_2\text{O}$  bubbles (20–45 vol% recalculated on the melt phase) in a haplogranitic melt, under magmatic  $T$  of 650–750 °C, confining  $P$  of 50 MPa,  $\gamma$  up to  $\sim 2$ , and  $\gamma_r$  of  $2 \times 10^{-4} \text{ s}^{-1}$ . We characterized the sample microstructures and bubble connectivity as a function of crystal content and shear strain, and have discussed implications for the natural magmas and eruptive dynamics.

## 2. Methods

### 2.1. Experimental methods

The experiments consisted of three main phases: (i) synthesis of crystal-bearing hydrated glasses, (ii) decompression-induced  $\text{H}_2\text{O}$ -bubble formation, and (iii) deformation in simple shear of the three-phase magmas.

#### 2.1.1. Synthesis of crystal-bearing hydrated glasses

The method of preparation is detailed in Supplementary Section 1.1.1 and a summary is given below. The anhydrous starting glass is a haplogranite (HPG8; composition in wt%: 78.6  $\text{SiO}_2$ , 12.5  $\text{Al}_2\text{O}_3$ , 4.6  $\text{Na}_2\text{O}$ , 4.2  $\text{K}_2\text{O}$ ). The HPG8 glass was chosen because (i) it

is rheologically well-characterized [Hess and Dingwell, 1996], (ii) its eutectic composition allows experiments at relatively low  $T$  without crystallization, and (iii) it simulates late-stage crystallization of evolved liquids such as rhyolitic melts. The HPG8 hydrations were performed in internally-heated pressure vessels (at the Institut des Sciences de la Terre d'Orléans, ISTO) in order to obtain glasses with 5.0 and 9.6 wt%  $\text{H}_2\text{O}$ , to which different amounts of plagioclase crystals (size of 50–90  $\mu\text{m}$ ) were manually added. Plagioclase crystals were chosen because they represent the main crystalline phase of silicic magmas, as phenocrysts or microcrysts. The crystal contents recalculated on the melt are 0, 21, 50, and 70 vol%, leading to bulk crystal volume ( $\Phi_{\text{c\_bulk\_3D}}$ , recalculated on a bubble-bearing basis) of about 0, 10, 30, and 50 vol%.

#### 2.1.2. Synthesis of a bubble-bearing magmas

The powder mixtures of plagioclase crystals and hydrated HPG8 glass were decompressed from 300 to 50 MPa at 850 °C in the Paterson gas-medium apparatus [Paterson and Olgaard, 2000; Australian Scientific Instruments Pty Ltd, at ISTO; Figure 1a], in order to trigger a bubble nucleation event of supercritical  $\text{H}_2\text{O}$  fluid (hereafter referred as to gas bubbles). The strategy was to obtain bulk amounts of bubbles around 20–40 vol%, ideally not connected to each other, in order to check whether further deformation will promote gas connectivity. The experimental details are given in Supplementary Section 1.1.2.

#### 2.1.3. Torsion experiments

Keeping the experimental setup as it was after decompression, deformation in right-lateral simple shear was carried out at  $P$  of 50 MPa,  $T$  of 650 or 750 °C,  $\gamma_r$  of  $2 \times 10^{-4} \text{ s}^{-1}$ , and  $\gamma$  from 0 to 2. Such  $\gamma$  are rather small compared to those observed at natural conduit margins or dome bases, but the aim was to determine the gas percolation thresholds occurring during the initiation of deformation. The experimental details and calculations confirming limited relaxation of the bubbles during quenching are given in Supplementary Section 1.1.3.

## 2.2. Analytical methods

After experiment, the sample was cut following a section parallel to the shear plane and exposing the longitudinal tangential surfaces (maximum shear

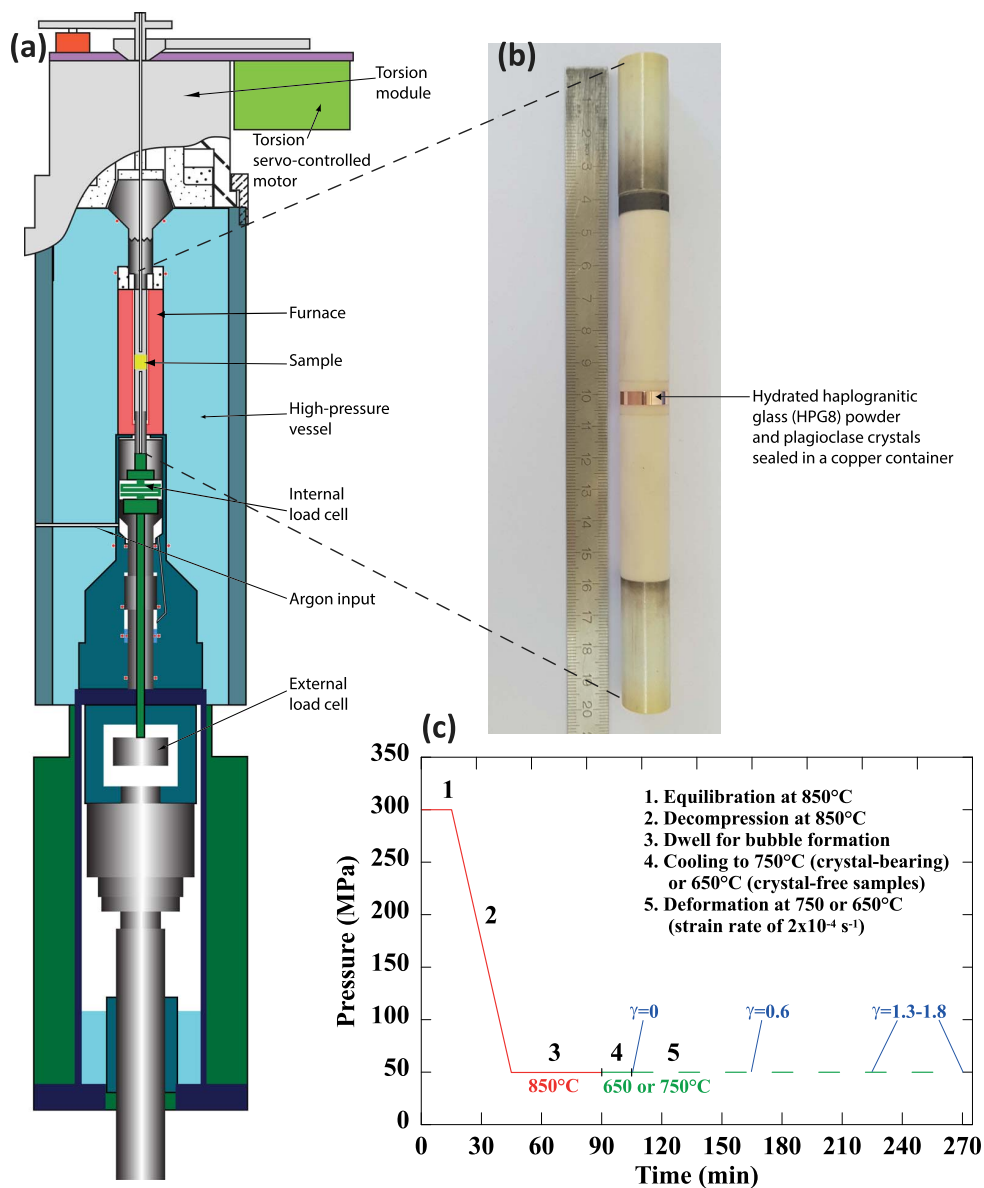


**Figure 1.** Experimental device and strategy. (a) Scheme of the Paterson gas-medium press, (b) Photography of the sample assembly, and (c) Pressure–temperature–time path showing the isothermal step (850 °C) of decompression-induced (300 to 50 MPa) bubble nucleation, followed by an isobaric (50 MPa) and isothermal (750 or 650 °C) step of sample torsion ( $\gamma < 2$ ) at a rate of  $2 \times 10^{-4} \text{ s}^{-1}$ .

strain) for microstructural analyses using a scanning electron microscope (SEM; Merlin Compact Zeiss at ISTO). The whole section was imaged at high resolution using the SEM, and the images were segmented using the SPO2003 image-processing software [Launeau and Robin, 1996, Launeau

and Cruden, 1998], in order to determine the two-dimensional (2D) contents, sizes, and orientations of the bubbles and the crystals, as detailed in Supplementary Section 1.2.1. A core sample bored perpendicularly to the shear plane was used for three-dimensional (3D) analyses using X-ray

computed tomography (XCT; Phoenix NanoTOM at ISTO). The 3D bulk porosity ( $\Phi_{b\_bulk\_3D}$ ) and the amount of bubbles connected to the sample borders ( $\Phi_{b\_connect\_3D}$ ) were determined by segmenting the XCT images using commercial software, such as VGStudio Max and Blob3D, as detailed in Supplementary Section 1.2.2. The plagioclase crystals were hardly discernible due to their low contrast of density with the glass and were not subjected to 3D analyses.

The glass H<sub>2</sub>O contents of the bubble-bearing samples were checked following the “by-difference” method using an electron microprobe (EMP; Cameca SX Five at ISTO). As some of the residual glasses were unexpectedly rich in H<sub>2</sub>O, they were double-checked by micro-Raman spectroscopy (ISTO), as detailed in Supplementary Section 1.2.3.

### 2.3. Calculations

The calculations mainly concerned the gas fraction and the bulk viscosity of the samples. The expected gas fraction was determined using the equation of Jaupart and Allègre [1991], which calculates the gas volume ( $\alpha_{melt}$ ) resulting from a closed-system degassing (in that gas bubbles remain in contact with the melt), as described in Supplementary Section 1.3.1.

The samples were not viscous enough at 750 °C to allow viscosity measurements in the Paterson press, so we estimated the bulk viscosity ( $\eta_{bulk}$ ) from Hess and Dingwell [1996] for the hydrated melt and using the equation of Truby *et al.* [2015] for the three-phase suspensions, as detailed in Supplementary Section 1.3.2.

## 3. Results

Four series with different bulk crystal contents ( $\Phi_{c\_bulk\_3D}$ ) of 0, 10, 30, 50 vol%, hereafter referred as to serie0, serie10, serie30, and serie50, respectively, were decompressed in the Paterson press for bubble formation and subsequent deformation in simple shear ( $P = 50$  MPa,  $T = 650\text{--}750$  °C,  $\dot{\gamma}_r = 2 \times 10^{-4}$  s<sup>-1</sup>) to finite deformations  $\gamma = 0$  (no deformation),  $\gamma = 0.6$ , and  $\gamma = 1.3\text{--}1.8$  (no run for serie10). The experimental conditions of the deformed bubble- and crystal-bearing magmas are given in Table 1. The analytical results are reported in Table 2 and detailed below.

### 3.1. Crystal-free series (serie0)

The SEM pictures of the samples from serie0 show relatively homogeneous spatial distributions of the bubbles (Figure 2a–c), in agreement with the absence of strain localization expected from the Newtonian behaviour of pure melts. Melt porosity,  $\Phi_{b\_melt\_2D}$ , is  $31 \pm 3$ , to  $24 \pm 2$  and  $30 \pm 4$  area%, at  $\gamma = 0, 0.6$ , and  $1.3$ , respectively (Figure 3a), in relatively good agreement with the porosities measured from the XCT images,  $\Phi_{b\_bulk\_3D}$ , which are  $30 \pm 3$ ,  $21 \pm 3$ , and  $15 \pm 3$  vol%, respectively. The content of bubbles connected to the sample outside measured from the XCT images,  $\Phi_{b\_connect\_3D}$ , represents about half of the  $\Phi_{b\_bulk\_3D}$  (i.e.,  $49 \pm 3$ ,  $52 \pm 3$ , and  $50 \pm 3$  vol%, at  $\gamma = 0, 0.6$ , and  $1.3$ , respectively). The 2D bubble number densities measured from the SEM images,  $BND_{2D}$ , are of  $10^{5.6\text{--}5.7 \pm 0.1}$  m<sup>-2</sup> (Figure 4a) and those determined using the XCT,  $BND_{3D}$ , are  $10^{10.5\text{--}10.6}$  m<sup>-3</sup>. In the undeformed sample, 95% of the bubbles have equivalent diameters of 20–40 μm, representing about half of the total vesicularity. The other half volume is made of bubbles with up to 300 μm diameter (Supplementary Figure 3a). Bubble eccentricity,  $R_b$ , increases from  $1.3 \pm 0.1$  to  $1.9 \pm 0.2$  and  $2.1 \pm 0.3$  with increasing  $\gamma$ , with a slight preferential orientation of the bubbles,  $\theta_b$  of  $\sim 22 \pm 6^\circ$  (Figure 4b). Glass H<sub>2</sub>O contents measured following the EMP by-difference method are  $3.6 \pm 0.7$  wt% at  $\gamma = 0$  and  $4.1 \pm 0.7$  wt% at  $\gamma = 1.3$ , giving bulk viscosities of  $10^{7.3}$  and  $10^{7.0}$  Pa·s, respectively.

### 3.2. Series with 10% crystals (serie10)

Serie10 consists of only a  $\gamma = 0$  (undeformed) sample and a  $\gamma = 0.6$  sample, since higher shear strains inevitably conducted to capsule tearing. The deformed sample shows incipient shear zones marked by discrete local reorganisation of the bubbles and crystals (Figure 2e).  $\Phi_{b\_melt\_2D}$  slightly decreases from  $31 \pm 3$  area% at  $\gamma = 0$  to  $27 \pm 3$  area% at  $\gamma = 0.6$  (Figure 3a). Recalculating bulk porosities (i.e. including crystals) give  $\Phi_{b\_bulk\_2D}$  of  $29 \pm 3$  area% at  $\gamma = 0$  and  $24 \pm 3$  area% at  $\gamma = 0.6$ , in good agreement with the XCT  $\Phi_{b\_bulk\_3D}$  of  $28 \pm 3$  vol% at  $\gamma = 0$  and  $18 \pm 3$  vol% at  $\gamma = 0.6$ .  $BND_{2D}$  is  $10^{5.6 \pm 0.2}$  m<sup>-2</sup> at  $\gamma = 0$  and  $10^{5.2 \pm 0.2}$  m<sup>-2</sup> at  $\gamma = 0.6$  (Figure 4a), and  $BND_{3D}$  is  $10^{9.2\text{--}9.3}$  m<sup>-3</sup>. In the undeformed sample, about 80% of the bubbles have diameters of 20–40 μm, but their

**Table 1.** Experimental conditions

Run #	Series #	$\Phi_{c\_melt\_3D}^a$ (vol%)	$H_2O_i^b$ (wt%)	Pre-deformation bubble forming					Shear at $P$ - $T$ ( $\gamma_r = 2 \times 10^{-4} s^{-1}$ )	
				Decompression (from 300 MPa and 850 °C) <sup>c</sup>			Cooling at $P$		$\tau_{def}^d$ (min)	$\gamma$
				$P$ (MPa)	$\tau_{DP}^d$ (min)	Dwell1 (min)	$T$ (°C)	Dwell2 (min)		
Pp17	serie0	0	5.0	50	19	45	650	15	-	0
Pp16	serie0	0	5.0	50	18	45	650	15	60	0.6
Pp15	serie0	0	5.0	50	18	45	650	15	120	1.3
Pp5	serie10	21	9.6	50	16	45	750	240	-	0
Pp7	serie10	21	9.6	50	18	45	750	15	60	0.6
Pp6	serie30	50	9.6	50	9	45	750	15	-	0
Pp8	serie30	50	9.6	50	19	45	750	15	60	0.6
Pp9	serie30	50	9.6	50	16	45	750	15	164	1.8
Pp12	serie50	70	9.6	50	18	45	750	15	-	0
Pp11	serie50	70	9.6	50	20	45	750	15	62	0.6
Pp10	serie50	70	9.6	50	17	45	750	15	145	1.5

<sup>a</sup> $\Phi_{c\_melt\_3D}$  is the content of plagioclase crystals manually added to the hydrated haplogranitic (HPG8) glass powder.

<sup>b</sup> $H_2O_i$  is the  $H_2O$  content of the hydrated glasses that were used for the Paterson experiments, calculated after Newman and Lowenstern [2002] at 950 °C and 170 MPa (for the crystal-free series) or 400 MPa (for the crystal-bearing series).

<sup>c</sup>Decompression follows a 15-min dwell at 300 MPa and 850 °C.

<sup>d</sup> $\tau_{DP}^c$  and  $\tau_{def}^c$  are the duration of the decompressions and deformations, respectively.

volumes only represent less than 10% of total vesicularity. More than one third of the vesicularity is occupied by bubbles with equivalent diameters of 220–240  $\mu m$  (Supplementary Figure 3b). The bubbles have  $R_b$  of  $1.0 \pm 0.1$  at  $\gamma = 0$  and  $1.3 \pm 0.1$  at  $\gamma = 0.6$ , showing no preferential orientation ( $\theta_b$  of  $20 \pm 43^\circ$ ) in the unsheared sample (Figure 4b). The glass  $H_2O$  contents are of  $6.1 \pm 0.7$  wt% at  $\gamma = 0$  and  $5.3 \pm 0.7$  wt% at  $\gamma = 0.6$ . The crystal contents,  $\Phi_{c\_bulk\_2D}$ , are of  $9 \pm 1$  area% at  $\gamma = 0$  and  $12 \pm 2$  area% at  $\gamma = 0.6$ . The crystal number densities,  $CND$ , are  $10^{4.8 \pm 0.2} m^{-2}$  at  $\gamma = 0$  and  $10^{5.1 \pm 0.3} m^{-2}$  at  $\gamma = 0.6$  (Figure 4a). The crystals have eccentricities,  $R_c$ , that are not varying from  $1.1 \pm 0.1$  with  $\gamma$ , and their main orientations,  $\theta_c$ , is  $15 \pm 33^\circ$  at  $\gamma = 0$  and  $18 \pm 3^\circ$  at  $\gamma = 0.6$  (Figure 4b).

### 3.3. Series with 30% crystals (serie30)

Serie30 shows shear zones of reorganised bubbles and crystals, evidencing an intensification of

strain localisation from  $\gamma = 0.6$  to 1.8 (Figure 2g,h).  $\Phi_{b\_melt\_2D}$  are  $20 \pm 3$ ,  $26 \pm 3$ ,  $26 \pm 12$  area% at  $\gamma = 0$ , 0.6, and 1.8, respectively (Figure 3a). Recalculating bulk porosities gives  $\Phi_{b\_bulk\_2D}$  of  $15 \pm 3$ ,  $20 \pm 3$ ,  $23 \pm 12$  area% at  $\gamma = 0$ , 0.6, and 1.8, respectively. The XCT  $\Phi_{b\_bulk\_3D}$  gives  $22 \pm 3$ ,  $25 \pm 3$  and  $15 \pm 3$  vol% at  $\gamma = 0$ , 0.6, and 1.8, respectively.  $BND_{2D}$  is  $10^{5.6-5.8 \pm 0.1} m^{-2}$  (Figure 4a) and  $BND_{3D}$  is  $10^{9.3} m^{-3}$  at  $\gamma = 0$  and 0.6, and  $10^{9.9} m^{-3}$  at  $\gamma = 1.8$ . The undeformed sample shows more than 90% of bubbles with 20- $\mu m$  diameters, the volume of which represents one third of total vesicularity. The rest of the vesicularity is mostly occupied by bubbles with equivalent diameters from 40 to 140  $\mu m$ , with some larger bubbles up to 240  $\mu m$  diameter (Supplementary Figure 3f). The bubbles have  $R_b$  of  $1.0 \pm 0.1$  at any  $\gamma$ , showing no preferential orientations ( $\theta_b$  of  $33-38^\circ$ ; Figure 4b). Glass  $H_2O$  content was only analysed at  $\gamma = 1.8$ , giving  $3.0 \pm 0.7$  wt%.  $\Phi_{c\_bulk\_2D}$  is  $28 \pm 1$  area% at  $\gamma = 0$ ,  $29 \pm 4$  area% at  $\gamma = 0.6$ , and  $33 \pm 4$  area% at  $\gamma = 1.8$ .

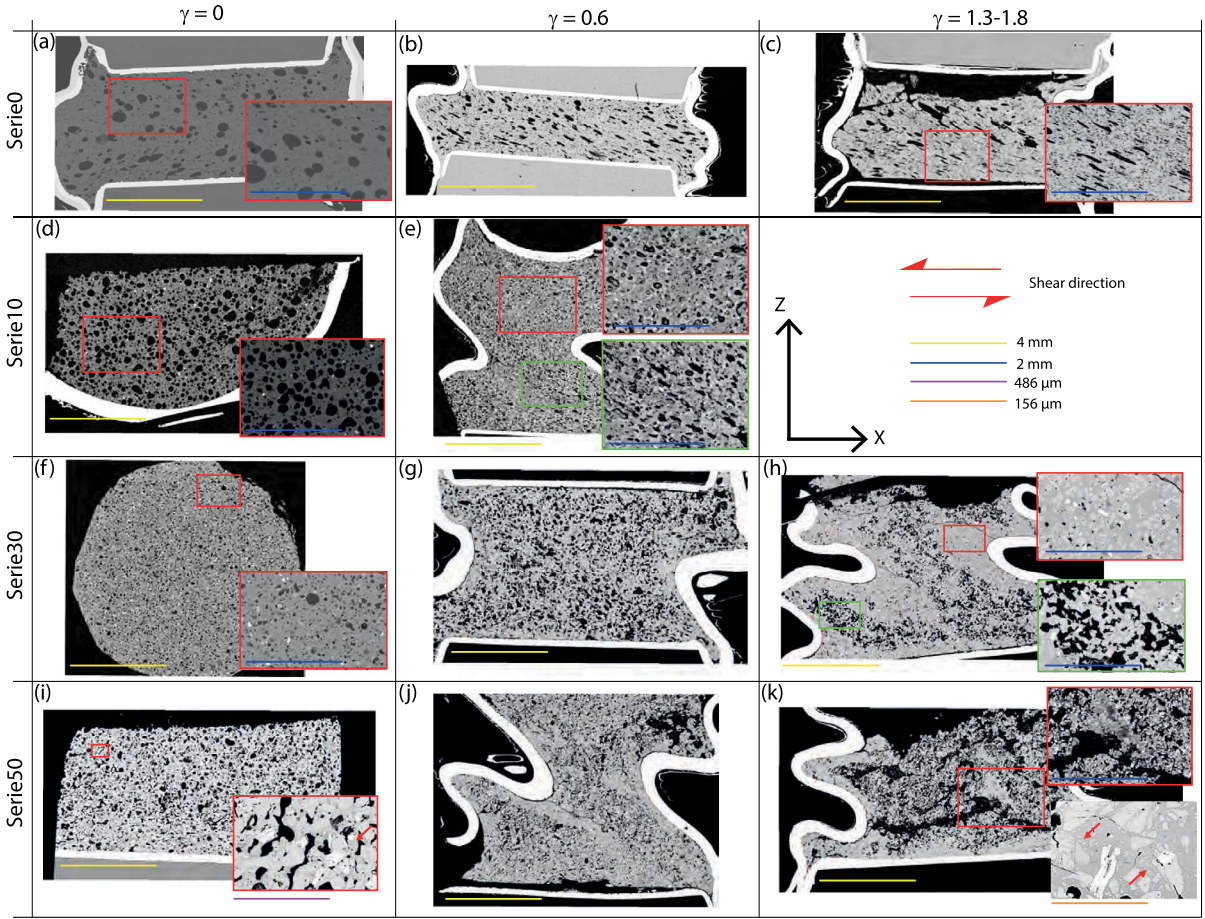


**Figure 2.** SEM pictures of the samples cut following the sketch shown in Supplementary Section 1.2.1. Increasing shear strain from  $\gamma = 0$  to 2 (from left to right) and crystal content from 0 to 50 vol% (from top to down) promotes the development of non-spherical bubbles and heterogeneities in bubble spatial distribution. All main pictures have a yellow scale bar of 4 mm and subpanels are enlargements (with different coloured scale bars). The red arrows in (i) and (k) point to crystal fragmentations.

The CND is  $10^{5.5-5.6 \pm 0.2} \text{ m}^{-2}$  at any  $\gamma$  (Figure 4a).  $R_c$  are not varying from  $1.1 \pm 0.1$  with  $\gamma$ .  $\theta_c$  are  $44 \pm 31^\circ$ ,  $58 \pm 38^\circ$ , and  $26 \pm 13^\circ$  in the samples at  $\gamma = 0, 0.6$ , and  $1.8$ , respectively (Figure 4b).

### 3.4. Series with 50% crystals (serie50)

Serie50 shows strong features of strain localization in the deformed samples, with alternation of strongly bubble-depleted zones and channelized bubble zones (Figure 2j,k).  $\Phi_{b\_melt\_2D}$  increases from  $21 \pm 2$ ,  $23 \pm 10$ ,  $44 \pm 17$  area% with  $\gamma$  increasing from 0, to 0.6 and 1.5 (Figure 3a). Bulk  $\Phi_{b\_bulk\_2D}$  gives  $14 \pm 2$ ,  $16 \pm 10$ , and  $23 \pm 17$  area% at  $\gamma = 0, 0.6$ , and

1.5, respectively, in good agreement with the XCT  $\Phi_{b\_bulk\_3D}$  of  $19 \pm 3$ ,  $16 \pm 3$  and  $25 \pm 3$  vol%.  $BND_{2D}$  is  $10^{6.1 \pm 0.1} \text{ m}^{-2}$  at  $\gamma = 0$  and 0.6, and  $10^{5.9 \pm 0.3} \text{ m}^{-2}$  at  $\gamma = 1.5$  (Figure 4a).  $BND_{3D}$  is  $10^{10.0-10.2} \text{ m}^{-3}$  at  $\gamma = 0$  and 0.6, and  $10^{9.5} \text{ m}^{-3}$  at  $\gamma = 1.5$ . In the undeformed sample, 95% of the bubbles have diameters of 20  $\mu\text{m}$ , representing about 25% of the total vesicularity. Another third of the volume is occupied by bubbles with equivalent diameters of 240–260  $\mu\text{m}$  (Supplementary Figure 3i). The bubbles have  $R_b$  of  $1.0 \pm 0.1$  at any  $\gamma$ , not showing significant preferential orientations ( $\theta_b$  from  $-13$  to  $+33^\circ$ , with standard deviations  $>35^\circ$ ; Figure 4b). The glass  $\text{H}_2\text{O}$  contents are  $4.9 \pm 0.7$  wt% at  $\gamma = 0$  and  $2.7 \pm 0.7$  wt% at  $\gamma = 1.5$ .

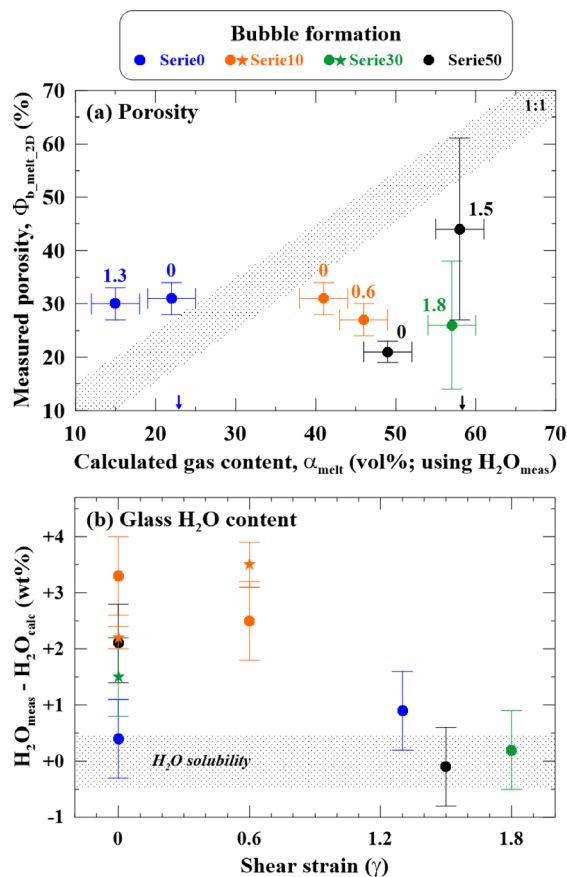


**Figure 3.** Bubble formation. (a) Measured porosity versus porosity calculated for a H<sub>2</sub>O degassing from the initial content (5.0 wt% for the crystal-free samples and 9.6 wt% for the others) to the final content measured in the residual glasses, after the equation of Jaupart and Allègre [1991]; the two arrows on the X-axis give the gas content calculated for an equilibrium H<sub>2</sub>O exsolution (i.e., final content is H<sub>2</sub>O solubility at 50 MPa); the vertical error bars are not statistical uncertainties but span the whole range of the measured values; (b) Difference between the H<sub>2</sub>O contents measured in the residual glasses (circles and stars using electron microprobe and Raman spectrometry, respectively; technical details in Supplementary Section 1) and H<sub>2</sub>O solubility at final pressure (dashed box), showing incomplete H<sub>2</sub>O exsolution in some samples.

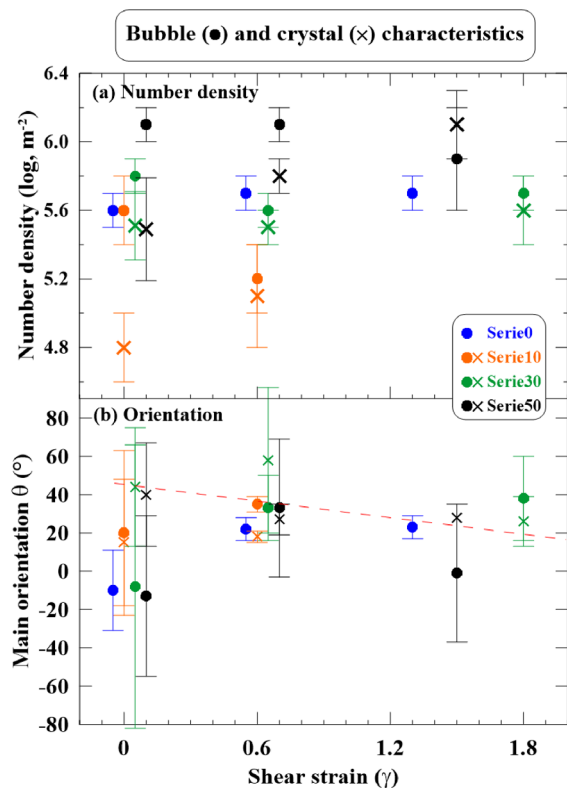


**Figure 4.** Bubble and crystal characteristics. (a) Number density and (b) Preferential orientations ( $0^\circ$  is parallel to shear direction), with the dashed red line giving the theoretical angles between particle major axis and shear direction calculated for solid particles with eccentricity of 1.1, using the formulation of Fernandez et al. [1983]; the X-axis values have been slightly shifted for clarity; the vertical bars are not statistical uncertainties but span the whole range of the measured values.

$\Phi_{c, \text{bulk}, 2D}$  is of 39–48 area% whatever  $\gamma$ . The CND increases from  $10^{5.5 \pm 0.3} \text{ m}^{-2}$  at  $\gamma = 0$  to  $10^{5.8 \pm 0.1} \text{ m}^{-2}$  at  $\gamma = 0.6$  and  $10^{6.1 \pm 0.2} \text{ m}^{-2}$  at  $\gamma = 1.5$  (Figure 4a).  $R_c$  are not varying from  $1.1 \pm 0.1$  with  $\gamma$ .  $\theta_c$  are  $40 \pm 27^\circ$ ,  $27 \pm 8^\circ$ , and  $28 \pm 2^\circ$  in the samples at  $\gamma = 0$ , 0.6, and 1.5, respectively (Figure 4b).



**Table 2.** Analytical results

Run #	Series #	$\gamma$	Glass				Crystals				Bubbles					Viscosity <sup>e</sup>				
			$\Phi_{b, \text{bulk}, 2D}$ (vol% $\pm 3$ )	$H_2O_{\text{calc}}$ <sup>a</sup> (wt%)	$H_2O_{\text{meas}}$ <sup>a</sup> (wt%)	$\Phi_{c, \text{bulk}, 2D}$ (area%)	Log CND <sub>2D</sub> ( $m^{-2}$ )	$R_c$ <sup>b</sup>	$\theta_c$ <sup>b</sup> (°)	$\Phi_{b, \text{bulk}, 3D}$ <sup>c</sup> (vol% $\pm 3$ )	$\Phi_{b, \text{connect}, 3D}$ <sup>c</sup> (% $\pm 3$ )	$\Phi_{b, \text{melt}, 2D}$ (area%)	Log BND <sub>3D</sub> ( $m^{-2}$ )	Log BND <sub>3D</sub> ( $m^{-2}$ )	$R_b$ <sup>b</sup>	$\theta_b$ <sup>b</sup> (°)	$\alpha_{\text{math}}$ <sup>d</sup> (vol%) with $H_2O_{\text{calc}}$ (wt%)	Log $\eta_{\text{meit}}/b_{\text{bulk}}$ (Pas)	Log $\eta_{\text{meit}}$ (Pas)	
Pp17	serie0	0	69	3.2	3.6	0	<i>n.a.</i>	<i>n.a.</i>	<i>n.a.</i>	30(28)	49	31 $\pm$ 3	5.6 $\pm$ 0.1	10.6	1.3 $\pm$ 0.1	-10 $\pm$ 21	27	22	7.1	7.3
Pp16	serie0	0.6	76	3.2	<i>n.a.</i>	0	<i>n.a.</i>	<i>n.a.</i>	<i>n.a.</i>	21(20)	52	24 $\pm$ 2	5.7 $\pm$ 0.1	10.6	1.9 $\pm$ 0.2	+22 $\pm$ 6	27	<i>n.a.</i>	<i>n.a.</i>	<i>n.a.</i>
Pp15	serie0	1.3	79	3.2	4.1	0	<i>n.a.</i>	<i>n.a.</i>	<i>n.a.</i>	15(21)	50	30 $\pm$ 4	5.7 $\pm$ 0.1	10.5	2.0 $\pm$ 0.3	+23 $\pm$ 6	27	15	6.8	7.0
Pp5	serie10	0	63	2.8	6.1(5.1)	9 $\pm$ 1	4.8 $\pm$ 0.2	1.1 $\pm$ 0.1	+15 $\pm$ 33	28(28)	59	29 $\pm$ 3	5.6 $\pm$ 0.2	9.3	1.0 $\pm$ 0.1	+20 $\pm$ 43	60	41	4.9	5.2
Pp7	serie10	0.6	65	2.8	5.3(5.9)	12 $\pm$ 2	5.1 $\pm$ 0.3	1.1 $\pm$ 0.1	+19 $\pm$ 3	18(23)	64	24 $\pm$ 3	5.2 $\pm$ 0.2	9.2	1.3 $\pm$ 0.1	+35 $\pm$ 4	60	46	5.2	5.4
Pp6	serie30	0	63	2.8	<i>n.a.</i> (4.3)	28 $\pm$ 1	5.5 $\pm$ 0.2	1.1 $\pm$ 0.1	+44 $\pm$ 31	22(22)	37	15 $\pm$ 3	5.8 $\pm$ 0.1	9.3	1.0 $\pm$ 0.1	-8 $\pm$ 74	60	<i>n.a.</i>	<i>n.a.</i>	<i>n.a.</i>
Pp8	serie30	0.6	57	2.8	<i>n.a.</i>	29 $\pm$ 4	5.5 $\pm$ 0.1	1.1 $\pm$ 0.1	+58 $\pm$ 38	25(27)	83	20 $\pm$ 3	5.6 $\pm$ 0.1	9.3	1.0 $\pm$ 0.1	+33 $\pm$ 17	60	<i>n.a.</i>	<i>n.a.</i>	<i>n.a.</i>
Pp9	serie30	1.8	62	2.8	3.0	33 $\pm$ 4	5.6 $\pm$ 0.2	1.1 $\pm$ 0.1	+26 $\pm$ 13	15(10)	80	23 $\pm$ 12	5.7 $\pm$ 0.1	9.9	1.0 $\pm$ 0.1	+38 $\pm$ 22	60	57	6.2	6.9
Pp12	serie50	0	53	2.8	4.9	48 $\pm$ 3	5.5 $\pm$ 0.3	1.1 $\pm$ 0.1	+40 $\pm$ 27	19(19)	87	14 $\pm$ 2	6.1 $\pm$ 0.1	10.2	1.0 $\pm$ 0.1	-13 $\pm$ 42	60	49	5.3	6.5
Pp11	serie50	0.6	54	2.8	<i>n.a.</i>	43 $\pm$ 4	5.8 $\pm$ 0.1	1.1 $\pm$ 0.1	+27 $\pm$ 8	16(15)	76	16 $\pm$ 10	6.4 $\pm$ 0.1	10.0	1.0 $\pm$ 0.1	+33 $\pm$ 36	60	<i>n.a.</i>	<i>n.a.</i>	<i>n.a.</i>
Pp10	serie50	1.5	49	2.8	2.7	39 $\pm$ 7	6.1 $\pm$ 0.2	1.1 $\pm$ 0.1	+28 $\pm$ 2	25(27)	99	39 $\pm$ 17	5.9 $\pm$ 0.3	9.5	1.0 $\pm$ 0.1	-1 $\pm$ 36	60	58	6.4	7.4

*n.a.* indicates not analyzed;

<sup>a</sup> $H_2O_{\text{calc}}$  is the  $H_2O$  solubility at 650 or 750 °C and 50 MPa calculated after Newman and Lowenstern [2002];  $H_2O_{\text{meas}}$  is the glass  $H_2O$  content measured by EMP (analytical uncertainty of  $\pm 0.7$  wt%) and by Raman spectroscopy in bracket (average of 2 to 3 analyses with statistical error from  $\pm 0.2$  to  $\pm 0.7$  wt%).

<sup>b</sup> $\theta_c$  and  $\theta_b$  are the orientations to the horizontal of the bubbles and crystals, respectively;  $R$  gives the bubble mean eccentricity as the ratio of the long axes to the short axes.

<sup>c</sup> $\Phi_{b, \text{bulk}, 3D}$  gives the bulk porosity measured on cubic samples of 1400- $\mu\text{m}$  side volume and at smaller scale (600- $\mu\text{m}$  side) in brackets;  $\Phi_{b, \text{connect}, 3D}$  gives the percentage of bubbles connected to the sample outside, as defined in Supplementary Section 1.

<sup>d</sup> $\alpha_{\text{meit}}$  is calculated after Jaupart and Allegre [1991] for a degassing from the  $H_2O$  content of the pre-hydrated glass ( $H_2O$ ) in Table 1) to either  $H_2O_{\text{calc}}$  or  $H_2O_{\text{meas}}$ .

<sup>e</sup> $\eta_{\text{meit}}$  is the viscosity of the hydrated melt calculated at 650 or 750 °C after Hess and Dingwell [1996] using  $H_2O_{\text{meas}}$ ;  $\eta_{\text{bulk}}$  is the viscosity of the three-phase (crystal, bubble, melt) suspension calculated after Truby *et al.* [2015] using  $\eta_{\text{meit}}$ ,  $\Phi_{c, \text{bulk}, 2D}$ , and  $\Phi_{b, \text{melt}, 2D}$  (see text and Supplementary Section 1 for details).

## 4. Discussion

### 4.1. Bubble nucleation and growth

Exsolving H<sub>2</sub>O from 9.6 to 2.8 wt% [solubility at 50 MPa and 750 °C; Newman and Lowenstern, 2002] corresponds to a calculated vesicularity of 58 vol% [Jaupart and Allègre, 1991; Supplementary Section 1 (Equation (1))]. Yet the average porosities measured in the decompressed samples are mostly below 35 vol% (Figure 3a). We propose two explanations to account for this deviation; incomplete H<sub>2</sub>O exsolution and partial loss of bubbles.

#### 4.1.1. Incomplete H<sub>2</sub>O exsolution

Checking the H<sub>2</sub>O contents of the residual glasses in the undeformed samples using both electron microprobe and Raman spectroscopy, revealed contents in the crystal-bearing samples higher by 1.5 to 3.5 wt% than expected for an equilibrium H<sub>2</sub>O exsolution (Figure 3b). This suggests incomplete H<sub>2</sub>O exsolution during the ~1.5 h ( $\tau_{DP} + D_{well2} + D_{well3}$  in Table 1) allocated to decompression-induced bubble nucleation. Yet, all series show equilibrium H<sub>2</sub>O exsolution (~3.0 wt% H<sub>2</sub>O) at  $\gamma$  of 1.5–1.8, that is, for another couple of hours spent at 50 MPa, thus confirming that H<sub>2</sub>O exsolution under the chosen experimental conditions requires more than 1 h to reach equilibrium. This strongly disagrees with the conclusions of Martel and Schmidt [2003] suggesting H<sub>2</sub>O exsolution timescales of less than 1 min in microlite-bearing rhyolitic melts at 860 °C, but agrees with complete bubble expansion requiring several hours. Therefore, we infer that in our experiments, the timescale of bubble expansion controlled H<sub>2</sub>O exsolution from the melt. In contrast, the undeformed crystal-free samples degassed to equilibrium, which we rather attribute to their lower initial H<sub>2</sub>O content (5.0 instead of 9.6 wt%) rather than the absence of crystals, since serie10 which contains 10 vol% crystals, shows the highest H<sub>2</sub>O exsolution disequilibrium. Further investigation would be required to validate the positive correlation between the initial H<sub>2</sub>O content of the melt and the timescale of bubble expansion, which in turn controls the H<sub>2</sub>O content of the residual melt.

#### 4.1.2. Partial loss of bubbles

Knowing that H<sub>2</sub>O exsolution was not completed in the H<sub>2</sub>O-rich samples, the gas fractions were

calculated using the final H<sub>2</sub>O contents measured in the residual glasses instead of using H<sub>2</sub>O solubility at 50 MPa. The results show that the measured porosities are lower by 10 to 30 vol% than expected for an equilibrium degassing (Figure 3a), suggesting that these samples lost a part of their bubble cargo. One explanation could be that the melt partially outgassed by bubble connection at some point during bubble growth, and partially collapsed via compaction. Yet the released gas pockets cannot escape the sealed capsule and were considered in the measurement of total vesicularity. Therefore, we infer that these gas pockets were heterogeneously distributed in the capsule corners and were not systematically visible on our SEM pictures (for instance, a large gas pocket is visible below the capsule roof in Figure 2c), so that they may miss from some porosity budget. This hypothesis is supported by the lack of clear relationships between the bubble deficiency and parameters such as H<sub>2</sub>O content, crystal content, or finite deformation.

#### 4.1.3. Pre-deformation porosity

The undeformed samples show melt vesicularities of 19–30 vol% (Figure 3a) and bubble number densities not varying by more than 0.5 log unit (Figure 4a), which suggests a comparable and reproducible process of bubble formation. Within this 0.5 log unit, however, BND increases with crystal content, as experimentally observed by Cáceres *et al.* [2021]. The bubble number densities of  $10^{9.3-10.6} \text{ m}^{-3}$  measured from the XCT images are lower by 1 log unit compared to those predicted in crystal-free magmas by the formulation of Toramaru [2006] for decompression rates of 0.1–1.0 MPa/s (i.e., BNDs of  $10^{10.5-11.5} \text{ m}^{-3}$ ), highlighting a possible role of the crystals in controlling nucleation sites for bubbles, as already pointed out by Cáceres *et al.* [2021]. In the undeformed samples from all series, more than half (and up to 95% in serie0 and serie50) of the bubbles have diameters of about 20  $\mu\text{m}$ . These small bubbles occupy about one third of total porosity in all series but serie0. In serie0, the volume of the small bubble population nearly disappeared at the expense of larger (220–240  $\mu\text{m}$  diameter) bubble volume (Supplementary Figure 3a). In serie50, the population of 20- $\mu\text{m}$  diameter bubbles coexists with some 240–260  $\mu\text{m}$  diameter bubbles (Figure 2i) representing one third of total porosity (Supplementary Figure 3i).

The homogeneous spatial distribution of the small 20–40  $\mu\text{m}$  bubbles (Figure 2a) confirms a process of homogeneous nucleation [Mourtada-Bonnefoi and Laporte, 2002], in agreement with the observations in natural and experimental products that plagioclase is not a wetting phase for nucleating  $\text{H}_2\text{O}$  bubbles [Navon *et al.*, 1998, Cáceres *et al.*, 2021]. The population of 200–300  $\mu\text{m}$  bubbles may have three possible origins: coalescence of the 20–40  $\mu\text{m}$  bubbles, a separate nucleation event, or pre-decompression bubbles. A separate nucleation event or bubble coalescence would lead to more or less similar bubble size distributions in the different series, which is not the case (Supplementary Figure 3a,d,f,i). Therefore, we argue in favour of bubbles that formed before decompression, as often observed in experiments starting with powdered material that is able to trap  $\text{H}_2\text{O}$  and air in the intergranular voids before melting [i.e., the “hydration bubbles” in Gardner *et al.*, 1999]. The number and size of these bubbles would then be affected by the crystal content in the glass powder. The undeformed samples of serie30 and serie50 show that bubbles started channelling along the crystals (Figure 2f,i). According to the model of Burgisser *et al.* [2017], crystal-free melts containing 20–30 vol% bubbles, number density of  $10^{9-11} \text{ m}^{-3}$ , and size of 200–300  $\mu\text{m}$ , would be impermeable, even with 50–70% connected porosity. In contrast, gas permeability measurements in natural crystal-bearing samples with connected porosities from 50 to 80% give permeabilities from  $\sim 10^{-14}$  to  $10^{-10} \text{ m}^2$  [Bain *et al.*, 2019]. Therefore, in absence of permeability measurements in our samples, it is not clear whether the gas percolation thresholds were met before deformation.

#### 4.1.4. Bulk viscosity

The bulk viscosities calculated using the formulation of Truby *et al.* [2015] range from  $10^{5.2-5.4} \text{ Pa}\cdot\text{s}$  for the series containing 10 vol% crystals at 750  $^\circ\text{C}$ ,  $10^{6.5-7.4} \text{ Pa}\cdot\text{s}$  for the series containing 30 and 50 vol% crystals at 750  $^\circ\text{C}$ , to  $10^{7.1-7.3} \text{ Pa}\cdot\text{s}$  for the crystal-free series at 650  $^\circ\text{C}$  (Table 2). The regime of low capillary number ( $Ca < 1$ ) calculated for our sample deformation conditions (see Supplementary Section 1.3.2 for details) results in considering the 20–30 bulk vol% bubbles as rigid particles that increase the hydrated melt viscosity by about 0.2 log unit (e.g. serie0 in Table 2). Adding crystals further increases bulk viscosity, from  $\sim 0.3$  log unit for 10 vol% added crystals to

$\sim 0.7$  log unit for 30 vol% crystals, and 1.0–1.2 log unit for 40–50 vol% crystals, which agrees with most of the common models of particle suspension rheology [see Mader *et al.*, 2013].

## 4.2. Effect of the crystal network on porosity development under small shear ( $\gamma < 2$ )

### 4.2.1. Crystalline fabric

The crystals were nearly isotropic in shape ( $R_c = 1.1 \pm 0.1$ ; Table 2), suggesting that the cutting of the labradorite block using the Selfrag apparatus did not permit to reproduce the elongated plagioclase crystals commonly observed in the natural magmas. This small anisotropy likely limited the development of strong crystalline fabrics in the sheared samples. Nevertheless, the crystals show main orientations that agree with those calculated as a function of  $\gamma$  by Fernandez *et al.* [1983] for solid particles of  $R_c = 1.1$  (Figure 4b). Yet, the high standard deviations associated with these angles, especially at  $\gamma = 0$  and 0.6, suggest that the crystalline fabric is very weak, with the exception of serie50 at  $\gamma = 0.6$  and 1.5, for which the crystalline fabrics are well marked (standard deviations  $< 10^\circ$ ). The serie30 and serie50 samples show crystal breakage features, evidenced by the appearance of a population of small crystals (Figure 2i,k) that are also visible in the 2D crystal size distributions (Supplementary Figure 4). Crystals breakage was also observed in crystal-rich samples deformed under low strains by Forien *et al.* [2011], likely resulting from intense stress localization at some grain contact.

### 4.2.2. Bubble spatial distribution

The melt porosity of 20–30 area% is maintained in whatever crystal content and  $\gamma$ , with the exception of one sample (Figure 5a), which agrees with the results of Pistone *et al.* [2012] obtained on their samples sheared at  $T$  high enough to prevent bubble loss through shear fracturing. Yet in details, increasing both bulk crystal content  $\geq 30$  vol% and finite strain, increases heterogeneities in bubble spatial distribution, as reflected by porosity variations up to  $\pm 20\%$  between bubble-poor and bubble-rich zones, with the variation being positively correlated to  $\gamma$  (Figure 5a). For these samples, the gas accumulated in local microstructures caused by the shear-induced crystal fabric (Figure 2h,k), in agreement with the observations of Laumonier *et al.* [2011]. In samples with

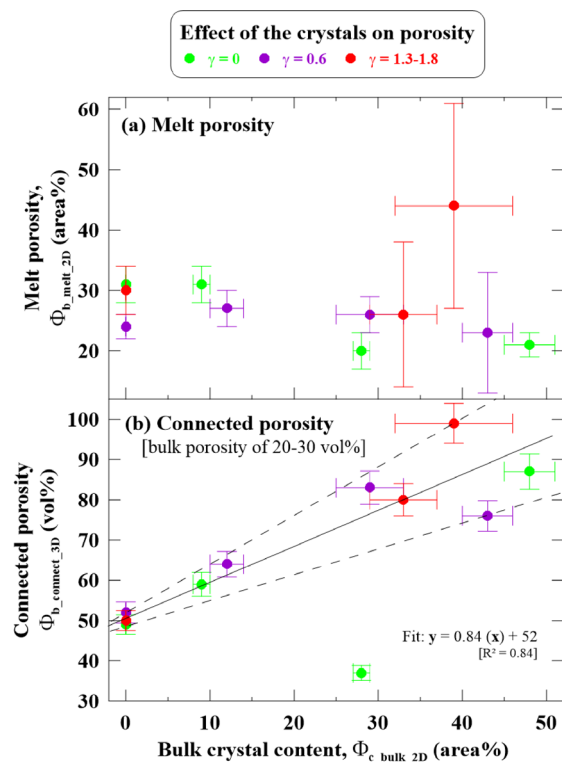


**Figure 5.** Effects of the crystals on (a) melt porosity and (b) connected porosity; the solid line indicates the linear fit of the data but one point ( $\gamma = 0$ ) from serie30 with an anomalously low connected porosity; the dashed lines contour the evolution of the connected porosity as a function of bulk crystallinity (0–50 vol%) for bulk vesicularities of 20–30 vol% and shear strain of  $0 < \gamma < 2$ .

bulk crystal contents  $< 30$  vol%, however, our results suggest that the spatial distribution of the bubbles remain homogeneous (variations below  $\pm 5$  vol%; Figure 5a).

#### 4.2.3. Connectivity development

At  $\gamma = 0$ , bubble connectivity increases with crystal content (Figure 6), reaching  $\sim 87\%$  connected porosity in the sample with bulk crystal contents of 50 vol% (Figure 5b; one exception is the undeformed sample of serie30 with only 37% connected porosity, for which we have no explanation). These results agree with those of Cáceres *et al.* [2021] who observed that phenocryst-bearing magma noticeably showed a higher degree of bubble coalescence, but

disagree with those of Okumura *et al.* [2012] who reported no clear effect of crystallinity (30–50 vol% recalculated with respect to the melt volume) on the degree of bubble coalescence and connectivity until melt vesicularities reached  $\sim 68$  vol%. This disagreement may be explained by differences in bubble texture. Indeed, their crystal-rich samples with vesicularity  $\sim 20$ –30 vol% (i.e. those decompressed to 20 MPa; number densities of  $\sim 10^{12} \text{ m}^{-3}$ ) do not show bubble channelling features, such as those observed in the undeformed samples of our serie50 (Figure 2). This could also result from different bulk viscosities, different bubble to crystal size ratios, or unimodal versus polymodal bubble size distributions (i.e. the  $\sim 200$ –300  $\mu\text{m}$  bubble population in our samples may have played a key role in early connectivity development).

In our samples, increasing bubble connectivity with increasing crystal content before shearing ( $\gamma = 0$ ) highlights the role of the crystal network on the decompression-induced formation of bubbles. Firstly, the crystals possibly influence bubble nucleation, by increasing bubble number density by up to 0.5 log unit with increasing crystal content (see log BND at  $\gamma = 0$  in Figure 4a). We speculate that physical processes at the origin of more bubble nuclei in crystal-richer magmas could involve modified gas-melt interfacial tensions or excess free energy. After nucleation, bubble growth must have been partly dictated by the crystal network, forcing bubble coalescence and channelling, eventually approaching full bubble connection in serie50 (i.e.  $> 80\%$  connectivity; Figures 5b and 6i). These observations confirm the results of the numerical modelling of Parmigiani *et al.* [2017] predicting maximum outgassing efficiency via 40–50% connected porosity in crystal-rich (40–70 vol%) magmas.

Increasing  $\gamma$  from 0 to 2 does not significantly influence the amount of connected porosity (Figure 5b), thus highlighting the large predominance of crystal content over shear strain up to  $\gamma = 2$  in favouring bubble connections. Fitting all the data but one (the low-connected sample at  $\gamma = 0$  from serie30) shows a positive linear correlation between connected porosity and bulk crystal content ( $y = 0.84x + 52$ ; Figure 5b), thus valid for silicic magmas with 20–30 vol% bulk vesicularity and sheared at low strain ( $\gamma < 2$ ) with shear rates of  $10^{-4} \text{ s}^{-1}$  under a low confining pressure of 50 MPa. The rather poor

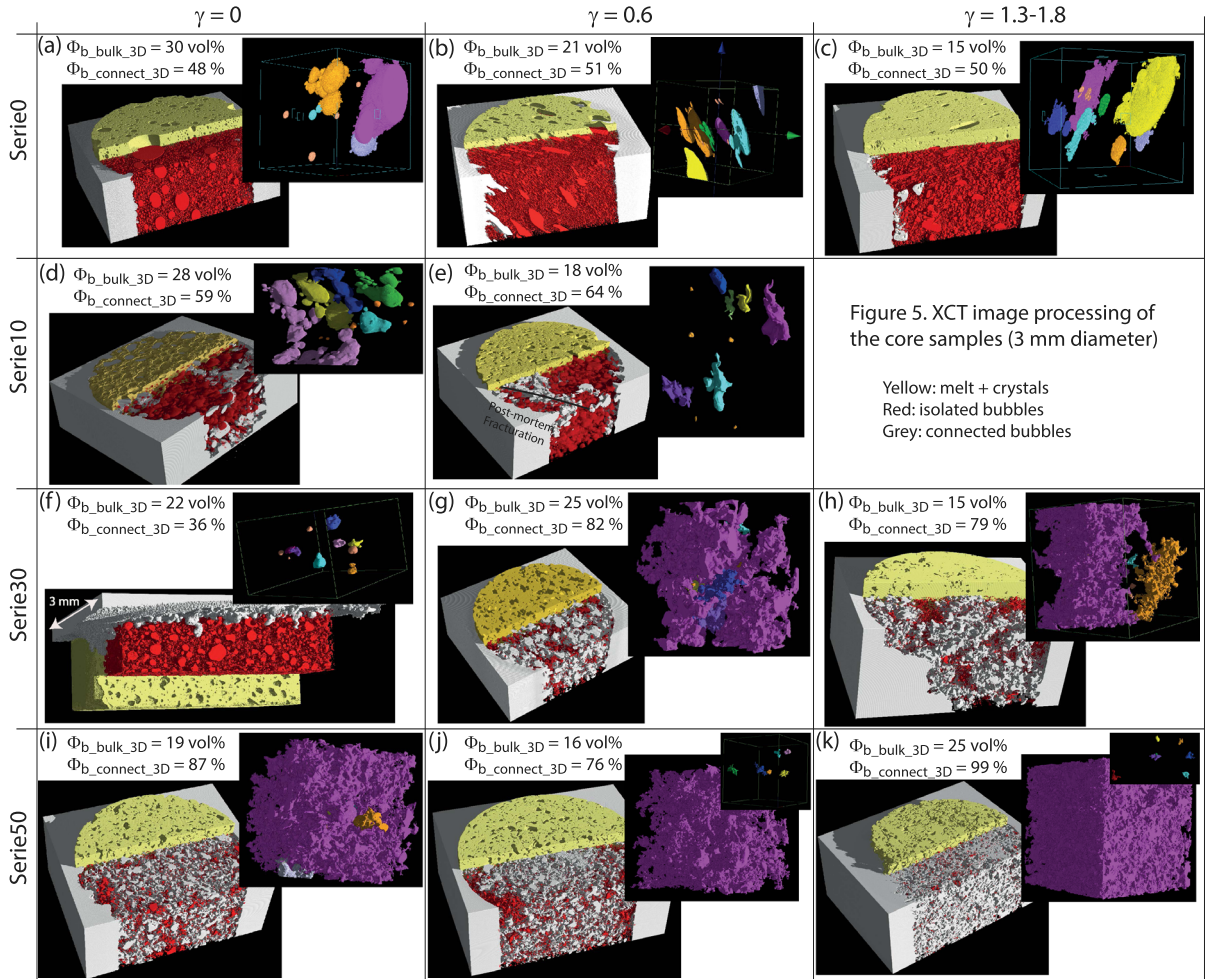


**Figure 6.** XCT image processing of the core samples (3 mm diameters) for increasing shear strain from  $\gamma = 0$  to 2 (from left to right) and crystal content from 0 to 50 vol% (from top to down). The left blocks were processed using VGStudioMax, with the melt and crystals in yellow, the isolated bubbles in red and the bubbles connected to the sample outside in grey.  $\Phi_{b\_bulk\_3D}$  and  $\Phi_{b\_connect\_3D}$  give the 3D percentage of bulk and connected bubbles, as defined in Supplementary Section 1. The upper right insets show details of the bubbles processed using Blob3D, with another colour code that show one colour per isolated bubble or identified network of connected bubbles. The black line in (e) highlights an alignment of bubbles connected to the sample outside, which denotes a post-experimental fracture.

coefficient of determination,  $R^2 = 0.84$ , mostly reflects a large variability of the connected porosity at high crystallinity ( $\pm 15\%$  for crystal content  $\sim 45 \text{ vol\%}$ ) with respect to crystal-free samples ( $\pm 2\%$ ; Figure 5b).

#### 4.3. Implications for natural volcanic systems

The experimental samples are silica-rich melts containing 20–30 vol% bubbles and 0 to 50 bulk vol%

plagioclase crystals that cover a range from natural moderately-porous obsidians to crystal-rich (mush-like) rhyolitic magmas. The 50–90  $\mu\text{m}$  crystal size typically scales microlites to microphenocrysts [e.g. Hammer *et al.*, 1999, Martel and Poussineau, 2007]. The low confining pressure of 50 MPa and the low shear strains ( $\gamma < 2$ ) applied to the samples simulate a shear initiation at shallow depth (about 2 km deep, considering rock density of  $2400 \text{ kg/m}^3$ ), such as

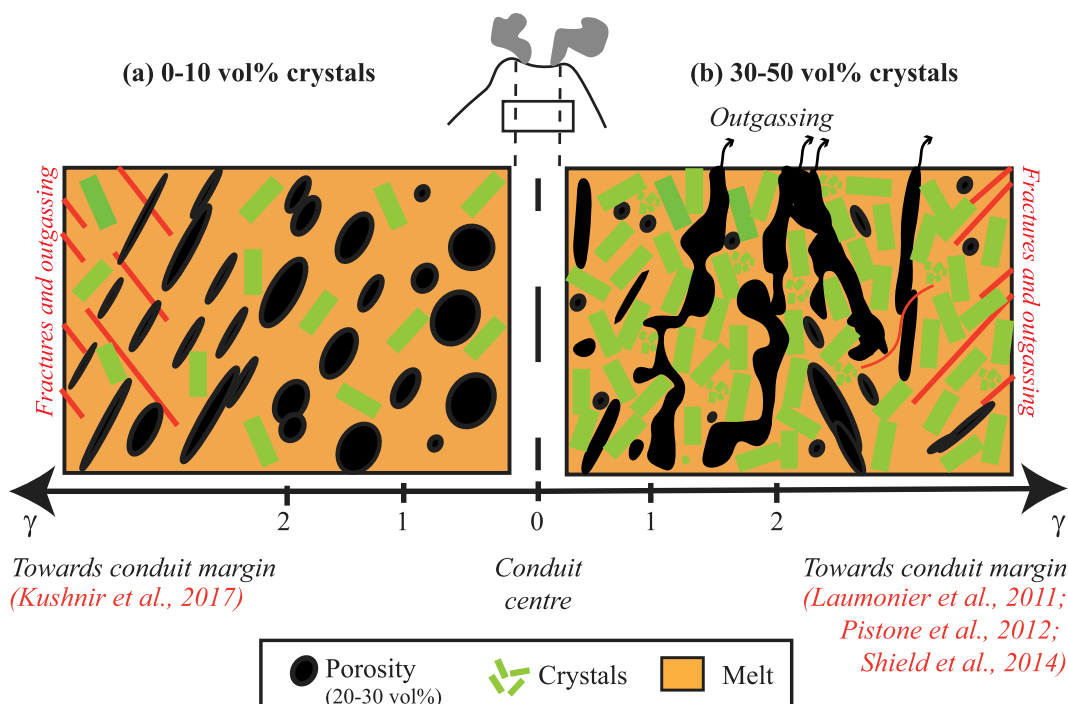


**Figure 7.** Schematic representation of bubble connectivity in magmas with (a) 0–10 vol% crystals or (b) 30–50 vol% crystals, deformed under shear at magmatic temperatures (650–750 °C), moderate shear-strain rates ( $2 \times 10^{-4} \text{ s}^{-1}$ ) and low pressures (50 MPa, that is at level of upper conduit to lava dome interior). The gas bubbles in crystal-poor magmas with 20–30 vol% porosity hardly connect under strain below  $\gamma = 2$ , so that outgassing requires fracture opening under high strains or strain rates, likely only reachable at conduit margins [Kushnir *et al.*, 2017]. In contrary, a dense crystalline fabric favours bubble connectivity under strains as low as  $\gamma = 2$  and bulk porosity of 20–30 vol%, so that outgassing may be an early process upon magma emplacement. Crystal fragmentation commonly occurs in crystal-rich magmas and heightens with increasing crystal content and strain. If temperature decreases and/or strain increases as expected at conduit margins, fractures may open and assist outgassing [Pistone *et al.*, 2012, Shields *et al.*, 2014].

in a volcanic upper conduit. Overall, these conditions may be representative of Vulcanian events or dome-related eruptions, during which a moderately-porous magma degasses and crystallizes microcrystals at shallow depths, eventually emplacing effusively (as domes or plugs) or erupting explosively (as surges), depending on outgassing efficiency. In particular, vesicularities of 20–30 vol% are representative of those measured in lava domes and blast-generated pyroclastic density currents, such as the ones generated in 1350 AD (P1) and 1902 at Montagne Pelée, Martinique [Martel *et al.*, 2000] and in 1980 at Mount St Helens, USA [Hoblitt and Harmon, 1993].

The implications of our results to volcanic systems are schematized in Figure 7 and detailed

below. Our results suggest that  $\text{H}_2\text{O}$  bubbles nucleating in undeformed aphyric or crystal-poor (0–10 vol%) magmas by decompression at rates of 0.1–1.0 MPa/s (i.e. bubble number densities around  $10^9\text{--}11 \text{ m}^{-3}$ ) can connect to 50% (Figure 6a,d), but the magma could still be impermeable mainly due to the moderate bulk porosity of 20–30 vol% [Burgisser *et al.*, 2017]. Such moderately-porous crystal-poor melts may reach permeability via a process of fracturing at high strains ( $\gamma > 2$ ) along the conduit margins, as experimentally demonstrated by Kushnir *et al.* [2017]. Adding crystals drastically increases bubble connectivity (>70%; Figure 5b), by favouring channelling even at low shear strains (Figure 2h,k). Channelling creates gas permeability of

the order of  $10^{-10}$  m<sup>2</sup>, which is two to five orders of magnitude higher than the other permeability processes at the equivalent bubble content [Collombet *et al.*, 2021]. Therefore, magmas with matrix crystallinity >30 vol% and vesicularity of 20–30 vol%, as commonly observed in lava domes [Boudon *et al.*, 2015], may show bubble connectivity >70% (Figure 5b) and gas permeabilities  $>10^{-12}$  m<sup>2</sup> [Bain *et al.*, 2019]. Our data suggest that bubble connectivity in low-porous (20–30 vol%) silica-rich magmas slightly sheared ( $\gamma < 2$ ; strain rate of  $10^{-4}$  s<sup>-1</sup>) at low confining pressure (50 MPa; about 2 km deep) increases linearly with crystal content (following  $y = 0.84x + 52$ , with  $y$  being the connected porosity in vol% and  $x$  being the bulk crystal content in area%; Figure 5b). In natural samples, connectivity would be enhanced by unequal bubble sizes that favour bubble coalescence [Lin and Lin, 2009], microtextures made of crystals with high aspect ratios [Lindoo *et al.*, 2017], and polydisperse crystal size distributions involving phenocrysts and microlites [Cáceres *et al.*, 2021]. Therefore, in comparison to crystal-poor magmas, crystal-rich melts are able to outgas much more easily (at lower  $\gamma$ ) for comparable temperature, pressure, and strain rate, confirming the effusive mode of crystal-rich lava-dome emplacement and the unnecessary to invoke dominant outgassing mechanisms other than channelling [Collombet *et al.*, 2021]. From a crystallinity point of view and regardless of melt H<sub>2</sub>O content and magma storage pressure, the gas-permeable nature of the 30–50 vol% crystal-bearing rhyolitic melts investigated in this study agrees with the eruptions of low magnitude reported by [Takeuchi *et al.*, 2021] and the crystallinity-controlled effusive eruptions reported by Popa *et al.* [2021]. Yet, the present experiments highlight the major control of an exsolved volatile phase (20–30 vol%) and low shear ( $\gamma < 2$ ) on the permeability development, with consequences on eruptive style that may deviate from those expected from the sole consideration of crystallinity and melt H<sub>2</sub>O content. Since low-sheared crystal-rich magmas at upper conduit level is permeable to gases, this poses the question of the mechanisms behind dome-related explosive eruptions, such as Vulcanian or Pelean explosions. External factors can be invoked, such as depressurization due to unloading by gravitational collapse of a part of the dome [Voight *et al.*, 1981]. Among internal factors of self-explosivity, one

could invoke processes capable of building up overpressure in gas bubbles from an initially permeable magma, such as a second boiling event in response to late-stage extensive microlite crystallization [Sparks, 1997] and gas volume reduction by silica-phase deposition in bubbles [Boudon *et al.*, 2015]. Another hypothesis for self-explosivity is permeability barriers and pressure accumulation via vertical rheological and lithological gradients in the magma column [e.g., Voight *et al.*, 1999].

## 5. Conclusions

By deforming silicic melts with 20–30 vol% H<sub>2</sub>O bubbles and 0 to 50 vol% crystals at magmatic temperatures (650–750 °C) and low confining pressures (50 MPa), we highlighted that:

- Torsion experiments using three-phase (bubbles, crystals, and melt) suspensions are valuable analogues to shear initiation in moderately-porous aphyric to crystal-bearing silicic magmas at shallow depth, such as in lava domes or upper conduits.
- Bubble connectivity linearly increases with crystal content.
- Increasing strain from  $\gamma = 0$  to 2 in crystal-bearing magmas drastically increases the heterogeneity in bubble spatial distribution, by concentrating pores in shear zones.
- Crystal-rich magmas develop gas permeability via a process of channelling in shear zones, even at moderate porosities (20–30 vol%) and low strains ( $\gamma < 2$ ).
- Natural crystal-rich magmas stalling in upper conduits or lava domes are thus likely permeable, so that violent dome explosions into devastating surges require additional mechanisms of gas pressurisation in shallow crystal-rich magmas.

## Conflicts of interest

Authors have no conflict of interest to declare.

## Acknowledgements

The authors greatly thank I. di Carlo, S. Erdmann, and P. Benoist for assistance with the SEM and EMP;

M. Hatton for the analyses using the elemental analyser; A. Slodczyk and F. Faranda for the analyses using Raman spectroscopy; P. Penhoud for the technical assistance with the X-ray microtomograph; and M. Beaulieu for the crystal block grinding using the Selfrag device at BRGM. This work is part of CD PhD thesis that was funded by the French MNRT grant. The study costs were provided by the CNRS-INSU TelluS program, the Agence Nationale de la Recherche (ANR-19-CE31-0007; LA), the EQUIPEX PLANEX project (ANR-11-EQPX-0036; B. Scaillet), and the LABEX VOLTAIRE project (ANR-10-LABX-100-01; B. Scaillet). The authors greatly thank B. J. Andrews and two anonymous reviewers for their helpful comments on a previous version of the manuscript, as well as R. Cioni and an anonymous reviewer for their comments on the present manuscript. We would also like to thank B. Scaillet for the editorial handling.

### Supplementary data

Supporting information for this article is available on the journal's website under <https://doi.org/10.5802/crgeos.214> or from the author.

### References

- Bain, A. A., Lamur, A., Kendrick, J. E., Lavallée, Y., Calder, E. S., Cortés, J. A., Butler, I. B., and Cortés, G. P. (2019). Constraints on the porosity, permeability and porous micro-structure of highly-crystalline andesitic magma during plug formation. *J. Volcanol. Geotherm. Res.*, 379, 72–89.
- Blower, J. (2001). Factors controlling permeability–porosity relationships in magma. *Bull. Volcanol.*, 63(7), 497–504.
- Boudon, G., Balcone-Boissard, H., Villemant, B., and Morgan, D. J. (2015). What factors control superficial lava dome explosivity? *Sci. Rep.*, 5, article no. 14551.
- Burgisser, A., Chevalier, L., Gardner, J. E., and Castro, J. M. (2017). The percolation threshold and permeability evolution of ascending magmas. *Earth Planet. Sci. Lett.*, 470, 37–47.
- Burgisser, A. and Gardner, J. E. (2005). Experimental constraints on degassing and permeability in volcanic conduit flow. *Bull. Volcanol.*, 67, 42–56.
- Cáceres, F., Scheu, B., Colombier, M., Hess, K.-U., Feisel, Y., Ruthensteiner, B., and Dingwell, D. B. (2021). The roles of microlites and phenocrysts during degassing of silicic magma. *Earth Planet. Sci. Lett.*, 577, article no. 117264.
- Cassidy, M., Manga, M., Cashman, K., and Bachmann, O. (2018). Controls on explosive-effusive volcanic eruption styles. *Nat. Commun.*, 9, article no. 2839.
- Castro, J. M., Cordonnier, B., Tuffen, H., Tobin, M. J., Puskas, L., Martin, M. C., and Bechtel, H. A. (2012). The role of melt-fracture degassing in defusing explosive rhyolite eruptions at volcan Chaiten. *Earth Planet. Sci. Lett.*, 333, 63–69.
- Collombet, M., Burgisser, A., Colombier, M., and Gaunt, E. (2021). Evidence for deep gas loss in open volcanic systems. *Bull. Volcanol.*, 83(7), 1–16.
- deGraffenried, R. L., Larsen, J. F., Graham, N. A., and Cashman, K. V. (2019). The influence of phenocrysts on degassing in crystal-bearing magmas with rhyolitic groundmass melts. *Geophys. Res. Lett.*, 46, 5127–5136.
- Degruyter, W., Bachmann, O., and Burgisser, A. (2010). Controls on magma permeability in the volcanic conduit during the climactic phase of the Kos Plateau Tuff eruption (Aegean Arc). *Bull. Volcanol.*, 72, 63–74.
- Eichelberger, J. C., Carrigan, C. R., Westrich, H. R., and Price, R. H. (1986). Non-explosive silicic volcanism. *Nature*, 323, 598–602.
- Fernandez, A. N., Febesse, J. L., and Mezure, J. F. (1983). Theoretical and experimental study of fabrics developed by different shaped markers in two-dimensional simple shear. *Bull. Soc. Géol. France*, 7-XXV(3), 319–326.
- Forien, M., Arbaret, L., Burgisser, A., and Champalier, R. (2011). Experimental constraints on shear-induced crystal breakage in magmas. *J. Geophys. Res.*, 116, article no. B08217.
- Gardner, J. E., Hilton, M., and Carroll, M. R. (1999). Experimental constraints on degassing of magma: isothermal bubble growth during continuous decompression from high pressure. *Earth Planet. Sci. Lett.*, 168, 201–218.
- Gaunt, H. E., Sammonds, P. R., Meredith, P. G., Smith, R., and Pallister, J. S. (2014). Pathways for degassing during the lava dome eruption of Mount St. Helens 2004–2008. *Geology*, 42(11), 947–950.
- Gonnermann, H. M., Giachetti, T., Fliedner, C.,



- Nguyen, C. T., Houghton, B. F., Crozier, J. A., and Carey, R. J. (2017). Permeability during magma expansion and compaction. *J. Geophys. Res., Solid Earth*, 122, 9825–9848.
- Hammer, J. E., Cashman, K. V., Hoblitt, R. P., and Newman, S. (1999). Degassing and microlite crystallization during pre-climactic events of the 1991 eruption of Mt Pinatubo, Philippines. *Bull. Volcanol.*, 60, 355–380.
- Hess, K.-U. and Dingwell, D. B. (1996). Viscosities of hydrous leucogranitic melts: non-Arrhenian model. *Am. Mineral.*, 81, 1297–1300.
- Hoblitt, R. P. and Harmon, R. (1993). Bimodal density distribution of cryptodome dacite from the 1980 eruption of Mount St Helens, Washington. *Bull. Volcanol.*, 55, 421–438.
- Jaupart, C. and Allègre, C. J. (1991). Gas content, eruption rate and instabilities of eruption regime in silicic volcanoes. *Earth Planet. Sci. Lett.*, 102, 413–429.
- Klug, C. and Cashman, K. V. (1996). Permeability development in vesiculating magmas: implications for fragmentation. *Bull. Volcanol.*, 58, 87–100.
- Kushnir, A. R. L., Martel, C., Champallier, R., and Arbaret, L. (2017). In situ confirmation of permeability development in shearing bubble-bearing melts and implications for volcanic outgassing. *Earth Planet. Sci. Lett.*, 458, 315–326.
- Laumonier, M., Arbaret, L., Burgisser, A., and Champallier, R. (2011). Porosity redistribution enhanced by strain localization in crystal-rich magmas. *Geology*, 39(8), 715–718.
- Launeau, P. and Cruden, A. R. (1998). Magmatic fabric acquisition mechanisms in a syenite: results of a combined anisotropy of magnetic susceptibility and image analysis study. *J. Geophys. Res.*, 103, 5067–5089.
- Launeau, P. and Robin, P.-Y. (1996). Fabric analysis using the intercept method. *Tectonophysics*, 267, 91–119.
- Lin, T.-J. and Lin, G.-M. (2009). Mechanisms of in-line coalescence of two-unequal bubbles in a non-Newtonian fluid. *Chem. Eng. J.*, 155, 750–756.
- Lindoo, A., Larsen, J. E., Cashman, K. V., and Oppenheimer, J. (2017). Crystal controls on permeability development and degassing in basaltic andesite magma. *Geology*, 45, 831–834.
- Mader, H. M., Llewellyn, E. W., and Mueller, S. P. (2013). The rheology of two-phase magmas: a review and analysis. *J. Volcanol. Geotherm. Res.*, 257, 135–158.
- Martel, C., Bourdier, J.-L., Pichavant, M., and Traineau, H. (2000). Textures, water content and degassing of silicic andesites from recent plinian and dome-forming eruptions at Mount Pelée volcano (Martinique, Lesser Antilles arc). *J. Volcanol. Geotherm. Res.*, 96, 191–206.
- Martel, C. and Iacono-Marziano, G. (2015). Timescales of bubble coalescence, outgassing, and foam collapse in decompressed rhyolitic melts. *Earth Planet. Sci. Lett.*, 412, 173–185.
- Martel, C. and Poussineau, S. (2007). Diversity of eruptive style inferred from the microlites of Mt. Pelée andesite (Martinique, Lesser Antilles). *J. Volcanol. Geotherm. Res.*, 166, 233–254.
- Martel, C. and Schmidt, B. C. (2003). Decompression experiments as an insight into magma ascent rates. *Contrib. Mineral. Petrol.*, 144, 397–415.
- Mourtada-Bonnefoi, C. and Laporte, D. (2002). Homogeneous bubble nucleation in rhyolitic magmas: an experimental study of the effect of H<sub>2</sub>O and CO<sub>2</sub>. *J. Geophys. Res.*, 107(B4), article no. 2066.
- Navon, O., Chekhmir, A., and Lyakhovskiy, V. (1998). Bubble growth in highly viscous melts: theory, experiments, and autoexplosivity of dome lavas. *Earth Planet. Sci. Lett.*, 160, 763–776.
- Newman, S. and Lowenstern, J. B. (2002). VOLATILE-CALC: a silicate melt–H<sub>2</sub>O–CO<sub>2</sub> solution model written in Visual Basic for Excel. *Comput. Geosci.*, 28(5), 597–604.
- Okumura, S., Nakamura, M., Nakano, T., Uesugi, K., and Tsuchiyama, A. (2012). Experimental constraints on permeable gas transport in crystalline silicic magmas. *Contrib. Mineral. Petrol.*, 164(3), 493–504.
- Okumura, S., Nakamura, M., Takeuchi, S., Tsuchiyama, A., Nakano, T., and Uesugi, K. (2009). Magma deformation may induce non-explosive volcanism via degassing through bubble networks. *Earth Planet. Sci. Lett.*, 281(3–4), 267–274.
- Okumura, S., Nakamura, M., Tsuchiyama, A., Nakano, T., and Uesugi, K. (2008). Evolution of bubble microstructure in sheared rhyolite: formation of a channel-like bubble network. *J. Geophys. Res., Solid Earth*, 113, article no. B07208.
- Parmigiani, A., Degruyter, W., Leclaire, S., Huber, C., and Bachmann, O. (2017). The mechanics of shal-

- low magma reservoir outgassing. *Geochem. Geophys. Geosyst.*, 18, 2887–2905.
- Paterson, M. S. and Olgaard, D. L. (2000). Rock deformation tests to large shear strains in torsion. *J. Struct. Geol.*, 22, 1341–1358.
- Pistone, M., Caricchi, L., Ulmer, P., Burlini, L., Ardia, P., Reusser, E., Marone, F., and Arbaret, L. (2012). Deformation experiments of bubble-and crystal-bearing magmas: rheological and microstructural analysis. *J. Geophys. Res., Solid Earth*, 117, article no. B05208.
- Popa, R. G., Bachmann, O., and Huber, C. (2021). Explosive or effusive style of volcanic eruption determined by magma storage conditions. *Nat. Geosci.*, 14, 781–786.
- Saar, M. O. and Manga, M. (1999). Permeability-porosity relationship in vesicular basalts. *Geophys. Res. Lett.*, 26(1), 111–114.
- Shields, J. K., Mader, H. M., Caricchi, L., Tuffen, H., Mueller, S., Pistone, M., and Baumgartner, L. (2016). Unravelling textural heterogeneity in obsidian: shear-induced outgassing in the Rocche Rosse flow. *J. Volcanol. Geotherm. Res.*, 310, 137–158.
- Shields, J. K., Mader, H. M., Pistone, M., Caricchi, L., Floess, D., and Putlitz, B. (2014). Strain-induced outgassing of three-phase magmas during simple shear. *J. Geophys. Res., Solid Earth*, 119(9), 6936–6957.
- Sparks, R. S. J. (1997). Causes and consequences of pressurization in lava domes. *Earth Planet. Sci. Lett.*, 160, 177–189.
- Stasiuk, M. V., Barclay, J., Carroll, M. R., Jaupart, C., Ratte, J. C., Sparks, R. S. J., and Tait, S. R. (1996). Degassing during magma ascent in the Mule Creek vent (USA). *Bull. Volcanol.*, 58(2–3), 117–130.
- Takeuchi, S., Nakashima, S., and Tomiya, A. (2008). Permeability measurements of natural and experimental volcanic materials with a simple permeameter: toward an understanding of magmatic degassing processes. *J. Volcanol. Geotherm. Res.*, 177(2), 329–339.
- Takeuchi, S., Nakashima, S., Tomiya, A., and Shinohara, H. (2005). Experimental constraints on the low gas permeability of vesicular magma during decompression. *Geophys. Res. Lett.*, 32, article no. L10312.
- Takeuchi, S., Toshida, K., Miura, D., Ito, H., and Uesawa, S. (2021). Relationships between magmatic properties and eruption magnitude of explosive eruptions at Japanese arc volcanoes during the last one hundred thousand years. *J. Volcanol. Geotherm. Res.*, 419, article no. 107345.
- Toramaru, A. (2006). BND (bubble number density) decompression rate meter for explosive volcanic eruptions. *J. Volcanol. Geotherm. Res.*, 154, 303–316.
- Truby, J. M., Mueller, S. P. E., Llewellyn, W., and Mader, H. M. (2015). The rheology of three-phase suspensions at low bubble capillary number. *Proc. R. Soc. A*, 471, article no. 20140557.
- Tuffen, H., Dingwell, D. B., and Pinkerton, H. (2003). Repeated fracture and healing of silicic magma generate flow banding and earthquakes? *Geology*, 31(12), 1089–1092.
- Voight, B., Glicken, H., Janda, R. J., and Douglass, P. M. (1981). Catastrophic rockslide avalanche of May 18. *U.S. Geol. Surv. Prof. Paper*, 1250, 347–377.
- Voight, B., Sparks, R. S. J., Miller, A. D., Stewart, R. C., Hoblitt, R. P., Clarke, A., Ewart, J., Aspinall, W. P., Baptie, B., Calder, E. S., Cole, P., Druitt, T. H., Hartford, C., Herd, R. A., Jackson, P., Lejeune, A. M., Lockhart, A. B., Loughlin, S. C., Luckett, R., Lynch, L., Norton, G. E., Robertson, R., Watson, I. M., Watts, R., and Young, S. R. (1999). Magma flow instability and cyclic activity at Soufriere Hills volcano, Montserrat, British West Indies. *Science*, 283(5405), 1138–1142.
- Westrich, H. R. and Eichelberger, J. C. (1994). Gas transport and bubble collapse in rhyolitic magma: an experimental approach. *Bull. Volcanol.*, 56(6–7), 447–458.
- Woods, A. W. and Koyaguchi, T. (1994). Transitions between explosive and effusive eruptions of silicic magmas. *Nature*, 370(6491), 641–644.
- Wright, H. M. N., Cashman, K. V., Gottesfeld, E. H., and Roberts, J. J. (2009). Pore structure of volcanic clasts: Measurements of permeability and electrical conductivity. *Earth Planet. Sci. Lett.*, 280(1–4), 93–104.



Research article

## Magma degassing and its impact on the Earth's atmosphere: from magma oceans to lava lakes

# A novel approach to volcano surveillance using gas geochemistry

Yves Moussallam<sup>Ⓜ,\*,a,b</sup>, Clive Oppenheimer<sup>Ⓜ,c</sup> and Bruno Scaillet<sup>Ⓜ,d</sup>

<sup>a</sup> Lamont-Doherty Earth Observatory, Columbia University, New York, USA

<sup>b</sup> Department of Earth and Planetary Sciences, American Museum of Natural History, New York, USA

<sup>c</sup> Department of Geography, University of Cambridge, Downing Place, Cambridge CB2 3EN, UK

<sup>d</sup> ISTO, 7327 Université d'Orléans-CNRS-BRGM, 1A rue de la Férollerie, 45071 Orléans cedex 2, France

E-mails: yves.moussallam@ldeo.columbia.edu (Y. Moussallam), co200@cam.ac.uk (C. Oppenheimer), bscaille@cnsr-orleans.fr (B. Scaillet)

**Abstract.** Identifying precursory phenomena is central to the short-range assessment and anticipation of volcanic hazards. The chemistry of gases, which may separate from magma at depth, is operationally monitored at many volcanoes worldwide to manage risk. However, owing to the complexity of volcanic degassing, decoding the message of gas geochemistry has proven challenging. Here, we report an approach to restoration of measured volcanic gas compositions that enables tracking of variations in the temperature and/or oxidation state of the source magma. We validate the approach with reference to independent estimates of melt oxidation state obtained by X-ray absorption near-edge structure (XANES) spectroscopy at the iron K-edge. We then apply the method to a global database of high temperature volcanic gases and to extended gas geochemical timeseries at Unzen, Aso, and Asama volcanoes, identifying hitherto unreported but significant changes in magma intensive parameters that preceded or accompanied changes in volcanic activity. Restoration of volcanic gas compositions offers a promising complement to monitoring strategies at active volcanoes, calling for more systematic operational surveillance of redox-sensitive gas species.

**Keywords.** Oxygen fugacity, Volcanic degassing, Volcanic gases, Redox, Volcano monitoring, Gas geochemistry.

*Manuscript received 31 March 2022, revised 1 September 2022, accepted 6 September 2022.*

## 1. Introduction

Volcanic gas measurements have been made for decades but their interpretation remains challenging. This challenge is particularly acute when gas observations and monitoring are applied to hazard assessment. The complexity arises from the multiple chemical and physical processes that can influence

gas flux, atomic and molecular composition, and isotopic signature measured at the surface. These include processes occurring within stored or migrating magma (e.g., exsolution, gas separation which depends on pressure, temperature, melt composition, and magma permeability and ascent rate, etc.), within fracture networks in solid rock through which gases pass (e.g., gas–rock interaction, cooling and re-equilibration), and in mixing with other fluids (including hydrothermal fluids and air).

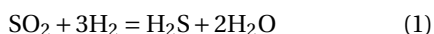
Increasingly systematic work on gas geochemistry

\* Corresponding author

began in the late 1950s to 1960s [Ellis, 1957, Matsuo, 1962]. In the 1980s and 1990s, several studies looked at the composition of volcanic gases collected at varying vent temperatures to identify process controlling their oxidation state. For instance, Giggenbach [1987] analysed fumarolic emissions (temperatures from 106 °C to 760 °C) at Whakaari/White Island (New Zealand). For high temperature gases, he identified three degassing scenarios: “A1”, “A2” and “A3” [see Figure 16 in Giggenbach, 1987]. Scenario A1 involves direct rise of the gas phase to the surface without internal equilibration or equilibration with the vent system. In scenario A2, the gas maintains equilibrium with the magma throughout ascent, the oxidation state of the gas being buffered by and equal to that of the magma, while in A3, a “fluid-dominated” regime, gas oxidation state is largely controlled by internal equilibrium (though in Giggenbach 1987’s description of the process, the gas could still exchange chemically with, and reduce, a stagnant melt).

Gerlach [1993] measured a series of high temperature volcanic gases with apparent equilibrium temperatures (AET) ranging from 935 °C to 1185 °C [see Ellis, 1957, Matsuo, 1962, Heald *et al.*, 1963 for earliest definitions of AET], collected from fissures and lava flow skylights during the Pu’u ‘Ō’ō eruption of Kīlauea. He found that the gas oxidation states (termed as, “apparent oxidation state” or AOS) plotted mostly parallel to rock redox buffers [see Figure 5 in Gerlach, 1993] and argued that redox equilibrium between the rock/magma and gas was maintained during cooling with buffering effective from molten to subsolidus conditions. This interpretation corresponds to scenario A2 of Giggenbach [1987] and is consistent with data and arguments of Allard *et al.* [1977] at Erta Ale, where they found the oxidation state of high temperature (1130 °C) volcanic gases to indicate equilibrium with the basaltic magma.

Shinohara *et al.* [1993] and Ohba *et al.* [1994] reported comparable studies of high temperature gases emitted from Satsuma-Iwojima and Unzen volcanoes, respectively. They concluded that addition of external water might play a role but found that temperature-oxygen fugacity ( $T$ - $fO_2$ ) relationships could be explained by the equilibrium:



This corresponds to an internal re-equilibration of the gas phase, essentially Giggenbach’s scenario A3.

Internal re-equilibration appears (though they do not make this explicit) also to be the process favoured by Menyailov *et al.* [1986], who measured 740 °C to 895 °C emissions from Momotombo between 1974 and 1984. They found the oxidation state of hotter gases to be closer to the quartz-fayalite-magnetite (QFM) buffer while that for cooler gases to be closer to the nickel-nickel oxide (NNO) buffer.

In the following decades, the view that the oxidation state of volcanic gases is buffered by the magma/rock during ascent and cooling (scenario A2) became generally accepted, exemplified by the wide-ranging synthesis of Symonds *et al.* [1994], who concluded that “lavas buffer  $fO_2$  in high temperature volcanic gases”.

More recently, Oppenheimer *et al.* [2018] argued that large variation in gas composition during degassing at the Kīlauea lava lake over a 850 °C to 1110 °C range in AET could be explained by closed system, gas-only cooling and re-equilibration [see Figure 3 in Oppenheimer *et al.*, 2018]. Compiling a global database of high temperature ( $T \geq 600$  °C) volcanic gases, Moussallam *et al.* [2019b] explained the  $T$ - $fO_2$  trend of the entire database by closed system, gas-only cooling and internal re-equilibration according to equilibrium (1) [see Figure 4A in Moussallam *et al.*, 2019b]. Both studies argue for the role of scenario A3 in explaining volcanic gas chemistry and confirm that emissions quench with negligible oxidation in air [e.g., Aiuppa *et al.*, 2007, Martin *et al.*, 2009], such that they preserve a signature of the original magmatic gas modified only by internal re-equilibration during cooling.

Here, we develop the application of these findings for interpretation of redox-sensitive species measured in high-temperature volcanic emissions. Taking the assumption that emitted gases cool from magmatic temperature following separation from their source melts, we explore estimation of either  $T$  or  $fO_2$  when finally in equilibrium with the magma. As the system is underdetermined, a further assumption of either the degree of gas cooling, or the magma oxidation state, is however necessary. We test the approach by comparing our results with independent determinations of melt oxidation state, before applying it to analysis of multiyear datasets of gas emissions from Uzen, Aso and Asama volcanoes and to a global database of volcanic gas observations.

## 2. Methodology

We used the global dataset of high temperature volcanic gases compiled by Moussallam *et al.* [2019b], supplemented with recently available data (Table S1). The dataset is limited to high temperature (>500 °C) gases, for which gas–rock or gas–fluid interactions are minimal [e.g., Giggenbach, 1996, Symonds *et al.*, 2001]. To quantify the cooling of volcanic gases between their escape from the melt and their last retained equilibrium temperature, we extended the compilation of Moussallam *et al.* [2019b], collecting melt temperature estimates from existing literature, mostly from petrological studies (i.e., geothermometry). In cases where such data were unavailable (the case for ten of the 37 volcanoes), we estimated melt temperature from reported bulk composition. The difference between estimated melt temperature and measured (or calculated) gas emission (or apparent equilibrium) temperature yields the amount of closed system cooling experienced by the gas. Using the reported gas composition as starting conditions, we restored each to its values at melt temperature by solving equilibrium (1) at 1 bar using thermodynamic parameters given in Ohba *et al.* [1994] for the temperature-dependent equilibrium constant ( $K$ ) and recalculating the gas composition such that  $K(T) = \log(X_{\text{SO}_2}^{-1} X_{\text{H}_2}^{-3} X_{\text{H}_2\text{S}} X_{\text{H}_2\text{O}}^2) - \log(P)$ , where  $X_i$  represents the mole fraction of component  $i$ , subject to the constraints, that the amounts of O, H and S in the gas mixture remain constant.

### 2.1. Example of restoration calculation

In this section, we elaborate the calculation method used in this study through a worked example. We take the case of volcanic gases measured in 1994 from the then active lava dome of Merapi volcano (Indonesia), in the course of the fifth International Association of Volcanology and Chemistry gas workshop [Giggenbach *et al.*, 2001]. Gases were collected

directly at the vent (Gendol fumarole) and had an exit temperature of 803 °C. Proportions (median of six analyses) of H<sub>2</sub>O, CO<sub>2</sub>, SO<sub>2</sub>, CO, H<sub>2</sub>S and H<sub>2</sub> gases were found to be 88.7, 5.56, 0.98, 0.0235, 0.13 and 0.5 mol%, respectively [Giggenbach *et al.*, 2001]. This gas analysis was employed also by Moussallam *et al.* [2019b, see methodology section] to illustrate the calculation of the AET and AOS. We pick up from this point to demonstrate restoration of either (i) the oxidation state at equilibrium with the magma if the magmatic temperature is known or (ii) the temperature at equilibrium with the magma if the magma oxidation state is known.

Costa *et al.* [2013] estimated temperatures for the Merapi magma of 900 to 1000 °C based on amphibole thermobarometry in products of the 2006 and 2010 eruptions. We use the median temperature of 950 °C as the magmatic temperature ( $T_{\text{mag}}$ ) in this example. The AET of the Merapi gas mixture measured by Giggenbach *et al.* [2001] can be calculated by the H<sub>2</sub>/H<sub>2</sub>O and H<sub>2</sub>S/SO<sub>2</sub> method, yielding an AET of 849 °C, or by the H<sub>2</sub>S/SO<sub>2</sub> and CO/CO<sub>2</sub> method, yielding an AET of 790 °C [see Moussallam *et al.*, 2019b for step-by-step calculation]. Since in this example the exit temperature (803 °C) was measured directly by thermocouple by Giggenbach *et al.* [2001] we use this value as the starting equilibrium temperature of the gas mixture. To calculate the AOS, we can use either the H<sub>2</sub>S/SO<sub>2</sub> and  $T$  method, yielding an AOS of  $\log f_{\text{O}_2}$  of  $-13.75$  or the H<sub>2</sub>/H<sub>2</sub>O and  $T$  method yielding an AOS of  $\log f_{\text{O}_2}$  of  $-14.02$  [see Moussallam *et al.*, 2019b, for step-by-step calculation]. We use the second estimate in this example, which corresponds to QFM + 0.6. Now that the starting (AET and AOS) and final ( $T_{\text{mag}}$ ) conditions are defined, we can proceed with the calculation.

The equilibrium constant ( $K$ ) of reaction (1) (SO<sub>2</sub> + 3H<sub>2</sub> = H<sub>2</sub>S + 2H<sub>2</sub>O) can be written (assuming all fugacity coefficients are 1) as  $\log K_1(T) = \log(X_{\text{SO}_2}^{-1} X_{\text{H}_2}^{-3} X_{\text{H}_2\text{S}} X_{\text{H}_2\text{O}}^2) - \log(P)$ , where  $X_i$  represents the mole fraction of component  $i$ . The equilibrium constant can also be written as  $\log K_2 = A + BT^{-2} + CT^{-1} + DT + E \ln T$ , where  $A$ ,  $B$ ,  $C$ ,  $D$ , and  $E$  are constants with values of 8.5667,  $-29,743$ , 10,449, 0.00047814 and  $-1.7784$ , respectively [taken from Ohba *et al.*, 1994 who obtained them from thermodynamic data at 1 bar in the NIST database of Chase, 1998].  $K_2$  can be calculated at any temperature. The problem is then to find  $X_{\text{SO}_2}$ ,

$X_{\text{H}_2}$ ,  $X_{\text{H}_2\text{S}}$ , and  $X_{\text{H}_2\text{O}}$ , at any temperature of interest such that  $K_1 = K_2$ . Because there are four unknowns, the solution isn't unique. However, we can assume the gas composition in terms of atomic (O, H and S) species as constant. We can then use a solver to find the values of  $X_{\text{SO}_2}$ ,  $X_{\text{H}_2}$ ,  $X_{\text{H}_2\text{S}}$ , and  $X_{\text{H}_2\text{O}}$  that satisfies all the constraints and then from those, calculate an AOS at the temperature of interest. For the Merapi 1994 case, the initial  $X_{\text{SO}_2}$ ,  $X_{\text{H}_2}$ ,  $X_{\text{H}_2\text{S}}$ , and  $X_{\text{H}_2\text{O}}$  values are 0.0102, 0.0052, 0.0013 and 0.9191, respectively, at an AET of 803 °C (AOS of  $\log f\text{O}_2 = -14.02 = \text{QFM} + 0.6$ ). At a  $T_{\text{mag}}$  of 950 °C, a solution to  $K_1 = K_2$  at fixed O, H and S species gives values of 0.0104, 0.0094, 0.0011 and 0.9151 for  $X_{\text{SO}_2}$ ,  $X_{\text{H}_2}$ ,  $X_{\text{H}_2\text{S}}$ , and  $X_{\text{H}_2\text{O}}$ , respectively. This solution corresponds to an AOS at magmatic temperature of  $\log f\text{O}_2 = -11.81 = \text{QFM} + 0.1$ .

The same procedure can be applied in the case where  $T_{\text{mag}}$  is unknown but the gas oxidation state at equilibrium with the melt (i.e., the melt oxidation state) is known. The calculations are performed starting at the initial AET and by increasing  $T$  incrementally until the AOS matches the target value. This value represents the temperature at equilibrium with the magma.

All results presented in this study were performed at a fixed pressure of 1 bar. While this is a simplification, we note that these types of calculations reproduce the variability found in natural observations extremely well, both in global compilations [Moussallam *et al.*, 2019b] and for individual volcanoes [Oppenheimer *et al.*, 2018]. We stress that the application of the method is limited to high temperature (>500 °C) magmatic gases for which gas–rock or gas–fluid interactions are minimal [e.g., Giggenbach, 1996, Symonds *et al.*, 2001].

### 3. Results

Initial conditions and final calculations are reported in Table S2. Figure 1 shows the oxidation state of volcanic gases from our global database plotted against the estimated closed system cooling they have experienced. The dataset shows a clear global trend towards oxidation of the gases as a function of cooling, as reported by Moussallam *et al.* [2019b]. Figure 1 shows the restorations of the oxidation state of each volcanic gas along individual cooling paths, back to magmatic temperatures. While original gas

oxidation states vary by five log units (from  $\log f\text{O}_2 = \text{QFM} + 4.1$  to  $\text{QFM} - 0.9$ ), restored oxidation states at magmatic temperature vary within two log units (from  $\log f\text{O}_2 = \text{QFM} + 0.7$  to  $\text{QFM} - 1.1$ ). Arc magmas are represented with a near normal distribution with an average of  $\log f\text{O}_2 = \text{QFM} + 0.0$  and standard deviation of  $\pm 0.3$  (the median is also QFM). This is somewhat more reduced than suggested by petrological estimates, being closer to inferred arc mantle conditions (see compilation in Matjuschkin *et al.* [2016] and their Figure 1), possibly reflecting changes in oxidation state on decompression [e.g., Burgisser and Scaillet, 2007]. Intraplate magmas are poorly represented in our database but tend to be more reduced, with an average of  $\text{QFM} - 0.5$  log units.

## 4. Discussion

### 4.1. Method validation

To test the validity of the approach and the underlying assumptions, we compare the restored oxidation state of volcanic gases at magmatic temperature to independent determinations of melt oxidation state by X-ray absorption near-edge structure (XANES) spectroscopy at the iron  $K$ -edge. Iron  $K$ -edge XANES in silicate glasses is a synchrotron-based technique used for the determination of the relative proportions of ferric ( $\text{Fe}^{3+}$ ) and ferrous ( $\text{Fe}^{2+}$ ) iron. The small (typically 2 to 10  $\mu\text{m}$ ) beam size achievable allows measurements of melt inclusions and matrix glasses that can be converted to oxygen fugacity ( $f\text{O}_2$ ) using the equation provided by Kress and Carmichael [1991] [full method detailed in Rose-Koga *et al.*, 2021]. Since melt oxidation state varies with differentiation [e.g., Kelley and Cottrell, 2012] and degassing [e.g., Moussallam *et al.*, 2014, 2016, 2019a], measurements must pertain to the time period when gas observations were made. We identified suitable measurements for four volcanoes: (i) Erta Ale, where gas measurements were made in January 2011 [Zelenski *et al.*, 2013], and November 2010 scoriae were analysed by XANES [de Moor *et al.*, 2013]. (ii) Etna, where gas measurements from 2009 at the Voragine and Bocca Nuova craters [Aiuppa *et al.*, 2011] are compatible with 2002–2013 tephra investigated by XANES [Gennaro *et al.*, 2020]. (iii) Kilauea, where gas measurements in 2013 [Oppenheimer *et al.*, 2018] are comparable in timing with

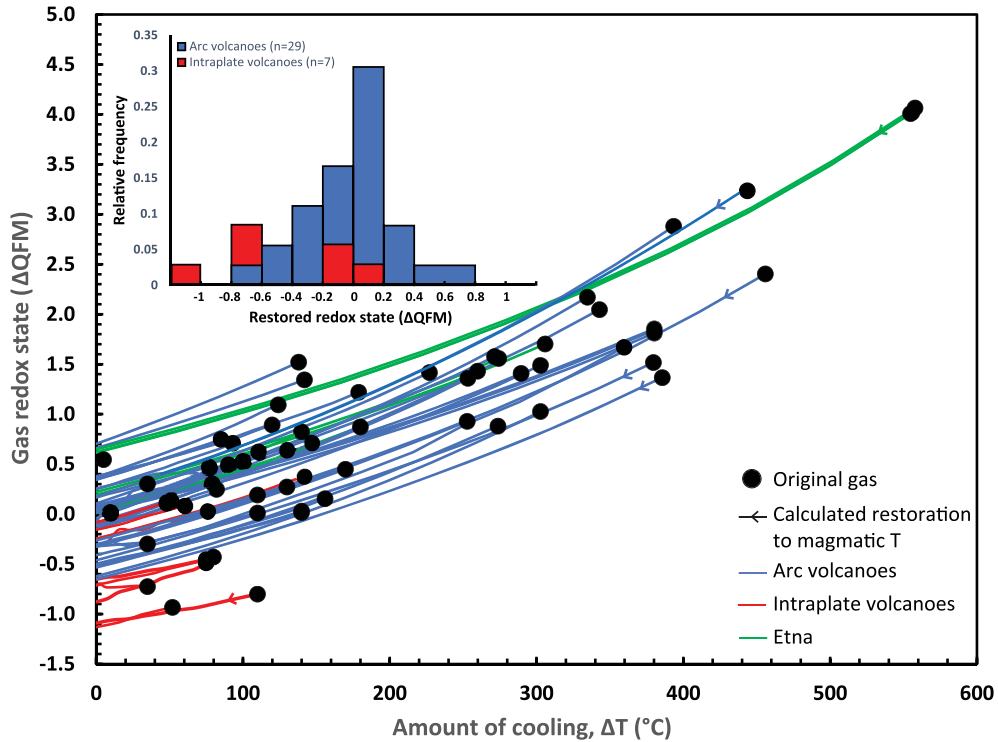


**Figure 1.** Oxidation state of volcanic gases (expressed as deviation from the QFM buffer) as a function of the difference between AET and the temperature of the associated melt. Lines show the results of recalculating the oxidation state of each gas composition back to its magmatic temperature. Upper left inset: non-stacked histogram showing the frequency of oxidation states (expressed as deviation from the QFM buffer) of arc and intraplate melts calculated by restoring volcanic gas compositions to their magmatic temperature.

2008 and 2010 tephra measured by XANES [Moussallam *et al.*, 2016]. (iv) Surtsey, where gases collected in 1965 [Sigvaldason and Elisson, 1968] [summarised in Gerlach, 1980] can be compared with XANES measurements of tephra erupted between 1963 and 1966 [Schipper and Moussallam, 2017].

The results are shown in Figure 2. Three of the four volcanoes investigated lie within one standard deviation of the 1:1 line. Gas and melt oxidation state data from Surtsey, however, differ by 0.4 log  $f_{O_2}$  units. In this case, the gas data were collected at 1125 °C, close to the estimated magmatic temperature of 1160 °C, so our calculations only slightly shifted the AOS. The broad agreement between restored oxidation state of volcanic gases at magmatic temperature and independently constrained melt oxidation state provides a first order corroboration of our approach. We note that there is no correlation between the oxidation

state of restored volcanic gases and melt temperature (Figure S1).

#### 4.2. Monitoring magma oxidation state and/or temperature at active volcanoes

To explore the application of the method, we apply it to three sets of observations from different volcanoes in Japan. In each case, the four species in equilibrium (1) were monitored in high-temperature gas emissions for extended periods. The first case pertains to two fumaroles, 20 m apart, on an active lava dome at Mt Unzen [Ohba *et al.*, 2008], and for which the gas observations can be evaluated in the context of detailed petrological information. The gases, whose exit temperatures differed, were sampled six times between May 1992 and October 1993. Unzen erupted 900 °C dacitic magmas generated from mixing of

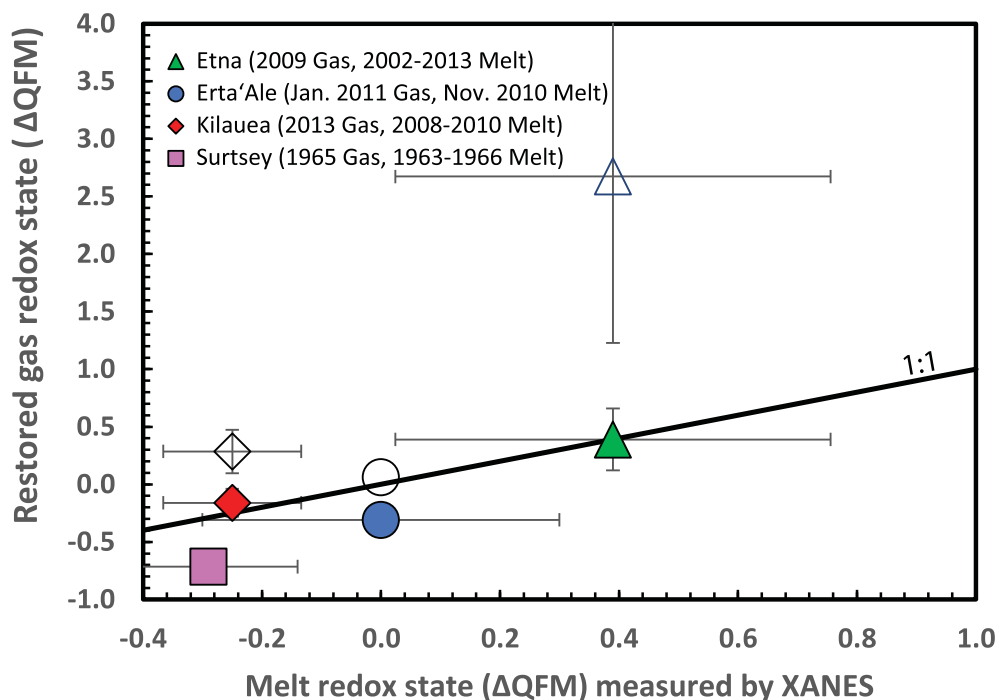


**Figure 2.** Restored oxidation state of volcanic gases (expressed as deviation from the QFM buffer) at magmatic temperature compared to oxidation state of corresponding melts measured by XANES on melt inclusions and matrix glasses. Gas measurements from Etna, Erta Ale, Kīlauea and Surtsey are from Aiuppa *et al.* [2011], Zelenski *et al.* [2013], Oppenheimer *et al.* [2018], and Sigvaldason and Elísson [1968] [as reported in Gerlach, 1980] respectively. XANES measurements are from de Moor *et al.* [2013], Gennaro *et al.* [2020], Moussallam *et al.* [2016], and Schipper and Moussallam [2017] respectively. Symbols are average values, error bars represent one standard deviation on the set of measurements used to calculate each average. Unfilled symbols show gas AOS prior to restoration.

andesite (1030 °C) and rhyodacite (800 °C) endmembers [Venezky and Rutherford, 1999]. While the AOS and AET of the gases varied widely (from QFM + 0.2 to QFM + 3.2 log units, and from 469 to 878 °C, respectively), once restored to a magmatic temperature of 900 °C, all measurements converge at  $\log fO_2 = \text{QFM} + 0.03$  with a standard deviation of  $\pm 0.04$  (Figure 3A).

If we restore the gas measurements to a fixed  $fO_2$  ( $\log fO_2 = \text{QFM} + 0.03$ ), then we can calculate temperature variations. These suggest an increase in  $T_{\text{mag}}$  of around 30 °C from May 1992 to February 1993, consistent with a decrease of around 0.7 wt% SiO<sub>2</sub> in the erupted dacite (implying augmentation of the andesitic component) [Nakada and Motomura, 1999]. A subsequent decrease in calculated melt temperature in October 1993 mirrors a trend of increasing silicate content (Figure 3B). This interpretation

is compatible with FeTi-oxide evidence, which suggests a groundmass temperature variation of 100 °C spanning the 1991–95 eruption and an overall 2 wt% variation in bulk SiO<sub>2</sub> content [Nakada and Motomura, 1999]. In the Unzen case, temporal variations in the restored syn-eruptive gases are minor, mirroring equally limited changes in the erupted magma. In the following case studies, restored gases record much larger variations.

The second case is that of Aso volcano spanning from 2003 until an eruption on 25 November 2014. We restored the data for gas emissions from Nakade crater [Shinohara *et al.*, 2018] back to a magmatic temperature of 1067 °C, the median value estimated for erupted lava in 2014 [Saito *et al.*, 2018; Figure 4A]. Assuming constant temperature, the computed melt oxidation state changed significantly in early 2012 to 2013 (Figure 5A). Until early 2012, the calculated melt



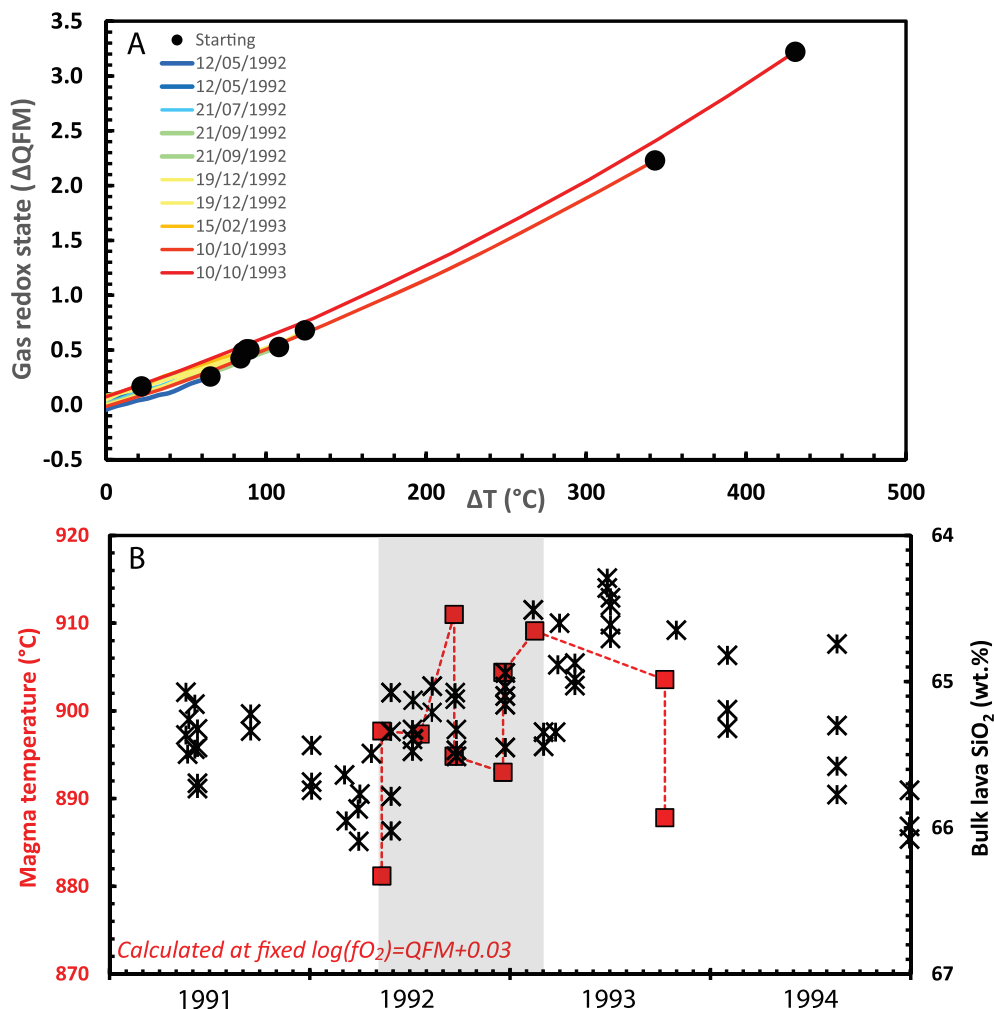


**Figure 3.** (A) Oxidation state of volcanic gases emitted at Unzen volcano (expressed as deviation from the QFM buffer) as a function of the difference between AET (apparent equilibrium temperature) and melt temperature. Lines show the results of recalculating the oxidation state of each gas composition back to its magmatic temperature. Starting conditions take gas compositions from direct sampling of two fumaroles from the active lava dome at Unzen between 1992 and 1993 [Ohba *et al.*, 2008]. (B) Evolution of the melt temperature at Unzen calculated from restored gas composition assuming a fixed melt oxidation state of  $\log fO_2 = QFM + 0.03$  compared with bulk rock composition (in  $SiO_2$  content) of the extruded dacitic dome lava [black crosses, from Nakada and Motomura, 1999]. Light grey shaded regions correspond to the period from May 1992 to February 1993 discussed in text.

oxidation state varies from  $QFM + 0.1$  to  $QFM - 0.3$  log units (average of  $QFM - 0.1$  and standard deviation of 0.1). From 2012 to 2014, the calculated melt oxidation state varies from  $QFM - 0.3$  to  $QFM - 0.6$  log units (average of  $QFM - 0.4$  and standard deviation of 0.05). Alternatively, if we fix the melt

oxidation state (e.g., at QFM), we can compute melt temperature (Figure 5B). Under this assumption, prior to 2012, the calculated melt temperature varies from 991 to 1094  $^{\circ}C$  (average of  $1041 \pm 32$   $^{\circ}C$ ), while between 2012 and 2014, it varies from 948 to 980  $^{\circ}C$  (average of  $963 \pm 11$   $^{\circ}C$ ).

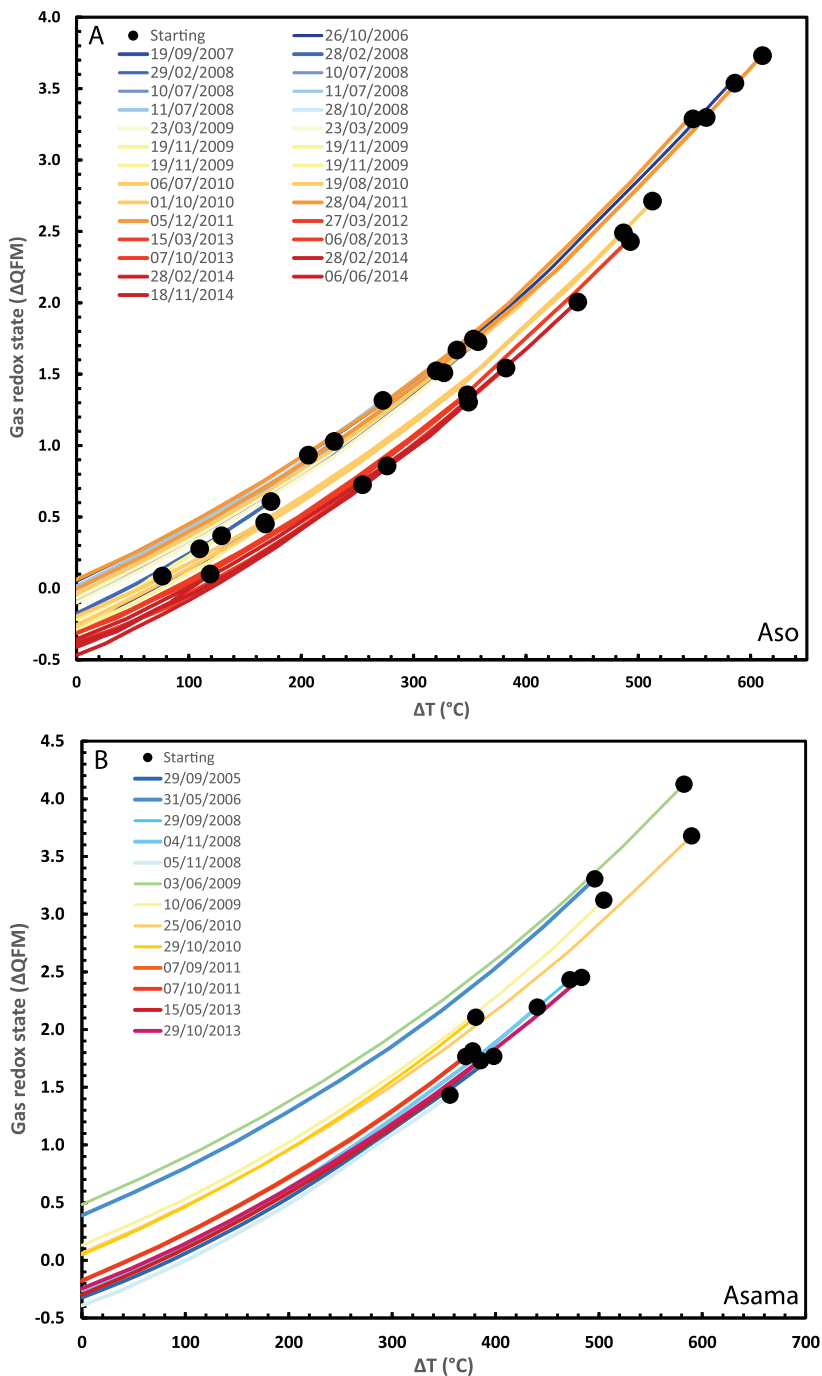


**Figure 4.** Oxidation state of volcanic gases emitted by Aso (A) and Asama (B) volcanoes (expressed as deviation from the QFM buffer) as a function of the difference between AET (apparent equilibrium temperature) and melt temperature. Lines show the results of recalculating the oxidation state of each gas composition back to its magmatic temperature, solving for the reaction  $\text{SO}_2 + 3\text{H}_2 = \text{H}_2\text{S} + 2\text{H}_2\text{O}$  at 1 bar using thermodynamic parameters in Ohba *et al.* [1994]. Starting conditions for Aso take gas compositions reported by Shinohara *et al.* [2018] for fumaroles gases measured by MultiGAS prior to the 25 November 2014 eruption. Starting conditions for Asama use gas compositions reported by Shinohara *et al.* [2015].

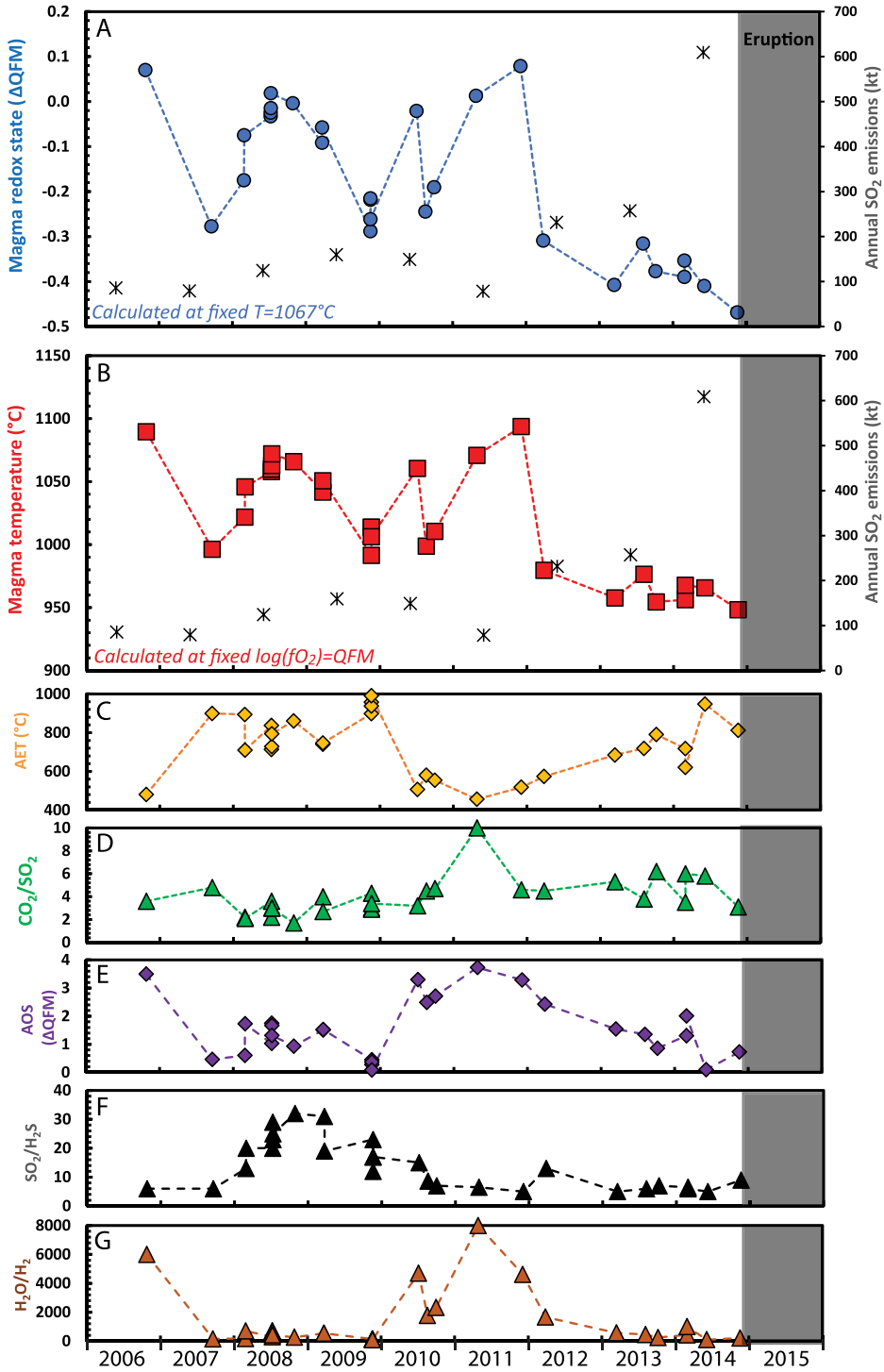


**Figure 5.** Evolution of the melt conditions at Aso volcano calculated from restored gas composition assuming (A) a fixed melt temperature of 1067 °C and (B) a fixed melt oxidation state of  $\log fO_2 = QFM+0.0$ .  $SO_2$  emission rate measurements in A and B (black crosses) are calendar-year averages OMI data from Carn *et al.* [2017] plotted mid-year. (C–G) Evolution of the apparent equilibrium temperature (AET),  $CO_2/SO_2$  ratio, apparent oxidation state (AOS),  $SO_2/H_2S$  and  $H_2O/H_2$  ratios from the original gas measurements [Shinohara *et al.*, 2018].

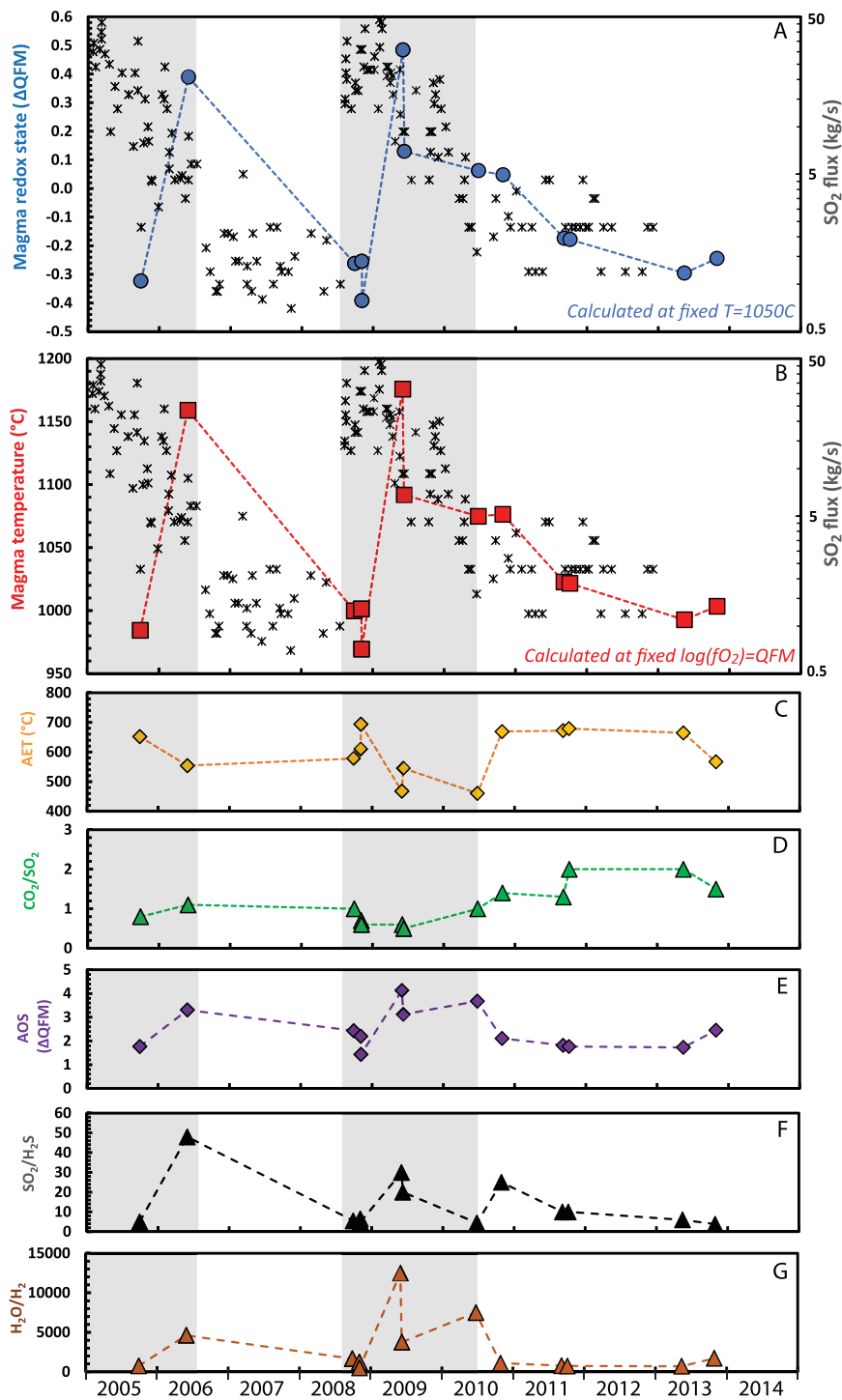


**Figure 6.** Caption continued on next page.

**Figure 6. (cont.)** Evolution of the melt conditions at Asama volcano calculated from restored gas composition assuming (A) a fixed melt temperature of 1050 °C and (B) a fixed melt oxidation state of  $\log fO_2 = \text{QFM} + 0.0$ .  $\text{SO}_2$  flux measurements in (A) and (B) (black crosses) are from Ohwada *et al.* [2013] (C–G). Evolution of the apparent equilibrium temperature (AET) and  $\text{CO}_2/\text{SO}_2$  ratio, apparent oxidation state (AOS),  $\text{SO}_2/\text{H}_2\text{S}$  and  $\text{H}_2\text{O}/\text{H}_2$  ratios from the original gas measurements [Shinohara *et al.*, 2015]. Light grey shaded regions correspond to periods of stronger degassing [Ohwada *et al.*, 2013, Shinohara *et al.*, 2015].

The apparent change in intensive conditions of the magma in 2012–2013 that we reveal might, with hindsight, be viewed an eruption precursor. It precedes a falling lake level in late 2013 [Shinohara *et al.*, 2018], and the opening of a new vent in January 2014 [Ichimura *et al.*, 2018], which was accompanied by a three-fold increase in  $\text{SO}_2$  emission rates (Figure 5A and B) and an abrupt increase in seismicity in late August 2014 [Sandarbata *et al.*, 2015]. We note that the unrestored data for 2012–2014 show no systematic excursions from baseline levels spanning the period 2006 to 2011, neither in major gas ratios such as  $\text{CO}_2/\text{SO}_2$ ,  $\text{H}_2\text{O}/\text{H}_2$ ,  $\text{SO}_2/\text{H}_2\text{S}$  nor in AET or AOS (Figure 5C–G).

The cooling inferred by calculations at fixed redox state could signify ascent and cooling of magma at shallow levels. Conversely, a reduction in melt oxidation state prior to eruption (for the fixed temperature calculations) could indicate reduction due to sulphur degassing on magma ascent [e.g., Anderson and Wright, 1972, Métrich *et al.*, 2009, Moussallam *et al.*, 2014, 2016, 2019a]. A combination of cooling and reduction is likely but cannot be disambiguated with the available gas data. We stress, however, that the gas restoration provides a unique locus for  $T$ – $fO_2$ , in which temporal trends are evident (Figure 4). Petrological study of products of the 2014 eruption [Saito *et al.*, 2018; using the melt, olivine–liquid, plagioclase–liquid and clinopyroxene–liquid geothermometers of Putirka, 2008] indicate a melt temperature of 1042–1092 °C, with melt inclusion compositions comparable to that of the groundmass and recording estimated temperatures of 1027–1081 °C.

Our third case pertains to Asama volcano spanning from 2004 to 2014, during which there were two periods of strong degassing and increased seismicity accompanying minor eruptions [Shinohara *et al.*, 2015]. Asama gases were restored back to a magmatic temperature of 1050 °C, based on estimates made for

eruptions in 2004 [Shimano *et al.*, 2005]. This implies significant variation in melt oxidation state between  $\text{QFM} - 0.4$  and  $\text{QFM} + 0.5$  log units over the observation period (Figure 6A). Alternatively, fixing the melt oxidation state (at QFM) suggests substantial melt temperature variation between 955 and 1240 °C (Figure 6B). The trends in changing magmatic conditions show some correspondence with variations in gas emission rates (Figure 6A,B), with the two spikes in melt temperature and/or oxidized conditions coinciding with the two periods of stronger gas emission and minor explosions (whose ejecta, at least in 2009, include only traces of juvenile material [Maeno *et al.*, 2010]).

Closer inspection suggests the elevated  $\text{SO}_2$  emissions preceded changes in magmatic conditions whose relative variations more closely mirror trends in seismicity [see Figure 3b in Ohwada *et al.*, 2013]. In contrast, the unrestored gas data show no systematic variations during, or prior to the periods of enhanced activity, neither in major gas ratios such as  $\text{CO}_2/\text{SO}_2$ ,  $\text{H}_2\text{O}/\text{H}_2$ ,  $\text{SO}_2/\text{H}_2\text{S}$  nor in AET or AOS (Figure 6C–G). Again, it is impossible to disambiguate changes in magma temperature from changes in oxidation state with the available data but the large variations evident in the end-member scenarios suggest a combination of the two processes since temperatures of 1240 °C are excessive, as are variations of melt oxidation state of nearly one log unit in  $fO_2$  within a year. The spikes in both parameters may indicate episodic supply of hotter and more oxidised magma to a relatively small magma chamber unable to buffer the changes rapidly.

## 5. Conclusion

We have restored the composition of high temperature volcanic gases, drawing from published data, back to their magmatic temperature. We found that our restored gas oxidation states at magmatic

temperature are consistent with the oxidation state of corresponding melts, where measured independently. We applied the restoration procedure to a global database of volcanic gases and found that the wide variation in oxygen fugacity indicated in the original dataset is greatly lessened when gases are restored to magmatic temperature. The oxidation state of arc magmas that we calculate from restored gas measurements shows a normal distribution centred on  $\log fO_2 = \text{QFM} + 0.0 \pm 0.3$ .

Our gas restoration approach further opens up the potential for applying gas monitoring data to track changes in magma oxidation states in real time if magma temperature is known, or to track changes in magma temperatures if magma oxidation state is known. Our reassessments of Unzen, Aso and Asama datasets suggest the potential to monitor, and sometimes discriminate between (given independent constraints) these parameters. We suggest that the operational application of the approach can complement monitoring and hazard assessment, revealing variations not evident from raw geochemical data and which may relate to critical processes known to drive abrupt changes in surface activity (including magma ascent and magma mixing). This requires careful attention to measurements of redox-sensitive gas species, which can be achieved using combinations of electrochemical sensors and spectrometric techniques.

### Conflicts of interest

Authors have no conflict of interest to declare.

### Acknowledgements

CO receives support from NERC (UKRI) under High-light Topic “V-PLUS”. BS acknowledges support from both LabEx VOLTAIRE (LABX-100-01) and EquipEx PLANEX (ANR-11-EQPX-0036) projects. We are grateful to Giovanni Chiodini for his review of an earlier version of this manuscript and to an anonymous reviewer.

### Supplementary data

Supporting information for this article is available on the journal's website under <https://doi.org/10.5802/crgeos.158> or from the author.

### References

- Aiuppa, A., Franco, A., Glasow, R. V., Allen, A. G., D'Alessandro, W., and Mather, T. A. (2007). The tropospheric processing of acidic gases and hydrogen sulphide in volcanic gas plumes as inferred from field and model investigations. *Atmospheric Chem. Phys.*, 7, 1441–1450.
- Aiuppa, A., Shinohara, H., Tamburello, G., Giudice, G., Liuzzo, M., and Moretti, R. (2011). Hydrogen in the gas plume of an open-vent volcano, Mount Etna, Italy. *J. Geophys. Res.*, 116, article no. B10204.
- Allard, P., Le Guern, F., and Sabroux, J. C. (1977). Thermodynamic and isotopic studies in eruptive gases. *Geothermics*, 5, 37–40.
- Anderson, A. T. and Wright, R. (1972). Phenocrysts and glass inclusions and their bearing on oxidation and mixing of basaltic magmas, Kilauea Volcano, Hawaii. *Am. Mineral.*, 57, 188–216.
- Burgisser, A. and Scaillet, B. (2007). Redox evolution of a degassing magma rising to the surface. *Nature*, 445, 194–197.
- Carn, S. A., Fioletov, V. E., McLinden, C. A., Li, C., and Krotkov, N. A. (2017). A decade of global volcanic SO<sub>2</sub> emissions measured from space. *Sci. Rep.*, 7, article no. 44095.
- Chase, M. W. (1998). *NIST-JANAF Thermochemical Tables*. American Chemical Society; American Institute of Physics for the National Institute of Standards and Technology, Washington, DC; Woodbury, NY.
- Costa, F., Andreastuti, S., Bouvet de Maisonneuve, C., and Pallister, J. S. (2013). Petrological insights into the storage conditions, and magmatic processes that yielded the centennial 2010 Merapi explosive eruption. *J. Volcanol. Geotherm. Res.*, 261, 209–235. Merapi eruption.
- de Moor, J. M., Fischer, T. P., Sharp, Z. D., King, P. L., Wilke, M., Botcharnikov, R. E., Cottrell, E., Zelenki, M., Marty, B., Klimm, K., Rivard, C., Ayalew, D., Ramirez, C., and Kelley, K. A. (2013). Sulfur degassing at Erta Ale (Ethiopia) and Masaya (Nicaragua) volcanoes: Implications for degassing processes and oxygen fugacities of basaltic systems. *Geochem. Geophys. Geosyst.*, 14, 4076–4108.
- Ellis, A. J. (1957). Chemical equilibrium in magmatic gases. *Am. J. Sci.*, 255, 416–431.
- Gennaro, E., Paonita, A., Iacono-Marziano, G., Moussallam, Y., Pichavant, M., Peters, N., and Martel, C.

- (2020). Sulphur behaviour and redox conditions in Etnean magmas during magma differentiation and degassing. *J. Petrol.*, 61, article no. ega095.
- Gerlach, T. M. (1980). Evaluation of volcanic gas analysis from Surtsey volcano, Iceland 1964–1967. *J. Volcanol. Geotherm. Res.*, 8, 191–198.
- Gerlach, T. M. (1993). Oxygen buffering of Kilauea volcanic gases and the oxygen fugacity of Kilauea basalt. *Geochim. Cosmochim. Acta*, 57, 795–814.
- Giggenbach, W. F. (1987). Redox processes governing the chemistry of fumarolic gas discharges from White Island, New Zealand. *Appl. Geochem.*, 2, 143–161.
- Giggenbach, W. F. (1996). Chemical composition of volcanic gases. In Scarpa, R. and Tilling, R. I., editors, *Monitoring and Mitigation of Volcano Hazards*, pages 202–226. Springer, Berlin, Heidelberg.
- Giggenbach, W. F., Tedesco, D., Sulistiyono, Y., Caprai, A., Cioni, R., Favara, R., Fischer, T. P., Hirabayashi, J.-I., Korzhinsky, M., Martini, M., Menyailov, I., and Shinohara, H. (2001). Evaluation of results from the fourth and fifth IAVCEI field workshops on volcanic gases, Vulcano island, Italy and Java, Indonesia. *J. Volcanol. Geotherm. Res.*, 108, 157–172.
- Heald, E. F., Naughton, J. J., and Barnes, I. L. (1963). The chemistry of volcanic gases: 2. Use of equilibrium calculations in the interpretation of volcanic gas samples. *J. Geophys. Res.*, 68, 545–557.
- Ichimura, M., Yokoo, A., Kagiya, T., Yoshikawa, S., and Inoue, H. (2018). Temporal variation in source location of continuous tremors before ash-gas emissions in January 2014 at Aso volcano, Japan. *Earth Planets Space*, 70, article no. 125.
- Kelley, K. A. and Cottrell, E. (2012). The influence of magmatic differentiation on the oxidation state of Fe in a basaltic arc magma. *Earth Planet. Sci. Lett.*, 329–330, 109–121.
- Kress, V. C. and Carmichael, I. S. E. (1991). The compressibility of silicate liquids containing Fe<sub>2</sub>O<sub>3</sub> and the effect of composition, temperature, oxygen fugacity and pressure on their redox states. *Contrib. Mineral. Petrol.*, 108, 82–92.
- Maeno, F., Suzuki, Y., Nakada, S., Koyama, E., Kaneko, T., Fujii, T., Miyamura, J., Onizawa, S., and Nagai, M. (2010). Course and ejecta of the eruption of Asama Volcano on 2 February 2009. *Bull. Volcanol. Soc. Jpn.*, 55, 147–154.
- Martin, R. S., Roberts, T. J., Mather, T. A., and Pyle, D. M. (2009). The implications of H<sub>2</sub>S and H<sub>2</sub> kinetic stability in high-T mixtures of magmatic and atmospheric gases for the production of oxidized trace species (e.g., BrO and NOx). *Chem. Geol.*, 263, 143–150.
- Matjuschkin, V., Blundy, J. D., and Brooker, R. A. (2016). The effect of pressure on sulphur speciation in mid- to deep-crustal arc magmas and implications for the formation of porphyry copper deposits. *Contrib. Mineral. Petrol.*, 171, article no. 66.
- Matsuo, S. (1962). Establishment of chemical equilibrium in the volcanic gas obtained from the lava lake of Kilauea, Hawaii. *Bull. Volcanol.*, 24, 59–71.
- Menyailov, I. A., Nikitina, L. P., Shapar, V. N., and Piliipenko, V. P. (1986). Temperature increase and chemical change of fumarolic gases at Momotombo Volcano, Nicaragua, in 1982–1985: Are these indicators of a possible eruption? *J. Geophys. Res. Solid Earth*, 91, 12199–12214.
- Métrich, N., Berry, A. J., O'Neill, H. St. C., and Susini, J. (2009). The oxidation state of sulfur in synthetic and natural glasses determined by X-ray absorption spectroscopy. *Geochim. Cosmochim. Acta*, 73, 2382–2399.
- Moussallam, Y., Edmonds, M., Scaillet, B., Peters, N., Gennaro, E., Sides, I., and Oppenheimer, C. (2016). The impact of degassing on the oxidation state of basaltic magmas: A case study of Kilauea volcano. *Earth Planet. Sci. Lett.*, 450, 317–325.
- Moussallam, Y., Longpré, M.-A., McCammon, C., Gomez-Ulla, A., Rose-Koga, E. F., Scaillet, B., Peters, N., Gennaro, E., Paris, R., and Oppenheimer, C. (2019a). Mantle plumes are oxidised. *Earth Planet. Sci. Lett.*, 527, article no. 115798.
- Moussallam, Y., Oppenheimer, C., and Scaillet, B. (2019b). On the relationship between oxidation state and temperature of volcanic gas emissions. *Earth Planet. Sci. Lett.*, 520, 260–267.
- Moussallam, Y., Oppenheimer, C., Scaillet, B., Gailard, F., Kyle, P., Peters, N., Hartley, M., Berlo, K., and Donovan, A. (2014). Tracking the changing oxidation state of Erebus magmas, from mantle to surface, driven by magma ascent and degassing. *Earth Planet. Sci. Lett.*, 393, 200–209.
- Nakada, S. and Motomura, Y. (1999). Petrology of the 1991–1995 eruption at Unzen: effusion pulsation and groundmass crystallization. *J. Volcanol. Geotherm. Res.*, 89, 173–196.
- Ohba, T., Hirabayashi, J., Nogami, K., Kusakabe, M., and Yoshida, M. (2008). Magma degassing process

- during the eruption of Mt. Unzen, Japan in 1991 to 1995: Modeling with the chemical composition of volcanic gas. *J. Volcanol. Geotherm. Res.*, 175, 120–132. Scientific drilling at Mount Unzen.
- Ohba, T., Hirabayashi, J., and Yoshida, M. (1994). Equilibrium temperature and redox state of volcanic gas at Unzen volcano, Japan. *J. Volcanol. Geotherm. Res.*, 60, 263–272.
- Ohwada, M., Kazahaya, K., Mori, T., Kazahaya, R., Hirabayashi, J., Miyashita, M., Onizawa, S., and Mori, T. (2013). Sulfur dioxide emissions related to volcanic activity at Asama volcano, Japan. *Bull. Volcanol.*, 75, article no. 775.
- Oppenheimer, C., Scaillet, B., Woods, A., Sutton, A. J., Elias, T., and Moussallam, Y. (2018). Influence of eruptive style on volcanic gas emission chemistry and temperature. *Nat. Geosci.*, 11, 678–681.
- Putirka, K. D. (2008). Thermometers and barometers for volcanic systems. *Rev. Mineral. Geochem.*, 69, 61–120.
- Rose-Koga, E. F., Bouvier, A.-S., Gaetani, G. A., Wallace, P. J., Allison, C. M., Andrys, J. A., de la Torre, C. A., Barth, A., Bodnar, R. J., Gartner, A. J. J. B., Butters, D., Castillejo, A., Chilson-Parks, B., Choudhary, B. R., Cluzel, N., Cole, M., Cottrell, E., Daly, A., Danyushevsky, L. V., DeVitre, M. J., Drignon, M. J., France, L., Gaborieau, M., Garcia, M. O., Gatti, E., Genske, F. S., Hartley, M. E., Hughes, E. C., Iveson, A. A., Johnson, E. R., Jones, M., Kagoshima, T., Katzir, Y., Kawaguchi, M., Kawamoto, T., Kelley, K. A., Koornneef, J. M., Kurz, M. D., Laubier, M., Layne, G. D., Lerner, A., Lin, K.-Y., Liu, P.-P., Lorenzo-Merino, A., Luciani, N., Magalhães, N., Marschall, H. R., Michael, P. J., Monteleone, B. D., Moore, L. R., Moussallam, Y., Muth, M., Myers, M. L., Narváez, D. F., Navon, O., Newcombe, M. E., Nichols, A. R. L., Nielsen, R. L., Pamukcu, A., Plank, T., Rasmussen, D. J., Roberge, J., Schiavi, F., Schwartz, D., Shimizu, K., Shimizu, N., Thomas, J. B., Thompson, G. T., Tucker, J. M., Ustunisik, G., Waelkens, C., Zhang, Y., and Zhou, T. (2021). Silicate melt inclusions in the new millennium: A review of recommended practices for preparation, analysis, and data presentation. *Chem. Geol.*, 570, article no. 120145.
- Saito, G., Ishizuka, O., Ishizuka, Y., Hoshizumi, H., and Miyagi, I. (2018). Petrological characteristics and volatile content of magma of the 1979, 1989, and 2014 eruptions of Nakadake, Aso volcano, Japan. *Earth Planets Space*, 70, article no. 197.
- Sandanbata, O., Obara, K., Maeda, T., Takagi, R., and Satake, K. (2015). Sudden changes in the amplitude-frequency distribution of long-period tremors at Aso volcano, southwest Japan. *Geophys. Res. Lett.*, 42, 10256–10262.
- Schipper, C. I. and Moussallam, Y. (2017). Temporal redox variation in basaltic tephra from Surtsey volcano (Iceland). *Bull. Volcanol.*, 79, article no. 71.
- Shimano, T., Iida, A., Yoshimoto, M., Yasuda, A., and Nakada, S. (2005). Petrological characteristics of the 2004 eruptive deposits of Asama volcano, central Japan. *Bull. Volcanol. Soc. Jpn.*, 50, 315–332.
- Shinohara, H., Giggenbach, W. F., Kazahaya, K., and Hedenquist, J. W. (1993). Geochemistry of volcanic gases and hot springs of Satsuma-Iwojima, Japan: following Matsuo. *Geochem. J.*, 27, 271–285.
- Shinohara, H., Ohminato, T., Takeo, M., Tsuji, H., and Kazahaya, R. (2015). Monitoring of volcanic gas composition at Asama volcano, Japan, during 2004–2014. *J. Volcanol. Geotherm. Res.*, 303, 199–208.
- Shinohara, H., Yokoo, A., and Kazahaya, R. (2018). Variation of volcanic gas composition during the eruptive period in 2014–2015 at Nakadake crater, Aso volcano, Japan. *Earth Planets Space*, 70, article no. 151.
- Sigvaldason, G. E. and Elísson, G. (1968). Collection and analysis of volcanic gases at Surtsey Iceland. *Geochim. Cosmochim. Acta*, 32, 797–805.
- Symonds, R. B., Gerlach, T. M., and Reed, M. H. (2001). Magmatic gas scrubbing: implications for volcano monitoring. *J. Volcanol. Geotherm. Res.*, 108, 303–341.
- Symonds, R. B., Rose, W. I., Bluth, G. J. S., and Gerlach, T. M. (1994). Volcanic-gas studies; methods, results, and applications. *Rev. Mineral. Geochem.*, 30, 1–66.
- Venezky, D. Y. and Rutherford, M. J. (1999). Petrology and Fe–Ti oxide reequilibration of the 1991 Mount Unzen mixed magma. *J. Volcanol. Geotherm. Res.*, 89, 213–230.
- Zelenski, M. E., Fischer, T. P., de Moor, J. M., Marty, B., Zimmermann, L., Ayalew, D., Nekrasov, A. N., and Karandashev, V. K. (2013). Trace elements in the gas emissions from the Erta Ale volcano, Afar, Ethiopia. *Chem. Geol.*, 357, 95–116.







Research article

## Magma degassing and its impact on the Earth's atmosphere: from magma oceans to lava lakes

# Hydrogen and hydrogen sulphide in volcanic gases: abundance, processes, and atmospheric fluxes

Alessandro Aiuppa <sup>\*,a</sup> and Yves Moussallam <sup>b</sup>

<sup>a</sup> Dipartimento di Scienze della Terra e del Mare, Università di Palermo, Palermo, Italy

<sup>b</sup> Lamont-Doherty Earth Observatory, Columbia University, New York, USA

E-mails: [alessandro.aiuppa@unipa.it](mailto:alessandro.aiuppa@unipa.it) (A. Aiuppa),  
[yves.moussallam@ldeo.columbia.edu](mailto:yves.moussallam@ldeo.columbia.edu) (Y. Moussallam)

**Abstract.** Hydrogen (H<sub>2</sub>) and hydrogen sulphide (H<sub>2</sub>S) are typically present at only minor to trace levels in volcanic gas emissions, and yet they occupy a key role in volcanic degassing research in view of the control they exert on volcanic gas reducing capacity (e.g., their ability to remove atmospheric O<sub>2</sub>). In combination with other major compounds, H<sub>2</sub> and H<sub>2</sub>S are also key to extracting information on source magma conditions (temperature and redox) from observed magmatic gas compositions. Here, we use a catalogue, compiled by extracting from the geological literature a selection of representative analyses of magmatic to mixed (magmatic–hydrothermal) gases, to review the processes that control H<sub>2</sub> and H<sub>2</sub>S abundance in volcanic gases. We show that H<sub>2</sub> concentrations and H<sub>2</sub>/H<sub>2</sub>O ratios in volcanic gases both exhibit strong positive temperature dependences, while H<sub>2</sub>S concentrations and H<sub>2</sub>S/SO<sub>2</sub> ratios are temperature insensitive overall. The high H<sub>2</sub> concentrations (and low H<sub>2</sub>S/SO<sub>2</sub> compositions, of ~0.1 on average) in high-temperature (>1000 °C) magmatic gases are overall consistent with those predicted thermodynamically assuming external redox buffering operated by the co-existing silicate melt, at oxygen fugacities ranging from ΔFMQ –1 to 0 (non-arc volcanoes) to ΔFMQ 0 to +2 (arc volcanoes) (where ΔFMQ is oxygen fugacity expressed as a log unit difference relative to the Fayalite–Magnetite–Quartz oxygen fugacity buffer). Lower temperature (<1000 °C) volcanic gases exhibit more oxidizing redox conditions (typically above the Nickel–Nickel Oxide buffer) that are caused by a combination of (i) gas re-equilibration during closed-system (gas-phase only) adiabatic cooling in a gas-buffered system, and (ii) heterogeneous (gas–mineral) reactions. We show, in particular, that gas-phase equilibrium in the H<sub>2</sub>–H<sub>2</sub>S–H<sub>2</sub>O–SO<sub>2</sub> system is overall maintained upon cooling down to ~600 °C, while quenching of higher temperature equilibria (at which Apparent Equilibrium Temperatures, AETs, largely exceed measured discharge temperatures) is more frequently observed for higher extents of cooling (e.g., at  $T < 600$  °C). In such lower temperature volcanic environments, gas–mineral reactions also become increasingly important, scavenging magmatic SO<sub>2</sub> and converting it into H<sub>2</sub>S and hydrothermal minerals (sulphates and sulphides). These heterogeneous reactions, when occurring, can also control the temperature dependence of the volcanic gas H<sub>2</sub>/H<sub>2</sub>O ratios. Finally, by using our volcanic gas dataset in tandem with recently published global volcanic SO<sub>2</sub> and CO<sub>2</sub> budgets,

---

\* Corresponding author

we provide refined estimates for total H<sub>2</sub>S (median, 1.4 Tg/yr; range, 0.9–8.8 Tg/yr) and H<sub>2</sub> (median, 0.23 Tg/yr; range, 0.06–1 Tg/yr) fluxes from global subaerial volcanism.

**Keywords.** Hydrogen, Hydrogen sulphide, Volcanic gases, Volcanic gas redox, Atmospheric fluxes.

*Manuscript received 15 March 2023, revised 4 September 2023, accepted 6 September 2023.*

## 1. Introduction

At the relatively oxidised redox conditions of present day Earth's upper mantle [e.g., Frost and McCammon, 2008, Stagno et al., 2013], the magmatic gas phase delivered to the atmosphere by shallow degassing, mantle-sourced magmas is dominated by oxidised molecular combinations of the elements H, C, O and S, e.g., by water (H<sub>2</sub>O) carbon dioxide (CO<sub>2</sub>) and sulphur dioxide (SO<sub>2</sub>) [e.g., Gerlach and Nordlie, 1975, Symonds et al., 1994, Giggenbach, 1996, Fischer and Chiodini, 2015]. However, volcanoes also release a variety of reduced gas species such as molecular hydrogen (H<sub>2</sub>) and hydrogen sulphide (H<sub>2</sub>S) that, while making up a relatively small fraction of the magmatic gas phase, convey information on a variety of magma-related topics and processes [e.g., Moussallam et al., 2019b, Moretti and Stefánsson, 2020]. For example, studying the release of H<sub>2</sub>, H<sub>2</sub>S and other reduced gas species (e.g., carbon monoxide, CO) from modern subaerial volcanoes helps setting constraints on the composition of the early atmosphere in the Hadean and the Archean [e.g., Kasting et al., 1993, Gaillard et al., 2015], and to predict the temporal evolution and progressive oxygenation of the atmosphere through geological time [e.g., Holland, 2002, Gaillard et al., 2011, Gaillard and Scaillet, 2014]. Measuring H<sub>2</sub> and H<sub>2</sub>S in combination with their oxidised complements H<sub>2</sub>O and SO<sub>2</sub> brings information on the redox conditions of magmatic gases [e.g., Ellis, 1957, Matsuo, 1962, Gerlach, 1979, 1982, 1993a,b, Shinohara et al., 1993, Ohba et al., 1994, Symonds et al., 1994, Burgisser and Scaillet, 2007, Oppenheimer et al., 2018, Moussallam et al., 2019b, 2022], and can potentially allow constraining oxygen fugacity of the source magmas. H<sub>2</sub> and H<sub>2</sub>S in volcanic gases can also effectively contribute to volcano monitoring [e.g., Kern et al., 2022]. For example, H<sub>2</sub>S is a key component of the hydrothermal gases released by quiescent, closed-conduit volcanoes [e.g., Giggenbach, 1980], so that monitoring the H<sub>2</sub>S/SO<sub>2</sub> ratio is critical to detecting (and interpreting) the magmatic unrest that proceeds volcanic activity resumption [e.g., Surono et al., 2012,

Moussallam et al., 2014b, Stix and de Moor, 2018, de Moor et al., 2019], and to distinguish internally triggered (volcano-related) gas changes from those caused by external factors (e.g., rainfall and/or water level changes) [Moretti et al., 2020, Moune et al., 2022]. A model for estimating magmatic variables (temperature and redox) from the combined analysis of H<sub>2</sub>S/SO<sub>2</sub> and H<sub>2</sub>/H<sub>2</sub>O ratios in volcanic plumes has recently been proposed that promises to become a useful volcano monitoring tool [Moussallam et al., 2022]. Volcano-released H<sub>2</sub> and H<sub>2</sub>S are dispersed into the atmosphere through volcanic plumes, where concentrations at ppm levels are typically observed, well in excess of those typical of ambient air [of respectively ~0.5 ppm and ~0.1–0.3 ppb; Seinfeld and Pandis, 2016]. Such in-plume H<sub>2</sub> and H<sub>2</sub>S measurements [e.g., Aiuppa et al., 2005, 2011] are useful to interpreting reaction mechanisms and rates, and ultimately lifetime of reduced compounds, during oxidative atmospheric processing, both near-vent [e.g., Martin et al., 2006, Roberts et al., 2019] and in the colder, more distal plumes [e.g., Aiuppa et al., 2007]. Although observations indicate H<sub>2</sub> and H<sub>2</sub>S are conserved during atmospheric dispersion over short timescales (seconds to days) [e.g., Aiuppa et al., 2007, 2011], these species are ultimately oxidised directly (by molecular oxygen, O<sub>2</sub>) or indirectly (via O<sub>2</sub>-derived radicals, such as hydroxyl radicals) during longer atmospheric transit, thus controlling the reducing power (e.g., the ability to act as atmospheric O<sub>2</sub> sinks) of volcanic gases [e.g., Stolper et al., 2021].

Despite their importance in such a variety of subjects, and notwithstanding that excellent reviews are available on magmatic and hydrothermal gases in general [e.g., Giggenbach, 1980, 1996, Symonds et al., 1994, Chiodini and Marini, 1998, Fischer and Chiodini, 2015, Henley and Fischer, 2021], no specific study has so far been devoted to reviewing abundance and source mechanisms of H<sub>2</sub> and H<sub>2</sub>S in volcanic gases. Also, estimates of global H<sub>2</sub> and H<sub>2</sub>S fluxes from subaerial volcanism remain subject to large uncertainties, owing to the sparse and limited dataset existing. For example, although natural (geogenic) H<sub>2</sub> emissions have received increasing

attention recently [e.g., Zgonnik, 2020], with Earth degassing being thought to sustain a cumulative global  $H_2$  flux of 6 [Gilat and Vol, 2012] to 23 [Zgonnik, 2020] Tg/yr, there are only two studies in the literature that specifically address the quantification of volcanic  $H_2$  emissions from two persistent active volcanoes [Etna in Sicily,  $\sim 0.00065$  Tg/yr; Aiuppa et al., 2011; and Erebus in Antarctica,  $\sim 0.001$  Tg/yr; Moussallam et al., 2012]. As such, current inventories of volcanic  $H_2$  fluxes to the atmosphere [0.2 to 0.7 Tg/yr; Warneck, 1988, Canfield et al., 2006, Stolper et al., 2021] are subject to large uncertainties. Likewise, the volcanogenic contribution to the global natural  $H_2S$  flux ( $\sim 7.7$  Tg/yr) is similarly poorly understood, with most estimates converging at  $\sim 1$  Tg/yr [see review by Watts, 2000] but with total range being as large as 1 to 37 Tg/yr [Halmer et al., 2002].

Here, we review our current understanding of the processes that govern  $H_2$  and  $H_2S$  abundance in volcanic gases. To this aim, we present an updated volcanic gas composition catalogue that we have put together from available literature information. We also use this catalogue, in combination with recently improved global volcanic  $SO_2$  and  $CO_2$  fluxes [Carn et al., 2017, Aiuppa et al., 2019, Fischer et al., 2019], to present an improved quantification of global volcanic  $H_2$  and  $H_2S$  fluxes.

## 2. Dataset

We compiled a dataset of 747 gas analyses by complementing recent [Aiuppa, 2015, Aiuppa et al., 2017, Moussallam et al., 2019b, 2022] and older [Symonds et al., 1994, Giggenbach, 1997] volcanic gas catalogues with newly published gas results. This dataset is not exhaustive, e.g., it is not meant to cover the entire mass of information present in the geological literature. Yet, we are confident our dataset is well representative of the compositional range of volcanic gases globally (see below).

The full dataset is available as Supplementary Tables 1 and 2. The dataset includes data for both high temperature ( $T > 600$  °C; Supplementary Table 1) magmatic gases and for lower temperature ( $T \leq 600$  °C; Supplementary Table 2) mixed (magmatic–hydrothermal) fluids. The 600 °C threshold, although somewhat arbitrary, is justified by the statistical distribution of the global volcanic arc gas population [Aiuppa et al., 2017], and is consistent with

the threshold used in similar recent studies [Moussallam et al., 2019b, 2022]. Some hydrothermal (temperature close to boiling) gas samples are also used but are limited to those volcanoes that have recently erupted and/or that have detectable  $SO_2$ —this latter gas is typically absent in hydrothermal fluids “strictu sensu”, that are covered by other reviews [e.g., Giggenbach, 1980, 1987, Chiodini and Marini, 1998, Fischer and Chiodini, 2015, Stix and de Moor, 2018]. The dataset is further categorised depending on tectonic setting in arc and non-arc volcanic gases, the latter including gases released by intraplate and continental rift volcanism [Aiuppa et al., 2021]. The Etna magmatic gases are plotted separately in view of the relatively enigmatic nature of volcanism at this specific locality.

The dataset combines compositional data for both fumaroles (Sample type “F” in Supplementary Tables 1 and 2) and for atmospheric gas plumes (Sample type “PL” in Supplementary Tables 1 and 2). We refer to the original studies (data sources in Supplementary Tables 1 and 2) for details on sampling and analytical procedures. Broadly speaking however, fumarole data (F) have been obtained by direct sampling (Sample Methodology “DS” in Supplementary Tables 1 and 2) [Symonds et al., 1994], in which fumarolic effluents are captured in-pre-evacuated gas flasks partially filled with a reactive solution [a NaOH solution in most applications; Giggenbach, 1996]. Incondensable gases (like  $H_2$ ) are concentrated in the head space (later analysed in the lab. via Gas Chromatography), while condensable gases (such as  $H_2S$ ) trapped by the solution are analysed by wet chemistry methods (typically by ion chromatography). Uncertainty in DS-derived gas concentrations is typically low ( $<5\%$  in most studies). Plume results (PL) are based on in-situ, near real-time gas concentration measurements with the Multi-GAS (Sample Methodology “MG” in Supplementary Tables 1 and 2), a widely used multi-sensor unit that analyses  $H_2$  and  $H_2S$  (among other species) with specific electrochemical sensors [Aiuppa et al., 2005, Shinohara, 2005]. In such a case, the Multi-GAS measured in-plume concentrations have been converted in air-free gas concentrations listed in Supplementary Tables 1 and 2. Typical associated uncertainty is  $\leq 15\text{--}20\%$ .

It is important to remind that, where available, magmatic gas compositions are reported in the form

of “restored” magmatic gas compositions at equilibrium temperature (identified by Sample type “F, R” in Supplementary Table 1). These restored gas compositions have been extracted mostly from Symonds et al. [1994], and have been obtained by the authors by applying (to measured fumarolic gas compositions) the procedure introduced by Gerlach [1993a]. This numerical procedure (i) identifies the causes of disequilibrium in volcanic gases (often due to sampling/conservation artefacts; e.g., air addition and oxidation), and (ii) iteratively removes the cause(s) of disequilibrium until an restored equilibrium gas (at a given equilibrium temperature) is obtained [Gerlach, 1993a, Symonds et al., 1994].

Our dataset, illustrated in a  $H_2O/10$ – $CO_2$ – $5 \cdot S_T$  space (where  $S_T$  is total sulphur, or  $SO_2 + H_2S$ ) (Figure 1), demonstrates the large heterogeneity of volcanic gas compositions found in previous inventories [e.g., Symonds et al., 1994, Aiuppa, 2015], and represents well the well-established [e.g., Symonds et al., 1994, Gerlach, 1982] chemical diversity between arc and within-plate/rift magmatic gases, with the former being typically more hydrous [e.g., Fischer, 2008, Taran and Zelenski, 2015] and the latter extremely variable in terms of their  $CO_2/S_T$  signatures [e.g., Aiuppa et al., 2021]. The two magmatic gas populations exhibit some overlap, as previously found [e.g., Aiuppa, 2015]. The lower temperature ( $T \leq 600$  °C) mixed gases are even more compositionally heterogeneous (Figure 1), and while many gas samples overlap with the magmatic gas range, many others plot in the  $CO_2$ -rich, S-poor compositional domain (top left portion of Figure 1), indicating some extent of sulphur loss [scrubbing; Symonds et al., 2001] during gas–water–rock hydrothermal interactions in the subsurface [e.g., Aiuppa et al., 2017].

### 3. Results

#### 3.1. Hydrogen and hydrogen sulphide abundances in volcanic gases

$H_2$  and  $H_2S$  are usually minor (<1 mol%) to trace (<0.1 mol%) components of volcanic gases [e.g., Giggenbach, 1996], although  $H_2$  concentrations exceeding 10 mol% have occasionally also been reported [see review of Zgonnik, 2020] and  $H_2S$  becomes increasingly important (e.g., a major species, >1 mol%) in low temperature hydrothermal steam samples [e.g., Giggenbach, 1980, 1997].

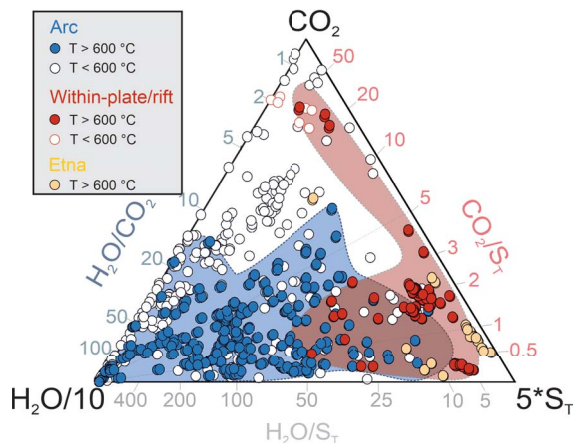


**Figure 1.** Triangular plots illustrating the compositional variability in the gas catalogue used (data from Supplementary Tables 1 and 2).

In our volcanic gas catalogue,  $H_2$  and  $H_2S$  concentrations span several orders of magnitude, from ultra-trace (< $10^{-6}$  mol%) to major (>1 mol%) levels (Supplementary Tables 1 and 2). In Figures 2a and b, the whole  $H_2$  and  $H_2S$  concentration dataset (in mol%) is illustrated as a function of measured gas outlet temperature.

Figure 2a shows that volcanic gas  $H_2$  concentrations exhibit a marked temperature dependence, particularly at  $T > 600$  °C.  $H_2$  concentrations are the highest (0.49–3.1% levels) in the hot ( $T > 1000$  °C) magmatic gases [Gerlach, 1979, 1980, 1982, 1993a,b, Symonds et al., 1994] from within-plate (e.g., Kilauea) and continental rift (e.g., Nyiragongo, Erta Ale) volcanoes. In arc magmatic gases,  $H_2$  concentrations decrease with decreasing temperature, from 0.1–1.7 mol% at 800–1100 °C to 0.002–0.38 mol% at ~600 °C. Etna’s magmatic gases plot at the boundary between arc and non-arc gases ( $H_2$  range: 0.14–2.1 mol%). The temperature dependence is more scattered in mixed (magmatic–hydrothermal) gases, in which  $H_2$  varies from as low as  $4 \times 10^{-6}$  mol% to as high as 0.867 mol%. Close-to-boiling fumaroles ( $T < 100$  °C) are especially diverse in their  $H_2$  contents that span more than 5 orders of magnitude.

$H_2S$  concentrations show no obvious temperature dependence in the global volcanic gas catalogue (Figure 2b). The  $H_2S$ -richest samples are again found in the “restored” magmatic gas analyses from within-plate and continental rift volcanoes ( $H_2S$  range: 0.04–3.2 mol%; mean  $0.9 \pm 0.55$  mol%). The range of  $H_2S$

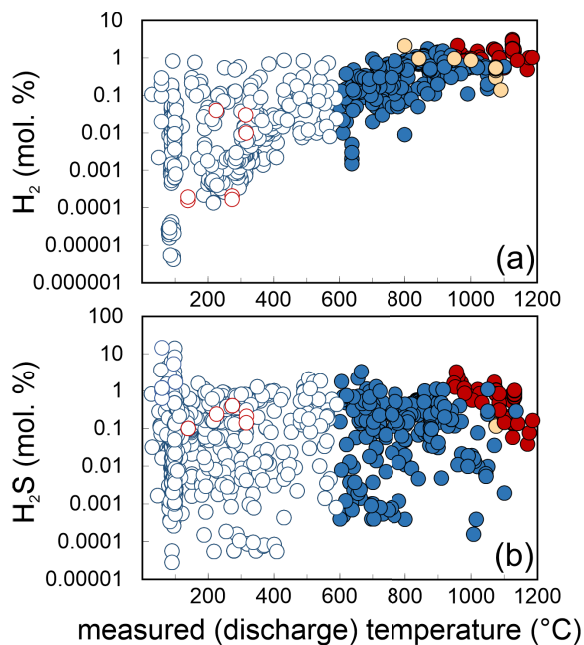


**Figure 2.** Scatter plots illustrating the dependence of (a)  $\text{H}_2$  and (b)  $\text{H}_2\text{S}$  concentrations on measured discharge temperature (data from Supplementary Tables 1 and 2). Symbols as in Figure 1. In this and following figures, error bars are not shown as smaller than the data symbols.

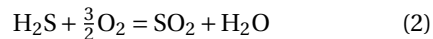
concentrations in arc magmatic gases is vast, from 0.00016 to 3.3 mol%. The mean arc gas  $\text{H}_2\text{S}$  concentration ( $0.25 \pm 0.55$  mol%) is lower than for non-arc volcanic gases ( $0.9 \pm 0.55$  mol%), but given the large spread of values the two populations are essentially overlapping. Colder ( $T \leq 600$  °C) magmatic-hydrothermal gases exhibit an even larger range of values, including the lowest (0.000028 mol%) and highest (14 mol%) values of the entire dataset. As for arc magmatic gases, no obvious pattern with temperature is observed (Figure 2a).

## 4. Discussion

### 4.1. Ratios between redox couples

A standard practise used when interpreting volcanic gas  $\text{H}_2$  and  $\text{H}_2\text{S}$  concentrations is to normalise them to their oxidised counterparts  $\text{H}_2\text{O}$  and  $\text{SO}_2$  [Gerlach, 1980, Giggenbach, 1996, 1987]. This practise developed on since early demonstrations [Ellis, 1957,

Matsuo, 1962] that high temperature volcanic gases approach a state of thermodynamic equilibrium, in which ratios between redox couples are controlled by equilibria:



In a set of seminal articles, Gerlach and co-workers [Gerlach, 1979, 1980, 1993a,b, Symonds et al., 1994] confirmed that the assumption of “full” equilibrium among all the different species in a volcanic gas mixture holds at magmatic temperatures. A useful concept introduced to test this full equilibrium state hypothesis was that of the so-called Correspondence Temperature (CT), the temperature at which the measured (in a specific volcanic gas sample) and equilibrium concentrations of a gas species match one another. As the CTs of the different gas species were found to converge to within a very narrow range in many high temperature gas samples [Gerlach, 1979, 1980, 1993a,b], the full equilibrium hypothesis could be proved.

However, as demonstrated in later work by Giggenbach [1987, 1996], the full equilibrium assumption is unlikely to hold in lower temperature gas samples, where different extents of re-equilibrations of the different redox couples (e.g., reactions (1) and (2)), as well as admixing with external (meteoric, atmospheric) fluids [Taran and Zelenski, 2015] and reaction with wall-rocks [Henley and Seward, 2018, Henley and Fischer, 2021], become likely eventualities. In such conditions, a conservative approach is to deal with specific redox reactions individually, e.g., to use plots that compare, for each specific redox couple, the analytically determined and equilibrium ratios. This approach, initially elaborated by Giggenbach [1987, 1996] and Chiodini et al. [1993], is followed below, where we update their results and corroborate their conclusions using the more complete, today available gas catalogue (Supplementary Tables 1 and 2).

At discharge conditions ( $P = 1$  bar), and at equilibrium, reactions (1) and (2) imply that ratios between redox couples will exhibit the following dependences on redox (as expressed by oxygen fugacity,  $f\text{O}_2$ ) and

temperature (in K):

$$\log \frac{H_2}{H_2O} = -\frac{12,707}{T} + 2.548 - \frac{1}{2} \log fO_2 \quad (3)$$

$$\log \frac{SO_2}{H_2S} = \frac{27,377}{T} - 3.986 + \frac{3}{2} \log fO_2 - \log X_{H_2O} \quad (4)$$

These equations are obtained by re-arranging the equilibrium constants  $K_1$  and  $K_2$  of (1) and (2) [we use thermodynamic data from Chase and National Institute of Standards and Technology (U.S.), 1998] and assuming ideal gas behaviour (fugacity coefficients  $\gamma = 1$ ).

The presence of redox sensitive elements in either the silicate melt/rock matrix (where iron is typically available in both +2 and +3 valence states) or in the gas phase (where sulphur is present in sufficient amounts in both -2 and +4 valence states) has long been proposed [e.g., Giggenbach, 1987, Gerlach, 1993a] to act as a buffer for oxygen fugacity in volcanic gases [see Moretti and Stefánsson, 2020, Moretti, 2021, Moretti and Neuville, 2021, for examples of recent reviews]. Gerlach [1993a,b] proposed that gas speciation in high temperature (>900 °C) magmatic gases is buffered by equilibrium redox exchange between gas and coexisting silicate melt. The same buffers can also operate at sub-solidus conditions, e.g., if gas reacts and equilibrates with the host rock matrix in which iron is present in minerals with two distinct oxidation states [e.g., Giggenbach, 1987]. It was however found that, in such lower temperature conditions, the buffering role of sulphur in the gas phase (where  $H_2S$  and  $SO_2$  are simultaneously present) becomes increasingly effective [e.g., Giggenbach, 1987, 1996], although the competing roles of homogeneous (gas-only) and heterogeneous (gas-mineral) reactions in controlling the volcanic gas redox budget remained debated [e.g., Henley and Fischer, 2021] (see below).

Irrespective of the buffering medium (either melt, rock, or gas),  $fO_2$  in (3) and (4) can conveniently be replaced by the temperature dependences imposed by the redox buffers [e.g., Eugster, 1977, Frost, 1991, see recent reviews by Cicconi et al. [2020], Moretti and Neuville [2021]]. The predicted (3), mineral-buffered or gas- $(H_2S/SO_2)$  buffered,  $H_2/H_2O$  ratios are graphically illustrated in Figure 3a. The same mineral buffered  $SO_2/H_2S$  ratios are illustrated in Figure 3b. These model trends implicate that, in mineral-buffered conditions (e.g., when gas redox is buffered by heterogeneous redox budget exchanges

with either the melt or the host rocks),  $H_2$  is expected to become increasingly abundant (relative to  $H_2O$ ), and  $H_2S$  increasingly depleted (relative to  $SO_2$ ), with increasing temperature (Figure 3). At fixed temperature,  $H_2/H_2O$  ratios are expected to decrease (and  $SO_2/H_2S$  to increase) as redox evolves from more reducing (e.g., redox buffered at the Fayalite–Magnetite–Quartz (FMQ) mineral buffer) to more oxidised (as expressed by the hematite–magnetite (HM) mineral buffer) conditions. Results of a comparison between modelled and measured (volcanic gases) ratios are summarised below (Figure 3).

#### 4.1.1. High-temperature magmatic gases

The measured volcanic gas  $H_2/H_2O$  ratios, as derived from the analytically determined gas concentrations, are illustrated in Figure 3a (and listed Supplementary Tables 1 and 2). Comparison with modelled compositions (see above) shows that the hot ( $T > 900$  °C) non-arc magmatic gases [Gerlach, 1980, 1993b, Symonds et al., 1994] have “restored” gas compositions that convert into  $H_2/H_2O$  (and  $SO_2/H_2S$  ratios; see Figure 3b) overlapping those predicted at equilibrium (3) and (4) in a melt-buffered gas system at ~FMQ, see Figures 3 and 4. As previously found [Gerlach, 1980, 1993a,b] therefore, the  $H_2$  and  $H_2S$  contents of such gases appear to be controlled by heterogeneous (melt–gas) redox exchanges. High temperature ( $T > 900$  °C) arc magmatic gases likewise approach the melt-buffered model lines, but the majority of them plot at lower  $H_2/H_2O$  (and higher  $SO_2/H_2S$ ) ratios relative to non-arc magmatic gases, close to the NNO (Nickel–Nickel-Oxide) mineral buffer model line (Figure 3). This apparent more oxidised (lower  $H_2/H_2O$  ratios) signature of arc gases is also well represented in Figure 4, and we will return to this point in later sections (cf. Section 4.3).

#### 4.1.2. Mixed magmatic–hydrothermal gases

Lower temperature magmatic gases (600 °C <  $T$  < 900 °C) and mixed (magmatic–hydrothermal) gases ( $T < 600$  °C) overall identify a compositional tendency of decreasing  $H_2/H_2O$  ratios with decreasing temperature (Figure 3a). This trend (qualitatively identified by the grey shaded region of Figure 3a) is manifestly steeper than the temperature dependences imposed by any of the mineral  $fO_2$  buffers (solid lines). Giggenbach [1987, 1996] took this as evidence of a marginal (if any) control exercised by

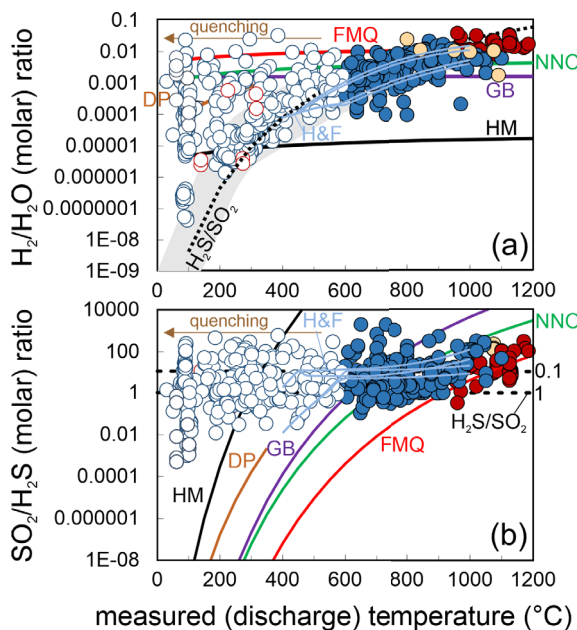
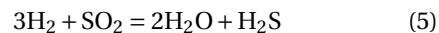


**Figure 3.** Temperature dependence of (a)  $\text{H}_2/\text{H}_2\text{O}$  and (b)  $\text{SO}_2/\text{H}_2\text{S}$  molar ratios in our volcanic gas catalogue (data from Supplementary Tables 1 and 2). Symbols as in Figure 1. The thick coloured lines are the predicted temperature dependences of the ratios imposed (at 1 bar) by the most common mineral and gas buffers. These are obtained by using Equations (3) and (4) and oxygen fugacity buffered by either the melt/rock matrix or sulphur species in the gas phase. The mineral buffer [see Frost, 1991, for the relevant  $f\text{O}_2$ - $T$  relationships] curves illustrated are: HM: Hematite–Magnetite; NNO: Nickel–Nickel Oxide; FMQ: Fayalite–Magnetite–Quartz; GB: FeO–FeO<sub>1.5</sub> buffer [Giggenbach, 1987]. The dashed line in (a) labelled  $\text{H}_2\text{S}/\text{SO}_2$  corresponds to the sulphur gas buffer of Giggenbach [1987], and is obtained by solving Equation (6) (at 1 bar) assuming equimolar amounts of  $\text{H}_2\text{S}$  and  $\text{SO}_2$  ( $\text{H}_2\text{S}/\text{SO}_2 = 1$ ) (a similar line at fixed  $\text{H}_2\text{S}/\text{SO}_2$  of 0.1 is also shown in panel (b)). The DP line is for gas ratios predicted using the empirically derived  $f\text{O}_2$  versus temperature dependence typical of hydrothermal systems [e.g., D’Amore and Panichi, 1980]. Thin light blue curves labelled H&F are the gas ratios predicted by the gas–mineral reactions of Henley and Fischer [2021] (the model runs illustrated in their original Figure 5 are shown).

**Figure 3. (cont.)** The majority of the mixed (magmatic–hydrothermal;  $T < 600$  °C) gases plot in panel (a) along a compositional array (grey dashed area) that overlaps with both (i) the  $\text{H}_2\text{S}/\text{SO}_2$  buffer lines, and (ii) the heterogeneous (gas–mineral) equilibria of Henley and Fischer [2021]. Many gas samples have higher  $\text{H}_2/\text{H}_2\text{O}$  ratio compositions than predicted by either homogeneous [Giggenbach, 1987] or heterogeneous [Henley and Fischer, 2021] reactions, likely indication preservation (quenching) of higher- $T$  equilibria. High- $T$  magmatic gases plot in between the NNO and FMQ mineral buffers, suggesting buffering from source silicate melt. See text for discussion.

redox budget exchanges between gases and silicate melts (in the supra-solidus regions) and/or with wall rocks (in the sub-solidus region). Rather, Giggenbach [1987, 1996] proposed that the  $\text{H}_2/\text{H}_2\text{O}$  ratios versus temperature dependence exhibited by volcanic gas samples (Figure 3a) can satisfactorily be explained by homogeneous (gas-phase only) redox reactions taking place during gas expansion and cooling, according to reaction:



from which:

$$\text{Log} \frac{\text{H}_2}{\text{H}_2\text{O}} = -\frac{1}{3} \text{Log} K_5 + \frac{1}{3} \text{Log} \frac{\text{H}_2\text{S}}{\text{SO}_2} - \frac{1}{3} f_{\text{H}_2\text{O}} \quad (6)$$

The basic principle behind Equations (5)–(6) is that the gas  $\text{H}_2/\text{H}_2\text{O}$  ratio will re-adjust (re-equilibrate) as temperature decreases (e.g., during gas ascent and adiabatic expansion from source (magma) to atmospheric discharge) in a gas-buffered regime in which  $\text{H}_2\text{S}$ – $\text{SO}_2$  coexistence will control the gas redox budget. Equation (6), at 1 bar and for equimolar amounts of  $\text{H}_2\text{S}$  and  $\text{SO}_2$  ( $\text{H}_2\text{S}/\text{SO}_2 = 1$ ), resolves into what Giggenbach [1987, 1996] referred as the  $\text{H}_2\text{S}/\text{SO}_2$  gas buffer (Figure 3).

The resulting model-derived (Equation (6)) temperature dependence of the  $\text{H}_2/\text{H}_2\text{O}$  ratios (dashed line labelled  $\text{H}_2\text{S}/\text{SO}_2$ ; Figure 3a) nicely reproduces the volcanic gas compositional array (grey band). Notably, this ability of coexisting  $\text{H}_2\text{S}$  and  $\text{SO}_2$  to buffer gas phase redox is entirely consistent with the temperature invariant, analytically determined

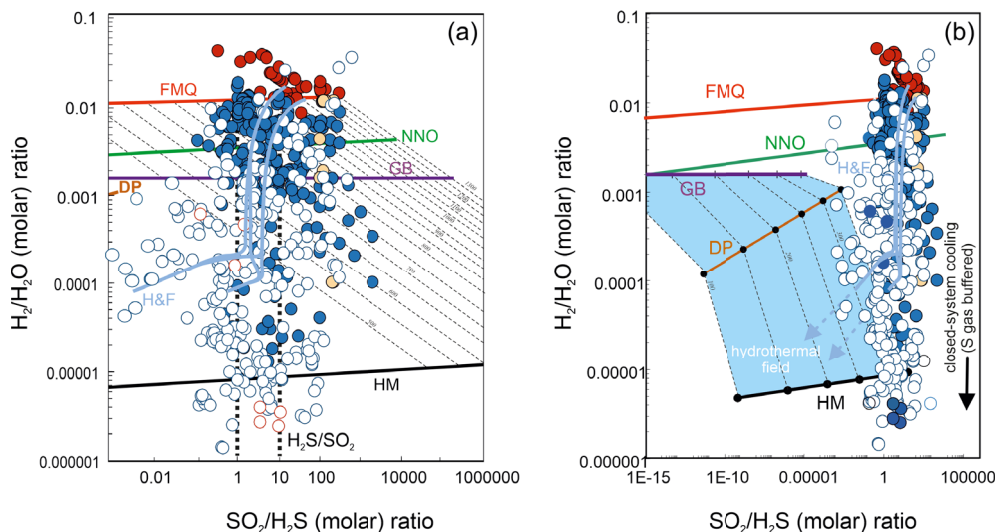


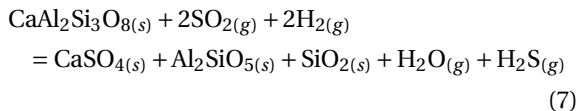
**Figure 4.** (a) Scatter plot of  $\text{SO}_2/\text{H}_2\text{S}$  versus  $\text{H}_2/\text{H}_2\text{O}$  molar ratios in our volcanic gas catalogue (data from Supplementary Tables 1 and 2). Symbols as in Figure 1. The thick coloured lines are the predicted gas molar ratios (from Equations (3) and (4)) for  $f\text{O}_2$ s calculated using the temperature dependences imposed by the FMQ, NNO, GB and HM mineral buffers (calculations are run over a range of temperatures, as expressed by the isotherms: dashed lines, in  $^\circ\text{C}$ ). The DP line is derived by using (for  $f\text{O}_2$  in Equations (3) and (4)) the empirical  $f\text{O}_2$  versus  $T$  dependence in hydrothermal systems [D’Amore and Panichi, 1980]; thin light blue curves labelled H&F are the gas ratios predicted by the gas–mineral reactions of Henley and Fischer [2021] (the model runs illustrated in their original Figure 5 are shown). (b) An expanded version of (a) illustrating the nominally  $\text{SO}_2$ -free field of hydrothermal steam samples (in the 100–350  $^\circ\text{C}$  temperature range). The magmatic to mixed (magmatic–hydrothermal) samples in our catalogue, having detectable  $\text{SO}_2$ , plot to the right of the hydrothermal field. Their  $\text{SO}_2/\text{H}_2\text{S}$  versus  $\text{H}_2/\text{H}_2\text{O}$  population is well reproduced by both homogenous [gas-phase only; dashed black lines; Giggenbach, 1987] or heterogeneous [Henley and Fischer, 2021] reactions. However, the H&F models predict progressively decreasing  $\text{SO}_2/\text{H}_2\text{S}$  ratios at increasing mineral–gas reactions (and with decreasing temperatures), while the majority of the gas samples define a vertical array that is more consistent with gas oxidations (e.g., decreasing  $\text{H}_2/\text{H}_2\text{O}$  ratios) during closed-system gas cooling in a S gas-buffered regime [dashed vertical back line, the  $\text{H}_2\text{S}/\text{SO}_2$  gas buffer of Giggenbach, 1987].

$\text{SO}_2/\text{H}_2\text{S}$  ratios (Figure 3b). Giggenbach [1987] concluded that the conversion of  $\text{SO}_2$  to  $\text{H}_2\text{S}$  during gas cooling, as implicated by the mineral buffer curves (Figure 3b), is inhibited by the rapid transit of magma sourced gases through host rocks, preventing gas–rock reactions to become effective (to achieve equilibrium). The temperature-invariant, measured  $\text{SO}_2/\text{H}_2\text{S}$  gas compositions in our dataset (Figure 3b) indeed suggest that sulphur speciation is little affected by gas–mineral reactions during cooling, although data align along a nearly horizontal trend at  $\text{SO}_2/\text{H}_2\text{S}$  of  $\sim 10$  ( $\text{H}_2\text{S}/\text{SO}_2$  of  $\sim 0.1$ ) rather than  $\sim 1$  [as implicated in the original  $\text{H}_2\text{S}/\text{SO}_2$  gas buffer of Giggenbach, 1987, 1996] (Figures 3b, 4).

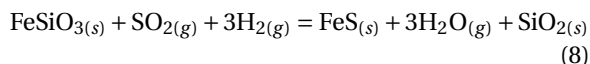
An alternative view to that of Giggenbach [1987] has recently been proposed by Henley and Fischer [2021]. The authors, based on field evidence arising from rock alteration assemblages found at extinct (now eroded) andesitic volcanoes [Henley and Berger, 2011, Henley et al., 2015], proposed that gas  $\text{H}_2/\text{H}_2\text{O}$  and  $\text{SO}_2/\text{H}_2\text{S}$  ratios are controlled by heterogeneous (mineral–gas) rather than homogenous (gas-only) reactions. The authors presented a comprehensive multi-component thermochemical modelling of gas–solid equilibria of magmatic  $\text{SO}_2$  reaction with primary rock-forming minerals. The key re-



action invoked by the authors is:



in which magmatic  $\text{SO}_2$  disproportionate into both oxidised (anhydrite) and reduced ( $\text{H}_2\text{S}$ ) sulphur forms while plagioclase is converted into a secondary Al-bearing hydrothermal mineral. Similar reactions can be written to account for the reaction of magmatic  $\text{SO}_2$  with ferromagnesian minerals, such as ferrosilite (Fe-rich pyroxene) [Henley and Fischer, 2021]:



This reaction nicely accounts for the pervasive precipitation of iron sulphides (e.g., pyrite and pyrrhotite) in hydrothermal systems.

The equilibrium constant of reaction (7):

$$K_7 = \frac{\text{H}_2\text{S}}{\text{SO}_2} \cdot \frac{1}{\text{SO}_2} \cdot \frac{1}{\text{H}_2\text{O}} \cdot \frac{1}{\left(\frac{\text{H}_2}{\text{H}_2\text{O}}\right)^2} \quad (9)$$

was rearranged by Henley and Fischer [2021] to obtain:

$$\begin{aligned} \text{Log} \frac{\text{H}_2\text{S}}{\text{SO}_2} = & \text{Log} K_7 + 2\text{Log} \frac{\text{H}_2}{\text{H}_2\text{O}} + \text{Log} S_T \\ & - \text{Log} \left( K_5 \cdot \left( \frac{\text{H}_2}{\text{H}_2\text{O}} \right)^3 P_{\text{tot}} + 1 \right) \end{aligned} \quad (10)$$

Equation (10) demonstrates that  $\text{SO}_2$ -mineral reactions can control both gas composition and redox state (e.g.,  $\text{H}_2/\text{H}_2\text{O}$  and  $\text{SO}_2/\text{H}_2\text{S}$  and Total gas phase sulphur,  $S_T$ ) at a given total pressure ( $P_{\text{tot}}$ ). Figures 3 and 4 illustrate examples of such gas–mineral reaction paths (light blue lines labelled H&F). The plotted model curves [we illustrate the example runs shown in the original Figure 5 of Henley and Fischer, 2021] are representative of closed-system multi-component (mineral–gas) equilibrium runs in a range of pressures (either 1 or 100 bars), gas–mineral ratios (either 10 or 100) and temperatures (400–1000 °C), and highlight the expected gas compositional changes in such gas–mineral reaction environments. The model reaction paths derived by Henley and Fischer [2021] indicate that, as reaction progresses (e.g., while gases increasingly react with host-rock minerals during their ascent, expansion and cooling), the  $\text{H}_2/\text{H}_2\text{O}$ ,  $\text{SO}_2/\text{H}_2\text{S}$  and  $S_T$  are all expected to decrease in the residual gas phase (8). The H&F model lines satisfactorily reproduce

the observed (volcanic gas)  $\text{H}_2/\text{H}_2\text{O}$  temperature dependence (Figure 3a). In the models, the predicted  $\text{SO}_2/\text{H}_2\text{S}$  ratios are relatively invariant in the 1000–600 °C temperature range, but then drop at <600 °C as  $\text{SO}_2$  is increasingly converted into  $\text{H}_2\text{S}$  and sulphates/sulphides (8) and (9) (Figures 3b and 4).

If either homogeneous (gas-only; Equation (5)) or heterogenous (gas–mineral; Equations (7)–(8)) reactions prevail (during ascent and cooling of magmatic gases from source to surface) cannot be unambiguously resolved from our model versus natural samples comparison. In principle, there is no reason to exclude both reaction mechanisms can indeed co-operate in a volcanic system in space and time. The heterogeneous (gas–mineral) reactions satisfactorily explain the transition of magmatic gases into nominal  $\text{SO}_2$ -free hydrothermal gases (dashed light blue arrows in Figure 4b), and are expected to prevail in mature hydrothermal systems where the transit of gas is sufficiently slow to insure gas–mineral titration effectively takes place, leading to  $\text{SO}_2$ -to- $\text{H}_2\text{S}$  conversion and sulphur loss to hydrothermal minerals. In more active magmatic systems, vice versa, it is well possible that gas transit through the host rocks is fast enough to prevent large  $\text{SO}_2$  scavenging from reactions with minerals. Our mixed (magmatic–hydrothermal) gases all contain detectable  $\text{SO}_2$ , and the  $\text{SO}_2/\text{H}_2\text{S}$  ratios are relatively temperature invariant (Figures 3b and 4a,b), implying the gas may remain closed to reactions with host rocks in many cases, in which case reaction (5) would keep a major control on gas chemistry and redox.

Neither homogeneous nor heterogenous reactions can explain the high  $\text{H}_2/\text{H}_2\text{O}$  ratio signature of many relatively low-temperature ( $T < 400$  °C) gas samples (Figure 3a). These  $\text{H}_2$ -rich compositions imply that re-equilibration (upon gas cooling) may eventually not take place at all, causing the surface discharge of relatively cold gases to preserve quenched, higher-temperature equilibrium conditions (see arrow labelled “quenching” in Figure 3). Ultimately, the extent of (gas or gas–mineral) re-equilibration will range from minimal to total in natural systems, depending on the local conditions and specific ascent/cooling histories of gases, as on their route to the surface.

#### 4.2. Use of hydrogen and hydrogen sulphides as geothermometers

The strong temperature dependence of  $H_2$  concentrations (Figure 2a) and  $H_2/H_2O$  ratios (Figure 3a), combined with relatively temperature-invariant  $SO_2/H_2S$  ratios (Figures 3b, 4a,b), suggest that gas chemistry and redox are often internally buffered (by the gas-phase reaction (5)). One possible way to test if/to what extent fast-reacting  $H_2$  rapidly attains equilibrium in an internally buffered volcanic gas phase (e.g., whose redox is controlled by the  $H_2S$ – $SO_2$  gas buffer) is to use Equation (5) to estimate Apparent Equilibrium Temperatures [AETs; e.g., Matsuo, 1962, Ohba et al., 1994, Moussallam et al., 2019b, 2022], and compare these with measured (discharge) temperatures. Deriving such AETs from measured  $H_2$ ,  $H_2O$ ,  $SO_2$  and  $H_2S$  compositions [e.g., Moussallam et al., 2019b, 2022] is especially important at open-vent volcanoes [Shinohara et al., 2011, 2015, 2018], in which gas observations are typically taken in “cold” atmospheric volcanic gas plumes, whose source vents are inaccessible to direct temperature measurements [this contrasts with closed-conduit volcanoes in which gas venting temperatures are measured concurrently with gas sampling at the fumarolic outlet; e.g., Ohba et al., 1994]. Such information on magma source temperatures can be recorded in the composition of the plume at condition that gas-melt equilibria (i) are established at magma  $T$ – $P$ -redox conditions, and (ii) conserved during gas cooling and mixing during atmospheric dispersion. Assumption (ii) is indeed verified by observations/models that suggest quenching of magmatic gas composition in volcanic plumes [in which source  $H_2/H_2O$  and  $SO_2/H_2S$  ratios are conserved during plume aging; Aiuppa et al., 2007, 2011].

Our gas catalogue here offers an opportunity to test condition (i) above and, ultimately, to verify if internal (gas-phase) redox buffering prevails in magmatic systems (over heterogeneous reactions).

We initially illustrate in Figure 5a the temperature dependence of the equilibrium constant of reaction (5) (expressed in the form of  $\text{Log } K_5$ ), as derived from thermodynamic data in Ohba et al. [1994]. This equilibrium line (solid black line in Figure 5a) is contrasted against analytical values of  $\text{Log } K_5$ , as derived by solving (for each sample in Supplementary Tables 1 and 2) Equation (6) using analytically deter-

mined  $H_2/H_2O$  and  $H_2S/SO_2$  ratios (water fugacity,  $f_{H_2O}$ , is calculated from measured  $X_{H_2O}$  and assuming 1 bar total pressure and ideal gas behaviour). This comparison shows that the “restored gas analyses” output analytical  $\text{Log } K_5$  values that perfectly overlap with the equilibrium curve: this merely reflects the accuracy of the gas restoration procedure of Gerlach [1980]. More significant is the observation that unrestored magmatic gases ( $600\text{ }^\circ\text{C} < T < 1100\text{ }^\circ\text{C}$ ) have analytically determined  $\text{Log } K_5$  that match closely equilibrium  $\text{Log } K_5$  values: for these samples, approach to equilibrium is proved by the close match between measured (discharge) temperatures and AETs (Figure 5b). Some mixed hydrothermal-magmatic gases also plot along (or at least very close to) the model equilibrium curve (Figure 5a), indicating that equilibrium conditions can still be achieved during gas cooling at temperatures of  $<600\text{ }^\circ\text{C}$  (and as low as  $\sim 200\text{ }^\circ\text{C}$ ; Figures 5a, b). However, in such a temperature range, and increasing number of samples output analytically derived  $\text{Log } K_5$  that diverge from the equilibrium line (Figure 5a): in these samples, AETs exceed measured (discharge) temperatures by several hundred degrees in some cases, again indicating quenching of higher temperature (magmatic) conditions, and or disequilibrium conditions. These are the same samples that in Figure 3a diverge from the main compositional-temperature array (grey band) toward higher  $H_2/H_2O$  ratios.

The conclusion we can take is that, as previously shown by Moussallam et al. [2019b] (see their Figure S1), at magmatic temperatures ( $>600\text{ }^\circ\text{C}$ ), gas compositions can allow estimating AETs that are within  $\pm 20\%$  of actual venting temperatures (Figure 5d). It is very interesting to realise however that even at lower ( $<600\text{ }^\circ\text{C}$ ) gas venting temperatures, quenching of higher temperature compositions, or disequilibrium conditions, is indeed common.

The calculations above do not necessarily imply that gas–mineral reactions (7)–(8) are altogether unimportant. Reactions between gas and host-rocks [e.g., Symonds et al., 2001, Henley and Fischer, 2021] are central to the formation of  $SO_2$ -poor hydrothermal steam samples [e.g., Giggenbach, 1980]. In the  $600\text{ }^\circ\text{C} < T < 1200\text{ }^\circ\text{C}$  temperature range however, the fraction of  $SO_2$  loss via reaction (7) and (8) is overall a limited fraction (of the total S load in the gas phase), thus exercising little to no effect on gas equilibria (Figure 5).

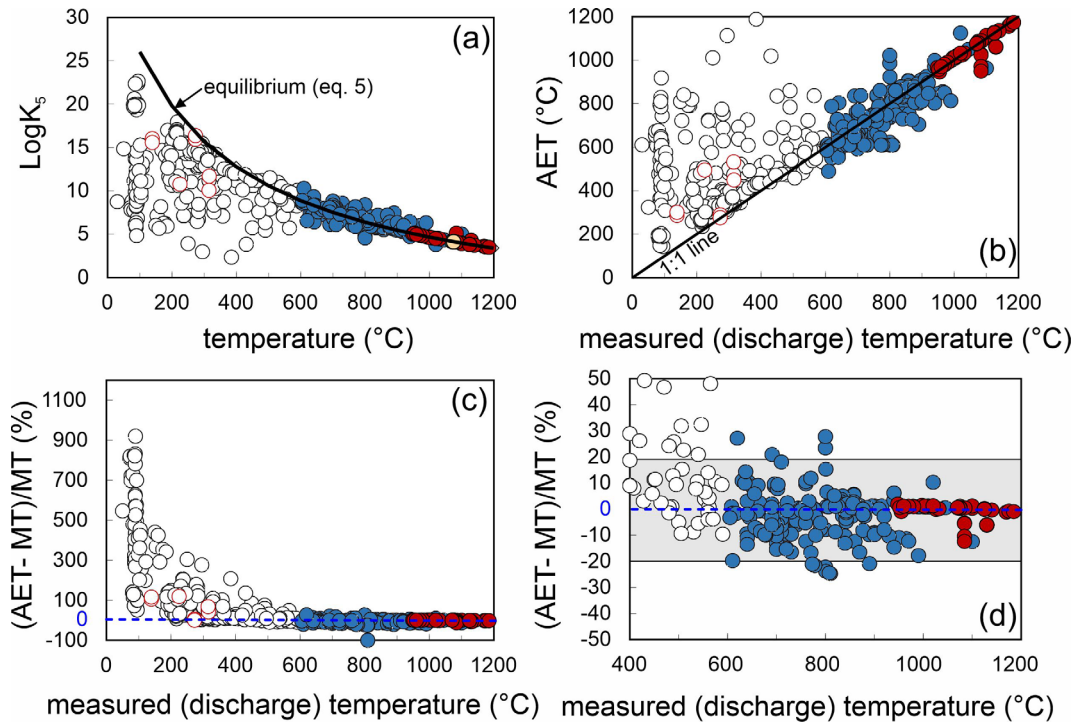


**Figure 5.** (a) Temperature dependence of the equilibrium constant of reaction (5) (expressed in the form of  $\text{Log}K_5$ ), as derived from thermodynamic data in Ohba et al. [1994]. The equilibrium line (solid black line) is contrasted against analytical values of  $\text{Log}K_5$ , as derived by solving (for each sample in Supplementary Tables 1 and 2) Equation (6) using analytically determined  $\text{H}_2/\text{H}_2\text{O}$  and  $\text{H}_2\text{S}/\text{SO}_2$  ratios (water fugacity,  $f_{\text{H}_2\text{O}}$ , is calculated from measured  $\text{XH}_2\text{O}$  and assuming 1 bar total pressure and ideal gas behaviour). (b) Apparent equilibrium temperatures (AET) [Matsuo, 1962, Ohba et al., 1994, Moussallam et al., 2022] derived from Equation (6) and analytically determined  $\text{H}_2/\text{H}_2\text{O}$  and  $\text{H}_2\text{S}/\text{SO}_2$  ratios for individual gas samples. High-temperature gases plot along the 1:1 line, e.g., they match closely measured discharge temperature ( $x$ -scale), implying equilibrium conditions. (c) The difference between Apparent equilibrium temperatures (AET) and measured temperatures (MT) approach 0 in high- $T$  gas samples, while AETs exceed MTs at lower temperatures (implying quenching of higher- $T$  equilibria). (d) A magnified version of (c), demonstrating AET and MT differ by  $< \pm 20\%$  at  $T > 600$  °C.

#### 4.3. Use of hydrogen and hydrogen sulphides to estimate oxygen fugacity

A matter that has remained debated for years is if, and to what extent, volcanic gas compositions reflect (and can therefore allow deriving) the redox conditions (oxygen fugacities) of the source magmas.

Gerlach [1982] found that their “restored” magmatic gas analyses from tholeiitic and alkaline intraplate volcanoes allow calculating gas oxygen fugacities that vary from  $\sim 10^{-8.5}$  to  $\sim 10^{-12}$  bar. He also found these  $f_{\text{O}_2}$  values to be strongly temperature

dependent, and to overall define a  $f_{\text{O}_2}$ -collection temperature trend parallel to the  $f_{\text{O}_2}$ - $T$  dependence imposed by the Fayalite–Magnetite–Quartz (FMQ) and Nickel–Nickel Oxide (NNO) redox buffers [Eugster, 1977, Frost, 1991]. From this, he concluded that “... lavas tend to buffer the  $\text{O}_2$  fugacities of their associated gases”. Confirmation to this hypothesis came from later studies [Gerlach, 1993a,b] in which the  $f_{\text{O}_2}$  values for (restored) magmatic gases from Kilauea were found to match the measured/calculated  $f_{\text{O}_2}$  values of Kilauea basalts. Again, Gerlach [1993a] concluded that “the evidence discussed above indi-

*cates that subaerial lavas buffer volcanic gas compositions emitted by Kilauea basalt along consistent  $fO_2$ - $T$  trend from molten to subsolidus temperatures". A strong temperature dependence of volcanic gas  $fO_2$  values was also found in the global compilation of Symonds et al. [1994].*

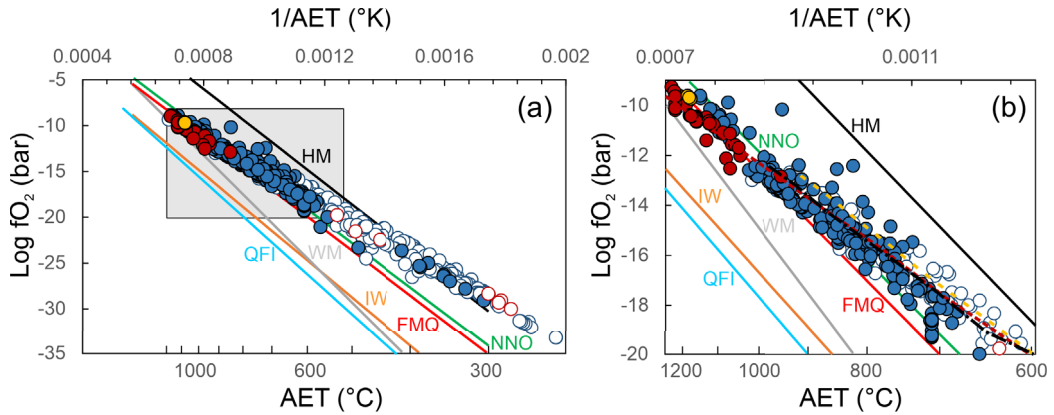
This “melt-buffering” hypothesis has recently been challenged in a series of studies by Oppenheimer et al. [2018] and Moussallam et al. [2019b, 2022] using evidence from novel gas plume observations, either in-situ or remote. Using results from Open Path Fourier Transform Infra-Red (OP-FTIR) spectroscopy observations of lava lake degassing at Kilauea volcano, Oppenheimer et al. [2018] found that gas composition varies with activity style and temperature. They found, in particular, that the volcanic gas phase becomes progressively oxidised as gas temperature progressively drops (below magmatic temperature), at a rate that is inconsistent with that predicted by external gas redox buffering by the coexisting silicate melt. They proposed that magmatic gas redox ( $fO_2$ ) is controlled by homogeneous (gas-phase only) redox re-equilibration upon adiabatic gas cooling. Using evidence from a global volcanic gas dataset, Moussallam et al. [2019b] generalised the conclusions of Oppenheimer et al. [2018], showing that the temperature dependence of volcanic gas  $fO_2$  is different (less steep) than that imposed by external melt redox buffers. Rather, they found that volcanic gas redox scales with the extent of gas cooling experienced by gases (as indicated by temperature difference between gas and the source melt). In this interpretation therefore, volcanic gas redox decouples from that of the melt, i.e., the melt redox information is altered in the gas during its adiabatic cooling (as gas bubbles separately rise within—and ultimately burst out of—the silicate melt). To capture this concept, Moussallam et al. [2022] proposed the use of the formulation “apparent oxidation state” or AOS which is the oxidation state of the gas mixture at its apparent equilibrium temperature. Moussallam et al. [2022] showed that if the magma temperature is known then the gas AOS can be restored to its true  $fO_2$  at equilibrium with the magma (i.e., the oxidation state of the magma can be calculated from the AOS).

Hydrogen and hydrogen sulphide are inherently central to this discussion, as Equations (3) and (4) can conveniently be re-arranged to estimate AOS from

measured/apparent temperature and either  $H_2/H_2O$  or  $SO_2/H_2S$  ratios. Figure 6a is a plot of derived  $fO_2$  values for gas samples in our catalogue, as derived from Equation (3) using measured  $H_2/H_2O$  ratios and AETs.  $fO_2$ s obtained by  $SO_2/H_2S$  ratios (and Equation (4)), also listed in Supplementary Tables 1 and 2, agree well with those derived from  $H_2/H_2O$  ratios. The whole volcanic gas population defines in Figure 6a a roughly linear temperature- $fO_2$  array which slope is manifestly less steep than that of any mineral buffer line. Overall, the volcanic gas population span from redox conditions between the NNO and FMQ buffers at temperatures of 900 °C or more, to redox close to the Hematite–Magnetite (HM) buffer at the low temperature (<400 °C) end of the population. Our results thus corroborate the results of Moussallam et al. [2019b, 2022] that volcanic gases become increasingly oxidised with decreasing temperatures. The high temperature ( $T > 600$  °C) magmatic gas field is magnified in Figure 6b.

We modelled the closed-system cooling of three gas compositions from Erta’ Ale [Le Guern et al., 1979], Satsuma-Iwojima [Shinohara et al., 1993] and Etna [Aiuppa et al., 2011]. The calculation method is detailed in Moussallam et al. [2019b, 2022] and results are shown in Figure 6b. This shows that even at low (<600 °C) temperature the oxidation state of volcanic gases having suffered limited interaction with the hydrothermal system can be explained by closed system cooling from magmatic temperature. This is an astonishing and very fortunate finding as it means that volcanic gases with AET as low as a few hundred degrees might preserve information of the oxidation state and/or temperature of the magma from which they escaped by simply applying the gas restoration calculations described in Moussallam et al. [2022]. For example, we can perform the same calculations but this time starting with the measured gas composition from Kawa Ijen volcano collected by Allard 1985 at a measured temperature of 244 °C but with an AET of ~343 °C and at an AOS at QFM+5. Restoring [using Moussallam et al., 2022] the volcanic gas composition back to a magmatic temperature (arbitrarily set to 1000 °C for the purpose of demonstration) would lead to a restored gas composition with an oxidation state and magmatic temperature of QFM+0.3.

The link between volcanic gas and silicate melt (magma) redox is more fully analysed in Figure 7.



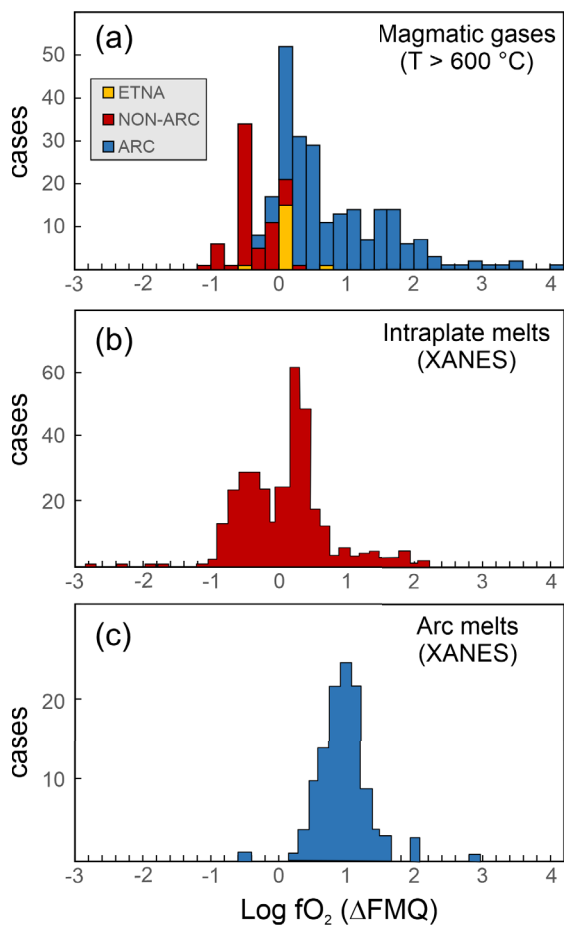
**Figure 6.** The temperature dependence of volcanic gas oxygen fugacities (a) apparent oxygen fugacities of individual gas samples (data from Supplementary Tables 1 and 2), as derived using Equation (2) from measured  $H_2/H_2O$  ratios and estimated Apparent Equilibrium Temperatures (AET; same as Figure 5). Calculated  $\text{Log } fO_2$  values vary linearly with  $1/\text{AET}$ , but the slope of the linear function is manifestly less steep than the  $\text{Log } fO_2 - 1/T$  dependence imposed by the most common mineral redox buffers [HM: Hematite–Magnetite; NNO: Nickel–Nickel Oxide; FMQ: Fayalite–Magnetite–Quartz; WM: Wustite–Magnetite; IW: Iron–Wustite; QFI: Quartz–Fayalite–Iron; see Frost, 1991, Moretti and Neuville, 2021]; (b) a magnified version of (a) comparing the  $\text{Log } fO_2 - 1/T$  dependence for high-temperature ( $>600\text{ }^\circ\text{C}$ ) volcanic gases. The dashed lines illustrate the gas evolution predicted from closed-system (gas cooling) calculations. The closed system model lines suitably reproduce the compositional trend (increasingly oxidised conditions upon cooling) described by natural samples.

Figure 7a is a frequency distribution diagram of derived (Equation (3)) apparent oxygen fugacities for magmatic gases (temperature  $> 600\text{ }^\circ\text{C}$ ). The figure demonstrates distinct redox conditions for non-arc and arc volcanic gases. In spite of some overlap, most arc volcanic gases have apparent  $fO_2$ s (as expressed as  $\Delta\text{FMQ} = \log fO_{2(\text{sample})} - \log fO_{2(\text{FMQ at AET})}$ ) at  $\Delta\text{FMQ} \geq 0$ , and as high as  $\Delta\text{FMQ} + 4$ ; whilst non-arc volcanic gases are generally more reduced  $\Delta\text{FMQ} \leq 0.2$ , and as low as  $\Delta\text{FMQ} - 1.2$ . This diversity is largely explained by the arc gas dataset containing many fumarole samples in the  $600\text{--}900\text{ }^\circ\text{C}$  temperature range, which have therefore cooled significantly below source magma temperatures, ultimately having become more oxidised during closed-system reactions [see Figure 6 and related discussions and see Figure 1 in Moussallam et al., 2022 showing the oxidation state of arc gases restored to magmatic temperature]. However, arc gases sampled at close to magmatic temperatures ( $T > 900\text{ }^\circ\text{C}$ ) still plot at higher redox than non-arc magmatic gases (Figure 7a; see also Figures 4 and 6b), implying that the volcanic gas  $fO_2$  difference is likely to reflect some distinct

redox conditions at source. Intraplate (Figure 7b) and arc (Figure 7c) melts have previously been shown to exhibit distinct redox [Cottrell et al., 2022]. We conclude, therefore, that these diverse magma  $fO_2$ s are well preserved in volcanic gases, provided adiabatic cooling and re-equilibration have not occurred (e.g., at  $T \gg 900\text{ }^\circ\text{C}$ ). It is important to remember, however, that melt redox has been found to vary upon magma de-compressional ascent and degassing, progressively becoming more reduced [e.g., Moussallam et al., 2014a, 2016, 2019a, Brounce et al., 2017, Helz et al., 2017] at low pressure [when S(IV) is lost to gas as  $\text{SO}_2$ , leading to an overall decrease of the magma redox budget; [Evans, 2012]]. As such, magmatic gas may, at some conditions (limited adiabatic cooling), reflect redox of shallow, surface-emplaced magma; however, it is unlikely to provide information on deep magma (and source mantle) redox [Moretti and Stefánsson, 2020].

#### 4.4. *Atmospheric fluxes*

Upon their atmospheric release from subaerial volcanoes, volcanogenic  $\text{H}_2$  and  $\text{H}_2\text{S}$  act as primary electron donors (e.g., as reducing compounds) in the atmosphere [e.g., Holland, 2002, Canfield et al., 2006]. As these volcanic gas species thus contribute largely to the reducing power (e.g., the ability to remove atmospheric  $\text{O}_2$ ) of volcanic gases, understanding their volcanic atmospheric fluxes is central to reconstructing the oxygenation history of the early atmosphere and the present atmospheric oxygen budget [Holland, 2002, Canfield et al., 2006, Stolper et al., 2021].



**Figure 7.** (a) Frequency distribution diagram of derived (Equation (3)) apparent oxygen fugacities for magmatic gases (temperature  $> 600^\circ\text{C}$ ), expressed as  $\Delta\text{FMQ} = \log f\text{O}_{2(\text{sample})} - \log f\text{O}_{2(\text{FMQ at AET})}$ . The figure demonstrates distinct redox conditions for non-arc and arc volcanic gases in the same range and magnitude as seen for intraplate (panel b) and arc (panel c) melts [redrawn from Cottrell et al., 2022].

As for the more abundant  $\text{CO}_2$  [Aiuppa et al., 2019, Werner et al., 2019, Fischer et al., 2019], the volcanic  $\text{H}_2$  and  $\text{H}_2\text{S}$  fluxes to the atmosphere cannot be measured directly by remote sensing, as no specific observational technique exists for this aim. Therefore, although some rare direct in-situ flux measurements exist [Aiuppa et al., 2013, Allard et al., 2014, Tamburello et al., 2019, Moune et al., 2022], most applications rely on the indirect approach

[Aiuppa et al., 2019, Fischer et al., 2019, Werner et al., 2019] of scaling gas ratios ( $\text{H}_2/\text{SO}_2$  and  $\text{H}_2\text{S}/\text{SO}_2$  ratios in this specific case) in volcanic emissions to the global volcanic  $\text{SO}_2$  flux budget [e.g., Carn et al., 2017, Fischer et al., 2019], which is well understood thanks to abundant UV spectroscopy observations from both ground [Arellano et al., 2021] and space [Carn et al., 2016]. The operation is, however, complicated by the large spread of  $\text{H}_2/\text{SO}_2$  and  $\text{H}_2\text{S}/\text{SO}_2$  ratios in volcanic gas emissions (Figure 8a–d), which has traditionally hampered the derivation of robust global estimates [Halmer et al., 2002, Canfield et al., 2006].

The two most recent attempts to estimate the  $\text{H}_2$  and  $\text{H}_2\text{S}$  fluxes from global subaerial volcanism are from Canfield et al. [2006] and Stolper et al. [2021] (Table 1).

Canfield et al. [2006] compiled 21 high quality volcanic gas analyses from volcanoes in a variety of geological context, including rift-related, hot-spot related, and in subduction zones related. They found volcanic gas  $\text{H}_2/\text{SO}_2$  and  $\text{H}_2\text{S}/\text{SO}_2$  ratios to vary widely even in such a limited dataset, total ranges being respectively of 0.02–24 and 0.007–2.7. The median volcanic gas  $\text{H}_2/\text{SO}_2$  and  $\text{H}_2\text{S}/\text{SO}_2$  ratios in their subset of volcanic gas samples are 0.8 ( $\text{H}_2/\text{SO}_2$ ) and 0.3 ( $\text{H}_2\text{S}/\text{SO}_2$ ). Ultimately, by using most representative ratio ranges in combination with a global  $\text{SO}_2$  flux estimate [Halmer et al., 2002] they quantified the global volcanic  $\text{H}_2$  and  $\text{H}_2\text{S}$  fluxes at 0.2–0.7 Tg/yr and 1.4–2.0 Tg/yr, respectively (Table 1).

Stolper et al. [2021] also based their  $\text{H}_2$  and  $\text{H}_2\text{S}$  flux estimates on major species’ global budgets—they used the more updated global volcanic  $\text{SO}_2$  and  $\text{H}_2\text{O}$  flux inventories of Fischer et al. [2019]. However, they adopted a different methodology for deriving best-estimates for  $\text{H}_2/\text{SO}_2$  and  $\text{H}_2\text{S}/\text{SO}_2$  ratios in “globally averaged volcanic gas emissions”. Instead of averaging results from measured  $\text{H}_2/\text{SO}_2$  and  $\text{H}_2\text{S}/\text{SO}_2$  ratios in volcanic gas samples, they relied on thermodynamically derived  $\text{H}_2/\text{SO}_2$  and  $\text{H}_2\text{S}/\text{SO}_2$  ratios, calculated (from relations similar to Equations (3) and (4) presented above) at temperature, pressure and redox ( $f\text{O}_2$ ) conditions of the source silicate melt. For example, they quantified the global volcanic  $\text{H}_2$  flux at 0.07–0.44 Tg/yr (Table 1) by combining the global volcanic  $\text{H}_2\text{O}$  flux of Fischer et al. [2019] with the thermodynamically derived (Equation (3))  $\text{H}_2/\text{H}_2\text{O}$  ratios at equilibrium with melt,

**Table 1.** Global volcanic H<sub>2</sub>S and H<sub>2</sub> fluxes (in Tg/yr) revisited

	Mean	SD	Mean	SD	50%	25%	75%	50%	25%	75%	50%	25%	75%			
S <sub>vge</sub>	SO <sub>2</sub> flux	24.9	2.3	CO <sub>2</sub> flux	36	2.4	H <sub>2</sub> S/SO <sub>2</sub>	0.1	0.06	0.6	H <sub>2</sub> S flux	1.3	0.8	8.3		
												H <sub>2</sub> /SO <sub>2</sub>	0.3	0.1	1.3	
W <sub>vge</sub>	SO <sub>2</sub> flux	-	-	CO <sub>2</sub> flux	11.6	3.9	H <sub>2</sub> S/CO <sub>2</sub>	0.008	0.006	0.043	H <sub>2</sub> S flux	0.08	0.05	0.4		
												H <sub>2</sub> /CO <sub>2</sub>	0.002	0.0005	0.012	
W <sub>vge</sub>	SO <sub>2</sub> flux	-	-	CO <sub>2</sub> flux	3.7	1.2	H <sub>2</sub> S/CO <sub>2</sub>	0.008	0.006	0.043	H <sub>2</sub> S flux	0.02	0.02	0.12		
												H <sub>2</sub> /CO <sub>2</sub>	0.002	0.0005	0.012	
Total	SO <sub>2</sub> flux	24.9	2.3	CO <sub>2</sub> flux	51.3	7.5					H <sub>2</sub> S flux	1.4	0.9	8.8		
Total	This study (S <sub>vge</sub> + W <sub>vge</sub> )													0.23	0.06	1.0
	Canfield et al. [2006]															0.2-0.7
	Stolper et al. [2021]															0.07-0.44

These are obtained by multiplying the global volcanic SO<sub>2</sub> and CO<sub>2</sub> fluxes of Fischer et al. [2019] by the median (molar) gas ratios in our catalogue (Supplementary Tables 1 and 2). See text. Uncertainty is quantified using 25 and 75 percentiles. We distinguish three volcano categories (S<sub>vge</sub>, magmatic W<sub>vge</sub> and hydrothermal W<sub>vge</sub>) as in Fischer and Aiuppa [2020]. Total fluxes are calculated by summing together the three flux contributions. Previous flux inventories by Canfield et al. [2006] and Stolper et al. [2021] are shown for comparison.



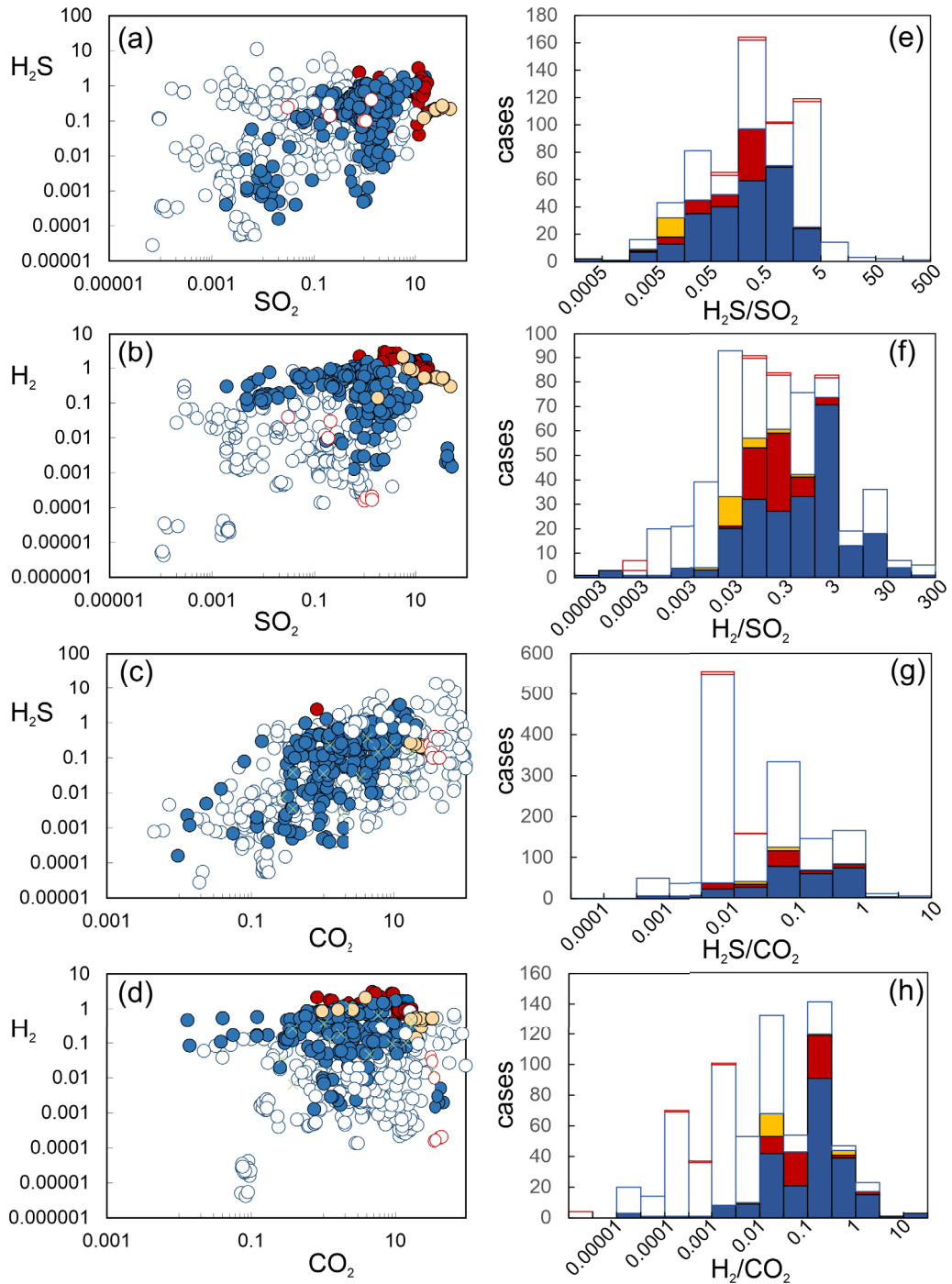


**Figure 8.** (a–d) Scatter plots of  $H_2S$  and  $H_2$  concentrations (data from Supplementary Tables 1 and 2) versus major species' concentrations (either  $SO_2$  or  $CO_2$ ). All concentrations in mol%. (e–h) Frequency distribution diagrams of volatile (molar) ratios used for flux calculations. See text, symbols as in Figure 2 except green crossed [hydrothermal steam samples from Chiodini and Marini, 1998].

using  $T$ ,  $P$ ,  $fO_2$  values relevant to modern subaerial magmas. Likewise, their global volcanic  $H_2S$  flux range of 0.05–4 Tg/yr was inferred from the global  $SO_2$  inventory of Fischer et al. [2019] and the thermodynamically estimated Equation (4) equilibrium (at melt  $T$ ,  $P$ ,  $fO_2$ )  $H_2S/SO_2$  ratios (Table 1). It is necessary to remember that Stolper et al. [2021] implicitly assume that surface volcanic gas emissions are controlled (buffered) by heterogeneous equilibrium with the coexisting silicate melt. However, this assumption, as previously discussed (cf. Section 4.3), likely holds only for the very few cases of gases emitted at magmatic temperature, but not for the many, lower temperature gas emissions seen at the vast majority of the active volcanoes worldwide (see Figures 3, 4, 6). For example, the range of estimated equilibrium  $H_2/H_2O$  ratios of Stolper et al. [2021] is 0.01 to 0.024, and therefore captures only the upper class (the “magmatic” range) of measured  $H_2/H_2O$  ratios in volcanic gases (Figures 3a and 5); the majority of the surface-emitted volcanic gases will be far more  $H_2$ -poor because of re-equilibration during homogeneous (closed-system) gas cooling (cf. Section 4.3). As magmatic gas  $H_2S/SO_2$  are overall preserved during gas cooling (Figures 3b, 5), their estimated range (0.000012–0.28) is representative of the measured gas composition range (Figure 8b).

We here attempt at a refined  $H_2$  and  $H_2S$  volcanic flux inventory (Table 1) by using our more complete volcanic gas catalogue (Supplementary Tables 1 and 2).

Our calculations stand on the approach developed in the most recent volcanic gas flux quantification efforts [Fischer et al., 2019, Fischer and Aiuppa, 2020], in which three categories of subaerial volcanoes are distinguished and separately treated (Table 1). A first category of Volcanic Gas Emitters ( $S_{vge}$ ) includes the strongly degassing volcanoes whose  $SO_2$  emissions can systematically be detected by satellites [e.g., Carn et al., 2017, Fischer et al., 2019]. These volcanoes typically release high-temperature,  $SO_2$ -rich gases, often from open-vent persistently degassing vents, and are believed to dominate the volcanic  $SO_2$  and  $CO_2$  flux inventories [e.g., Aiuppa et al., 2017, 2019, Carn et al., 2017, Fischer et al., 2019, Werner et al., 2019, Fischer and Aiuppa, 2020]. Our high-temperature ( $T > 600$  °C; Supplementary Table 1),  $S_T$ -rich (Figure 1) magmatic gases are inherently the most representative of such emission

category. These have median  $H_2S/SO_2$  (Figure 8a–e) and  $H_2/SO_2$  (Figure 8b–f) ratios of respectively 0.1 and 0.3 (25%–75% percentiles: 0.06–0.6 and 0.1–1.3, respectively; Table 1). From these, and scaling to the global volcanic flux  $SO_2$  of Fischer et al. [2019] (24.9 Tg/yr), we infer the  $S_{vge}$  contribution to the global (subaerial) volcanic  $H_2$  and  $H_2S$  flux at 1.3 Tg/yr (confidence interval, 0.8–8.3) and 0.23 Tg/yr (confidence interval, 0.06–1). The other two categories correspond to the Weak Gas Emitters ( $W_{vge}$ ) [Fischer et al., 2019, Fischer and Aiuppa, 2020] that include both (a) recently active (but now dormant) volcanoes whose  $SO_2$  emissions are too small to be resolved from space (the “magmatic”  $W_{vge}$ ), or (b) quiescent volcanoes in hydrothermal stage of activity (the “hydrothermal”  $W_{vge}$ ) that do not release  $SO_2$  at all, and in which sulphur is essentially released in  $H_2S$  form. For  $W_{vge}$ , we therefore cannot rely on a  $SO_2$  flux proxy. Rather, we use the  $CO_2$  flux estimates of Fischer et al. [2019], in combination with  $H_2S/CO_2$  (Figure 8c–g) and  $H_2/CO_2$  (Figure 8d–h) ratios. Our mixed (magmatic–hydrothermal), lower temperature ( $T \leq 600$  °C; Supplementary Table 2) volcanic gas population exactly corresponds to the category of “magmatic”  $W_{vge}$ , and exhibits  $H_2S/CO_2$  and  $H_2/CO_2$  ratios of 0.008 (0.006–0.043) and 0.002 (0.0005–0.012) (Table 1). Hydrothermal  $W_{vge}$  are not explicitly covered by our review, but their compositions [see data from Chiodini and Marini, 1998] overlap with the magmatic”  $W_{vge}$  compositional range (Figures 8g and h), so we can use the composition of the latter. In summary, therefore, we infer that  $W_{vge}$  contribute  $\sim 0.1$  Tg  $H_2S$  and  $\sim 0.0016$  Tg  $H_2$  yearly. It is important to stress that the population of  $W_{vge}$  spans orders of magnitude in terms of  $H_2S/CO_2$  and  $H_2/CO_2$  (Figures 8c–d and g–h) ratios, so our flux estimates for this specific category are very poorly constrained. However, this has limited impact on our estimated total fluxes of  $H_2S$  (1.4 Tg/yr; 0.9–8.8) and  $H_2$  (0.23 Tg/yr; 0.06–1) fluxes, which are by far dominated by  $S_{vge}$ . We conclude that, while thus  $W_{vge}$  are important volcanic  $CO_2$  sources [Table 1; Fischer et al., 2019, Fischer and Aiuppa, 2020], their contribution to global volcanic subaerial fluxes of reduced, hydrogenated compounds is irrelevant. This reflects the  $H_2$ -poor signature of low temperature gas emissions (Figures 2, 3, 5, 8)—caused by gas oxidation during cooling (Figure 6) (cf. Section 4.3)—and the removal of water-soluble sulphur during magmatic

gas interactions with liquid-dominated hydrothermal systems [e.g., Aiuppa et al., 2017], which determines the prevailing low  $\text{H}_2\text{S}/\text{CO}_2$  compositions (Figures 1, 8g). Our estimated total volcanic  $\text{H}_2\text{S}$  and  $\text{H}_2$  fluxes are at the lower range of the estimates of Canfield et al. [2006], and at the very middle of the flux range of Stolper et al. [2021] (Table 1).

Our results indicate that global volcanism contributes little ( $\sim 1\%$ ; range 0.3–4.3%) to the cumulative (global) geogenic  $\text{H}_2$  flux [ $\sim 23$  Tg/yr; Zgonnik, 2020]. For comparison, anthropogenic  $\text{H}_2$  emissions [ $\sim 11$  Tg/yr; Ehhalt and Rohrer, 2009] are 1 to 2 orders of magnitude higher than volcanic emissions. In contrast, our best-estimate for the volcanic  $\text{H}_2\text{S}$  flux (1.4 Tg/yr) implies volcanoes do make up a non-trivial ( $\sim 18\%$ ) fraction of the global natural  $\text{H}_2\text{S}$  flux [ $\sim 7.7$  Tg/yr; Watts, 2000]. Volcanic degassing contributes nearly 3 times less  $\text{H}_2\text{S}$  than today anthropogenic emissions [3.3 Tg/yr; Watts, 2000].

## 5. Summary and conclusions

We have reviewed our present understanding of the processes that govern the abundance of reduced hydrogenated compounds in volcanic gases. Our review shows that the apparent oxygen fugacities of high-temperature volcanic gases range from  $\Delta\text{FMQ} -1$  to 0 (for non-arc volcanoes) to  $\Delta\text{FMQ} 0$  to +2 (for arc volcanoes), and are therefore comparable to the redox conditions of the source silicate melts. A variety of processes can alter gas composition and redox state ( $\text{H}_2/\text{H}_2\text{O}$  and  $\text{H}_2\text{S}/\text{SO}_2$  ratios) as the gases expand within the melt and cool, and/or after they separate from magma on their route to the surface. Data in our catalogue, when interpreted in the context of existing models of homogeneous (gas) or heterogeneous (gas–mineral) reactions, suggest that in many cases the fast-reacting  $\text{H}_2/\text{H}_2\text{O}$  couple rapidly re-equilibrates during cooling (e.g., in low temperature gas environments) in a gas-buffered system which redox is controlled by coexisting  $\text{H}_2\text{S}$  and  $\text{SO}_2$  (which  $\text{H}_2\text{S}/\text{SO}_2$  ratio is ultimately conserved at  $\sim 0.1$  on average). This gas-phase (closed-system) re-equilibration upon cooling causes the gas to become more oxidised than the original (source) magma [Oppenheimer et al., 2018, Moussallam et al., 2019b]. Conversion of magmatic  $\text{SO}_2$  to hydrothermal  $\text{H}_2\text{S}$  (and precipitation of sulphates/sulphides) is instead favoured by slower transit of the gas through the

host rocks, causing more prolonged gas–water–rock interactions to occur. This condition [Henley and Fischer, 2021] certainly prevails in more mature, liquid-dominated, and stable (less magma fed) hydrothermal systems [Chiodini and Marini, 1998]. Our volcanic gas dataset, combined with recently published global volcanic  $\text{SO}_2$  and  $\text{CO}_2$  budgets, implies total  $\text{H}_2\text{S}$  and  $\text{H}_2$  fluxes from global subaerial volcanism of 1.4 Tg/yr (range, 0.9–8.8 Tg/yr) and 0.23 Tg/yr (range, 0.06–1 Tg/yr), respectively.

## Declaration of interests

The authors do not work for, advise, own shares in, or receive funds from any organization that could benefit from this article, and have declared no affiliations other than their research organizations.

## Acknowledgements

This research received financial support from the Ministero dell'Università e Ricerca (Italy, Grant n. 2017LMNLAW), from the Dipartimento della Protezione Civile and the INGV (under grant “Sviluppo del sistema unico (INGV-Università) di monitoraggio vulcanico e rilevamento precoce dei maremoti e delle esplosioni parossistiche di Stromboli”), and from the PNRR PE Project “Return”. This work was initially inspired by participation of AA to the International School “Understanding Oxygen fugacity in Geoscience” 5–9 September 2022, Trieste, Italy (<https://fo2school.units.it/>), and the organisers of the school (Luca Ziberna and Vincenzo Stagno especially) are warmly thanked.

## Supplementary data

Supporting information for this article is available on the journal's website under <https://doi.org/10.5802/crgeos.235> or from the author.

## References

- Aiuppa, A. (2015). Volcanic-gas monitoring. In Schmidt, A., Fristad, K. E., and Elkins-Tanton, L. T., editors, *Volcanism and Global Environmental Change*, pages 81–96. Cambridge University Press, Cambridge, UK.

- Aiuppa, A., Casetta, F., Coltorti, M., Stagno, V., and Tamburello, G. (2021). Carbon concentration increases with depth of melting in Earth's upper mantle. *Nat. Geosci.*, 14, 697–703.
- Aiuppa, A., Fischer, T. P., Plank, T., and Bani, P. (2019). CO<sub>2</sub> flux emissions from the Earth's most actively degassing volcanoes, 2005–2015. *Sci. Rep.*, 9, article no. 5442.
- Aiuppa, A., Fischer, T. P., Plank, T., Robidoux, P., and Di Napoli, R. (2017). Along-arc, inter-arc and arc-to-arc variations in volcanic gas CO<sub>2</sub>/ST ratios reveal dual source of carbon in arc volcanism. *Earth-Sci. Rev.*, 168, 24–47.
- Aiuppa, A., Franco, A., Glasow, R. V., Allen, A. G., D'Alessandro, W., and Mather, T. A. (2007). The tropospheric processing of acidic gases and hydrogen sulphide in volcanic gas plumes as inferred from field and model investigations. *Atmos. Chem. Phys.*, 7, 1441–1450.
- Aiuppa, A., Inguaggiato, S., McGonigle, A. J. S., O'Dwyer, M., Oppenheimer, C., Padgett, M. J., Rouwet, D., and Valenza, M. (2005). H<sub>2</sub>S fluxes from Mt. Etna, Stromboli, and Vulcano (Italy) and implications for the sulfur budget at volcanoes. *Geochim. Cosmochim. Acta*, 69, 1861–1871.
- Aiuppa, A., Shinohara, H., Tamburello, G., Giudice, G., Liuzzo, M., and Moretti, R. (2011). Hydrogen in the gas plume of an open-vent volcano, Mount Etna, Italy. *J. Geophys. Res.*, 116, B10204.
- Aiuppa, A., Tamburello, G., Di Napoli, R., Cardellini, C., Chiodini, G., Giudice, G., Grassa, F., and Pedone, M. (2013). First observations of the fumarolic gas output from a restless caldera: Implications for the current period of unrest (2005–2013) at Campi Flegrei. *Geochem. Geophys. Geosyst.*, 14(10), 4153–4169.
- Allard, P., Aiuppa, A., Beatuducel, F., Gaudin, D., Di Napoli, R., Calabrese, S., Parello, F., Crispi, O., Hammouya, G., and Tamburello, G. (2014). Steam and gas emission rate from La Soufriere volcano, Guadeloupe (Lesser Antilles): Implications for the magmatic supply during degassing unrest. *Chem. Geol.*, 384, 76–93.
- Arellano, S., Galle, B., Apaza, F., Avard, G., Barrington, C., Bobrowski, N., Bucarey, C., Burbano, V., Burton, M., Chacón, Z., Chigna, G., Clarito, C. J., Conde, V., Costa, F., De Moor, M., Delgado-Granados, H., Di Muro, A., Fernandez, D., Garzón, G., Gunawan, H., Haerani, N., Hansteen, T. H., Hidalgo, S., Inguaggiato, S., Johansson, M., Kern, C., Kihlman, M., Kowalski, P., Masias, P., Montalvo, F., Möller, J., Platt, U., Rivera, C., Saballos, A., Salerno, G., Taisne, B., Váscónez, F., Velásquez, G., Vita, F., and Yalire, M. (2021). Synoptic analysis of a decade of daily measurements of SO<sub>2</sub> emission in the troposphere from volcanoes of the global ground-based network for observation of volcanic and atmospheric change. *Earth Syst. Sci. Data*, 13, 1167–1188.
- Brounce, M., Stolper, E., and Eiler, J. (2017). Redox variations in Mauna Kea lavas, the oxygen fugacity of the Hawaiian plume, and the role of volcanic gases in Earth's oxygenation. *Proc. Natl. Acad. Sci. USA*, 114, 8997–9002.
- Burgisser, A. and Scaillet, B. (2007). Redox evolution of a degassing magma rising to the surface. *Nature*, 445, 194–197.
- Canfield, D. E., Rosing, M. T., and Bjerrum, C. (2006). Early anaerobic metabolisms. *Philos. Trans. R. Soc. Lond. B*, 361, 1819–1834. Discussion 1835–1836.
- Carn, S. A., Clarisse, L., and Prata, A. J. (2016). Multi-decadal satellite measurements of global volcanic degassing. *J. Volcanol. Geotherm. Res.*, 311, 99–134.
- Carn, S. A., Fioletov, V. E., McLinden, C. A., Li, C., and Krotkov, N. A. (2017). A decade of global volcanic SO<sub>2</sub> emissions measured from space. *Sci. Rep.*, 7, article no. 44095.
- Chase, M. W. and National Institute of Standards and Technology (U.S.) (1998). *NIST-JANAF Thermochemical Tables*. American Chemical Society; American Institute of Physics for the National Institute of Standards and Technology, Washington, DC; Woodbury, NY.
- Chiodini, G., Cioni, R., and Marini, L. (1993). Reactions governing the chemistry of crater fumaroles from Vulcano Island, Italy, and implications for volcanic surveillance. *Appl. Geochem.*, 8, 357–371.
- Chiodini, G. and Marini, L. (1998). Hydrothermal gas equilibria: the H<sub>2</sub>O-H<sub>2</sub>-CO<sub>2</sub>-CO-CH<sub>4</sub> system. *Geochim. Cosmochim. Acta*, 62, 2673–2687.
- Cicconi, M. R., Moretti, R., and Neuville, D. R. (2020). Earth's electrodes. *Elements*, 16, 157–160.
- Cottrell, E., Birner, S., Brounce, M., Davis, E., Waters, L., and Kelley, K. (2022). Oxygen fugacity across tectonic settings. In Moretti, R. and Neuville, D. R., editors, *Magma Redox Geochemistry*, Geophysical Monograph 266. American Geophysical Union, John Wiley & Sons.

- D'Amore, F. and Panichi, C. (1980). Evaluation of deep temperatures of hydrothermal systems by a new gas geothermometer. *Geochim. Cosmochim. Acta*, 44, 549–556.
- de Moor, J. M., Stix, J., Avard, G., Muller, C., Corrales, E., Diaz, J. A., Alan, A., Brenes, J., Pacheco, J., Aiuppa, A., and Fischer, T. P. (2019). Insights on hydrothermal–magmatic interactions and eruptive processes at Poás Volcano (Costa Rica) from high-frequency gas monitoring and drone measurements. *Geophys. Res. Lett.*, 46, 1293–1302.
- Ehhalt, D. H. and Rohrer, F. (2009). The tropospheric cycle of H<sub>2</sub>: a critical review. *Tellus B Chem. Phys. Meteorol.*, 61, 500–535.
- Ellis, A. J. (1957). Chemical equilibrium in magmatic gases. *Am. J. Sci.*, 255, 416–431.
- Eugster, H. P. (1977). Compositions and thermodynamics of metamorphic solutions. In *Thermodynamics in Geology: Proceedings of the NATO Advanced Study Institute Held in Oxford, England, September 17–27, 1976*, pages 183–202. D. Reidel Publishing Company, Dordrecht, Holland/Boston, USA.
- Evans, K. A. (2012). The redox budget of subduction zones. *Earth-Sci. Rev.*, 113, 11–32.
- Fischer, T. P. (2008). Fluxes of volatiles (H<sub>2</sub>O, CO<sub>2</sub>, N<sub>2</sub>, Cl, F) from arc volcanoes. *Geochem. J.*, 42, 21–38.
- Fischer, T. P. and Aiuppa, A. (2020). AGU Centennial Grand Challenge: Volcanoes and deep carbon global CO<sub>2</sub> emissions from subaerial volcanism—Recent progress and future challenges. *Geochem. Geophys. Geosyst.*, 21, article no. e2019GC008690.
- Fischer, T. P., Arellano, S., Carn, S., Aiuppa, A., Galle, B., Allard, P., Lopez, T., Shinohara, H., Kelly, P., Werner, C., Cardellini, C., and Chiodini, G. (2019). The emissions of CO<sub>2</sub> and other volatiles from the world's subaerial volcanoes. *Sci. Rep.*, 9, article no. 18716.
- Fischer, T. P. and Chiodini, G. (2015). Chapter 45 – Volcanic, magmatic and hydrothermal gases. In Sigurdsson, H., editor, *The Encyclopedia of Volcanoes*, pages 779–797. Academic Press, Amsterdam, 2nd edition.
- Frost, B. R. (1991). Introduction to oxygen fugacity and its petrologic importance. *Rev. Mineral. Geochem.*, 25, 1–9.
- Frost, D. J. and McCammon, C. A. (2008). The redox state of Earth's mantle. *Annu. Rev. Earth Planet. Sci.*, 36, 389–420.
- Gaillard, F. and Scaillet, B. (2014). A theoretical framework for volcanic degassing chemistry in a comparative planetology perspective and implications for planetary atmospheres. *Earth Planet. Sci. Lett.*, 403, 307–316.
- Gaillard, F., Scaillet, B., and Arndt, N. T. (2011). Atmospheric oxygenation caused by a change in volcanic degassing pressure. *Nature*, 478, 229–232.
- Gaillard, F., Scaillet, B., Pichavant, M., and Iacono-Marziano, G. (2015). The redox geodynamics linking basalts and their mantle sources through space and time. *Chem. Geol.*, 418, 217–233.
- Gerlach, T. M. (1979). Evaluation and restoration of the 1970 volcanic gas analyses from Mount Etna, Sicily. *J. Volcanol. Geotherm. Res.*, 6, 165–178.
- Gerlach, T. M. (1980). Evaluation of volcanic gas analyses from Kilauea volcano. *J. Volcanol. Geotherm. Res.*, 7, 295–317.
- Gerlach, T. M. (1982). Interpretation of volcanic gas data from tholeiitic and Alkaline Mafic Lavas. *Bull. Volcanol.*, 45, 235–244.
- Gerlach, T. M. (1993a). Oxygen buffering of Kilauea volcanic gases and the oxygen fugacity of Kilauea basalt. *Geochim. Cosmochim. Acta*, 57(4), 795–814.
- Gerlach, T. M. (1993b). Thermodynamic evaluation and restoration of volcanic gas analysis: An example based on modern collection and analytical methods. *Geochem. J.*, 27, 305–322.
- Gerlach, T. M. and Nordlie, B. E. (1975). The C-O-H-S gaseous system; Part II, Temperature, atomic composition, and molecular equilibria in volcanic gases. *Am. J. Sci.*, 275, 377–394.
- Giggenbach, W. F. (1980). Geothermal gas equilibria. *Geochim. Cosmochim. Acta*, 44, 2021–2032.
- Giggenbach, W. F. (1987). Redox processes governing the chemistry of fumarolic gas discharges from White Island, New Zealand. *Appl. Geochem.*, 2, 143–161.
- Giggenbach, W. F. (1996). Chemical composition of volcanic gases. In Scarpa, R. and Tilling, R. I., editors, *Monitoring and Mitigation of Volcano Hazards*, pages 221–256. Springer Verlag, Berlin.
- Giggenbach, W. F. (1997). The origin and evolution of fluids in magmatic-hydrothermal systems. In Barnes, H. L., editor, *Geochemistry of Hydrothermal Ore Deposits*, pages 737–796. John Wiley & Sons Inc, New York.
- Gilat, A. L. and Vol, A. (2012). Degassing of primordial hydrogen and helium as the major energy source

- for internal terrestrial processes. *Geosci. Front.*, 3, 911–921.
- Halmer, M. M., Schmincke, H.-U., and Graf, H.-F. (2002). The annual volcanic gas input into the atmosphere, in particular into the stratosphere: a global data set for the past 100 years. *J. Volcanol. Geotherm. Res.*, 115, 511–528.
- Helz, R. T., Cottrell, E., Brounce, M. N., and Kelley, K. A. (2017). Olivine-melt relationships and syneruptive redox variations in the 1959 eruption of Kīlauea Volcano as revealed by XANES. *J. Volcanol. Geotherm. Res.*, 333–334, 1–14.
- Henley, R. W. and Berger, B. R. (2011). Magmatic-vapor expansion and the formation of high-sulfidation gold deposits: Chemical controls on alteration and mineralization. *Ore Geol. Rev.*, 39, 63–74.
- Henley, R. W. and Fischer, T. P. (2021). Sulfur sequestration and redox equilibria in volcanic gases. *J. Volcanol. Geotherm. Res.*, 414, article no. 107181.
- Henley, R. W., King, P. L., Wykes, J. L., Renggli, C. J., Brink, F. J., Clark, D. A., and Troitzsch, U. (2015). Porphyry copper deposit formation by sub-volcanic sulphur dioxide flux and chemisorption. *Nat. Geosci.*, 8, 210–215.
- Henley, R. W. and Seward, T. M. (2018). Gas–solid reactions in arc volcanoes: Ancient and modern. *Rev. Mineral. Geochem.*, 84, 309–349.
- Holland, H. D. (2002). Volcanic gases, black smokers, and the great oxidation event. *Geochim. Cosmochim. Acta*, 66, 3811–3826.
- Kasting, J. F., Egglar, D. H., and Raeburn, S. P. (1993). Mantle redox evolution and the oxidation state of the Archean atmosphere. *J. Geol.*, 101, 245–257.
- Kern, C., Aiuppa, A., and de Moor, J. M. (2022). A golden era for volcanic gas geochemistry? *Bull. Volcanol.*, 84, article no. 43.
- Le Guern, F., Carbonnelle, J., and Tazieff, H. (1979). Erta'ale lava lake: heat and gas transfer to the atmosphere. *J. Volcanol. Geotherm. Res.*, 6, 27–48.
- Martin, R. S., Mather, T. A., and Pyle, D. M. (2006). High-temperature mixtures of magmatic and atmospheric gases. *Geochem. Geophys. Geosyst.*, 7(4), 1–14.
- Matsuo, S. (1962). Establishment of chemical equilibrium in the volcanic gas obtained from the lava lake of Kilauea, Hawaii. *Bull. Volcanol.*, 24, 59–71.
- Moretti, R. (2021). Ionic syntax and equilibrium approach to redox exchanges in melts: basic concepts and the case of iron and sulfur in degassing magmas. In *Magma Redox Geochemistry*, AGU Geophysical Monograph 266, pages 115–138. John Wiley & Sons, New York.
- Moretti, R., Komorowski, J.-C., Ucciani, G., Moune, S., Jessop, D., de Chabalier, J.-B., Beauducel, F., Bonifacie, M., Burtin, A., Vallée, M., Deroussi, S., Robert, V., Gibert, D., Didier, T., Kitou, T., Feuillet, N., Allard, P., Tamburello, G., Shreve, T., Saurel, J.-M., Lemarchand, A., Rosas-Carbajal, M., Agrinier, P., Le Friant, A., and Chaussidon, M. (2020). The 2018 unrest phase at La Soufrière of Guadeloupe (French West Indies) andesitic volcano: Scrutiny of a failed but prodromal phreatic eruption. *J. Volcanol. Geotherm. Res.*, 393, article no. 106769.
- Moretti, R. and Neuville, D. R. (2021). *Magma Redox Geochemistry*. Geophysical Monograph 266, AGU Geophysical Monograph Series. John Wiley & Sons, Hoboken, NJ, USA.
- Moretti, R. and Stefánsson, A. (2020). Volcanic and geothermal redox engines. *Elements*, 16, 179–184.
- Moune, S., Moretti, R., Burtin, A., Jessop, D. E., Didier, T., Robert, V., Bonifacie, M., Tamburello, G., Komorowski, J.-C., Allard, P., and Buscetti, M. (2022). Gas monitoring of volcanic-hydrothermal plumes in a tropical environment: The case of La Soufrière de Guadeloupe Unrest Volcano (Lesser Antilles). *Front. Earth Sci.*, 10, article no. 795760.
- Moussallam, Y., Edmonds, M., Scaillet, B., Peters, N., Gennaro, E., Sides, I., and Oppenheimer, C. (2016). The impact of degassing on the oxidation state of basaltic magmas: A case study of Kīlauea volcano. *Earth Planet. Sci. Lett.*, 450, 317–325.
- Moussallam, Y., Longpré, M.-A., McCammon, C., Gomez-Ulla, A., Rose-Koga, E. F., Scaillet, B., Peters, N., Gennaro, E., Paris, R., and Oppenheimer, C. (2019a). Mantle plumes are oxidised. *Earth Planet. Sci. Lett.*, 527, article no. 115798.
- Moussallam, Y., Oppenheimer, C., Aiuppa, A., Giudice, G., Moussallam, M., and Kyle, P. (2012). Hydrogen emissions from Erebus volcano, Antarctica. *Bull. Volcanol.*, 74, 2109–2120.
- Moussallam, Y., Oppenheimer, C., and Scaillet, B. (2019b). On the relationship between oxidation state and temperature of volcanic gas emissions. *Earth Planet. Sci. Lett.*, 520, 260–267.
- Moussallam, Y., Oppenheimer, C., and Scaillet, B. (2022). A novel approach to volcano surveillance using gas geochemistry. *C. R. Géosci.*, 356, 71–84.

- Moussallam, Y., Oppenheimer, C., Scaillet, B., Gailard, F., Kyle, P., Peters, N., Hartley, M., Berlo, K., and Donovan, A. (2014a). Tracking the changing oxidation state of Erebus magmas, from mantle to surface, driven by magma ascent and degassing. *Earth Planet. Sci. Lett.*, 393, 200–209.
- Moussallam, Y., Peters, N., Ramírez, C., Oppenheimer, C., Aiuppa, A., and Giudice, G. (2014b). Characterisation of the magmatic signature in gas emissions from Turrialba Volcano, Costa Rica. *Solid Earth*, 5, 1341–1350.
- Ohba, T., Hirabayashi, J., and Yoshida, M. (1994). Equilibrium temperature and redox state of volcanic gas at Unzen volcano, Japan. *J. Volcanol. Geotherm. Res.*, 60, 263–272.
- Oppenheimer, C., Scaillet, B., Woods, A., Sutton, A. J., Elias, T., and Moussallam, Y. (2018). Influence of eruptive style on volcanic gas emission chemistry and temperature. *Nat. Geosci.*, 11, 678–681.
- Roberts, T., Dayma, G., and Oppenheimer, C. (2019). Reaction rates control high-temperature chemistry of volcanic gases in air. *Front. Earth Sci.*, 7, article no. 154.
- Seinfeld, J. H. and Pandis, S. N. (2016). *Atmospheric Chemistry and Physics: From Air Pollution to Climate Change*. John Wiley & Sons, New York, USA.
- Shinohara, H. (2005). A new technique to estimate volcanic gas composition: plume measurements with a portable multi-sensor system. *J. Volcanol. Geotherm. Res.*, 143, 319–333.
- Shinohara, H., Giggenbach, W. F., Kazahaya, K., and Hedenquist, J. W. (1993). Geochemistry of volcanic gases and hot springs of Satsuma-Iwojima, Japan: following Matsuo. *Geochem. J.*, 27, 271–285.
- Shinohara, H., Matsushima, N., Kazahaya, K., and Ohwada, M. (2011). Magma-hydrothermal system interaction inferred from volcanic gas measurements obtained during 2003–2008 at Meakan-dake volcano, Hokkaido, Japan. *Bull. Volcanol.*, 73, 409–421.
- Shinohara, H., Ohminato, T., Takeo, M., Tsuji, H., and Kazahaya, R. (2015). Monitoring of volcanic gas composition at Asama volcano, Japan, during 2004–2014. *J. Volcanol. Geotherm. Res.*, 303, 199–208.
- Shinohara, H., Yokoo, A., and Kazahaya, R. (2018). Variation of volcanic gas composition during the eruptive period in 2014–2015 at Nakadake crater, Aso volcano, Japan. *Earth Planet. Space*, 70, 1–21.
- Stagno, V., Ojwang, D. O., McCammon, C. A., and Frost, D. J. (2013). The oxidation state of the mantle and the extraction of carbon from Earth's interior. *Nature*, 493, 84–88.
- Stix, J. and de Moor, J. M. (2018). Understanding and forecasting phreatic eruptions driven by magmatic degassing. *Earth Planet. Space*, 70, article no. 83.
- Stolper, D. A., Higgins, J. A., and Derry, L. A. (2021). The role of the solid earth in regulating atmospheric O<sub>2</sub> levels. *Am. J. Sci.*, 321, 1381–1444.
- Surono, Jousset, P., Pallister, J., Boichu, M., Buongiorno, M. F., Budisantoso, A., Costa, F., Andreas-tuti, S., Prata, E., Schneider, D., Clarisse, L., Humaida, H., Sumarti, S., Bignami, C., Griswold, J., Carn, S., Oppenheimer, C., and Lavigne, F. (2012). The 2010 explosive eruption of Java's Merapi volcano—A '100-year' event. *J. Volcanol. Geotherm. Res.*, 241–242, 121–135.
- Symonds, R. B., Gerlach, T. M., and Reed, M. H. (2001). Magmatic gas scrubbing: implications for volcano monitoring. *J. Volcanol. Geotherm. Res.*, 108, 303–341.
- Symonds, R. B., Rose, W. I., Bluth, G. J. S., and Gerlach, T. M. (1994). Volcanic-gas studies; methods, results, and applications. *Rev. Mineral. Geochem.*, 30, 1–66.
- Tamburello, G., Moune, S., Allard, P., Venugopal, S., Robert, V., Rosas-Carbajal, M., Deroussi, S., Kitou, G.-T., Didier, T., Komorowski, J.-C., Beauducel, F., De Chabaliere, J.-B., Le Marchand, A., Le Friant, A., Bonifacie, M., Dessert, C., and Moretti, R. (2019). Spatio-temporal relationships between fumarolic activity, hydrothermal fluid circulation and geophysical signals at an arc volcano in degassing unrest: La soufrière of guadeloupe (French West Indies). *Geosciences (Switzerland)*, 9(11), article no. 480.
- Taran, Y. and Zelenski, M. (2015). In *Systematics of Water Isotopic Composition and Chlorine Content in Arc-volcanic Gases*, Geological Society, London, Special Publications 410, pages 237–262. Geological Society of London.
- Warneck, P. (1988). *Chemistry of the Natural Atmosphere*, volume 41 of *International Geophysics Series*. Academic Press, San Diego, CA.
- Watts, S. F. (2000). The mass budgets of carbonyl sulfide, dimethyl sulfide, carbon disulfide and hydrogen sulfide. *Atmos. Environ.*, 34, 761–779.

- Werner, C., Fischer, T. P., Aiuppa, A., Edmonds, M., Cardellini, C., Carn, S., Chiodini, G., Cottrell, E., Burton, M., and Shinohara, H. (2019). Carbon dioxide emissions from subaerial volcanic regions. In *Deep Carbon Past to Present*. Cambridge University Press, Cambridge, UK.
- Zgonnik, V. (2020). The occurrence and geoscience of natural hydrogen: A comprehensive review. *Earth-Sci. Rev.*, 203, article no. 103140.





Research article

Magma degassing and its impact on the Earth's atmosphere: from magma oceans to lava lakes

# Constraining sulphur yields of trachytic and phonolitic volcanic eruptions: Tambora, Vesuvius, Laacher See and Campi Flegrei

Bruno Scaillet<sup>Ⓢ,\*<sup>a</sup></sup>, Clive Oppenheimer<sup>Ⓢ,<sup>b</sup></sup>, Raffaello Cioni<sup>Ⓢ,<sup>c</sup></sup>, Stephane Scaillet<sup>Ⓢ,<sup>a</sup></sup>,  
Yves Moussallam<sup>Ⓢ,<sup>d,e</sup></sup>, Gaëlle Prouteau<sup><sup>a</sup></sup> and Joan Andujar<sup>Ⓢ,<sup>a</sup></sup>

<sup>a</sup> ISTO, CNRS-Université d'Orléans-BRGM, 1a rue de la Férollerie, 45071, Orléans, France

<sup>b</sup> Department of Geography, University of Cambridge, Downing Place, Cambridge, CB2 3EN, UK

<sup>c</sup> Earth Sciences Dept., Università di Firenze, Via La Pira 4 50121 Firenze, Italy

<sup>d</sup> Lamont-Doherty Earth Observatory, Columbia University, New York, USA

<sup>e</sup> American Museum of Natural History, Department of Earth and Planetary Sciences, NY 10024, New York, USA

*E-mail:* [bscaille@cnsr-orleans.fr](mailto:bscaille@cnsr-orleans.fr) (B. Scaillet)

**Abstract.** Evolved alkaline magmas have fuelled renowned large explosive eruptions, including that of Tambora in 1815. Very high sulphur yields to the atmosphere have been suggested for some prominent phonolite–trachyte eruptions, influencing assessments of their potential climatic impacts. However, the implications of alkalinity on volatile abundances in melts remain only partially understood. Here, we draw on available petrological and thermodynamical constraints, accounting for uncertainty in pre-eruptive magma redox state, to quantify pre-eruptive sulphur budgets for several prominent phonolite–trachyte eruptions. We thereby calculate upper limits for sulphur yields for the 13 kyr calBP Laacher See eruption (3–15 Tg S), the plinian component of the 39.85 ka Campanian Ignimbrite (2–9 Tg S), and the 1890 calBCE “Avellino” and 79 CE eruptions of Vesuvius. Our findings demonstrate that alkali-rich magmas do not outstrip dacite or rhyolite arc compositions in respect of sulphur abundance and can inform both climate modelling efforts and the search for the eruptions' signatures in ice core records.

**Keywords.** Eruption, Sulphur, Laacher See, Tambora, Vesuvius, Campi Flegrei.

**Funding.** Labex VOLTAIRE project (ANR-10-LABX-100-01), Equipex PLANEX (ANR-11-EQPX-0036), NERC grant NE/N009312/1.

*Manuscript received 12 June 2024, revised 9 October 2024, accepted 10 October 2024.*

---

\* Corresponding author

## 1. Introduction

Volcanic eruptions can propel large quantities of radiatively important and chemically reactive species into the atmosphere [e.g., Robock *et al.*, 2009, Timmermann, 2012, Oppenheimer, 2002, Oppenheimer *et al.*, 2014, Cadoux *et al.*, 2015]. The atmospheric and climatic consequences have been widely studied drawing on evidence from direct observations [e.g., Guo *et al.*, 2004], indirect and proxy records [e.g., Büntgen *et al.*, 2020] and modelling efforts [e.g., Toohey *et al.*, 2019]. While many factors come into play in influencing the climatic impact of a given eruption, the primary forcing agent is recognised as stratospheric sulphate aerosol and thus estimates of sulphur yields for past eruptions are a first order requirement for efforts to understand their climatic and societal consequences. Much attention has been given to determination of stratospheric sulphur yields but significant uncertainties remain in the estimates [Scaillet and Oppenheimer, 2024]. For example, estimates drawing on evidence from the rock record are sensitive to uncertainties in tephra mass (eruption magnitude), the abundance and composition of any vapour phase in the pre-eruptive reservoir, and the behaviour of volatile elements during storage and eruption [e.g., Marshall *et al.*, 2022, Metcalfe *et al.*, 2023, Venugopal *et al.*, 2020, Schiavi *et al.*, 2020, Schmidt and Black, 2022, Scaillet and Oppenheimer, 2023, 2024].

Sulphur yields can now be estimated with a range of spaceborne sensors [e.g., Pardini *et al.*, 2017, Taylor *et al.*, 2018]. Despite challenges in validation, this approach is regarded as the gold standard of eruptive sulphur yield quantification during an eruption, as it involves spectroscopic measurement of abundances of sulphur-bearing gases and aerosol. Sulphur yields of past events are also estimated from polar ice core records [e.g., Sigl *et al.*, 2015] drawing on understanding of global atmospheric dispersion of point source tracer injections in the stratosphere. This approach also entails substantial uncertainties, for instance in the case of ice core signals that are not attributed to a particular volcano (the vast majority), the source location (and its proximity to the deposition site) is unknown. In effect, measurement of traces (ppb) of the emitted sulphur is used to extrapolate to global sulphur yields (Tg).

The third approach draws on petrological analyses of the erupted rocks [Devine *et al.*, 1984] along

with petrological arguments [Scaillet *et al.*, 2003]. In this case, it is not the emitted sulphur that is measured but rather the non-emitted sulphur that is evaluated, based on analyses of sulphur contents in crystal-hosted glass inclusions and of matrix glass. The difference in these quantities is then used to estimate syn-eruptive sulphur yields by scaling to the estimated total eruptive rock mass [which itself typically has high uncertainty; Engwell *et al.*, 2015, Bonadonna *et al.*, 2015]. Realisation that this approach failed to yield estimates even close to the satellite-measured sulphur yields of eruptions, such as those of El Chichón in 1982 and Pinatubo in 1991, fuelled recognition that volatile-saturated pre-eruptive magmas may already contain an abundant sulphur-rich gas phase [e.g., Luhr *et al.*, 1984, Westrich and Gerlach, 1992, Scaillet *et al.*, 1998, Wallace and Edmonds, 2011]. This became known as the “excess sulphur” problem, and it is particularly acute for eruptions of evolved magmas, though less so for basaltic ones [e.g., Sharma *et al.*, 2004]. The amount of this sulphur is not captured by the “petrologic method” [Devine *et al.*, 1984]. Rather, it has been inferred from wider geochemical, petrological and geophysical knowledge of magma bodies [notably drawing on experimental petrology studies and thermodynamic calculations, e.g., Scaillet and Pichavant, 2003]. An alternative approach uses apatite as a proxy for volatile contents of magmas [e.g., Stock *et al.*, 2016, Humphreys *et al.*, 2021] but this also requires assumptions, in particular how to relate the volatile contents of apatite with those of the coexisting melt and gas, in addition to apatite occurrence. There remain few and sometimes inconclusive constraints on S partitioning between apatite and melt/fluid [e.g., Peng *et al.*, 1997, Parat and Holtz, 2005]. While promising, this method requires further experimental work.

In general, very few eruptions before the satellite remote sensing era have been identified with any degree of confidence in ice core records (this requires geochemical fingerprinting of tephra grains in the ice cores). Thus, when all we have to go on are the proximal deposits of large eruptions, estimates of sulphur yield must rely on petrological and eruption magnitude assessments. While significant progress has been made in understanding the behaviour of sulphur in silicic magmas [e.g., Carroll and Webster, 1994, Scaillet *et al.*, 1998, Clemente *et al.*,

2004, Scaillet and Macdonald, 2006, Keppler, 2010, Zajacz *et al.*, 2012, Masotta *et al.*, 2016], permitting estimation of sulphur yields of quartz-oversaturated felsic arc magmas [e.g., Scaillet *et al.*, 2003], for quartz-undersaturated, or alkali-rich magmas, the constraints are limited. This is despite recognition that the presence of alkalis increases sulphur solubility [e.g., Carroll and Rutherford, 1987, Ducea *et al.*, 1994] and hence sulphur carrying capacity.

In addition to Tambora 1815 [Oppenheimer, 2003], renowned eruptions of alkali-rich phonolite to trachyte magmas include those of Campi Flegrei, Somma-Vesuvius (Italy) and Laacher See (Germany). In the case of the 13 kyr calBP [Reinig *et al.*, 2021] eruption of Laacher See, estimates of sulphur yield range up to 150 Tg [Schmincke *et al.*, 1999] influencing the parameterisation of climate models [e.g., Textor *et al.*, 2003, Niemeier *et al.*, 2020] as well as the search for potential sulphur signatures of the episode in polar ice core records [Baldini *et al.*, 2018, Abbott *et al.*, 2021]. Our aim here is to re-assess sulphur yields of Laacher See and other significant phonolite–trachyte eruptions drawing on improved understanding of volatile behaviour in alkaline magmas and focusing on eruptions for which pre-eruptive conditions—pressure ( $P$ ), temperature ( $T$ ),  $H_2O$  content and, crucially, redox state—are experimentally constrained. We use relationships between the fugacities of key S-bearing species ( $H_2S$ ,  $SO_2$ ) and their concentrations in phonolite liquids to quantify the partial pressures of corresponding species in pre-eruptive magma reservoirs. We focus on the more evolved portions of erupted magmas since they are likely to accumulate volatiles during reservoir growth.

## 2. Methodology

We follow Anderson Jr *et al.* [1989] and Scaillet and Pichavant [2003] in calculating the partial pressures of dissolved volatile species using thermodynamic models and volatile concentrations measured in melt inclusions (MI). We consider primarily the role of  $H_2O$ ,  $CO_2$  and S-bearing species. For the latter, we use fugacity-concentration relationships established by Moncrieff [2000], as reported in Burgisser *et al.* [2012]. Since the melt compositions we are concerned with are broadly phonolitic, we use the water solubility model of Carroll and Blank [1997],

established using a sodic phonolite. For  $CO_2$ , the model used is that of Burgisser *et al.* [2012], which is also calibrated on Na-rich phonolite. As shown below, the majority of eruptions had dissolved  $CO_2$  contents below detection (<20 ppm), indicating partial pressures of  $CO_2$  below 10 MPa, the fluid being essentially a mixture of water and sulphur (+Cl). For any species  $i$ , the relationships between fugacity,  $f_i$ , mole fraction,  $X_i$ , and partial pressure,  $P_i$ , is given by:

$$f_i = \Sigma \gamma_i X_i P_i \quad (1)$$

where  $\gamma_i$  is the fugacity coefficient that describes departure from ideal gas behaviour. In all cases, we have computed  $\gamma_i$  from a Modified Redlich Kwong equation of state using coefficients from Holloway [1987] and Ferry and Baumgartner [1987]. We treat the gas as an ideal mixture of real gases (Lewis and Randall rule), i.e.,  $\gamma_i$  is that of the pure species  $i$  at given  $P$  and  $T$ .

The total pressure is given by:

$$\Sigma P_i = P_{tot} \quad (2)$$

which we can recast as:

$$P_{H_2O} + P_{CO_2} + P_{H_2S} + P_{SO_2} = P_{tot} \quad (3)$$

In the results presented below, the retrieved  $P_{tot}$  was checked against independent phase equilibrium constraints for pre-eruptive conditions. To accommodate uncertainties in  $f_{O_2}$ , we carried out calculations assuming that S is present either as  $H_2S$  (reduced, or around the Quartz-Fayalite-Magnetite buffer, QFM) or  $SO_2$  (oxidized, i.e. 2 log units above QFM).

Evaluating the S yield related to the release of the gas phase present in the reservoir requires assessment of the quantity of this phase, a notoriously challenging task [Wallace *et al.*, 1995]. Geochemical analyses based on trace element behaviour point to proportions ranging from 1 to 6 wt% of the gas phase (expressed as bubbles in the magmatic reservoir) which holds all volatiles, including  $H_2O$ ,  $CO_2$  and S-bearing species, the high end corresponding with the apical portion of evolved magma reservoirs [Wallace *et al.*, 1995]. Gas amounts of 5–6 wt% are thought to correspond to a percolation threshold, beyond which bubbles interconnect, preventing accumulation of higher gas contents [Wallace, 2001]. Comparison of the sulphur yield of eruptions for which both petrological constraints and remote sensing, or ice core constraints on sulphur yield are available shows that, in most cases, both approaches agree if a gas content in

the reservoir of about 5 wt% is assumed [Scaillet *et al.*, 2003].

Estimation of gas content can also be achieved using the bulk vesicularity of pumice clasts, as recently shown for the rhyolite of the Changbaishan (Paektu) Millennium eruption in north Korea [Scaillet and Oppenheimer, 2023]. Here, the bulk gas content of magma at fragmentation (the sum of dissolved and exsolved volatiles) is restored assuming equilibrium conditions between gas and melt for both H<sub>2</sub>O and CO<sub>2</sub> volatiles, which represent more than 95 wt% of the total volatile complement of evolved magmas. The calculation uses established solubility laws of H<sub>2</sub>O and CO<sub>2</sub> in phonolitic liquids [Carroll and Blank, 1997, Burgisser *et al.*, 2012] and a modified Redlich–Kwong equation of state for describing the fugacities of corresponding species in the gas phase [Holloway, 1987]. Once that bulk H<sub>2</sub>O and CO<sub>2</sub> contents are known, the amount of excess gas, if present, at reservoir conditions can be calculated if the pre-eruptive pressure is adequately constrained. The calculation assumes also that the magma retains volatiles during ascent, which has been shown to hold for felsic eruptions along a significant part of their ascent path [e.g., Newman *et al.*, 1988]. The lower melt viscosity of phonolitic magmas [Andújar and Scaillet, 2012] may permit loss of gas during early stages of magma ascent, however.

An example of such calculation is shown in Figure 1, using a bulk vesicularity of 0.75, and pre-eruption *P–T* of 200 MPa and 800 °C. These *P–T* values are typical for evolved reservoirs, including for those feeding phonolitic–trachytic eruptions [Scaillet *et al.*, 2008, Fabbriozio and Carroll, 2008, Andújar *et al.*, 2010]. We show the effect of remaining CO<sub>2</sub> in the matrix glass at fragmentation, for two H<sub>2</sub>O contents in matrix glass (0.5 wt% and 1 wt%), on the restored amount of gas in a reservoir holding a phonolitic melt at 200 MPa and 800 °C. In Figure 1, a magma reaching 10 ppm CO<sub>2</sub> and 0.5 wt% H<sub>2</sub>O in the residual (matrix) glass at fragmentation yields a gas content of 4 wt%. Such a magma would have a silicate melt with 1.05 wt% dissolved H<sub>2</sub>O and 434 ppm dissolved CO<sub>2</sub>. Increasing the residual H<sub>2</sub>O content of the matrix glass at fragmentation to 1 wt% (orange curve) would increase the gas amount to slightly over 5 wt% with the dissolved H<sub>2</sub>O content increasing to 2.46 wt% and the dissolved CO<sub>2</sub> decreasing to 319 ppm.

The residual volatiles in the matrix glass at frag-

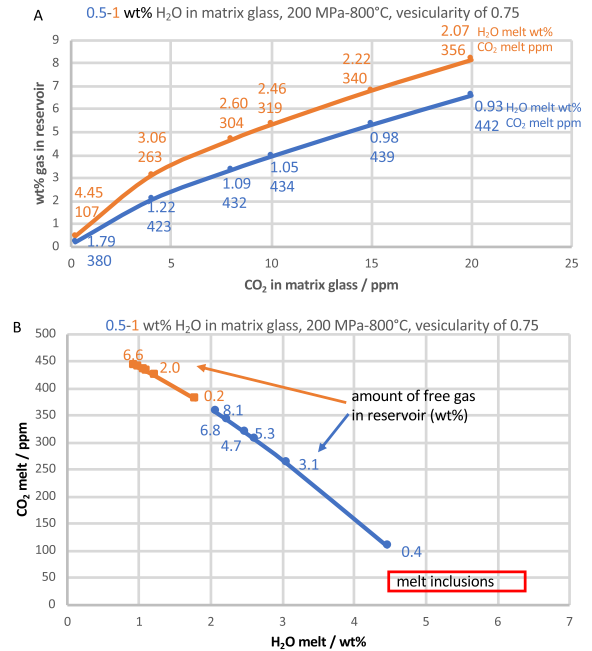


**Figure 1.** (a) evolution of gas mass fraction in the reservoir with the residual CO<sub>2</sub> content in the matrix glass for two H<sub>2</sub>O content in the matrix glass: blue 1 wt% H<sub>2</sub>O and orange 0.5 wt% H<sub>2</sub>O. Both sets of calculations are performed for a terminal bulk vesicularity of 0.75. The dissolved H<sub>2</sub>O (wt%) and CO<sub>2</sub> (ppm) contents of the melt phase in the reservoir are shown along each curve. (b) Same data as in (a) but showing how the dissolved H<sub>2</sub>O and CO<sub>2</sub> contents in the melt vary. The red box shows typical pre-eruptive conditions for phonolitic–trachytic magmas, inferred from the analyses of dissolved volatiles in crystal-hosted glass inclusions.

mentation are poorly constrained for phonolitic eruptions, in particular the CO<sub>2</sub>. For silicic magmas (rhyolites) available data typically show H<sub>2</sub>O in the range 0–2 wt% and up to 20–30 ppm CO<sub>2</sub> [e.g., Newman *et al.*, 1988, Wadsworth *et al.*, 2020] and it is likely that phonolitic magmas display comparable values. In Figure 1b, the same calculations are shown but using a conventional diagram of dissolved H<sub>2</sub>O–CO<sub>2</sub> contents in the silicate melt. The data define a single isobaric trend, showing how the amount of excess gas varies with residual CO<sub>2</sub> for two different residual H<sub>2</sub>O contents. As in Figure 1a, increasing

CO<sub>2</sub> content leads to an increase in the amount of excess gas but also to an increase in dissolved CO<sub>2</sub> content at pre-eruptive conditions. These calculations can be compared with typical pre-eruptive H<sub>2</sub>O–CO<sub>2</sub> contents of phonolitic magmas as inferred from H<sub>2</sub>O–CO<sub>2</sub> analyses in melt inclusions, which typically reveal elevated water contents (up to 6–7 wt%) and CO<sub>2</sub> contents below detection limit [e.g. Cioni, 2000]. Inspection of Figure 1b suggests that phonolitic magmas have excess gas contents corresponding with the low end of the range inferred for silicic magmas [Scaillet *et al.*, 2003, Wallace, 2005].

Since we lack precise knowledge of residual volatiles in phonolitic to trachytic matrix glass at fragmentation, in the following we assume a gas content in the reservoir of 5 wt%, bearing in mind that it likely represents a maximum in most cases.

A critical aspect in performing calculations of S yields is the accuracy of melt sulphur contents, which are widely determined by electron microprobe analyses of glass inclusions in phenocrysts. This instrument affords relatively low detection limits, of order of 50–200 ppm depending on analytical conditions. Figure 2 illustrates how the calculated mass of emitted sulphur varies with melt sulphur contents, based on a notional eruption of 4 km<sup>3</sup> of DRE magma, initially stored at 200 MPa, with 5–6 wt% H<sub>2</sub>O and 20 ppm CO<sub>2</sub> in melt along with sulphur, and coexisting with 5 wt% of excess gas. The calculations are shown for both reduced and oxidized conditions. For the reduced case, taking the case of a magma whose pre-eruptive S content is at 200 ppm (and 5 wt% H<sub>2</sub>O in melt), produces a yield of about 9.3 Tg S. Varying the S abundance by ±50 ppm corresponds to a range in the S yield from 5.3 Tg (150 ppm S) to 14.3 Tg (250 ppm). In other words a typical 50 ppm analytical uncertainty, equivalent to the standard deviation of that element in a group of melt inclusions of a single event, propagates into 50% uncertainty in the calculated S yield from the gas phase.

While the situation for oxidized conditions seems less critical, an uncertainty of order 50% in S yield still emerges. The two curves shown for reduced conditions illustrate also that the melt water content is a critical parameter. An increase of H<sub>2</sub>O content of 1 wt% (from 5 to 6 wt%) for the same magma reduces S yield by around 30% to 6.3 Tg. It is thus essential to quantify as precisely as possible pre-eruptive conditions in order to calculate volatile yields associated

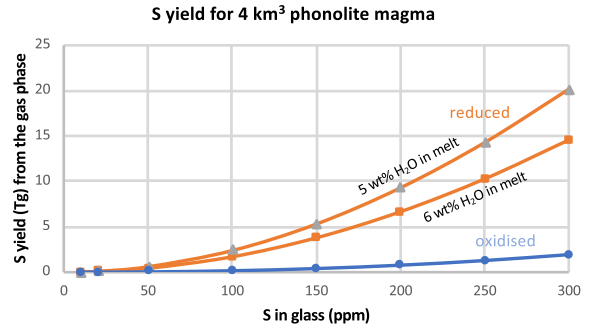


**Figure 2.** Variation of the sulphur yield with pre-eruptive melt sulphur content (S in glass) for a phonolitic magma stored at 200 MPa, 760 °C and with 5 wt% excess gas, calculated for either reduced (pyrrhotite-bearing) or oxidized conditions. For reduced conditions, results are shown for two pre-eruptive melt water contents. A variation in ±50 ppm of sulphur in matrix glass corresponds to a variation of the calculated sulphur yield of ±50%.

with volcanic eruptions.

### 2.1. Caveats

Our method is primarily aimed at estimating the S content of bubbles, whether in the residual melt or trapped along with a melt inclusion inside a phenocryst. If at equilibrium, the bubble composition is independent of its location (inside a melt inclusion within the crystal or outside the crystal). Methods have been developed to determine the composition of gas bubbles coexisting with melt inclusions in phenocrysts [e.g., Wallace *et al.*, 2015, 2021, Aster *et al.*, 2016], including their solid compounds or precipitates [e.g. Venugopal *et al.*, 2020, Schiavi *et al.*, 2020]. These reveal that a significant part of CO<sub>2</sub> and S of the MI and coexisting bubble in basaltic rocks resides in the bubble. What could affect our calculations is if the bubbles in the melt inclusions are shrinkage bubbles arising from cooling, or in other words, if exsolution of volatiles has occurred after entrapment as inferred for mafic compositions [e.g. Wallace *et al.*, 2015, Venugopal *et al.*, 2020, Schiavi *et al.*, 2020], thereby changing the amount of S (and CO<sub>2</sub>) dissolved in the melt inclusion pre-eruptively, which would change the corresponding fugacities. However, while exsolution during cooling is conceivable for low viscous mafic melts, the colder and viscous

felsic melts we consider here are much less susceptible. The fact that S contents of matrix glass are comparable to those of melt inclusions in explosively erupted felsic magmas [e.g., Westrich and Gerlach, 1992] is direct evidence for limited exsolution of S before the glass transition temperature is crossed.

Conversely, some of the S present in the excess fluid in the reservoir could condense as a solid phase during eruption (i.e. upon cooling) [Rose Jr, 1977, Schmauss and Keppler, 2014], such as shown for the Pinatubo 1991 eruption [Jakubowski *et al.*, 2002]. This process would reduce the amount of S released to the atmosphere. An additional process excluded in our calculations is breakdown of S-bearing minerals, such as pyrrhotite or anhydrite, during magma ascent. For “cold” magmas, however, this process is kinetically inhibited, as shown by Gerlach *et al.* [1996] for the 1991 Pinatubo eruption.

The preceding discussion illustrates some key sources of uncertainty in the petrologic method, in addition to uncertainties in eruption magnitude and proportion of exsolved fluid, which both scale linearly with S yield. In most cases, eruption magnitude is uncertain at least to a factor of two [Scaillet and Oppenheimer, 2024]. While these sources of uncertainty may seem very large, even spaceborne observations of eruption yields are subject to comparable uncertainty, as are extrapolations of ice core S abundances to total S yields to the stratosphere.

### 3. Application

The essential figures calculated for each event are listed in Table 1, while Figure 3 compares the S content of the corresponding fluid phase with that estimated for other arc-related magmas.

#### 3.1. *Tambora*

We first consider the 1815 eruption of Tambora, for which independent estimates of sulphur yield are available based on recorded deposition of sulphur in bipolar ice cores. These indicate a stratospheric injection of 28 Tg of S [Toohey and Sigl, 2017], approximately three times the amount measured for the Pinatubo emission. A recent re-evaluation of volatile yields (based on melt inclusions) has concluded that about 74 Tg S were emitted from melt degassing [Pouget *et al.*, 2023]. The eruption, with an estimated

output of 30–40 km<sup>3</sup> DRE of magma [Self *et al.*, 2004, Kandlbauer and Sparks, 2014] is around 4–8 times greater in magnitude than that of Pinatubo. From Self *et al.* [2004] and Andújar and Scaillet [2012], the magma was stored at a pressure of around 100 MPa, a temperature of 935 °C, with a melt water content of about 3 wt% at an  $fO_2$  around QFM+2. The average sulphur content of melt inclusions ranges from 689 to 775 ppm [Self *et al.*, 2004, Pouget *et al.*, 2023] and in the following we take a value midway between these two studies (732 ppm).

For reduced conditions, the fluid phase would have more than 30 wt% sulphur, while for oxidised conditions the sulphur content would be around 11 wt% (Table 1, Figure 3). For a 5 wt% gas phase in the reservoir and 35 km<sup>3</sup> DRE of magma, the upper bounds for the sulphur released from the excess gas are 1415 Tg (reduced) and 502 Tg (oxidised), the lower value being already more than 10 times the stratospheric S injection estimated based on ice core records. For 1 wt% excess gas, the corresponding amounts are 283 and 100 Tg S, respectively. Considering the inferred high  $fO_2$  [Self *et al.*, 2004], the lower bounds of these ranges seem more appropriate. This suggests that had the reservoir been gas-saturated, the amount of such a free gas phase was <1 wt%, or <0.5 wt% considering that a significant part of S yield comes from melt degassing alone [Self *et al.*, 2004, Pouget *et al.*, 2023]. The low vesicularity of Tambora pumices [<60%, Suhendro *et al.*, 2021] compared with other plinian eruptions of felsic magmas [70–80%, Thomas *et al.*, 1994], is consistent with a low pre-eruptive excess gas content. This first example already illustrates that the assumption of abundant gas in the reservoir may not be universal, calling for a case by case approach when calculating past S emissions. Gas loss prior to eruption during magma storage has been inferred for the so-called Millenium Eruption of Paektu [Scaillet and Oppenheimer, 2023] and the 1815 Tambora event may be an additional example.

#### 3.2. *Laacher See*

Pre-eruptive conditions have been experimentally determined by Harms *et al.* [2004] and Berndt *et al.* [2001]. These works concluded that the uppermost part of the magma reservoir, which yielded most (4 km<sup>3</sup> DRE) of the erupted material was

**Table 1.** Volatile contents, fluid phase compositions and calculated sulphur yields of famous phonolite–trachyte eruptions

	Tambora		Laacher See		Campanian Ignimbrite (Plinian)		Vesuvius Pompei		Vesuvius Avellino	
	Reduced	Oxidised	Reduced	Oxidised	Reduced	Oxidised	Reduced	Oxidised	Reduced	Oxidised
P, bar	1010	800	1796	1760	1950	1950	1940	1920	2020	1900
T, °C <sup>a</sup>	935	935	760	760	760	760	815	815	785	785
H <sub>2</sub> O, wt% <sup>a</sup>	0.030	0.030	0.056	0.056	0.060	0.060	0.063	0.063	0.060	0.060
CO <sub>2</sub> , ppm <sup>a</sup>	20	20	20	20	20	20	20	20	20	20
S, ppm <sup>a</sup>	732	732	270	270	100	100	200	200	560	560
<i>f</i> H <sub>2</sub> O, bar <sup>b</sup>	510	510	1209	1209	1330	1330	1422	1422	1330	1330
<i>f</i> CO <sub>2</sub> , bar <sup>c</sup>	197	197	197	197	197	197	197	197	197	197
<i>f</i> H <sub>2</sub> S, bar <sup>d</sup>	331		45		6		25		194	
<i>f</i> SO <sub>2</sub> , bar <sup>e</sup>		95		10		1		5		52
PH <sub>2</sub> O, bar	555	548	1639	1633	1830	1830	1799	1797	1763	1748
PCO <sub>2</sub> , bar	154	162	122	123	116	116	117	118	114	118
PH <sub>2</sub> S, bar	296	0	35	0	5	0	19	0	143	0
PSO <sub>2</sub> , bar	0	88	0	7	0	1	0	3	0	37
Fluid composition, molar										
XH <sub>2</sub> O	0.550	0.685	0.912	0.928	0.938	0.938	0.927	0.936	0.873	0.920
XCO <sub>2</sub>	0.152	0.203	0.068	0.070	0.060	0.060	0.060	0.061	0.056	0.062
XH <sub>2</sub> S	0.293		0.020		0.002		0.010		0.071	
XSO <sub>2</sub>		0.110		0.004		0.000		0.002		0.019
Fluid composition, wt%										
H <sub>2</sub> O	0.3725	0.4355	0.8179	0.8330	0.8621	0.8647	0.8485	0.8569	0.7631	0.8067
CO <sub>2</sub>	0.2525	0.3151	0.1488	0.1538	0.1337	0.1341	0.1349	0.1373	0.1202	0.1334
H <sub>2</sub> S	0.3750		0.0333		0.0042		0.0166		0.1167	
SO <sub>2</sub>		0.2494		0.0131		0.0012		0.0058		0.0599
S fluid, wt%	0.3516	0.1247	0.0312	0.0066	0.0039	0.0006	0.0155	0.0029	0.1094	0.0299
Bulk S content, wt%	0.352	0.125	0.156	0.033	0.020	0.003	0.078	0.015	0.547	0.150
Fluid, wt%	0.01	0.01	0.05	0.05	0.05	0.05	0.05	0.05	0.05	0.05
vol magma, km <sup>3</sup>	35	35	4.04	4.04	23	23	0.50	0.5	0.1	0.1
mass S, Tg	283	100	14.5	3.1	10.3	1.6	0.89	0.17	1.26	0.34

<sup>a</sup> The pre-eruptive temperature. dissolved H<sub>2</sub>O, S and CO<sub>2</sub> contents come from: Tambora: Self et al. [2004], Pouget et al. [2023], Andújar and Scaillet [2012]; Laacher See: Harms et al. [2004], Berndt et al. [2001], Harms and Schmincke [2000]; Campanian Ignimbrite: Signorelli et al. [2001], Marianelli et al. [2006]; Vesuvius: Scaillet et al. [2008], Cioni [2000], Signorelli et al. [1999].

<sup>b</sup>  $f_{\text{H}_2\text{O}} = 10^{((\text{Log}(\text{wt}\% \text{H}_2\text{O}) - \text{Log}(0.0329))/0.7238)}$ , from Carroll and Blank [1997].

<sup>c</sup>  $f_{\text{CO}_2} = 10^{((\text{Log}(\text{wt}\% \text{CO}_2) - \text{Log}(0.000005611))/1.112)}$ , from Burgisser et al. [2012].

<sup>d</sup>  $f_{\text{H}_2\text{S}} = 10^{((\text{Log}(\text{wt}\% \text{S}) - \text{Log}(0.004))/0.501)}$ , from Burgisser et al. [2012].

<sup>e</sup>  $f_{\text{SO}_2} = 10^{((\text{Log}(\text{wt}\% \text{S}) - \text{Log}(0.01))/0.437)}$ , from Burgisser et al. [2012].

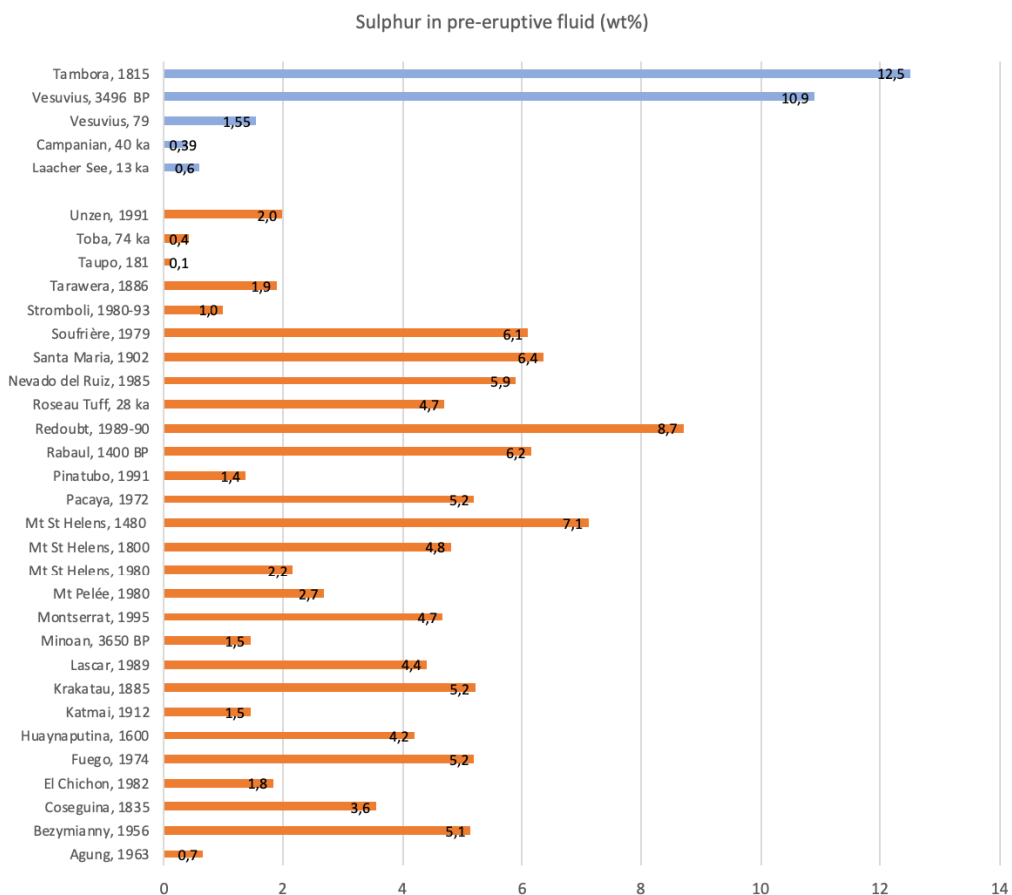


**Figure 3.** The sulphur content of the excess gas phase (in wt%) in the reservoir of several volcanic eruptions, calculated using petrologic and thermodynamic constraints on pre-eruptive  $P$ - $T$ - $H_2O$ - $fO_2$  conditions. Data for calco-alkaline magmas are from Scaillet *et al.* [2003]. See text for details of calculations.

comparatively cool (about 760 °C), water-rich (5–6 wt% dissolved  $H_2O$ ) and possibly gas-saturated, and in the pressure range of 150 to 200 MPa. This magma appears to have been relatively oxidised, based on  $S^{6+}/S^{2-}$  ratios in melt inclusions [Harms and Schmincke, 2000] and the presence of hauyne in the mineral assemblage [Wörner and Schmincke, 1984, Berndt *et al.*, 2001]. The sulphur coming from melt degassing of that part has been estimated at 0.45 Tg [Harms and Schmincke, 2000]. The low-ermost, more mafic part of the erupted magma (2.3 km<sup>3</sup> DRE), is thought to have been gas-free, reflecting its lower water content (4 wt%  $H_2O$ ). Accordingly, its contribution to the sulphur yield corresponds to the sulphur exsolved from melt during

decompression, estimated as 1.45 Tg [Harms and Schmincke, 2000].

Analyses of melt inclusions from the upper part of the Laacher See reservoir indicate a pre-eruptive S content average of 270 ppm [Harms and Schmincke, 2000]. Calculations of S-species fugacities and partial pressures, and the corresponding fluid phase compositions are reported in Table 1. The sulphur content of the fluid varies between 3.1 wt% (reduced) and 0.7 wt% (oxidised), falling within the range estimated for typical arc magmas [Scaillet *et al.*, 2003] (Figure 3). Assuming an upper value of gas content in reservoirs of 5 wt% (which includes the contribution of all gas species) and taking a magma DRE volume of 4 km<sup>3</sup>, then, depending on redox state, the Laacher



See eruption may have released up to 1.5 Tg (oxidised) or 13.6 Tg (reduced) sulphur in addition to that released by the melt [ $0.45 + 1.45 = 1.9$  Tg, Harms and Schmincke, 2000]. This amounts to a total release of sulphur in the range 3–15 Tg.

### 3.3. *Campanian ignimbrite*

The 39.85 ka BP [Giaccio *et al.*, 2017] Campanian Ignimbrite erupted an estimated 155–265 km<sup>3</sup> DRE (or  $4.1\text{--}6.9 \times 10^{14}$  kg) of magma [Marti *et al.*, 2016, Silleni *et al.*, 2020]. Phase equilibrium constraints show that the upper part of the magma body was stored at pressures of 140 to 200 MPa, at a temperature of 740–780 °C, and at or close to H<sub>2</sub>O saturation, i.e. with dissolved H<sub>2</sub>O in the melt of about 6 wt% [Fabrizio and Carroll, 2008], the latter consistent with melt inclusion constraints [Marianelli *et al.*, 2006]. These temperature estimates are significantly lower than those based on clinopyroxene-melt thermometry [900–950 °C; Forni *et al.*, 2016], suggesting that clinopyroxene may record early stages of magma evolution and not later pre-eruptive conditions.

The pre-eruptive sulphur content of the melt has been studied in some detail by Signorelli *et al.* [2001] by analysing melt inclusions in phenocrysts belonging to the early plinian phase of the event, which ejected an estimated 23 km<sup>3</sup> DRE of magma [Marti *et al.*, 2016]. Melt inclusions in phenocrysts inferred to record pre-eruptive conditions (salitic pyroxenes) have sulphur contents below the detection limit of electron microprobe (EMPA) (approximately 200 ppm for the given analytical conditions). Whole rock analyses (which are representative of matrix glass analyses owing to the low crystal content of the rock of about 5%) indicate values of 110–140 ppm of undegassed sulphur [Signorelli *et al.*, 2001]. Sulphur measurements made by Marianelli *et al.* [2006] of various MI from both the fallout or ignimbrite deposits range from below 100 ppm for the H<sub>2</sub>O-rich MI to over 500 ppm for H<sub>2</sub>O-poor MI. For our calculations, we take a pre-eruptive sulphur content of 100 ppm, assuming that the H<sub>2</sub>O-rich portion represents the top part of the reservoir which fueled the plinian column. The prevalence of pyrrhotite inclusions in pyroxene suggests reduced conditions [Signorelli *et al.*, 2001]. MELTs simulation of liquid lines of descent has also suggested that the redox state during crystallization was around QFM [Fowler *et al.*,

2007]. Some petrological information on volatiles is available for both H<sub>2</sub>O and CO<sub>2</sub> but not for sulphur for the voluminous ignimbrite component of the deposit [Moretti *et al.*, 2019], precluding evaluation of its pre-eruptive sulphur budget.

The results (Table 1) indicate a sulphur content of the gas phase of 0.4 wt% under reduced conditions (Figure 3). For the 23 km<sup>3</sup> (DRE) magma erupted in the plinian phase, the sulphur yield arising from exsolved gas (5 wt%) in the reservoir under reduced conditions amounts to 9.7 Tg. This is similar to the 10 Tg S erupted by the 1991 Pinatubo eruption which ejected 5 km<sup>3</sup> DRE of magma [Guo *et al.*, 2004], underscoring the fact that alkaline magmas do not necessarily eject more S than calc-alkaline magmas. Similar calculations performed for oxidised conditions (all SO<sub>2</sub>) yield a sulphur fluid content of 0.15 wt% (Figure 3) and a bulk sulphur yield of 0.8 Tg, which is a tenth of the reduced scenario. Taking the higher estimate inferred for the plinian phase as representative of the entire erupted magma would imply a total S yield of order 100 Tg S. Note, however, that this scaling implies a constant gas content in the reservoir, which is unlikely considering the propensity of gas bubbles to migrate upwards, as demonstrated for the Bishop Tuff [Wallace *et al.*, 1995]. It also assumes that all eruptive components (plinian, ignimbrite) are equally able to release their volatiles into the atmosphere, which is also unlikely [e.g., Pecchia *et al.*, 2023].

### 3.4. *Vesuvius*

The erupted volume of phonolite to tephriphonolite magmas for the renowned 79 CE eruption is estimated as 1.5 km<sup>3</sup> DRE [Cioni *et al.*, 2008], around a third that of Pinatubo's 1991 eruption. Pre-eruptive conditions of the phonolite magma have been defined via phase equilibrium and melt inclusion studies [Cioni, 2000, Scaillet *et al.*, 2008] indicating a reservoir pressure of  $200 \pm 20$  MPa, temperature of  $815 \pm 10$  °C and water-rich conditions (6–6.5 wt%). The sulphur content of phonolitic melt inclusions was found to be below the EMPA detection limit [200 ppm, Cioni, 2000], therefore we take this figure as the maximum sulphur concentration at the top of the reservoir. Similarly, the CO<sub>2</sub> content was found to be below the FTIR analysis detection limit [Cioni, 2000], and therefore we use a pre-eruptive

value of 20 ppm. Redox conditions have been estimated to lie around the NNO solid buffer, consistent with presence of sulphide globules.

For these conditions, our calculations indicate that the fluid phase in the apical portion of the magma body had a sulphur content of 1.6 wt% (Table 1, Figure 3), if reduced, corresponding to a sulphur yield for the phonolitic part of the deposit [about 0.5 km<sup>3</sup> DRE, Cioni *et al.*, 2008] of around 0.8 Tg, comparable to that released by the 1980 El Chichón eruption [Mexico, Krueger *et al.*, 2008]. Alternatively, for oxidising conditions, with SO<sub>2</sub> prevalent over H<sub>2</sub>S in the fluid, then we calculate a sulphur content of the fluid of 0.3 wt% yielding 0.1 Tg of sulphur to the atmosphere.

Pre-eruptive conditions for the Bronze Age Avellino plinian eruption, dated 1890 calBCE [Sevink *et al.*, 2021], are similar to those for the 79 CE “Pompeii” eruption in terms of *P–T–H<sub>2</sub>O* [Scaillet *et al.*, 2008, Balcone-Boissard *et al.*, 2012]. The sulphur content appears to have been higher than for the 79 CE eruption, averaging 560 ppm [Signorelli *et al.*, 1999]. This gives a sulphur content in the fluid of 11 wt% for reduced, or 3 wt% for oxidised, conditions. The modest magnitude, estimated as 0.9 km<sup>3</sup> DRE, of which 0.1 km<sup>3</sup> were phonolite [Cioni *et al.*, 2008, Sulpizio *et al.*, 2010], translates into a sulphur yield of less than 1.5 Tg in both cases (1.2–0.17 Tg, respectively).

## 4. Discussion

Our estimated upper limits for the sulphur yields of these renowned eruptions are comparatively modest, with the possible exception of the Campanian Ignimbrite. The restored gas+melt S contents (i.e. S content of the magma before eruption, excluding that locked in sulphide/sulphate minerals, which is not available for degassing) range from 37 ppm up to 5130 ppm (Table 1). In detail, considering the likely redox state (with regard to S) of erupted magmas (oxidized for Laacher See and sulphide-bearing for the others), the bulk content of S is in general of order several 10<sup>2</sup> ppm and not several 10<sup>3</sup> ppm, except for Avellino. This parameter is compared with the values calculated for calc-alkaline magmas by Scaillet *et al.* [2003] using the same general methodology (Figure 4).

Excluding the case of Avellino eruption, the bulk S contents of alkaline magmas appear to be slightly lower than those of arc magmas. This could reflect the oxidized nature of calc-alkaline magmas which allows efficient mafic-to-felsic S transfer during fractionation, by inhibiting extensive sulphide fractionation [e.g. Scaillet and Macdonald, 2006]. However, the case of Laacher See, an oxidized yet S-poor magma, does not fit with such a scenario. The apparent low S content of alkaline felsic magmas may primarily reflect the source rather than a process but additional data are clearly needed to furnish a more robust statistical lens on this question.

The sulphur yield of alkaline magmas is positively correlated with the volume (DRE) of magma emitted, falling along the same trend defined by arc magmas (Figure 5). At a given volume a dispersion of 1–2 orders of magnitude in sulphur yield is apparent, in particular for large eruptions, stressing that eruption size alone is not a good guide to S yield (and potential climate impact).

Below we consider our S estimates for alkaline magmas in the light of previous estimates, and discuss their relevance in the context of climate proxies and modelling efforts.

### 4.1. *Laacher See*

Schmincke *et al.* [1999] and Harms and Schmincke [2000] estimated syn-eruptive exsolution and degassing of order 2 Tg S for the Laacher See eruption. Drawing an analogy with Pinatubo 1991, Schmincke *et al.* [1999] suggested the total yield could have been as much as 150 Tg S. Based on more specific consideration of the mineralogy and petrology of Laacher See’s products, Harms and Schmincke [2000] suggested a total yield of at least 10 Tg S, speculating that it may have been “appreciably more”. A subsequent work acknowledging the implications of redox state suggested a range of 1.7–49 Tg S [Textor *et al.*, 2003]. More recently, Baldini *et al.* [2018] argued for a release of order 42 Tg S drawing on scaling arguments and sulphur emissions data for other non-basaltic eruptions. This high emission led them to suggest a prominent sulphur anomaly in the Greenland Ice Sheet Project 2 (GISP2) core might represent the Laacher See eruption, though this match has been discounted by subsequent high-precision dating of the eruption [Reinig *et al.*, 2021]. They also

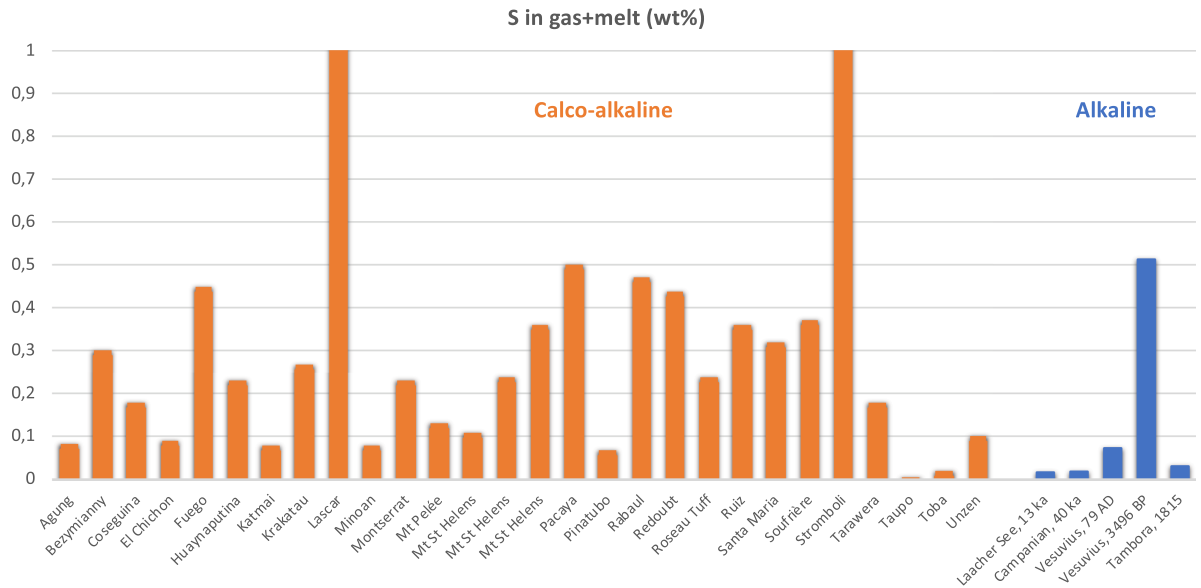


**Figure 4.** The calculated bulk sulphur content stored in both melt and pre-existing gas phases. Data from calco-alkaline magmas are from Scaillet *et al.* [2003]. The values corresponding to Lascar and Stromboli volcanoes are beyond the range shown (7 and 36 wt% sulphur respectively).

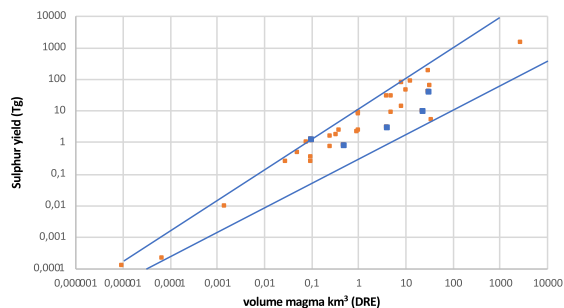


**Figure 5.** Relationship between volume of magma erupted and corresponding sulphur yield for calco-alkaline (orange) and alkaline (blue) magmas. The data for calco-alkaline magmas are from Scaillet *et al.* [2003].

suggested that with such a high sulphur yield, the eruption may have played a role in triggering the Younger Dryas.

A study by Graf and Timmreck [2001] presented a simulation of the climate response to the Laacher See eruption, based on a 7.5 Tg S injection. Though not intended as palaeoclimate simulations, work by Niemeier *et al.* [2020] nevertheless has some bearing on understanding dispersal of the Laacher See ash

and gas emissions and their radiative effects. They modelled sulphur chemistry and ash dispersion for a range of scenarios predicated on a “Laacher See-type” eruption with 0.75, 7.5 and 50 Tg S emissions. Based on our upper limit of 3–15 Tg of S, the lower emission scenarios would be more representative for understanding the potential climatic impacts of the Laacher See eruption, and for targeting any search of polar ice core records for its signature (which will ultimately rest on geochemical fingerprinting of ash grains). We stress that the oxidised nature of erupted rocks points to an S yield for the Laacher See event lying at the lower end of our calculated range, *i.e.* 3 Tg S.

The 3 Tg S estimate corresponding to oxidised conditions, as suggested by petrological arguments, may seem counterintuitive but the lower sulphur content of the gas phase at high  $fO_2$  is an unavoidable consequence of the higher solubility of sulphur in silicate melt at high  $fO_2$  [Carroll and Rutherford, 1987]: in other words higher sulphur contents are achieved with lower  $P_{SO_2}$  relative to  $P_{H_2S}$ : As readily apparent from Equation (1), a lower  $P_{SO_2}$  translates into a lower mole fraction of  $SO_2$  in the coexisting fluid phase, and thus a lower sulphur content.

#### 4.2. Campanian ignimbrite

Our calculations for the Campanian Ignimbrite allow for a sizeable sulphur release (up to an order of magnitude greater than that of the 1991 Pinatubo eruption). However, they are not consistent with far higher estimates, exceeding 1 Pg S [Scaillet *et al.*, 2003, and reported in Fedele *et al.*, 2007]. Meanwhile, Marti *et al.* [2016] estimated a yield of 84–89 Tg S. Clearly, it is the mass of erupted magma that makes this event potentially important from the viewpoint of S yield, not intrinsically high S content of the magma (Figure 2).

Curiously, very few data are presently available for S content in MI in minerals from the different CI deposits. This is probably because most of the MI have S concentrations below typical EMPA detection limits, although some data [Webster *et al.*, 2003] suggest SO<sub>2</sub> contents up to 2800 ppm. The genesis of the CI magma is debated, and reflects complex open-system processes of crystallization, assimilation and recharge [Fowler *et al.*, 2007]. Based on MI data, Marianelli *et al.* [2006] suggested that the plinian phase (corresponding to >20 km<sup>3</sup> of magma) was fed by magma which had ascended from the main magma body to a depth of 2–3 km depth. If this is the case, the presence of a large amount of fluid phase in the deeper (6–8 km) reservoir could be questioned. Recent work has also suggested that a large part of the magma erupted derived from thermal reactivation of a large body of crystal mush in the deeper reservoir [Forni *et al.*, 2016, Di Salvo *et al.*, 2020]. In this scenario, the process by which a free, S-bearing, fluid phase accumulates in the reservoir is unclear [see Parmigiani *et al.*, 2016]. Further progress in estimating the S release to the atmosphere for CI eruption requires deeper understanding of the petrogenesis of the magma combined with more comprehensive MI studies. The behaviour of volatiles associated with ignimbrite formation (*i.e.*, processes accompanying and following column collapse) also requires further study [*e.g.*, Peccia *et al.*, 2023].

#### 4.3. Vesuvius

We note that our low estimated yield of sulphur for the 79 CE eruption is consistent with the lack of a prominent sulphur anomaly in Greenland ice cores at depths consistent with the age of the 79 CE eruption [Plunkett *et al.*, 2022].

### 5. Concluding remarks

Our calculations highlight the important role of redox conditions, with estimates of sulphur yields for the considered eruptions differing by an order of magnitude depending on whether reduced or oxidised conditions apply. Clearly oxidising conditions, which enhance the solubility of sulphur in silicate melts, limit sulphur partition into the fluid phase. Other factors being equal, higher temperature should have the same effect because increasing temperature increases sulphur solubility in silicate melts [*e.g.*, Clemente *et al.*, 2004].

The role of chlorine needs to be addressed as well. Experiments have shown that addition of chlorine increases the solubility of sulphur by a factor of up to two in rhyodacite melt [Botcharnikov *et al.*, 2004]. Phonolite and trachyte magmas are generally Cl-rich [*e.g.*, Signorelli and Carroll, 2000], hence an abundance of chlorine may affect sulphur behaviour as well. The results of Botcharnikov *et al.* [2004] suggest that our calculated sulphur contents for the gas phase could be overestimated by 50% or more. We note however that in the case of Vesuvius, whose mafic melt inclusions hold up to 2000 ppm S [Cioni *et al.*, 1995], the Cl-rich character of felsic MI (up to 1 wt% Cl) did not act to sustain high S contents during magma evolution, possibly because sulphur was continuously scavenged into the fluid during fractionation.

Our results clearly discount any suggestion that alkaline magmas, *i.e.*, trachytes and phonolites, are special in respect of sulphur emissions during explosive eruptions. Excluding perhaps the case of Campanian Ignimbrite, the other eruptions we have considered yield sulphur emissions comparable with, or even lower than, those associated with the 1991 Pinatubo eruption. It appears also that there is considerable variability between alkaline magmas. Without robust petrological control, simple extrapolation from one case to another (even for similar chemistries such as with Vesuvius 79 CE and Avellino) is inadvisable.

While we restrict our work to only four centres for which volcanological and petrological knowledge is extensive, we note that many other alkaline provinces deserve similar attention: oceanic island volcanoes can erupt voluminous quantities of trachyte or phonolite, such as manifested in the

Canary islands [Andújar *et al.*, 2008]. Further prominent examples include the Kenyan flood phonolites, which comprise more than 50,000 km<sup>3</sup> of Miocene lavas and tephra deposits [Macdonald, 2002], and alkaline volcanic centres of the West Antarctic Rift System. More experimental work is needed to quantify the S behaviour in alkaline undersaturated magmas, in particular in the presence of a multicomponent fluid phase, in addition to the requirements for detailed petrological understanding of erupted products.

### Declaration of interests

The authors do not work for, advise, own shares in, or receive funds from any organization that could benefit from this article, and have declared no affiliations other than their research organizations.

### Funding

This work was partly funded by labex VOLTAIRE project (ANR-10-LABX-100-01) and equipex PLANEX (ANR-11-EQPX-0036). CO acknowledges support from NERC grant NE/N009312/1.

### Acknowledgements

The manuscript greatly benefited from the constructive comments of two anonymous reviewers and from the efficient editorial handling of Francois Chabaux.

### References

- Abbott, P. M., Niemeier, U., Timmreck, C., *et al.* (2021). Volcanic climate forcing preceding the inception of the Younger Dryas: implications for tracing the Laacher See eruption. *Quater. Sci. Rev.*, 274, article no. 107260.
- Anderson Jr, A. T., Newman, S., Williams, S. N., Druitt, T. H., Skirius, C., and Stolper, E. (1989). H<sub>2</sub>O, CO<sub>2</sub>, Cl, and gas in Plinian and ash-flow Bishop rhyolite. *Geology*, 17(3), 221–225.
- Andújar, J., Costa, F., and Martí, J. (2010). Magma storage conditions of the last eruption of Teide volcano (Canary Islands, Spain). *Bull. Volcanol.*, 72, 381–395.
- Andújar, J., Costa, F., Martí, J., Wolff, J. A., and Carroll, M. R. (2008). Experimental constraints on pre-eruptive conditions of phonolitic magma from the caldera-forming El Abrigo eruption, Tenerife (Canary Islands). *Chem. Geol.*, 257(3–4), 173–191.
- Andújar, J. and Scaillet, B. (2012). Relationships between pre-eruptive conditions and eruptive styles of phonolite–trachyte magmas. *Lithos*, 152, 122–131.
- Aster, E. M., Wallace, P. J., Moore, L. R., Watkins, J., Gazel, E., and Bodnar, R. J. (2016). Reconstructing CO<sub>2</sub> concentrations in basaltic melt inclusions using Raman analysis of vapor bubbles. *J. Volcanol. Geotherm. Res.*, 323, 148–162.
- Balcone-Boissard, H., Boudon, G., Ucciani, G., Villemant, B., Cioni, R., Civetta, L., and Orsi, G. (2012). Magma degassing and eruption dynamics of the Avellino pumice Plinian eruption of Somma–Vesuvius (Italy). Comparison with the Pompeii eruption. *Earth Planet. Sci. Lett.*, 331, 257–268.
- Baldini, J. U., Brown, R. J., and Mawdsley, N. (2018). Evaluating the link between the sulfur-rich Laacher See volcanic eruption and the Younger Dryas climate anomaly. *Clim. Past*, 14(7), 969–990.
- Berndt, J., Holtz, F., and Koepke, J. (2001). Experimental constraints on storage conditions in the chemically zoned phonolitic magma chamber of the Laacher See volcano. *Contrib. Mineral. Petrol.*, 140(4), 469–486.
- Bonadonna, C., Biass, S., and Costa, A. (2015). Physical characterization of explosive volcanic eruptions based on tephra deposits: propagation of uncertainties and sensitivity analysis. *J. Volcanol. Geotherm. Res.*, 296, 80–100.
- Botcharnikov, R. E., Behrens, H., Holtz, F., Koepke, J., and Sato, H. (2004). Sulphur and chlorine solubility in Mt. Unzen rhyodacitic melt at 850 C and 200 MPa. *Chem. Geol.*, 213(1–3), 207–225.
- Büntgen, U., Arseneault, D., Boucher, É., *et al.* (2020). Prominent role of volcanism in Common Era climate variability and human history. *Dendrochronologia*, 64, article no. 125757.
- Burgisser, A., Oppenheimer, C., Alletti, M., Kyle, P. R., Scaillet, B., and Carroll, M. R. (2012). Backward tracking of gas chemistry measurements at Erebus volcano. *Geochem. Geophys. Geosyst.*, 13(11), article no. Q11010.
- Cadoux, A., Scaillet, B., Bekki, S., Oppenheimer,

- C., and Druitt, T. H. (2015). Stratospheric ozone destruction by the Bronze-Age Minoan eruption (Santorini volcano, Greece). *Sci. Rep.*, 5, article no. 12243.
- Carroll, M. R. and Blank, J. G. (1997). The solubility of H<sub>2</sub>O in phonolitic melts. *Am. Mineral.*, 82(5–6), 549–556.
- Carroll, M. R. and Rutherford, M. J. (1987). The stability of igneous anhydrite: experimental results and implications for sulphur behavior in the 1982 El Chichon trachyandesite and other evolved magmas. *J. Petrol.*, 28(5), 781–801.
- Carroll, M. R. and Webster, J. D. (1994). Volatiles in Magmas. *Rev. Mineral. Geochem.*, 30(1), 231–279.
- Cioni, R. (2000). Volatile content and degassing processes in the AD 79 magma chamber at Vesuvius (Italy). *Contrib. Mineral. Petrol.*, 140(1), 40–54.
- Cioni, R., Bertagnini, A., Santacroce, R., and Andronico, D. (2008). Explosive activity and eruption scenarios at Somma-Vesuvius (Italy): towards a new classification scheme. *J. Volcanol. Geotherm. Res.*, 178(3), 331–346.
- Cioni, R., Civetta, L., Marianelli, P., Metrich, N., Santacroce, R., and Sbrana, A. (1995). Compositional layering and syn-eruptive mixing of a periodically refilled shallow magma chamber: the AD 79 Plinian eruption of Vesuvius. *J. Petrol.*, 36(3), 739–776.
- Clemente, B., Scaillet, B., and Pichavant, M. (2004). The solubility of sulphur in hydrous rhyolitic melts. *J. Petrol.*, 45(11), 2171–2196.
- Devine, J. D., Sigurdsson, H., Davis, A. N., and Self, S. (1984). Estimates of sulphur and chlorine yield to the atmosphere from volcanic eruptions and potential climatic effects. *J. Geophys. Res.: Solid Earth*, 89(B7), 6309–6325.
- Di Salvo, S., Avanzinelli, R., Isaia, R., Zanetti, A., Druitt, T., and Francalanci, L. (2020). Crystal-mush reactivation by magma recharge: Evidence from the Campanian Ignimbrite activity, Campi Flegrei volcanic field, Italy. *Lithos*, 376, article no. 105780.
- Ducea, M. N., McInnes, B. I., and Wyllie, P. J. (1994). Sulphur variations in glasses from volcanic rocks: effect of melt composition on sulphur solubility. *Int. Geol. Rev.*, 36(8), 703–714.
- Engwell, S. L., Aspinall, W. P., and Sparks, R. S. J. (2015). An objective method for the production of isopach maps and implications for the estimation of tephra deposit volumes and their uncertainties. *Bull. Volcanol.*, 77(7), 1–18.
- Fabbrizio, A. and Carroll, M. R. (2008). Experimental constraints on the differentiation process and pre-eruptive conditions in the magmatic system of Phlegraean Fields (Naples, Italy). *J. Volcanol. Geotherm. Res.*, 171(1–2), 88–102.
- Fedele, F. G., Giaccio, B., Isaia, R., Orsi, G., Carroll, M., and Scaillet, B. (2007). *The Campanian Ignimbrite Factor: Towards a Reappraisal of the Middle to Upper Palaeolithic 'transition'*. Left Coast Press, Walnut Creek, CA.
- Ferry, J. M. and Baumgartner, L. (1987). Thermodynamic models of molecular fluids at the elevated pressures and temperatures of crustal metamorphism. *Rev. Mineral. Geochem.*, 17(1), 323–365.
- Forni, F., Bachmann, O., Mollo, S., De Astis, G., Gelman, S. E., and Ellis, B. S. (2016). The origin of a zoned ignimbrite: Insights into the Campanian Ignimbrite magma chamber (Campi Flegrei, Italy). *Earth Planet. Sci. Lett.*, 449, 259–271.
- Fowler, S. J., Spera, F. J., Bohrsen, W. A., Belkin, H. E., and De Vivo, B. (2007). Phase equilibria constraints on the chemical and physical evolution of the Campanian Ignimbrite. *J. Petrol.*, 48(3), 459–493.
- Gerlach, T. M., Westrich, H. R., and Symonds, R. B. (1996). Preeruption vapor in magma of the climactic Mount Pinatubo eruption: Source of the giant stratospheric sulfur dioxide cloud. In Newhall, C. G. and Punongbayan, R. S., editors, *Fire and Mud: Eruptions and Lahars of Mount Pinatubo, Philippines*, pages 415–433. Philippine Institute of Volcanology and Seismology, Quezon City.
- Giaccio, B., Hajdas, I., Isaia, R., Deino, A., and Nomade, S. (2017). High-precision C dating and Ar/Ar dating of the Campanian Ignimbrite (Y-5) reconciles the time-scales of climatic-cultural processes at 40 ka. *Sci. Rep.*, 7, article no. 45940.
- Graf, H. F. and Timmreck, C. (2001). A general climate model simulation of the aerosol radiative effects of the Laacher See eruption (10,900 BC). *J. Geophys. Res.: Atmospheres*, 106(D14), 14747–14756.
- Guo, S., Bluth, G. J. S., Rose, W. I., Watson, I. M., and Prata, A. J. (2004). Re-evaluation of SO<sub>2</sub> release of the 15 June 1991 Pinatubo eruption using ultraviolet and infrared satellite sensors. *Geochem. Geophys. Geosyst.*, 5(4), article no. Q04001.

- Harms, E., Gardner, J. E., and Schmincke, H. U. (2004). Phase equilibria of the Lower Laacher See Tephra (East Eifel, Germany): constraints on pre-eruptive storage conditions of a phonolitic magma reservoir. *J. Volcanol. Geotherm. Res.*, 134(1–2), 125–138.
- Harms, E. and Schmincke, H. U. (2000). Volatile composition of the phonolitic Laacher See magma (12,900 yr BP): implications for syn-eruptive degassing of S, F, Cl and H<sub>2</sub>O. *Contrib. Mineral. Petrol.*, 138(1), 84–98.
- Holloway, J. R. (1987). Igneous fluids. *Rev. Mineral. Geochem.*, 17(1), 211–233.
- Humphreys, M. C., Smith, V. C., Coumans, J. P., Riker, J. M., Stock, M. J., de Hoog, J. C. M., and Brooker, R. A. (2021). Rapid pre-eruptive mush reorganisation and atmospheric volatile emissions from the 12.9 ka Laacher See eruption, determined using apatite. *Earth Planet. Sci. Lett.*, 576, article no. 117198.
- Jakubowski, R. T., Fournelle, J., Welch, S., Swope, R. J., and Camus, P. (2002). Evidence for magmatic vapor deposition of anhydrite prior to the 1991 climactic eruption of Mount Pinatubo, Philippines. *Am. Mineral.*, 87(8–9), 1029–1045.
- Kandlbauer, J. and Sparks, R. S. J. (2014). New estimates of the 1815 Tambora eruption volume. *J. Volcanol. Geotherm. Res.*, 286, 93–100.
- Kepler, H. (2010). The distribution of sulphur between haplogranitic melts and aqueous fluids. *Geochim. Cosmochim. Acta*, 74(2), 645–660.
- Krueger, A., Krotkov, N., and Carn, S. (2008). El Chichón: The genesis of volcanic sulphur dioxide monitoring from space. *J. Volcanol. Geotherm. Res.*, 175(4), 408–414.
- Luhr, J. F., Carmichael, I. S., and Varekamp, J. C. (1984). The 1982 eruptions of El Chichón Volcano, Chiapas, Mexico: mineralogy and petrology of the anhydrite bearing pumices. *J. Volcanol. Geotherm. Res.*, 23(1–2), 69–108.
- Macdonald, R. (2002). Magmatism of the Kenya Rift Valley: a review. *Earth Environ. Sci. Trans. R. Soc. Edinburgh*, 93(3), 239–253.
- Marianelli, P., Sbrana, A., and Proto, M. (2006). Magma chamber of the Campi Flegrei supervolcano at the time of eruption of the Campanian Ignimbrite. *Geology*, 34(11), 937–940.
- Marshall, L. R., Maters, E. C., Schmidt, A., Timmreck, C., Robock, A., and Toohey, M. (2022). Volcanic effects on climate: recent advances and future avenues. *Bull. Volcanol.*, 84(5), article no. 54.
- Marti, A., Folch, A., Costa, A., and Engwell, S. (2016). Reconstructing the plinian and cognimbrite sources of large volcanic eruptions: A novel approach for the Campanian Ignimbrite. *Sci. Rep.*, 6(1), article no. 21220.
- Masotta, M., Kepler, H., and Chaudhari, A. (2016). Fluid-melt partitioning of sulphur in differentiated arc magmas and the sulphur yield of explosive volcanic eruptions. *Geochim. Cosmochim. Acta*, 176, 26–43.
- Metcalfe, A., Moune, S., Moretti, R., Komorowski, J. C., and Aubry, T. J. (2023). Volatile emissions from past eruptions at La Soufrière de Guadeloupe (Lesser Antilles): insights into degassing processes and atmospheric impacts. *Front. Earth Sci.*, 11, article no. 1143325.
- Moncrieff, D. H. S. (2000). *Sulphur solubility behaviour in evolved magmas: An experimental study*. Doctoral dissertation, University of Bristol.
- Moretti, R., Arienzo, I., Di Renzo, V., et al. (2019). Volatile segregation and generation of highly vesiculated explosive magmas by volatile-melt fining processes: the case of the Campanian Ignimbrite eruption. *Chem. Geol.*, 503, 1–14.
- Newman, S., Epstein, S., and Stolper, E. (1988). Water, carbon dioxide, and hydrogen isotopes in glasses from the ca. 1340 AD eruption of the Mono Craters, California: Constraints on degassing phenomena and initial volatile content. *J. Volcanol. Geotherm. Res.*, 35(1–2), 75–96.
- Niemeier, U., Richter, J. H., and Tilmes, S. (2020). Differing responses of the quasi-biennial oscillation to artificial SO<sub>2</sub> injections in two global models. *Atmos. Chem. Phys.*, 20(14), 8975–8987.
- Oppenheimer, C. (2002). Limited global change due to the largest known Quaternary eruption, Toba ≈ 74 kyr BP? *Quat. Sci. Rev.*, 21(14–15), 1593–1609.
- Oppenheimer, C. (2003). Climatic, environmental and human consequences of the largest known historic eruption: Tambora volcano (Indonesia) 1815. *Prog. Phys. Geogr.*, 27(2), 230–259.
- Oppenheimer, C., Fischer, T., and Scaillet, B. (2014). Volcanic degassing: process and impact. In Holland, H. D. and Turekian, K. K., editors, *Treatise on Geochemistry*, pages 111–179. Elsevier, Oxford, second edition.
- Parat, F. and Holtz, F. (2005). Sulfur partition coefficient

- cient between apatite and rhyolite: the role of bulk S content. *Contrib. Mineral. Petrol.*, 150(6), 643–651.
- Pardini, F., Burton, M., Vitturi, M. D. M., Corradini, S., Salerno, G., Merucci, L., and Di Grazia, G. (2017). Retrieval and intercomparison of volcanic SO<sub>2</sub> injection height and eruption time from satellite maps and ground-based observations. *J. Volcanol. Geotherm. Res.*, 331, 79–91.
- Parmigiani, A., Faroughi, S., Huber, C., Bachmann, O., and Su, Y. (2016). Bubble accumulation and its role in the evolution of magma reservoirs in the upper crust. *Nature*, 532(7600), 492–495.
- Peccia, A., Moussallam, Y., Plank, T., DallaSanta, K., Polvani, L., Burgisser, A., Larsen, J., and Schaefer, J. (2023). A new multi-method assessment of stratospheric sulfur load from the Okmok II caldera-forming eruption of 43 BCE. *Geophys. Res. Lett.*, 50(21), article no. e2023GL103334.
- Peng, G., Luhr, J. F., and Mcgee, J. J. (1997). Factors controlling sulfur concentrations in volcanic apatite. *Am. Mineral.*, 82(11–12), 1210–1224.
- Plunkett, G., Sigl, M., Schwaiger, H. F., et al. (2022). No evidence for tephra in Greenland from the historic eruption of Vesuvius in 79 CE: implications for geochronology and paleoclimatology. *Clim. Past*, 18, 45–65.
- Pouget, M., Moussallam, Y., Rose-Koga, E. F., and Sigurdsson, H. (2023). A reassessment of the sulfur, chlorine and fluorine atmospheric loading during the 1815 Tambora eruption. *Bull. Volcanol.*, 85(11), article no. 66.
- Reinig, F., Wacker, L., Jöris, O., et al. (2021). Precise date for the Laacher See eruption synchronizes the Younger Dryas. *Nature*, 595, 66–69.
- Robock, A., Ammann, C. M., Oman, L., Shindell, D., Levis, S., and Stenchikov, G. (2009). Did the Toba volcanic eruption of ~74 ka B.P. produce widespread glaciation? *J. Geophys. Res.*, 114(D10), article no. D10107.
- Rose Jr, W. I. (1977). Scavenging of volcanic aerosol by ash: atmospheric and volcanologic implications. *Geology*, 5(10), 621–624.
- Scaillet, B., Clémente, B., Evans, B. W., and Pichavant, M. (1998). Redox control of sulphur degassing in silicic magmas. *J. Geophys. Res.: Solid Earth*, 103(B10), 23937–23949.
- Scaillet, B., Luhr, J., and Carroll, M. R. (2003). Petrological and volcanological constraints on volcanic sulphur emissions to the atmosphere. *Geophys. Monogr. Am. Geophys. Union*, 139, 11–40.
- Scaillet, B. and Macdonald, R. (2006). Experimental and thermodynamic constraints on the sulphur yield of peralkaline and metaluminous silicic flood eruptions. *J. Petrol.*, 47(7), 1413–1437.
- Scaillet, B. and Oppenheimer, C. (2023). Reassessment of the sulfur and halogen emissions from the Millennium Eruption of Changbaishan (Paektu) volcano. *J. Volcanol. Geotherm. Res.*, 442, article no. 107909.
- Scaillet, B. and Oppenheimer, C. (2024). On the budget and atmospheric fate of sulfur emissions from large volcanic eruptions. *Geophys. Res. Lett.*, 51(12), article no. e2023GL107180.
- Scaillet, B. and Pichavant, M. (2003). Experimental constraints on volatile abundances in arc magmas and their implications for degassing processes. *Geol. Soc. Lond. Spec. Publ.*, 213(1), 23–52.
- Scaillet, B., Pichavant, M., and Cioni, R. (2008). Upward migration of Vesuvius magma chamber over the past 20,000 years. *Nature*, 455(7210), 216–219.
- Schiavi, F., Bolfan-Casanova, N., Buso, R., et al. (2020). Quantifying magmatic volatiles by Raman microtomography of glass inclusion-hosted bubbles. *Geochem. Perspect. Lett.*, 16, 17–24.
- Schmauss, D. and Keppler, H. (2014). Adsorption of sulphur dioxide on volcanic ashes. *Am. Mineral.*, 99(5–6), 1085–1094.
- Schmidt, A. and Black, B. A. (2022). Reckoning with the rocky relationship between eruption size and climate response: toward a volcano-climate index. *Annu. Rev. Earth Planet. Sci.*, 50(1), 627–661.
- Schmincke, H. U., Park, C., and Harms, E. (1999). Evolution and environmental impacts of the eruption of Laacher See Volcano (Germany) 12,900 a BP. *Quat. Int.*, 61(1), 61–72.
- Self, S., Gertisser, R., Thordarson, T., Rampino, M. R., and Wolff, J. A. (2004). Magma volume, volatile emissions, and stratospheric aerosols from the 1815 eruption of Tambora. *Geophys. Res. Lett.*, 31(20), article no. L20608.
- Sevink, J., Bakels, C., Van Hall, R., and Dee, M. (2021). Radiocarbon dating distal tephra from the Early Bronze Age Avellino eruption (EU-5 in the coastal basins of southern Lazio (Italy): uncertainties, results, and implications for dating distal tephra. *Quat. Geochronol.*, 63, article no. 101154.



- Sharma, K., Blake, S., Self, S., and Krueger, A. J. (2004). SO<sub>2</sub> emissions from basaltic eruptions, and the excess sulfur issue. *Geophys. Res. Lett.*, 31(13), article no. L13612.
- Sigl, M., Winstrup, M., McConnell, J. R., et al. (2015). Timing and climate forcing of volcanic eruptions for the past 2,500 years. *Nature*, 523(7562), 543–549.
- Signorelli, S. and Carroll, M. R. (2000). Solubility and fluid-melt partitioning of Cl in hydrous phonolitic melts. *Geochim. Cosmochim. Acta*, 64(16), 2851–2862.
- Signorelli, S., Vaggelli, G., and Romano, C. (1999). Pre-eruptive volatile (H<sub>2</sub>O, F, Cl and S) contents of phonolitic magmas feeding the 3550-year old Avelino eruption from Vesuvius, southern Italy. *J. Volcanol. Geotherm. Res.*, 93(3–4), 237–256.
- Signorelli, S., Vaggelli, G., Romano, C., and Carroll, M. (2001). Volatile element zonation in Campanian Ignimbrite magmas (Phlegrean Fields, Italy): evidence from the study of glass inclusions and matrix glasses. *Contrib. Mineral. Petrol.*, 140(5), 543–553.
- Silleni, A., Giordano, G., Isaia, R., and Ort, M. H. (2020). The magnitude of the 39.8 ka Campanian Ignimbrite eruption, Italy: method, uncertainties and errors. *Front. Earth Sci.*, 8, article no. 543399.
- Stock, M. J., Humphreys, M. C., Smith, V. C., Isaia, R., and Pyle, D. M. (2016). Late-stage volatile saturation as a potential trigger for explosive volcanic eruptions. *Nat. Geosci.*, 9(3), 249–254.
- Suhendro, I., Toramaru, A., Miyamoto, T., Miyabuchi, Y., and Yamamoto, T. (2021). Magma chamber stratification of the 1815 Tambora caldera-forming eruption. *Bull. Volcanol.*, 83(10), 1–20.
- Sulpizio, R., Cioni, R., Di Vito, M. A., Mele, D., Bonasia, R., and Dellino, P. (2010). The Pomici di Avelino eruption of Somma-Vesuvius (3.9 ka BP). Part I: stratigraphy, compositional variability and eruptive dynamics. *Bull. Volcanol.*, 72, 539–558.
- Taylor, I. A., Preston, J., Carboni, E., Mather, T. A., Grainger, R. G., Theys, N., Hidalgo, S., and Kilbride, B. M. (2018). Exploring the Utility of IASI for Monitoring Volcanic SO<sub>2</sub> Emissions. *J. Geophys. Res.: Atmospheres*, 123(10), 5588–5606.
- Textor, C., Sachs, P. M., Graf, H. F., and Hansteen, T. H. (2003). The 12 900 years BP Laacher See eruption: estimation of volatile yields and simulation of their fate in the plume. *Geol. Soc. Lond. Spec. Publ.*, 213(1), 307–328.
- Thomas, N., Jaupart, C., and Vergnolle, S. (1994). On the vesicularity of pumice. *J. Geophys. Res.: Solid Earth*, 99(B8), 15633–15644.
- Timmreck, C. (2012). Modeling the climatic effects of large explosive volcanic eruptions. *Wiley Interdiscip. Rev. Clim. Change*, 3(6), 545–564.
- Toohey, M., Krüger, K., Schmidt, H., Timmreck, C., Sigl, M., Stoffel, M., and Wilson, R. (2019). Disproportionately strong climate forcing from extratropical explosive volcanic eruptions. *Nat. Geosci.*, 12(2), 100–107.
- Toohey, M. and Sigl, M. (2017). Volcanic stratospheric sulfur injections and aerosol optical depth from 500 BCE to 1900 CE. *Earth Syst. Sci. Data*, 9, 809–831.
- Venugopal, S., Schiavi, F., Moune, S., Bolfan-Casanova, N., Druitt, T., and Williams-Jones, G. (2020). Melt inclusion vapour bubbles: the hidden reservoir for major and volatile elements. *Sci. Rep.*, 10(1), article no. 9034.
- Wadsworth, F. B., Llewellyn, E. W., Vasseur, J., Gardner, J. E., and Tuffen, H. (2020). Explosive-effusive volcanic eruption transitions caused by sintering. *Sci. Adv.*, 6(39), article no. eaba7940.
- Wallace, P. J. (2001). Volcanic SO<sub>2</sub> emissions and the abundance and distribution of exsolved gas in magma bodies. *J. Volcanol. Geotherm. Res.*, 108(1–4), 85–106.
- Wallace, P. J. (2005). Volatiles in subduction zone magmas: concentrations and fluxes based on melt inclusion and volcanic gas data. *J. Volcanol. Geotherm. Res.*, 140(1–3), 217–240.
- Wallace, P. J., Anderson Jr, A. T., and Davis, A. M. (1995). Quantification of pre-eruptive exsolved gas contents in silicic magmas. *Nature*, 377(6550), 612–616.
- Wallace, P. J. and Edmonds, M. (2011). The sulphur budget in magmas: evidence from melt inclusions, submarine glasses, and volcanic gas emissions. *Rev. Mineral. Geochem.*, 73(1), 215–246.
- Wallace, P. J., Kamenetsky, V. S., and Cervantes, P. (2015). Melt inclusion CO<sub>2</sub> contents, pressures of olivine crystallization, and the problem of shrinkage bubbles. *Am. Mineral.*, 100(4), 787–794.
- Wallace, P. J., Plank, T., Bodnar, R. J., Gaetani, G. A., and Shea, T. (2021). Olivine-hosted melt inclusions: a microscopic perspective on a complex magmatic world. *Annu. Rev. Earth Planet. Sci.*,

- 49(1), 465–494.
- Webster, J. D., De Vivo, B., and Tappen, C. (2003). Volatiles, magmatic degassing and eruptions of Mt. Somma-Vesuvius: constraints from silicate melt inclusions, Cl and H<sub>2</sub>O solubility experiments and modeling. In *Developments in Volcanology*, volume 5, pages 207–226. Elsevier, Amsterdam.
- Westrich, H. R. and Gerlach, T. M. (1992). Magmatic gas source for the stratospheric SO<sub>2</sub> cloud from the June 15, 1991, eruption of Mount Pinatubo. *Geology*, 20(10), 867–870.
- Wörner, G. and Schmincke, H. U. (1984). Mineralogical and chemical zonation of the Laacher See tephra sequence (East Eifel, W. Germany). *J. Petrol.*, 25(4), 805–835.
- Zajacz, Z., Candela, P. A., Piccoli, P. M., and Sanchez-Valle, C. (2012). The partitioning of sulphur and chlorine between andesite melts and magmatic volatiles and the exchange coefficients of major cations. *Geochim. Cosmochim. Acta*, 89, 81–101.

# *Comptes Rendus*

---

## *Géoscience*

### **Objectif de la revue**

Les *Comptes Rendus Géoscience — Sciences de la Planète* sont une revue électronique évaluée par les pairs de niveau international, qui couvre l'ensemble des domaines des sciences de la Terre et du développement durable.

Ils publient des articles originaux de recherche, des articles de synthèse, des mises en perspective historiques, des textes à visée pédagogique, ou encore des actes de colloque, en anglais ou en français, sans limite de longueur et dans un format aussi souple que possible (figures, données associées, etc.).

Depuis 2020, les *Comptes Rendus Géoscience — Sciences de la Planète* sont publiés avec le centre Mersenne pour l'édition scientifique ouverte, selon une politique vertueuse de libre accès diamant, gratuit pour les auteurs (pas de frais de publication) comme pour les lecteurs (accès libre, immédiat et pérenne).

**Directeur de la publication :** Étienne Ghys.

**Rédacteurs en chef :** Éric Calais, Michel Campillo, François Chabaux, Ghislain de Marsily.

**Éditeurs associés :** Jean-Claude André, Pierre Auger, Mustapha Besbes, Sylvie Bourquin, Yves Bréchet, Marie-Lise Chanin, Philippe Davy, Henri Décamps, Sylvie Derenne, Michel Faure, François Forget, Claude Jaupart, Jean Jouzel, Eric Karsenti, Amaëlle Landais, Sandra Lavorel, Yvon Le Maho, Mickaele Le Ravalec, Hervé Le Treut, Benoit Noetinger, Carole Petit, Valérie Plagnes, Pierre Ribstein, Didier Roux, Bruno Scaillet, Marie-Hélène Tusseau-Vuillemin, Élisabeth Vergès.

**Secrétaire éditoriale :** Adenise Lopes.

### **À propos de la revue**

Les *Comptes Rendus Géoscience — Sciences de la Planète* sont exclusivement publiés au format électronique.

Toutes les informations sur la revue, ainsi que le texte intégral de l'ensemble des articles, sont disponibles sur son site internet, à l'adresse <https://comptes-rendus.academie-sciences.fr/geoscience/>.

### **Informations pour les auteurs**

Pour toute question relative à la soumission d'un manuscrit, merci de consulter le site internet de la revue : <https://comptes-rendus.academie-sciences.fr/geoscience/>.

### **Contact**

Académie des sciences

23 quai de Conti

75006 Paris (France)

[cr-geoscience@academie-sciences.fr](mailto:cr-geoscience@academie-sciences.fr)



# COMPTES RENDUS DE L'ACADÉMIE DES SCIENCES

## *Géoscience* *Sciences de la Planète*

Volume 356, n° S1, 2024

### **Special issue / Numéro spécial**

Magma degassing and its impact on the Earth's atmosphere: from magma oceans to lava lakes / *Impact atmosphérique du dégazage magmatique : des océans de magma aux lacs de lave*

### **Guest editors / Rédacteurs en chef invités**

Manuel Moreira (Institut des Sciences de la Terre d'Orléans Université d'Orléans-CNRS-BRGM 1a rue de la Férollerie 45071 Orléans France), Bruno Scaillet (Institut des Sciences de la Terre d'Orléans Université d'Orléans-CNRS-BRGM 1a rue de la Férollerie 45071 Orléans France) and Clive Oppenheimer (Department of Geography, University of Cambridge, Downing Place, Cambridge CB2 3EN, UK)

### **Cover illustration / Illustration de couverture**

The persistent lava lake lying at the bottom of the crater of Ambrym volcano in Vanuatu, and the plume of gases and aerosol discharged by the convecting magma column sustaining the lava lake (credit: C. Oppenheimer).

## Contents / Sommaire

### **Bruno Scaillet, Clive Oppenheimer, Manuel Moreira**

Magma degassing and its impact on Earth's atmosphere: from magma oceans to lava lakes ..... 1-3

### **Stéphane Labrosse, Adrien Morison, Paul James Tackley**

Solid-state mantle convection coupled with a crystallising basal magma ocean ..... 5-21

### **Christèle Sanloup, Clémence Leroy, Benjamin Cochain, Tobias Grützner, Qi Chen, Yoshio Kono, Guoyin Shen**

Iodine speciation in basaltic melts at depth ..... 23-33

### **Francesco Vetere, Olivier Namur, Francois Holtz, Renat Almeev, Paola Donato, Francesco Frondini, Michele Cassetta, Alessandro Pisello, Diego Perugini**

Influence of volatiles (H<sub>2</sub>O and CO<sub>2</sub>) on shoshonite phase equilibria ..... 35-52

### **Camille Daffos, Caroline Martel, Laurent Arbaret, Rémi Champallier**

Bubble connectivity in experimentally-sheared crystal-bearing silicic melts ..... 53-70

### **Yves Moussallam, Clive Oppenheimer, Bruno Scaillet**

A novel approach to volcano surveillance using gas geochemistry ..... 71-84

### **Alessandro Aiuppa, Yves Moussallam**

Hydrogen and hydrogen sulphide in volcanic gases: abundance, processes, and atmospheric fluxes ..... 85-108

### **Bruno Scaillet, Clive Oppenheimer, Raffaello Cioni, Stéphane Scaillet, Yves Moussallam, Gaëlle Prouteau, Joan Andujar**

Constraining sulphur yields of trachytic and phonolitic volcanic eruptions: Tambora, Vesuvius, Laacher See and Campi Flegrei ..... 109-126

COMPTON'S FRIENDS OF THE ARTS SOCIETY  
DEPARTMENT OF SCIENCE



GOOD! JOIN US NOW!  
2021